



JOHANNES GUTENBERG
UNIVERSITÄT MAINZ

**The effect of primary cilia dysfunction in the retinal pigment epithelium
on retinal degeneration**

Dissertation

submitted to attain the academic degree
„**Doctor of Natural Sciences (Dr. rer. nat.)**“

Faculty of Biology
Johannes Gutenberg University Mainz

Sandra Schneider
Born on 10.10.1990 in Mannheim

Mainz, June 2023

Dean: Prof. Dr. Eckhard Thines
Institute of Molecular Physiology

1. Rapporteur: Prof. Dr. Helen Louise May-Simera
Institute of Molecular Physiology

2. Rapporteur: Prof. Dr. Uwe Wolfrum
Institute of Molecular Physiology

Date of the oral examination:

Annotation

The thesis presented here is cumulative and consists of 3 published publications (I, II, III) and a submitted manuscript (I). This work is written in English by mutual agreement with the first reviewer.

Publication I:

Patnaik SR, Kretschmer V, Brücker L, **Schneider S**, Volz AK, Oancea-Castillo LDR, May-Simera H: *Bardet-Biedl Syndrome proteins regulate cilia disassembly during tissue maturation*. Cell Mol Life Sci. 2019 Feb; 76(4):757-775. PMID: 30446775.

Publication II:

Schneider S, De Cegli R, Nagarajan J, Kretschmer V, Matthiessen PA, Intartaglia D, Hotaling N, Ueffing M, Boldt K, Conte I, May-Simera HL: *Loss of ciliary gene Bbs8 results in physiological defects in the retinal pigment epithelium*. Front Cell Dev Biol. 2021 Feb 18; 9:607121. PMID: 33681195.

Publication III:

Schneider S, Hotaling N, Campos M, Patnaik SR, Bharti K, May-Simera HL: *Generation of an inducible RPE-specific Cre transgenic-mouse line*. PLoS One. 2018 Nov 15; 13(11):e0207222. PMID: 30440011.

Manuscript I:

Kretschmer V*, **Schneider S***, Matthiessen PA, Reichert D, Hotaling N, Glasßer G, Lieberwirth I, Bharti K, De Cegli R, Conte I, Nandrot EF, May-Simera HL: *Ablation of primary cilia exclusively in the RPE leads to retinal degeneration and visual impairment*. Submitted to PLOS Biology.

Congress contributions

Excerpts of this dissertation have been presented at congresses:

- 12.07.2019 **Young Researcher Vision Camp**, Leibertingen, Germany
-
- 14.07.2019 *Presentation*: “Possible role of epithelial-to-mesenchymal transition underlying retinal pigment epithelium phenotype in cilia mutant mice”

Poster: Schneider S, Kretschmer V, Sehn E, May-Simera HL: “Ablation of primary cilia exclusively in the RPE leads to a pathogenic phenotype and consequent retinal degeneration”
- 22.03.2019 **Pro Retina Research Colloquium**, Potsdam, Germany
-
- 23.03.2019 *Poster*: Schneider S, Boxhorn S, May-Simera HL: “Possible role of epithelial-to-mesenchymal transition underlying retinal pigment epithelium phenotype in cilia mutant mice”
- 02.10.2018 **EMBO Workshop “Cilia 2018”**, Copenhagen, Denmark
-
- 05.10.2018 *Poster*: Schneider S, Boxhorn S, Schröder S, May-Simera HL: “Possible role of epithelial-to-mesenchymal transition underlying retinal pigment epithelium phenotype in cilia mutant mice”
- 24.04.2018 **3rd Life Science Meeting JGU**, Mainz, Deutschland

Presentation: “Generation of an inducible RPE-specific Cre transgenic mouse line”
- 13.04.2018 **Pro Retina Research Colloquium**, Potsdam, Germany
-
- 14.04.2018 *Poster*: Schneider S, Hotaling N, Arnheiter H, Bharti K, May-Simera HL: “Generation of an inducible RPE-specific Cre transgenic mouse line”
- 30.06.2017 **Young Researcher Vision Camp**, Leibertingen, Germany
-
- 02.07.2017 *Poster*: Schneider S, Hotaling N, Bharti K, May-Simera HL: “Complete ablation of the primary cilium in the retinal pigment epithelium using conditional transgenic mice”

List of abbreviations

AAVs	Adeno-associated viruses
ABCA4 / ABCR	ATP-binding cassette protein
AMD	Age-related macular degeneration
BBC	Basal body complex
BBS / LMBBS	Bardet-Biedl Syndrome / Laurence-Moon-Bardet-Biedl syndrome
CC	Connecting cilium
CD51	Integrin α -V
CEP290	Centrosomal protein 290
CNTF	ciliary neurotrophic factor
CP	Ciliary pocket
CR	Ciliary rootlet
CRALBP	Cellular retinaldehyde-binding protein
CRBP	Cellular retinol binding protein
EMT	Epithelial-to-mesenchymal transition
FAK	Focal adhesion kinase
fas-L	Fas-ligand
FGF	Fibroblast growth factor
GAS6	Growth-arrest-specific protein 6
GCL	Ganglion cell layer
IFT	Intraflagellar transport
ILG	Insulin-like growth factor
INL	Inner nuclear layer
IPL	Inner plexiform layer
IRBP	Interstitial retinol binding protein
IRD	Inherited retinal dystrophies
IS	Inner Segment
LCA10	Leber congenital amaurosis 10
LEDGF	Lens epithelium-derived growth factor
LRAT	Lecithin-Retinol-Acyltransferase
MCT-1	Mono-carboxylate transporter-1
MCT-3	Mono-carboxylate transporter-3
MerTK	Receptor-tyrosinase c-mer
MFG-E8	Milk fat globule-EGF8
MKS1	MKS Transition Zone Complex Subunit 1

List of abbreviations

MT	Microtubule
MTOC	Microtubule-organizing center
ON	Optic nerve
ONL	Outer nuclear layer
OPL	Outer plexiform layer
OS / POS	Outer segment / Photoreceptor outer segment
PDGF	Platelet-derived growth factor
PEDF	Pigment epithelium-derived factor
PM	Plasma membrane
PR	Photoreceptor
RDH5	11-cis-retinol dehydrogenase
RP	Retinitis pigmentosa
RPE	Retinal pigment epithelium
RPE65	Retinal pigment epithelium-specific 65 kDa protein
ST	Synaptic terminal
TGF- β	Transforming growth factor- β
TIMP	Tissue inhibitor of matrix metalloprotease
Tyrp2	Tyrosinase-related protein-2
USH1C	Usher syndrome 1C
VEGF	Vascular endothelial growth factor
YL	Y-Linkers
ZO-1	Zona occludens-1 / Tight junction protein 1

Table of contents

1	Introduction	1
1.1	Anatomy and physiology of the mammalian eye	1
1.2	Retina and RPE – A functional unit	2
1.2.1	Retina	2
1.2.1.1	Photoreceptor	3
1.2.2	Retinal pigment epithelium	4
1.2.2.1	Absorption of light	5
1.2.2.2	Epithelial transport	6
1.2.2.3	Glia/buffering of ions / homeostasis of the subretinal space	6
1.2.2.4	Visual cycle	6
1.2.2.5	Phagocytosis of photoreceptor outer segments	7
1.2.2.6	Secretion	8
1.3	Cilia	8
1.3.1	Cilia structure and function	9
1.3.2	Intraflagellar transport	10
1.3.3	Primary cilia and disease	11
1.3.4	Bardet-Biedl syndrome	12
1.3.4.1	Prevalence and epidemiology	12
1.3.4.2	Clinical features	12
1.3.4.3	Genetics of BBS and BBS proteins	13
1.3.5	Cilia in the RPE	14
2	Aim	15
3	Publications	17
	Publication I – Bardet–Biedl Syndrome proteins regulate cilia disassembly during tissue maturation (Published)	19
	Publication II – Loss of Ciliary Gene <i>Bbs8</i> Results in Physiological Defects in the Retinal Pigment Epithelium (First Author; Published)	21
	Publication III – Generation of an inducible RPE-specific Cre transgenic-mouse line (First Author; Published)	23
	Manuscript I – Ablation of primary cilia exclusively in the RPE leads to retinal degeneration and visual impairment in mice (Co-First Author; submitted)	25
4	Summary and discussion of the results	27
4.1	Effects of primary cilia dysfunction caused by <i>Bbs8</i> knockout on the mouse RPE	27
4.2	Effects of primary cilia loss exclusively in the RPE on the mouse RPE and visual function	29
5	Outlook	33
6	Summary	37
7	Zusammenfassung	39
8	Appendix	41
8.1	References	41
8.2	Allocation of the contributions made to the individual publications	44
8.3	CV	47
8.4	Acknowledgment	48
8.5	Publication IV – Tissue-dependent differences in Bardet-Biedl syndrome gene expression (Published)	49
9	Affidavit	51

1 Introduction

Defects in any ocular cell-type can cause various eye diseases, leading to visual impairment and, ultimately, blindness. These visual impairments have a reportedly higher prevalence in the ageing society, i.e., 6.24/1000 people aged 50–54 years and 68.6/1000 people aged 90–94 years, were blind in 2020 (Bourne *et al.*, 2021). In 2020, the ‘Vision Loss Expert Group of the Global Burden of Disease Study’ estimated 295 million people to have moderate to severe visual impairments, including retinal diseases such as age-related macular degeneration (AMD), glaucoma and diabetic retinopathy. Approximately 43.3 million people worldwide were estimated to suffer from blindness, whereas due to population growth the number of blind people could increase to up to 61.0 million by 2050 (Bourne *et al.*, 2021). A vast number of these retinal diseases are inherited and are associated with retinal degeneration, making the retina one of the most important tissues in the eye. Retinal degeneration and subsequent visual impairment is the most common phenotype associated with dysfunctional primary cilia; a small appendage-like organelle found in almost every vertebrate cell that is responsible for signaling (Waters and Beales, 2011; May-Simera, Nagel-Wolfrum and Wolfrum, 2017). As the eye is composed of a variety of ciliated cell types, it is not surprising that more than 100 genes have been associated with retinal dystrophies encode proteins, which localize to the cilium and/or the basal body (Sánchez-Bellver, Toulis and Marfany, 2021). Thus far, most research on retinal degeneration associated with ciliary dysfunction focuses on the neural retina of the eye. This is because the retina contains a highly specialized primary cilium in the photoreceptor (PR) cells (see **1.2.1**). However, the eye also contains other ciliated tissues and cell types, such as the cornea and the ciliary body among others. One of the most important, especially for the health of the retina, is the retinal pigment epithelium (RPE). The RPE has close contact to the retina and RPE cells engulf the outer segments of the photoreceptor making the RPE essential for retinal health (May-Simera, Nagel-Wolfrum and Wolfrum, 2017). Previous studies could show that RPE maturation defects precede photoreceptor degeneration (May-Simera *et al.*, 2018). However, how defects of the RPE affects retinal health and contributes to retinal degeneration has not yet been comprehensively studied and is therefore the overarching aim of this thesis.

1.1 Anatomy and physiology of the mammalian eye

The vertebrate eye can be divided into three layers: The outer layer, middle layer, and an inner layer. The outer layer consists of the cornea and the sclera. The cornea’s purpose is to refract and transmit light to the lens and the retina at the back of the eye. Furthermore,

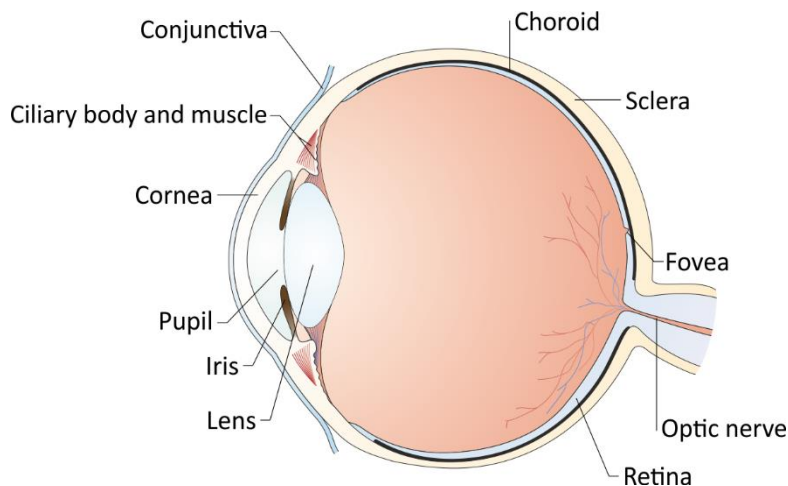


Figure 1: Schematic representation of the human eye.

Light enters the front part of the eye through the cornea and is transmitted through the pupil, lens, and vitreous cavity to the light-sensitive retina at the back of the eye. The sclera forms a connective tissue to protect the eyeball. The optic nerve, constituted by the axons coming from the retinal ganglion cells, transmits the visual signals to the brain. The proportions are sketchy and not to scale. Adapted from Wright *et al.*, 2010.

it protects the eye against infections and structural damage. The sclera, which forms a connective tissue coat to protect the eyeball, is responsible for maintaining the eyeball's shape.

The corneal limbus connects those two structures. The middle layer is composed of the iris, ciliary body, and the choroid. By controlling the size of the pupil, the iris regulates the amount of light reaching the retina. The ciliary

body is responsible for accommodation and aqueous humor production. The choroid is the vascularized layer, located between the sclera and the retina, providing oxygen and nutrients to the outer retinal layers. The inner layer is a complex layered structure of neuronal cells, known as the retina. The retina, where the light sensitive photoreceptors are located, is the place where light is captured and processed. For retinal health, the RPE, which comprised of highly polarized, pigmented epithelial cells, is indispensable. The RPE cells have a close functional interaction with the photoreceptor cells of the retina, enabling the RPE to fulfill a variety of important functions to maintain the retinal health and thus, visual function (**Figure 1**; see also **1.2.2**) (Strauss, 2005; Willoughby *et al.*, 2010; Wright *et al.*, 2010).

1.2 Retina and RPE – A functional unit

Inherited retinal dystrophies (IRD) are a group of diseases associated with retinal degeneration and visual impairment, making the retina the most important tissue to examine. However, since the retina and the RPE are seen as a “functional unit” and numerous IRD causing genes are primary cilia related, the RPE should not be left out of consideration (Waters and Beales, 2011; May-Simera, Nagel-Wolfrum and Wolfrum, 2017).

1.2.1 Retina

The unique organization of the vertebrate retina, which makes up the inner layer of the eye and surrounds the vitreous, is well-orchestrated for capturing and processing of visual signals. During embryogenesis, the retina emerges from the inner wall of the optic cup, while the outer wall from the optic cup becomes the RPE. This incident leads to the fact that both

the retina and the RPE being considered together as a functional unit, and without their close interconnection, visual function is impaired (Willoughby *et al.*, 2010; Wright *et al.*, 2010).

The retina is composed of six classes of neurons: (I) photoreceptors, (II) bipolar cells, (III) horizontal cells, (IV) amacrine cells, (V) ganglion cells, and (VI) Müllerian glia. While the latter functions as a supportive organizational backbone of the retina, the photoreceptors are responsible for capturing and processing the visual signals. Furthermore, the bipolar cells, amacrine cells, horizontal cells, and the Müllerian glia cells process the visual signals generated by the photoreceptors, ultimately transmitting them through the optic nerve to the brain (Willoughby *et al.*, 2010; Wright *et al.*, 2010). All these cells are arranged in parallel and form different layers of the retina: outer segments (OS), inner segments (IS), outer nuclear layer (ONL), outer plexiform layer (OPL), inner nuclear layer (INL), inner plexiform layer (IPL), ganglion cell layer (GCL), and optic nerve (ON). While the nuclei of the photoreceptors are located in the ONL, the photoreceptors connect with bipolar and horizontal cells in the OPL. The plexiform layers OPL and IPL are located around the INL, which is comprised of the nuclei of the Müllerian glia, the bipolar cells, the amacrine, and the horizontal cells. In the IPL, the bipolar and amacrine cells connect with ganglion cells (**Figure 2**). The nuclei of the ganglion cells lie in the GCL, whereas their axons lie in the ON (Willoughby *et al.*, 2010).

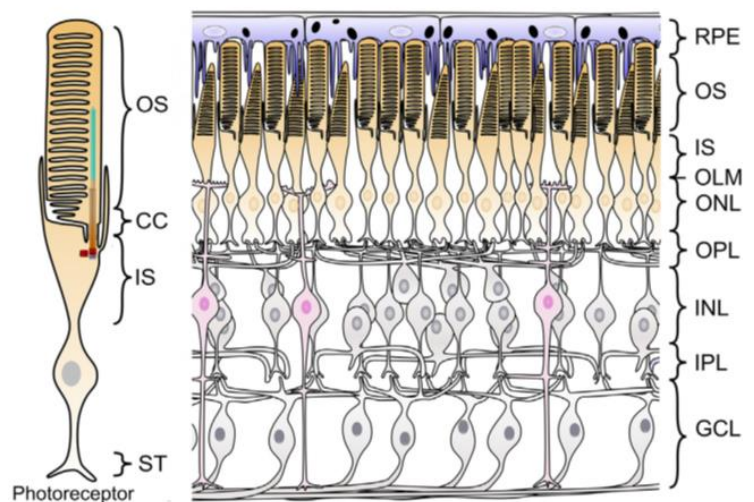


Figure 2: Schematic representation of the retinal layers and a photoreceptor. Cross-section through the retina, which consists of numerous cell layers composed of different cell types. The specialized primary cilium of the photoreceptor (PR) is highlighted. Number of different cell types is not proportionally representative. RPE: retinal pigment epithelium; OS: outer segment; IS: inner segment; OLM: outer limiting membrane; ONL: outer nuclear layer; OPL: outer plexiform layer; INL: inner nuclear layer; IPL: inner plexiform layer; GCL: ganglion cell layer; CC: connecting cilium; ST: synaptic terminal. May-Simera *et al.*, 2017.

1.2.1.1 Photoreceptor

The photoreceptor (PR) cells of the neural retina are the only cell-type in the mammalian body able to capture light and, contain a specialized primary cilium. With their unique structure and functions, the highly light-sensitive PR are the place where visual phototransduction takes place. Their chemical output is processed by the interneurons (bipolar cells, horizontal cells and amacrine cells) and transmitted to the visual cortex by ganglion cells. PR cells consist of four components: the outer segment (OS; POS) and the inner segment (IS),

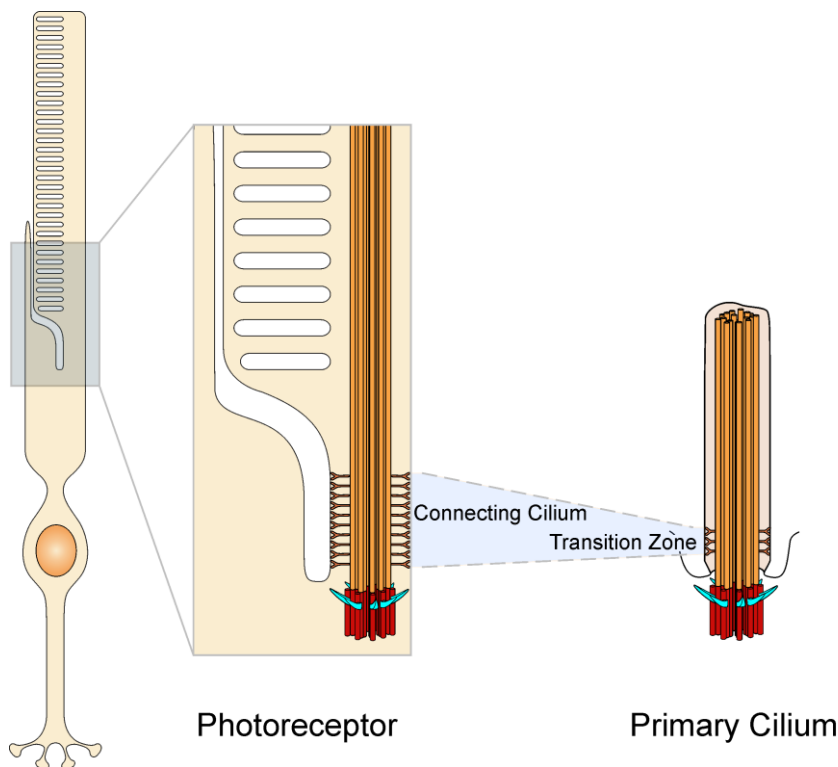


Figure 3: Schematic comparison of a photoreceptor and a primary cilium.

The rough structure of a primary cilium (right) and a photoreceptor outer segment (left, middle). The OS comprises the axoneme, while the connecting cilium can be seen analogously with the transition zone of the primary cilium. Adapted from May-Simera *et al.*, 2017.

connected by the connecting cilium (CC) and a synaptic terminal (ST) (**Figure 2**). The CC, corresponding to the transition zone of a primary cilium, and the POS form a highly modified primary cilium (May-Simera, Nagel-Wolfrum and Wolfrum, 2017) (**Figure 3**). The POS are tightly packed with the rhodopsin-encompassing discs, which are damaged by photo-oxidative energy. Consequently, the PR shed the ends of the POS that are phagocytosed by the RPE. How-

ever, to maintain visual function, the POS must be renewed constantly. Since the cellular machinery for protein and lipid biosynthesis is located in the IS, all required components for POS morphogenesis, maintenance and their sensory function must be transported to the POS. To enable this transport between the POS and IS, the specialized cilium of the PR and its transport machinery, known as intraflagellar transport (IFT), are indispensable (Chuang, Zhao and Sung, 2007; Fliegauf, Benzing and Omran, 2007; Wright *et al.*, 2010; Ishikawa and Marshall, 2011; May-Simera, Nagel-Wolfrum and Wolfrum, 2017).

One of the reasons for the importance of primary cilia for the retina and therefore vision is that at least 53 out of 158 of the identified genes associated with retinal dystrophies encode proteins, which localize to the cilium and/or the basal body, and vice versa, mutations in more than 100 ciliary genes have been associated with retinal dystrophies (Estrada-Cuzcano *et al.*, 2012; Sánchez-Bellver, Toulis and Marfany, 2021). Due to its numerous functions, the RPE is indispensable for health and maintenance of the retina, and a defect in one of these tissues affects the other. This leads to the fact that both are considered as a functional unit.

1.2.2 Retinal pigment epithelium

The RPE is a monolayer of pigmented epithelial cells, which intercalates between the photoreceptors and the choriocapillaris. The RPE cells form long apical microvilli, which engulf

the POS. The basolateral membrane of the RPE faces the Bruch's membrane, which separates the RPE from the choriocapillaris (Strauss, 2005; Willoughby *et al.*, 2010). With its numerous functions, which are explained further below, the RPE is indispensable for maintenance and health of the retina (**Figure 4**). As part of the blood-retina barrier, it is responsible for exchange of substances. From the subretinal space, the RPE transports ions, water, and metabolic end-products to the blood. In turn, it takes up nutrients (i.e., glucose, retinol) and transports it to the photoreceptors. Furthermore, the RPE is responsible for the visual cycle of retinal. As photoreceptors are not capable to re-isomerize all-*trans*-retinal into 11-*cis*-retinal, the RPE takes over this function. This is important to maintain the excitability of the photoreceptors – the basic prerequisite for visual function. Phagocytosis of shed POS is another important function of RPE cells. The RPE digests the POS and reprocesses essential substances, which then are transported back into the PR. Thus, new POS can be built. Due to its melanin pigmentation, the RPE absorbs incident light energy, which is focused by the lens on the retina (Strauss, 2005).

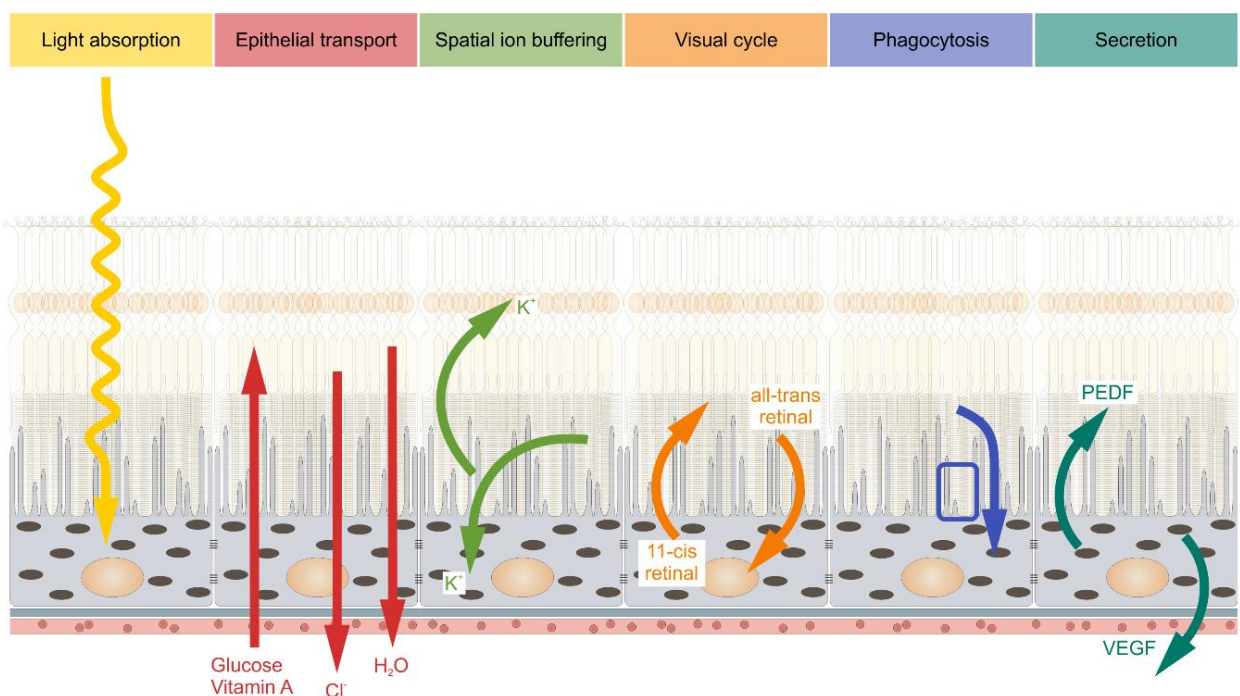


Figure 4: Schematic representation of the major functions of the RPE.

By intercalating between the retina and the choroid, the RPE performs functions essential to the health and maintenance of the retina, which are: light absorption, epithelial transport, spatial ion buffering, visual cycle, phagocytosis and secretion. PEDF: pigment epithelium-derived growth factor; VEGF: vascular epithelium growth factor. Adapted from Strauss, 2005.

1.2.2.1 Absorption of light

Incident light is focused onto the macula lutea by the lens. This pools photo-oxidative energy in the retina. Due to its melanin pigmentation, the RPE is capable of absorbing scattered light. Concentrated photo-oxidative energy in the retina leads to a damage of the POS, which then must be renewed. RPE cells accomplish this by phagocytosis of the destroyed

POS. However, RPE cells must be resistant against free radicals, photo-oxidative exposure, and light energy. Light-dark cycle-dependent movement of melanosomes, antioxidants, and repair mechanism of damaged molecules achieves this (Strauss, 2005).

1.2.2.2 Epithelial transport

With its location between the choroid and the POS, the RPE forms with its many lateral tight-junctions a blood-retina barrier. This blood-retina barrier is essential for protection of from influences coming from the blood through epithelial transport. This epithelial transport includes supply of nutrients to the photoreceptors, removal of water and metabolites from the retina, as well as control of the ion homeostasis in the subretinal space. Furthermore, the blood-retina barrier is important for immune reactions of the eye. Photoreceptors are dependent on a constant supply of metabolites, such as glucose, retinal, and ω -3 fatty acids. Those metabolites are taken up from the blood by the RPE and transferred to the PR. Furthermore, the RPE has to transfer water, ions and metabolic end products from the retina towards the blood. Due to its high density, the retina has a high metabolic rate. The high metabolic activity results in accumulation of metabolic water in the retina, as well as in the production of lactic acid. All these substances have to be transferred out of the retina. Water is transported out from the subretinal space by the RPE cells via a Cl^- -dependent active transport. This Cl^- -dependent transport is in turn driven by a Na^+/K^+ -ATPase. RPE cells remove a large amount of lactic acid via the mono-carboxylate transporter-1 (MCT-1) and the mono-carboxylate transporter-3 (MCT-3) (Strauss, 2005).

1.2.2.3 Glia/buffering of ions / homeostasis of the subretinal space

Due to other cell types in the retina, changes in the subretinal space can occur very quickly. To maintain signal transduction of visual information, the RPE has to compensate these changes rapidly. To obtain proper compensation, fast epithelial transport is needed. Therefore, the RPE has voltage-dependent ion channels. In dark conditions, the cGMP-dependent cation channels of the POS are open and Na^+ and Ca^{2+} enter the PR. This influx is counterbalanced by an outflow of K^+ . When light excites the PR, the cGMP-dependent channels close and less K^+ streams out. Additionally, Na^+/K^+ -ATPase takes up K^+ back into the PS resulting in a 2.5-fold lower K^+ -concentration in the subretinal space. With its apical membrane, which is dominated by K^+ conductance, the RPE compensates this (Strauss, 2005).

1.2.2.4 Visual cycle

The visual cycle is essential for maintaining visual functions. This does not only happen in the RPE, but also further in the discs of the POS. Absorption of a photon by rhodopsin leads to an isomerization of its chromophore, 11-*cis* retinal into all-*trans* retinal. Subsequently,

all-*trans* retinal conjugated with phosphatidylethanolamine is transported to the cytosolic space by an ATP-binding cassette protein (ABCA4 or ABCR). In the cytoplasm, a membrane bound retinol-dehydrogenase reduces all-*trans* retinal to all-*trans* retinol. All-*trans* retinol is transported into the subretinal space where it is loaded to an interstitial retinol binding protein (IRBP), and afterwards transported into the RPE. In the RPE all-*trans* retinol is transferred to the cellular retinol binding protein (CRBP) and delivered to a protein complex composed to Lecithin-Retinol-Acyltransferase (LRAT), Retinal pigment epithelium-specific 65 kDa protein (RPE65), 11-*cis*-retinol dehydrogenase (RDH5) and cellular retinaldehyde-binding protein (CRALBP). This protein complex catalyzes the reaction from all-*trans* retinol to 11-*cis* retinal: “*esterification of retinol by adding an acyl group (LRAT), re-isomerization using the energy from ester-hydrolysis (RPE65) and oxidation (RDH5)*” (Strauss, 2005). CRALBP accelerates this reaction and binds 11-*cis* retinal to release it afterwards to IRBP which transports it back to the photoreceptors. The photoreceptor is able to be activated again by light excitation.

The visual cycle has to be adapted to different conditions such as vision in darkness or light. Therefore, the storage of retinal and the adaptation of the reaction speed of the visual cycle are important. Vision in darkness requires a lower turnover rate of the visual cycle compared to vision in light. Whereas, in fast transition from dark into light a large amount of 11-*cis* retinal is required. This amount of 11-*cis* retinal is provided by various retinal pools of retinal binding proteins. The amount of 11-*cis* retinal in the rod outer segments is the first pool. After reduction of the level of the first pool, refilling is started by uptake from the IRBP in the subretinal space, which forms the second pool. CRALBP refills the second pool and can be refilled by RPE65 (Strauss, 2005; Wright *et al.*, 2010).

1.2.2.5 Phagocytosis of photoreceptor outer segments

As mentioned in section 1.2.1.1, photo-oxidative energy in the retina leads to a damage of the POS. To maintain visual function, the POS must be renewed constantly. This occurs diurnally via phagocytosis by the RPE. The interplay of the tree receptors CD36, receptor-tyrosinasekinase c-mer (MerTK) and $\alpha_v\beta_5$ integrin are involved into regulation of phagocytosis by the RPE. The macrophage scavenger receptor CD36 is required for internalization of the POS, MerTK activates phagocytosis and $\alpha_v\beta_5$ integrin initiates phagocytosis, and is required for binding of the POS. Furthermore, $\alpha_v\beta_5$ integrin is a complex of two proteins: α_v integrin (CD51) and β_5 integrin (Sheppard, 2002). $\alpha_v\beta_5$ integrin is activated by the RPE-specific glycoprotein milk fat globule-EGF8 (MFG-E8). This activation is as well essential for POS binding. Following this, focal adhesion kinase (FAK) is activated and phosphorylates MerTK. MerTK is now activated and in turn activates a second messenger cascade. Growth-arrest-specific protein 6 (GAS6), the natural ligand of MerTK, is expressed in the retina and

overexpressed in the RPE. However, the mechanisms underlying the activation of MerTK are not known (Strauss, 2005).

1.2.2.6 Secretion

RPE cells interact on either side with PR and epithelial cells of the choriocapillaris, respectively. For this communication various factors are secreted by RPE cells, i.e., ATP, Fas-ligand (Fas-L), fibroblast growth factors (FGF-1, FGF-2, FGF-5), transforming growth factor- β (TGF- β), insulin-like growth factor-1 (ILG-1), ciliary neurotrophic factor (CNTF), platelet-derived growth factor (PDGF), vascular endothelial growth factor (VEGF), lens epithelium-derived growth factor (LEDGF), interleukins, tissue inhibitor of matrix metalloprotease (TIMP) and pigment epithelium-derived factor (PEDF). In the healthy eye, certain factors are constantly secreted, like PEDF, VEGF and TIMP. Pathological conditions, like hypoxia and metabolic stress, lead to secretion of other factors (Strauss, 2005).

1.3 Cilia

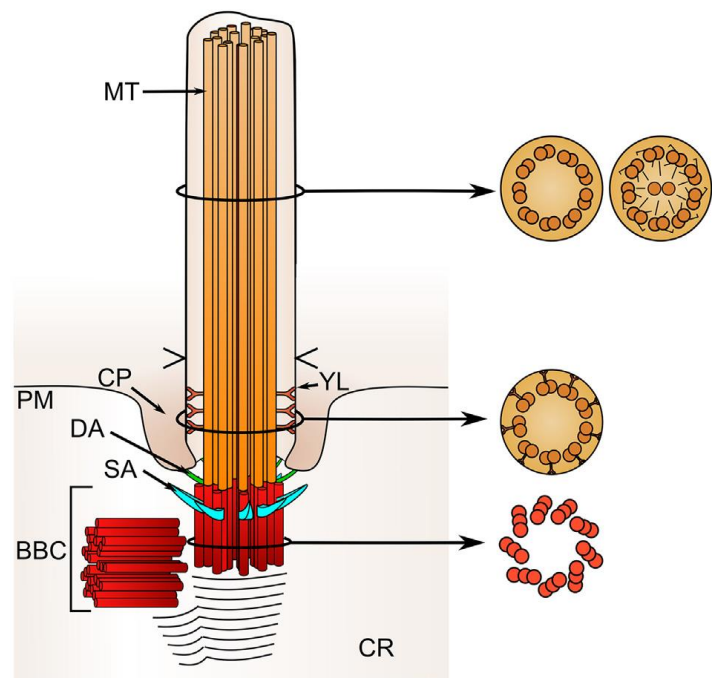
As mentioned above, the retina and the RPE, which are both ciliated tissues of the eye, are considered as a functional unit. Cilia are microtubule-based organelles extending from the cell membrane on almost every cell type in vertebrates. After being neglected for years, cilia have emerged as key organelles in a variety of developmental and physiological processes. Defects in ciliary assembly and function lead to a wide range of diseases, collectively termed ciliopathies. Since many of the symptoms are attributed to primary cilia dysfunction, it is fundamental to understand the primary cilium thus being able to unravel pathological mechanisms underlying ciliopathies and designing new treatment strategies (Fliegauf, Benzing and Omran, 2007; Ishikawa and Marshall, 2011; May-Simera, Nagel-Wolfrum and Wolfrum, 2017). As already pointed out, primary cilia are indispensable for visual function. In the retina, the highly specialized primary cilia transport components needed for POS morphogenesis, maintenance, and sensory function (Chuang, Zhao and Sung, 2007; Fliegauf, Benzing and Omran, 2007; May-Simera, Nagel-Wolfrum and Wolfrum, 2017). However, as part of this work, we demonstrated that in mouse RPE, primary cilia can only be found during development and disassemble as the tissue matures, highlighting their role in signaling during development (**Publication I**). With more than 100 ciliary genes being associated with retinal dystrophies and therefore accounting for almost 25% of retinal diseases, primary cilia dysfunction has been associated with a growing number of non-syndromic retinal dystrophies (Sánchez-Bellver, Toulis and Marfany, 2021).

1.3.1 Cilia structure and function

All cilia share a common structural composition that is composed of a long microtubule-based axoneme surrounded by a membrane interconnected with the plasma membrane of the cell. The axoneme itself is composed of nine peripheral microtubules-doublets (outer doublets) arranged in parallel. These microtubules-doublets are constituted of one complete microtubule (A tubule) and an attached incomplete second microtubule (B tubule) (Fliegeauf, Benzing and Omran, 2007; Ishikawa and Marshall, 2011; May-Simera, Nagel-Wolfrum and Wolfrum, 2017) (**Figure 5**).

Figure 5: Schematic representation of a cilium.

The axoneme is composed of nine peripheral microtubule (MT)-doublets extending from the microtubule-triplets of the mother centriole. Motile cilia have an additional central pair of MT-doublets, radial spikes, and inner and outer dynein arms to drive their motility, while primary cilia are comprised of only the nine peripheral MT-doublets. At the transition zone the axoneme is connected to the ciliary membrane by Y-linkers (YL). The ciliary pocket (CP) is formed at the base of the cilium via invagination of the plasma membrane (PM). Both the mother centriole (basal body) and the daughter centriole form the basal body complex (BBC). The ciliary rootlet (CR) extends away from the basal body complex. The cross sections through ciliary compartments show the typical structure of the axoneme ($9 \times 2+0$ microtubule arrangement with Y-linkers (YL))



and the centrioles ($9 \times 3+0$ microtubule arrangement) of the basal body. DA: Distal appendages, SA: Sub-distal appendages, > <: basal plate (motile cilia). May-Simera *et al.*, 2017.

While primary cilia are comprised of a '9+0' structure with nine outer doublets, motile cilia consist of a '9+2' structure with nine outer doublets and a pair of central microtubules (central pair). The microtubule doublets of motile cilia are connected by nexin and radial spokes that extend into the axonemal center and are necessary for ciliary movement. Furthermore, dynein arms are attached to the A tubules to support ciliary bending (Fliegeauf, Benzing and Omran, 2007; Ishikawa and Marshall, 2011; May-Simera, Nagel-Wolfrum and Wolfrum, 2017). However, the nonmotile kinocilium of mechanosensitive hair cells, composed of a '9+2' structure, demonstrates that a '9+2' structure does not automatically lead to motility of cilia (May-Simera, Nagel-Wolfrum and Wolfrum, 2017). At the proximal end, the nine outer doublets elongate from the basal body, a specialized centriole showing a '9+3' microtubular structure, where the microtubules are embedded in the pericentriolar material. During cell cycle quiescence, centrioles move to the apical cell membrane, where the mother centriole, which has subdistal and distal appendages, gives rise to the axoneme and

functions as a microtubule-organizing center (MTOC) for cytoplasmic microtubules. At the distal end of the centrioles, the microtubules-triplets convert into the microtubules-doublets, also known as the transition zone (TZ), which emerges as being crucial for regulation of ciliary function (Fliegauf, Benzing and Omran, 2007; Ishikawa and Marshall, 2011; Kobayashi and Dynlacht, 2011; May-Simera, Nagel-Wolfrum and Wolfrum, 2017). At the ciliary distal end, also referred to as ciliary tip, the microtubule plus ends are located. Here, the axoneme is assembled or disassembled and the switchover between anterograde and retrograde intraflagellar transport takes place. Furthermore, the ciliary tip – in addition to the ciliary membrane – harbors many signaling components (Ishikawa and Marshall, 2011; May-Simera, Nagel-Wolfrum and Wolfrum, 2017).

Although motile cilia and primary cilia share a common architecture, they exert numerous tissue-specific functions during development, tissue morphogenesis and physiology. Due to the ability to move, motile cilia are crucial for processes involving extracellular fluid flow. To generate fluid movement, a huge number of motile cilia beat coordinated in wave-like patterns (Fliegauf, Benzing and Omran, 2007; Ishikawa and Marshall, 2011). In contrast to that, non-motile primary cilia transduce extracellular stimuli, such as signaling molecules or osmolarity, thus initiating signaling pathways within the cells (Fliegauf, Benzing and Omran, 2007; Ishikawa and Marshall, 2011; May-Simera, Nagel-Wolfrum and Wolfrum, 2017).

1.3.2 Intraflagellar transport

As cilia lack the ability to synthesize all proteins required for assembly, function and maintenance, those molecules must be transported from the site of synthesis to the cilium. While trafficking to the base of the cilium occurs via polarized vesicle trafficking, a more specialized form of trafficking is required for trafficking towards the ciliary tip. The protein transport along the ciliary axoneme is known as intraflagellar transport (IFT) and is conducted by protein complexes, also known as IFT particles. This transport occurs bidirectionally: anterograde towards the ciliary tip and retrograde towards the ciliary base. A functional IFT is essential for cilia assembly, function, and its homeostasis. In many diseases, including retinal degeneration and Bardet-Biedl Syndrome, IFT is disrupted (Hao and Scholey, 2009; Goetz and Anderson, 2010; Ishikawa and Marshall, 2011). IFT particles are enriched in the periciliary region near the basal body and are subdivided into two large complexes: IFT complex A and IFT complex B. IFT complex A consists of IFT43, IFT121, IFT122, IFT139, IFT140 and IFT144, and IFT complex B, consists of IFT20, IFT22, IFT25, IFT27, IFT46, IFT52, IFT54, IFT57, IFT70, IFT74, IFT80, IFT81, IFT88, IFT172. While IFT complex A is responsible for the retrograde transport, the IFT complex B performs the anterograde transport, which is essential for assembly and a proper function of cilia. At the ciliary base,

the IFT machinery and its cargo is assembled and via the motor protein kinesin-2 the anterograde transport is conducted. Along with the IFT particles and the cargo, the inactive retrograde IFT-dynein motor protein is also carried towards the ciliary tip. At the ciliary tip, the IFT machinery undergo a turnover, including inactivation of the anterograde motor protein, cargo unloading and dissociation of the IFT complexes. For the retrograde transport, the IFT machinery is assembled again, cargo together with the inactivated anterograde motor protein is uploaded and the retrograde motor protein dynein is activated. At the ciliary base, the IFT machinery is disassembled (**Figure 6**) (Hao and Scholey, 2009; Ishikawa and Marshall, 2011; May-Simera, Nagel-Wolfrum and Wolfrum, 2017).

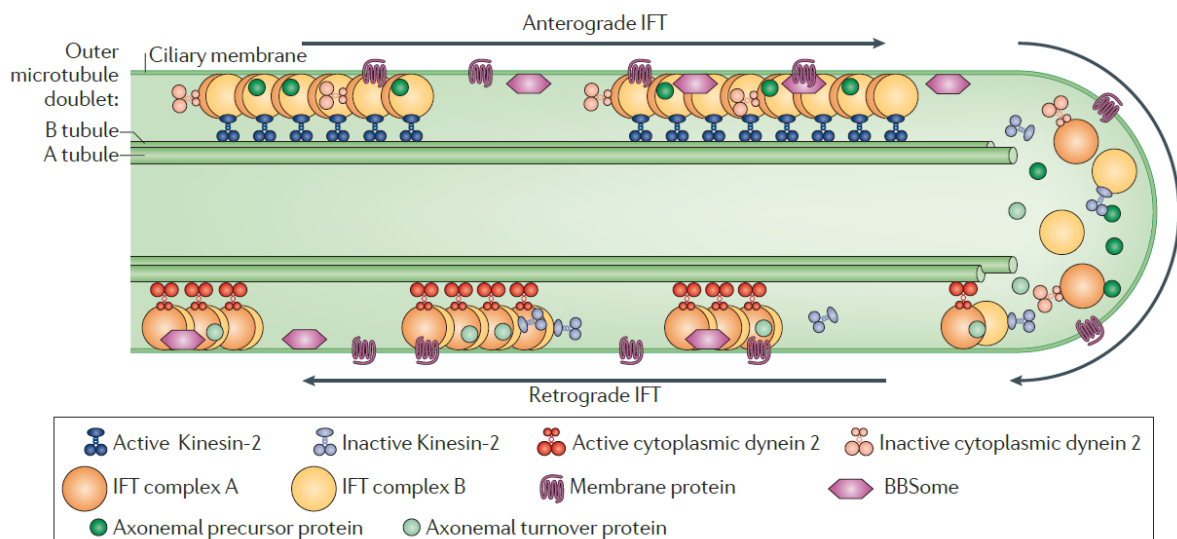


Figure 6: Intraflagellar transport machinery.

The anterograde intraflagellar transport (IFT) motor, Kinesin-2, transport IFT complexes, axonemal precursor proteins and inactive dynein 2 to the ciliary tip. At the ciliary tip, the IFT trains release the axonemal proteins and experience a rearrangement of their conformation to drive retrograde IFT. Dynein 2 is activated and mediates the retrograde IFT towards the cell body. Ishikawa and Marshall, 2011.

1.3.3 Primary cilia and disease

Disorders associated with mutations in cilia-related genes resulting in defective cilia are termed ciliopathies. Since almost every cell comprises a primary cilium, cilia dysfunction leads to a variety of different phenotypes. The fact that over 40 genes are associated with ciliopathies, many phenotypic overlaps within the different ciliopathies are found (Waters and Beales, 2011; May-Simera, Nagel-Wolfrum and Wolfrum, 2017). Retinal degeneration is one of the most common phenotypes associated with all syndromic ciliopathies. Thus, it is not surprising that over 100 ciliary genes have been associated with retinal dystrophies (Sánchez-Bellver, Toulis and Marfany, 2021). Furthermore, primary cilia dysfunction has been associated with a growing number of non-syndromic retinal dystrophies, such as retinitis pigmentosa (RP) (Tobin and Beales, 2009; Waters and Beales, 2011; May-Simera, Nagel-Wolfrum and Wolfrum, 2017). This is shown in **Table 1**.

Table 1: Phenotypic overlap among ciliopathies. Adapted from Tobin and Beales, 2009.

	BBS	MKS	JBTS	JATD	OFD1	MKKS	SLS	NPH	LCA	ALMS
Retinopathy	✓	✓	✓	✓			✓	✓	✓	✓
Obesity	✓									✓
Polydactyly	✓	✓	✓	✓	✓	✓				
Kidney disease	✓	✓	✓	✓	✓		✓	✓		
Situs inversus	✓	✓	✓				✓			
Cognitive impairment	✓	✓	✓		✓			✓	✓	✓

BBS, Bardet-Biedl syndrome; MKS, Meckel Gruber syndrome; JBTS, Joubert syndrome; JATD, Jeune syndrome; OFD1, Oro-facial-digital syndrome type 1; SLS, Senior-Loken syndrome; NPH, Nephronophthisis; ALMS, Alstrom syndrome.

1.3.4 Bardet-Biedl syndrome

In 1866, John Zachariah Laurence and Robert Moon described siblings suffering retinal dystrophy, obesity, locomotor, and cognitive impairments (Forsythe and Beales, 2013). Between 1920 and 1922, George Bardet and Arthur Biedl described other siblings similarly affected. However, in addition they observed post-axial polydactyly. Henceforth that condition was called Laurence-Moon-Bardet-Biedl syndrome (LMBBS). Nowadays the standard term is Bardet-Biedl syndrome (BBS) (Forsythe and Beales, 2013; Valverde, Castro-Sánchez and Álvarez-Satta, 2015). Since BBS patients exhibit multisystemic features associated with primary cilia dysfunction, BBS is considered as the archetypical ciliopathy since patients exhibit all phenotypes associated with ciliary dysfunction (**Table 1**) (Waters and Beales, 2011; May-Simera, Nagel-Wolfrum and Wolfrum, 2017).

1.3.4.1 Prevalence and epidemiology

BBS is a rare disease with low prevalence ranging from 1:125,00-1:160,000 in Europe and 1:100,000-1:140,00 in Northern America. However, due to consanguinity isolated populations like Faroe Islands or Newfoundland show higher prevalence (1:3,700, respectively 1:17,500) (Valverde, Castro-Sánchez and Álvarez-Satta, 2015).

1.3.4.2 Clinical features

BBS has diverse clinical manifestations, showing distinct inter- and intra-familial variability. Additionally, many symptoms are not present in younger people. They develop a BBS phenotype throughout the first decade of life, resulting in a diagnosis in late childhood or early adulthood (Forsythe and Beales, 2013; Valverde, Castro-Sánchez and Álvarez-Satta, 2015). Retinitis pigmentosa is the most frequent phenotype of BBS. Furthermore, 72-92% of the patients suffer from obesity. **Table 2** summaries the clinical features of BBS and their frequency among the patients. In the absence of genetic testing, four primary features or three

primary and two secondary features are required for the final diagnosis of BBS (Beales *et al.*, 1999; Forsythe and Beales, 2013).

Table 2: Clinical features of BBS and their prevalence.

Primary features	
Rod-cone dystrophy	93%
Obesity	72-92%
Polydactyly	63-81%
Learning Disabilities	61%
Genital anomalies	59-98%
Renal anomalies	53%
Secondary features	
Speech deficit	54-81%
Brachydactyly / syndactyly	46-100% / 8-95%
Developmental delay	50-91%
Ataxia / poor coordination / imbalance	40-86%
Diabetes mellitus	6-48%
Dental anomalies	51%
Left ventricular hypertrophy / congenital heart disease	7%

1.3.4.3 Genetics of BBS and BBS proteins

BBS is a rare autosomal recessive disease. However, the phenotypic variability and genetic heterogeneity suggest an oligogenic inheritance (Valverde, Castro-Sánchez and Álvarez-Satta, 2015). To date over 21 different BBS genes have been identified so far and all of them are inevitable for proper cilia function. Due to new analysis methods, the number of known BBS genes is still likely to increase (Suspitsin and Imyanitov, 2016).

BBS1, BBS2, BBS4, BBS5, BBS7, BBS8 and BBS9 form the BBSome, a 438 kDa multiprotein complex. The BBSome locates to cytoplasmic non-membranous centriolar satellites and to the ciliary membrane. The BBSome interacts with BBS3, a GTPase, and Rab8. Together they facilitate IFT. An impairment of any protein of the BBSome leads to a dysfunctional cilium causing degeneration and cell death (Forsythe and Beales, 2013; Valverde, Castro-Sánchez and Álvarez-Satta, 2015; May-Simera, Nagel-Wolfrum and Wolfrum, 2017). BBS6, BBS10 and BBS12 are members of the group II chaperonin family present in the pericentriolar material and basal bodies. They show the architecture of a chaperonin; however, without conserved specific insertion regions. They form a chaperonin complex together with six other group II chaperonins of the CCT/TRiC family. This chaperonin complex is responsible for a proper folding and assembly of the BBSome. All other BBS genes are associated with cilia function, either at the basal body (BBS13, BBS14, BBS15, BBS16) or they have other cilia-related function (BBS3, BBS11, BBS19, BBS20, NPHP1) (Forsythe and Beales, 2013;

Valverde, Castro-Sánchez and Álvarez-Satta, 2015; Suspitsin and Imyanitov, 2016; May-Simera, Nagel-Wolfrum and Wolfrum, 2017). Most of the BBS patients show mutations in *BBS1* or *BBS10* (23.3% and 20%, respectively). At least 21 genes associated with BBS: BBS1-12, BBS13 (MKS1), BBS14 (CEP290), BBS15 (WDCPC), BBS16 (SDCCAG8/C2ORF86), BBS17-21. Mutations of these genes are found in 70-80% of all patients, suggesting that there must be more genes. In *BBS1* and *BBS10* the majority of those mutations are found (Forsythe and Beales, 2013; Valverde, Castro-Sánchez and Álvarez-Satta, 2015).

The BBS proteins are expressed in many different tissues, such as the RPE, retina or kidney, of ciliated organisms. Their importance for maintenance and function of cilia makes them necessary for development and homeostasis of the tissue.

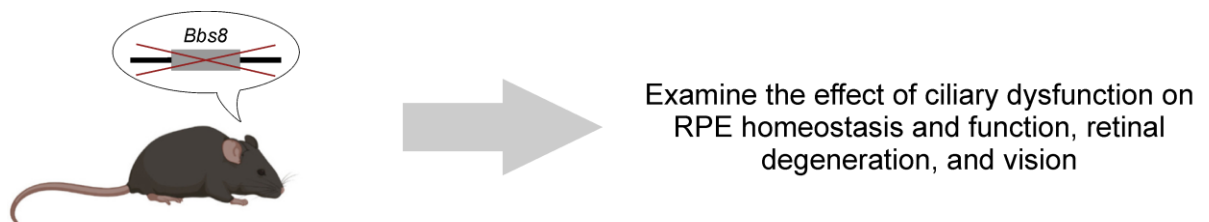
1.3.5 Cilia in the RPE

Primary cilia are present on almost every vertebrate cell type. They play important roles in many physiological and developmental processes. However, defects in assembly, disassembly or function leads to a wide range of diseases, with retinal degeneration being the most common phenotype (Fliegau, Benzing and Omran, 2007; Ishikawa and Marshall, 2011; May-Simera, Nagel-Wolfrum and Wolfrum, 2017). So far, most research on retinal degeneration has focused predominantly on the highly specialized primary cilium of the PR. However, the contribution of defective primary cilia in other ocular cell types has not yet been comprehensively studied (May-Simera, Nagel-Wolfrum and Wolfrum, 2017; May-Simera *et al.*, 2018). It has been shown that primary cilia are crucial for development and maturation of the RPE and that their dysfunction impairs RPE function, which is essential for PR health and activity (May-Simera *et al.*, 2018). Beyond this, nothing is known about the effect of dysfunctional primary cilia on PR health and visual function.

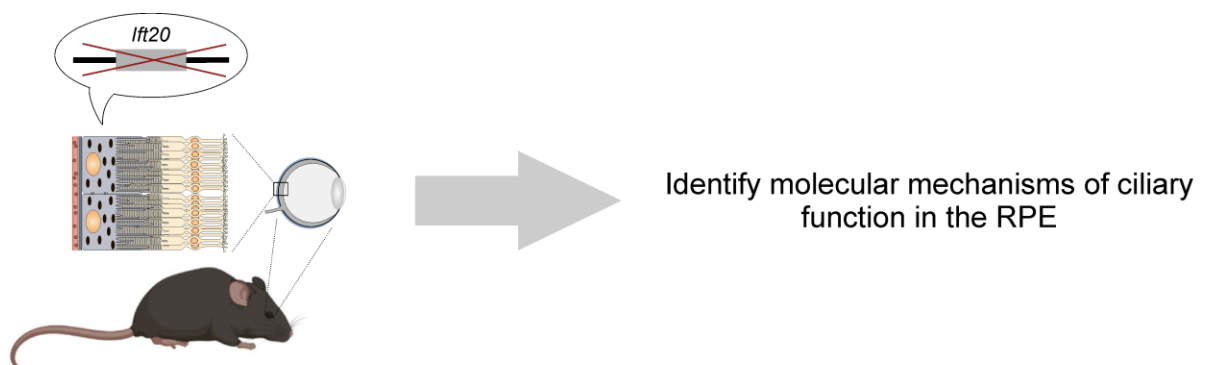
2 Aim

In order to fully understand how primary cilia dysfunction causes retinal degeneration and subsequently visual impairment, it is necessary to not only study primary cilia defects in the retina but also in other ciliated ocular tissues. One of them, the RPE, is of great importance as it is essential for retinal homeostasis and health. Therefore, this thesis aims to unravel the events occurring after primary cilia dysfunction in the RPE and leading to retinal degeneration. To do so, two knockout mouse models have been used, a global knockout of *Bbs8* and a conditional knockout of *Ift20*. The latter, aiming to ablate primary cilia exclusively in the RPE. This overall aim could then be divided into 2 aims:

Aim 1: Effects of primary cilia dysfunction caused by *Bbs8* knockout on the mouse RPE.



Aim 2: Effects of primary cilia loss exclusively in the RPE on the mouse RPE and visual function.



Using the *Bbs8* knockout mouse model in Aim 1, we sought to identify the mechanisms of ciliary function in the RPE on a cellular and molecular level. This resulted in **Publication I**, and **II**. In Aim 2, we wanted to examine the effect of ciliary dysfunction in the RPE on RPE homeostasis and function, retinal degeneration, and vision (**Manuscript I**). To be able to better study the role of RPE-specific role of primary cilia, an inducible RPE-specific Cre transgenic-mouse line was developed and characterized (**Publication III**).

3 Publications

Publication I:

Patnaik SR, Kretschmer V, Brücker L, **Schneider S**, Volz AK, Oancea-Castillo LDR, May-Simera H: *Bardet-Biedl Syndrome proteins regulate cilia disassembly during tissue maturation*. Cell Mol Life Sci. 2019 Feb; 76(4):757-775. PMID: 30446775.

Publication II:

Schneider S, De Cegli R, Nagarajan J, Kretschmer V, Matthiessen PA, Intartaglia D, Hotaling N, Ueffing M, Boldt K, Conte I, May-Simera HL: *Loss of ciliary gene Bbs8 results in physiological defects in the retinal pigment epithelium*. Front Cell Dev Biol. 2021 Feb 18; 9:607121. PMID: 33681195.

Publication III:

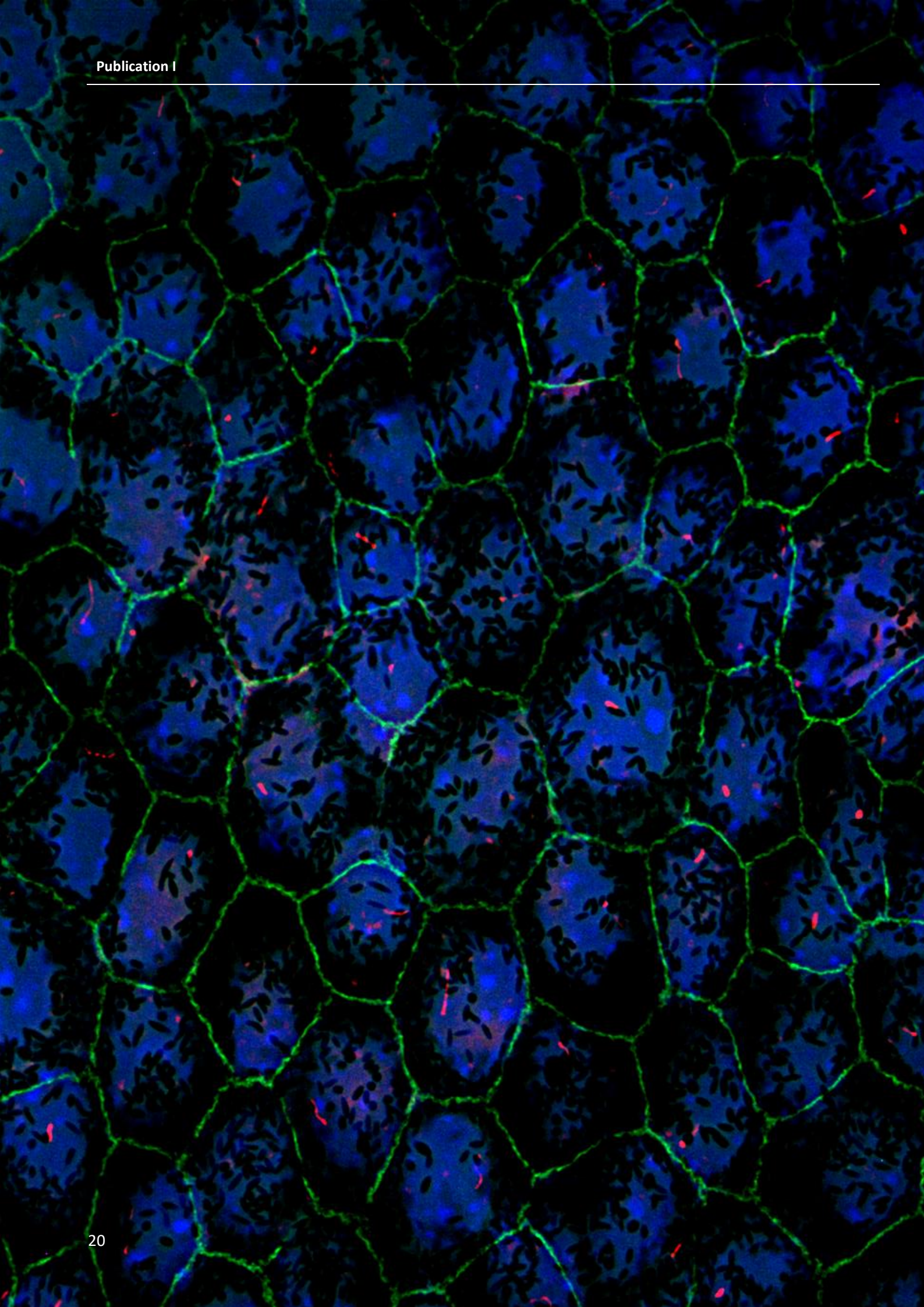
Schneider S, Hotaling N, Campos M, Patnaik SR, Bharti K, May-Simera HL: *Generation of an inducible RPE-specific Cre transgenic-mouse line*. PLoS One. 2018 Nov 15; 13(11):e0207222. PMID: 30440011.

Manuscript I:

Kretschmer V*, **Schneider S***, Matthiessen PA, Reichert D, Hotaling N, Glasßer G, Lieberwirth I, Bharti K, De Cegli R, Conte I, Nandrot EF, May-Simera HL: *Ablation of primary cilia exclusively in the RPE leads to retinal degeneration and visual impairment*. Submitted to PLoS Biology.

Publication I – Bardet–Biedl Syndrome proteins regulate cilia disassembly during tissue maturation (Published)

In this publication, we show that in the mouse RPE primary cilia are only temporarily present during development and retract as the tissue matures. This is accompanied by expression of ciliary disassembly components *in vivo*. Thus, we focused on the molecular control of these processes and could demonstrate that ciliary-associated BBS proteins interact with Inversin and regulate its expression at the base of the cilium. Consequently, Inversin inhibits HEF1/AurA, inactivating HDAC6, thus, preventing ciliary disassembly. β -catenin remains acetylated and phosphorylated and thereby undergoes proteasomal degradation. Upon BBS suppression, Inversin expression decreases, leading to the phosphorylation and activation of AurA via HEF1, resulting in upregulation of HDAC6, which in turn deacetylates β -catenin. β -catenin ultimately translocates to the nucleus where it activates canonical Wnt signaling. Furthermore, we show that primary cilia dysfunction in *Bbs8* knockout mice resulted in abnormal patterning of the RPE due in part to defective RPE maturation. However, this was not further examined in the scope of this publication. Therefore, we aimed to investigate the effect of *Bbs8* knockout on the RPE in more detail.





Bardet–Biedl Syndrome proteins regulate cilia disassembly during tissue maturation

Sarita Rani Patnaik¹ · Viola Kretschmer¹ · Lena Brücker¹ · Sandra Schneider¹  · Ann-Kathrin Volz¹ · Liliana del Rocio Oancea-Castillo² · Helen Louise May-Simera¹ 

Received: 19 April 2018 / Revised: 24 October 2018 / Accepted: 2 November 2018 / Published online: 16 November 2018
© Springer Nature Switzerland AG 2018

Abstract

Primary cilia are conserved organelles that mediate cellular communication crucial for organogenesis and homeostasis in numerous tissues. The retinal pigment epithelium (RPE) is a ciliated monolayer in the eye that borders the retina and is vital for visual function. Maturation of the RPE is absolutely critical for visual function and the role of the primary cilium in this process has been largely ignored to date. We show that primary cilia are transiently present during RPE development and that as the RPE matures, primary cilia retract, and gene expression of ciliary disassembly components decline. We observe that ciliary-associated BBS proteins protect against HDAC6-mediated ciliary disassembly via their recruitment of Inversin to the base of the primary cilium. Inhibition of ciliary disassembly components was able to rescue ciliary length defects in BBS deficient cells. This consequently affects ciliary regulation of Wnt signaling. Our results shed light onto the mechanisms by which cilia-mediated signaling facilitates tissue maturation.

Keywords Retinal dystrophy · Ciliopathy · Signaling pathways · Proteasomal degradation · Signaling inhibitors

Introduction

Primary cilia are microtubule-based organelles that protrude from the cellular membrane and are anchored by modified centrioles referred to as basal bodies. Cells use primary cilia as specific sensory organelles to detect external cues and mediate intracellular signaling during cell differentiation, organogenesis and tissue homeostasis. Cilia are involved in several signaling pathways including Wingless-related integration site (Wnt), Hedgehog (Hh) and platelet-derived growth factor receptor α (PDGFR α) [1–4], are evolutionarily conserved and vital for diverse organisms ranging from metazoans to mammals. Although they are present on almost

every cell type [5], not all cells retain their cilium throughout development and adulthood. In many tissues, for example the Organ of Corti in the mammalian cochlea [6], the luminal epithelial cells within mammary gland [7] and corneal endothelial cells in the eye [8], the cilium is vital during development but disassembles upon maturation. However, the physiological consequences of ciliary disassembly are largely unexplored. Cilia can disassemble in response to environmental stress [9], during differentiation or cell cycle progression [10, 11]. This shortening or absorption of the cilium will inevitably influence its signaling and functional role [12–16].

The importance of cilia during organogenesis and function of the vertebrate eye is well documented, particularly in photoreceptor cells [17, 18]. However, we only recently showed that the retinal pigment epithelium (RPE), a pigmented monolayer epithelium essential for photoreceptor development and visual function, also relies on the primary cilium for maturation through the regulation of canonical Wnt signaling [19]. Numerous reports have shown that RPE-derived cell lines are ciliated in vitro [20, 21] and although ciliary assembly and disassembly pathways have been studied in these models, the precise mechanisms are still being determined. The effect of these processes on downstream

Electronic supplementary material The online version of this article (<https://doi.org/10.1007/s00018-018-2966-x>) contains supplementary material, which is available to authorized users.

✉ Helen Louise May-Simera
hmaysime@uni-mainz.de

¹ Cilia Cell Biology, Institute of Molecular Physiology, Johannes-Gutenberg University, 55128 Mainz, Germany

² Institute of Developmental Biology and Neurobiology, Johannes-Gutenberg University, 55128 Mainz, Germany

signaling pathways has not been established [22, 23]. Moreover, RPE ciliogenesis and ciliary disassembly have not been investigated in vivo. Although reports have suggested that cilia in the RPE are retained throughout adulthood [24], a report from Nishiyama suggested that they disappear in the adult rat RPE [25]. Therefore, we set out to investigate the extent of ciliation in developing vertebrate RPE and to understand the molecular mechanisms underlying ciliary disassembly during development.

Various ciliary proteins including Bardet–Biedl Syndrome (BBS) and Nephronophthisis (NPHP) proteins show ciliary localization [26] and regulate cilia length [27, 28]. BBS proteins have been shown to direct ciliary trafficking, whereas many of the NPHP proteins function as ciliary gatekeepers [26, 28–31]. Certain mutations in the genes encoding these proteins can cause severe ciliopathy phenotypes including retinal degeneration, cystic kidneys, central obesity and situs inversus [32, 33].

Ciliary disassembly is known to be regulated by various cell cycle regulators. This process is mediated by human enhancer of filamentation 1 (HEF1/NEDD9) [34], which translocates from focal adhesions to the basal body, a structure derived from the mother centriole at the base of the cilium. Translocation of the scaffold protein HEF1 activates Aurora A kinase (AurA), which in turn activates histone deacetylase 6 (HDAC6), destabilizing the microtubule axoneme and thereby causing ciliary disassembly [22]. Inversin (NPHP2) influences ciliary disassembly by regulating AurA [35] and Wnt signaling [36]. BBSome-interacting protein 1 (BBIP10/BBS18), an accessory BBS protein, has been shown to directly interact with HDAC6, thereby modulating acetylation and stabilization of cytoplasmic microtubules [37]. BBS proteins have also been shown to modulate Wnt signaling via degradation of β -catenin [19, 38, 39], which is controlled by precise coordination of phosphorylation and dephosphorylation events [40, 41].

In this study, we investigated the influence of ciliary disassembly components in the developing RPE in vivo and in vitro. Furthermore, we sought to elucidate how BBS proteins mediate ciliary disassembly and how this influences downstream signaling cascades involved in tissue morphogenesis.

Results

Primary cilia are transiently expressed in the developing RPE

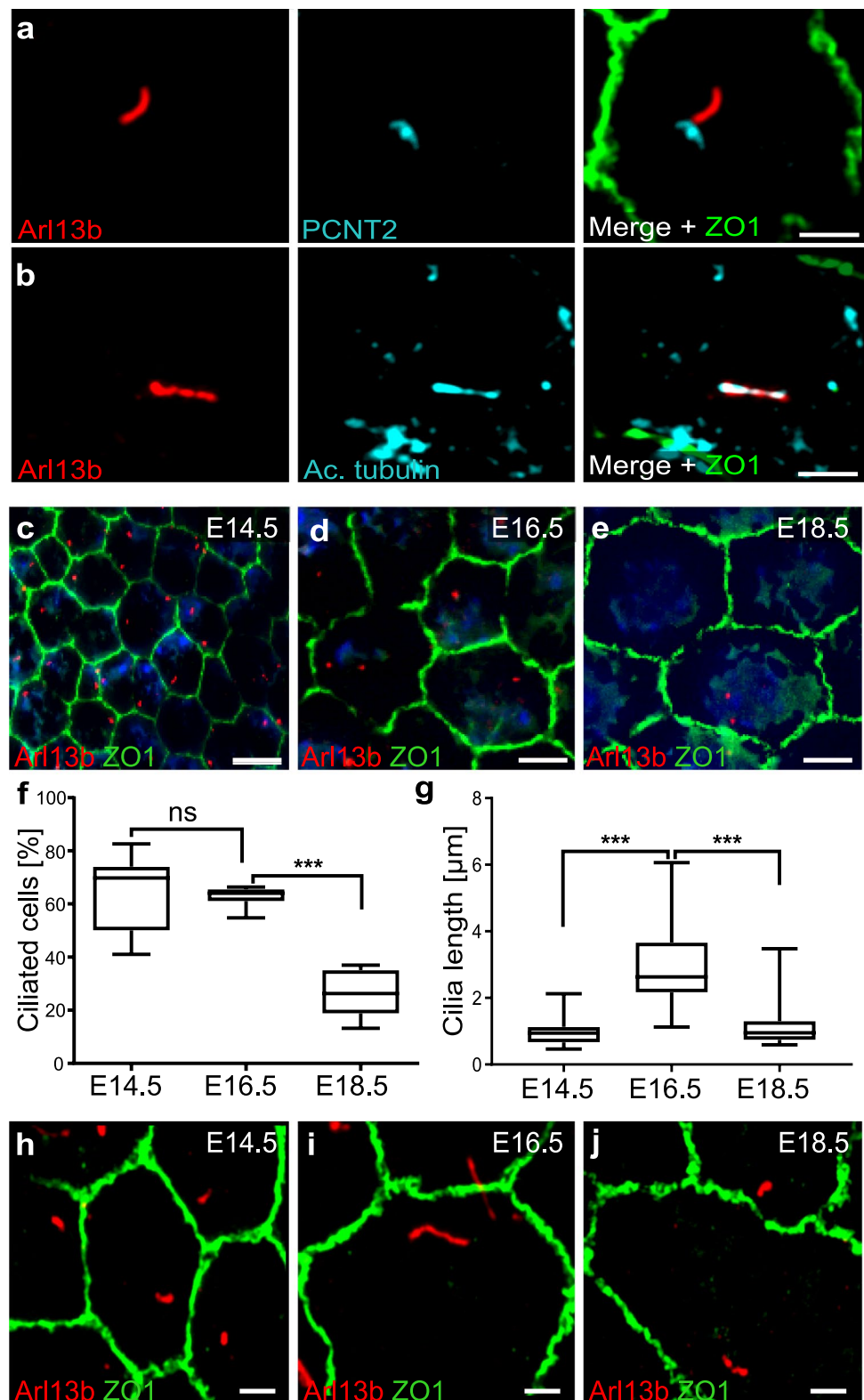
We characterized primary cilia expression in mouse flat-mount RPE at different stages of development using immunohistochemistry, RNA expression and electron microscopy. An antibody against ADP Ribosylation Factor-Like GTPase

13B (Arl13b) was used to identify primary cilia. Co-staining with other cilia (acetylated α -tubulin) and basal body markers (Pericentrin2, GT335) confirmed Arl13b as a reliable cilia marker in the RPE (Fig. 1a, b; Supp. Figure 1a–d). Tight junction marker Zonula occludens-1 (ZO-1) (Fig. 1a, b; Supp. Figure 1b, c) and β -catenin were used as membrane markers to visualize cell borders (Supp. Figure 1d). We performed stainings at various time points from E14.5 onward and observed that the expression of primary cilia in the developing RPE diminishes as the RPE matures (Fig. 1c–f). E14.5 was the earliest time point at which cilia were reliably observed and E18.5 was chosen instead of post-natal stages in order to circumvent embryonic lethality. The highest percentage of ciliated cells was observed at E14.5 and E16.5 (69.8 and 64%, respectively). By E18.5, only 26% of cells in the RPE were ciliated, suggesting that the primary cilium had retracted in the majority of the cells (Fig. 1f). Changes in cilia length accompanied cilia retraction, decreasing from 2.63 μ m at E16.5 to 0.95 μ m at E18.5 (Fig. 1g–j). In support of developmentally dependent transient expression of the primary cilium, we also observed differences in ciliation between the center and periphery of the RPE (compare Fig. 1c–e and Supp. Figure 1e–h). Ciliated cells were rarely identified after E18.5. In P1 and adult RPE, only a few cells could be identified with short stumpy Arl13b and acetylated α -tubulin positive cilia (Fig. 2a; Supp. Figure 1i–k). As previously documented [42], we also observed a developmental increase in cell size (Fig. 1c–e, Supp. Figure 1e–g). Because many cells were observed with cilia at embryonic time-points, these data suggest that the primary cilium retracts as the RPE develops.

To confirm retraction of the primary cilium in mature RPE tissues, we prepared transmission electron micrographs (TEM) of mouse RPE at multiple time points and imaged all identifiable basal body or ciliary axoneme profiles. All profiles were classified into one of the three categories that we defined as follows: basal bodies or centrioles with no attached membrane vesicles were categorized as Class I, whereas Class II profiles were identified as basal bodies containing a membranous attachment (the ciliary vesicle). Class III profiles were those with an extended ciliary axoneme into the extracellular space (Fig. 2b). Class I profiles are likely over-represented as an artifact of sectioning through a basal body of a Class II and III structure that had an attached membrane or axoneme in a different cutting plane. Consistent with an increase in ciliary disassembly, the number of Class III profiles decreased with RPE maturation (Fig. 2c). Combined, these data are consistent with our observations on immunohistochemistry and imply that primary cilia disassemble upon maturation of the RPE.

To further support retraction of the primary cilium, we measured changes in gene expression of two ciliary genes, *Arl13b* and *Ift88* in isolated mouse RPE cells using

Fig. 1 The primary cilium is transiently expressed during RPE development. Representative high-resolution immunofluorescence images of E16.5 mouse RPE flatmounts labeled with antibodies against ciliary structures show co-localization of Arl13b and acetylated α -tubulin extending from the basal body (**a, b**). Arl13b (axoneme marker, red); Pericentrin 2 (PCNT2, basal body marker, cyan); acetylated α -tubulin (Ac. tubulin, axoneme marker, cyan); Zona Occludens (ZO-1, cell junctions, green). Low magnification immunofluorescence images show ciliation (number of ciliated cells) at three embryonic timepoints (**c–e**). Boxplots show a significant decrease in the number of ciliated cells from E14.5 to E18.5 (**f**). E14.5 $n = 1700$ cells, E16.5 $n = 750$ cells, E18.5 $n = 650$ cells. Boxplots of cilia length demonstrate that mouse RPE cilia are longest at E16.5 (**g**). $n = 25$ for each age group. High-resolution immunofluorescence images of cilia (Arl13b, red) highlight differences in ciliary length between E14.5 and E18.5 (**h–j**) as quantified in **g**. Three or more animals were used per data set. Statistics were done using the Dunnett's multiple comparison test $***p \leq 0.001$; *ns* not significant. Scale bars: **a, b, h, i, j** 2 μm ; **c–e** 10 μm



quantitative real-time PCR (qRT-PCR). We developed a method to isolate pure RPE cells from embryonic mouse eyes and confirmed cell purity by determining lack of choroidal or retinal-specific gene expression (Supp. Figure 2a–c).

Gapdh was taken as the housekeeping control as its expression remained stable from E14.5 through to P7 in control and knockout mouse RPE (Supp. Figure 2d, e). Expression of both cilia genes peaked at E16.5 and decreased as the

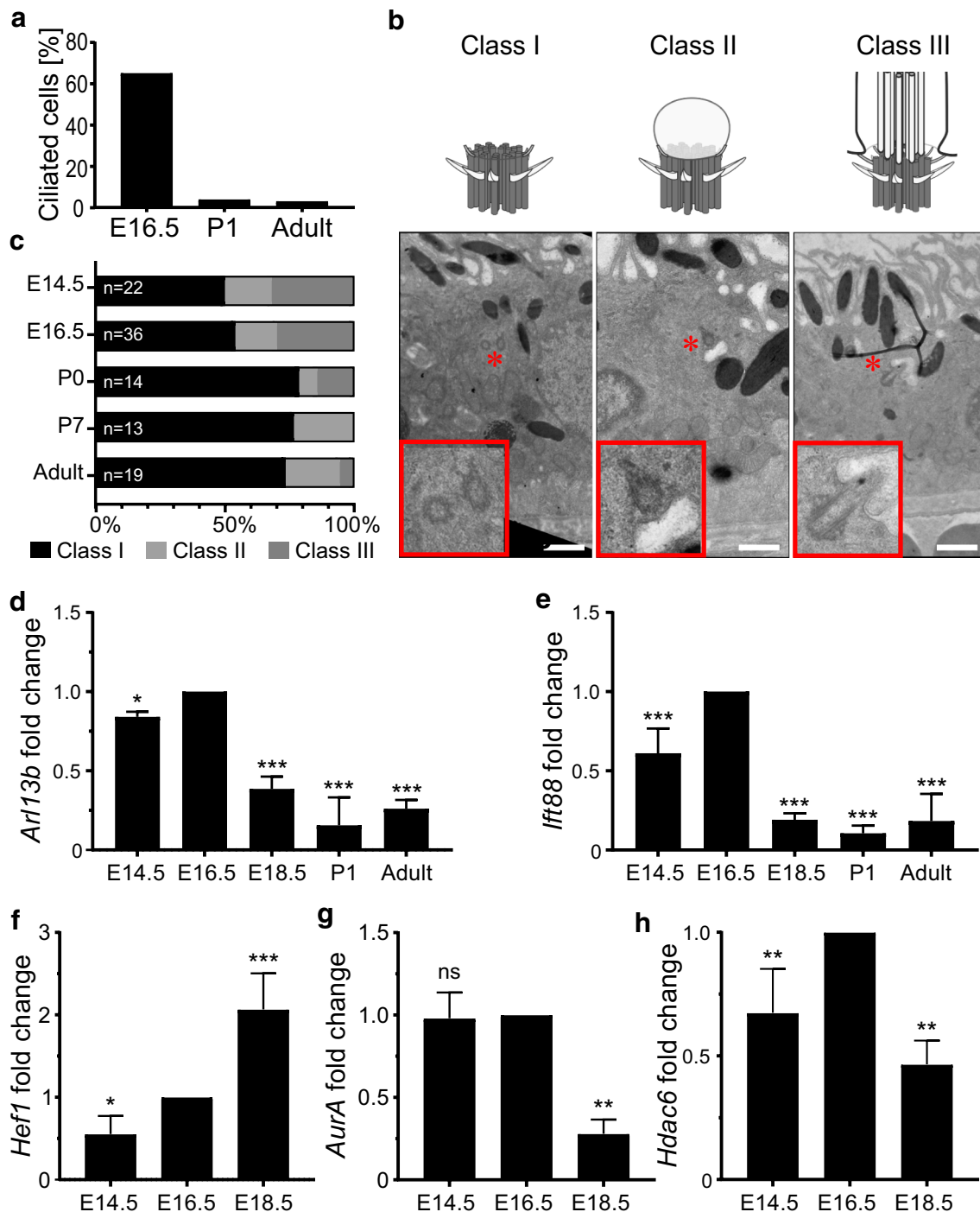


Fig. 2 Primary cilia disassemble during mouse RPE development. Quantification of ciliation in mouse RPE at E16.5, post-natal day 1 (P1) and adult show that the number of ciliated cells drastically decreased after birth (a). Transmission electron micrographs of basal bodies or ciliary axoneme profiles (marked by red asterisks) of adult mouse RPE (b). Schematics show classification of ciliary structures into different classes (I, II and III), depending on the absence (class I) or presence of a membranous attachment (the ciliary vesicle) (class II) or ciliary axoneme (class III). Quantification of class I-III profiles shows that the number of class III profiles decrease as the RPE

matures (c). Gene expression as measured by quantitative real-time PCR from isolated primary mouse RPE cells show altered expression of ciliary (*Arl13b* and *Ifi88*) and ciliary disassembly markers (*Hef1*, *Aura* and *Hdac6*) (d-h). Fold changes and significance were calculated relative to E16.5. Values represent data from three or more independent animals (biological repeats) each with three technical repeats per data set. Statistics were done using the Dunnett's multiple comparison test * $p \leq 0.05$; ** $p \leq 0.01$; *** $p \leq 0.001$; ns not significant. Scale bars: 2 μ m

tissue matured (Fig. 2d, e). Because ciliary retraction in the RPE may be actively controlled via ciliary disassembly, we also analyzed the gene expression of *Hef1*, *AurA* and *Hdac6* [22, 43, 44], which are known regulators of ciliary disassembly. Expression of ciliary disassembly components changed dynamically as the cilium retracted (Fig. 2f–h). *Hef1* expression increased gradually from E14.5 to E18.5. Expression of *AurA* and *Hdac6* was decreased by ~50% between E16.5 and E18.5. This suggests that *AurA* and *Hdac6* expressions are highest just before ciliary disassembly is observed and decline by E18.5, at which point the majority of cilia have disassembled.

Taken together, these data demonstrate that the primary cilium is disassembled upon maturation of the RPE. Temporal and spatial patterning of ciliation across the RPE matches the known mechanism of maturation for this tissue. The present data and our previous work [19] support the hypothesis that the transient expression of the primary cilium is required for RPE maturation, which occurs in an organized pattern. To further understand the mechanism of ciliary disassembly, we next sought to investigate how ciliary proteins contribute to the process of ciliary disassembly.

Loss of BBS proteins affects ciliated RPE

We focused on Bardet–Biedl syndrome (BBS) proteins in view of our prior observation that BBS proteins regulate primary cilia length and ciliary trafficking [27]. BBS6 (MKKS) is a component of the BBS chaperonin complex thought to be required for BBSome assembly. BBS8 (TTC8) is a component of the BBSome complex required for ciliary trafficking. We observed that RPE tissue from *Bbs6* knockout (*Bbs6*^{-/-}) mouse embryos displayed fewer ciliated cells at E16.5. The knockout cilia were shorter ($0.87 \pm 0.67 \mu\text{m}$) compared to WT ($2.25 \pm 0.94 \mu\text{m}$) littermates (Fig. 3a–d). In addition to changes in cilia length, we also observed changes in cell size in *Bbs6* knockout mouse embryos. In WT, we saw little variation in cell size between neighboring cells. However, in *Bbs6*^{-/-} we observed an increase in average cell size and broader distribution of cell size (Fig. 3a; Supp. Figure 3a, b). This abnormal patterning reflects disrupted RPE maturation as we had seen for *Bbs8*^{-/-} in our previous paper [19]. Abnormal patterning is possibly a consequence of dysregulation of cell junction components such as Occludin and Epithelial Cadherin (Cadherin 1). Occludin is an integral membrane protein found at tight junctions [45], and Epithelial Cadherin [46] is a major component of adherens junctions, both of which are essential for the regulation of RPE intercellular junction integrity and function, and apical basal polarity. Ras-related protein Rab-27A (Rab27) and Myosin VIIA (Myo7a) are both required for melanosome transport in the RPE, dysfunction of which leads to defective visual cycle [47]. Expression of these genes is seen as a marker

and benchmark for RPE maturation and their disruption can contribute to aberrant epithelial morphology. We observed a downregulation of *Cdh1*, *Ocln*, *Rab27a* and *Myo7a* as quantified by qRT-PCR (Supp. Figure 3c). *Bbs8* knockout (*Bbs8*^{-/-}) embryos also showed reduced number of ciliated RPE cells at E16.5 compared to that of WT (Fig. 3e, f, Supp. Figure 3c) although less significant changes in gene expression were observed.

To further elucidate the mechanisms by which BBS molecules regulate ciliary disassembly, we utilized an in vitro culture system by knocking down (KD) BBS8 or BBS6 using short interfering RNA (siRNA) in hTERT-RPE1 cells. This cell line has previously been used to characterize ciliary disassembly and is derived from human RPE tissue. Knockdown was validated by RT-qPCR and Western blotting (Supp. Figure 4a–d). Cells were serum-starved to induce ciliogenesis. Similar to the in vivo mouse RPE, we observed fewer ciliated cells upon BBS8 and BBS6 KD (24.9 ± 11.6 and $24.1 \pm 9.62\%$) compared to the non-targeting siRNA control (NTC, $74.7 \pm 9.77\%$) (Fig. 3g, h). In the remaining cells that retained cilia, cilia length was also significantly reduced compared to NTC (NTC: $3.58 \mu\text{m}$, BBS8 KD: $2.26 \mu\text{m}$, BBS6 KD: $2.62 \mu\text{m}$) (Fig. 3i).

Interaction of BBS proteins with mediators of ciliary disassembly

Next, we sought to identify whether additional BBS proteins interact with Inversin, a protein known to be involved in *AurA* mediated ciliary disassembly [35]. Since we had previously shown that BBS8 directly interacts with Inversin during regulation of Wnt signaling in development of the RPE [19], we wanted to see if this interaction extended to other BBS proteins. Using GFP-traps, we were able to pull down overexpressed BBS6-myc and BBS2-myc with Inversin-eGFP in HEK293T cells (Fig. 4a, b). To confirm the physical interaction between Inversin and BBS6 in situ, a proximity ligation assay (PLA) was performed using antibodies against endogenous Inversin and overexpressed myc-BBS6. Positive PLA events shown as distinct fluorescent foci confirmed the interaction (Fig. 4c).

In an immortalized murine kidney medullary (KM) cell line, Inversin is localized to the base of the cilium as seen by Inversin co-localization with acetylated α -tubulin in the majority of ciliated cells (Fig. 4d, e). These cells were used as endogenous Inversin is better detectable in these cells upon immunocytochemistry. Furthermore, the Wnt signaling and ciliary phenotype are recapitulated in these cells [27]. In KM cells derived from *Bbs6* knockout (*Bbs6*^{-/-}) mice, significantly fewer cilia showed Inversin localization at the base, and Inversin expression was more dispersed throughout the cytoplasm (Fig. 4d, f). Combined these data suggest

Fig. 3 Absence of BBS proteins decreases RPE ciliation *in vivo* and *in vitro*. Representative immunofluorescence images of E16.5 mouse RPE flatmounts from wildtype and *Bbs6*^{-/-} littermates, labeled with antibodies against the primary cilium (Arl13b; red, acetylated α -tubulin (Ac. tubulin); cyan) and cell junctions (Zona Occludens (ZO-1); green) (a, c). Boxplots of ciliation (b) and cilia length (d) show a significant decrease in cilia number and cilia length in *Bbs6* knockout animals. Representative immunofluorescence images of E16.5 mouse RPE flatmounts from wildtype and *Bbs8*^{-/-} littermates, labeled with antibodies against Arl13b; red and ZO-1; green show a reduced number of ciliated cells in *Bbs8* knockout mice (e). Boxplots confirmed the significant reduction of ciliated cells in *Bbs8* knockout RPE (f). Representative immunofluorescence images of primary cilia labeled with antibodies against Arl13b; green and polyglutamylated tubulin (GT335); red in BBS8 and BBS6 KD hTERT-RPE1 compared to non-targeting control (NTC) (g). Graphical representation of percentage of ciliated cells (NTC $n=250$, BBS8 KD $n=150$ and BBS6 KD $n=200$) (h) and cilia length (i) of control in comparison to KD cells. White asterisks (*) label cells lacking cilia. Three or more individual animals were used per sample set. Statistical analyses in b, d and f were performed using two-tailed Mann–Whitney U test, where $***p < 0.001$. For d $n=40$ cells per genotype. Statistical analyses in h and i were done using the Dunnett's multiple comparison test $***p \leq 0.001$. Scale bars: a, e 10 μm ; b 2 μm ; g 10 μm , magnified images 5 μm . KD Knockdown

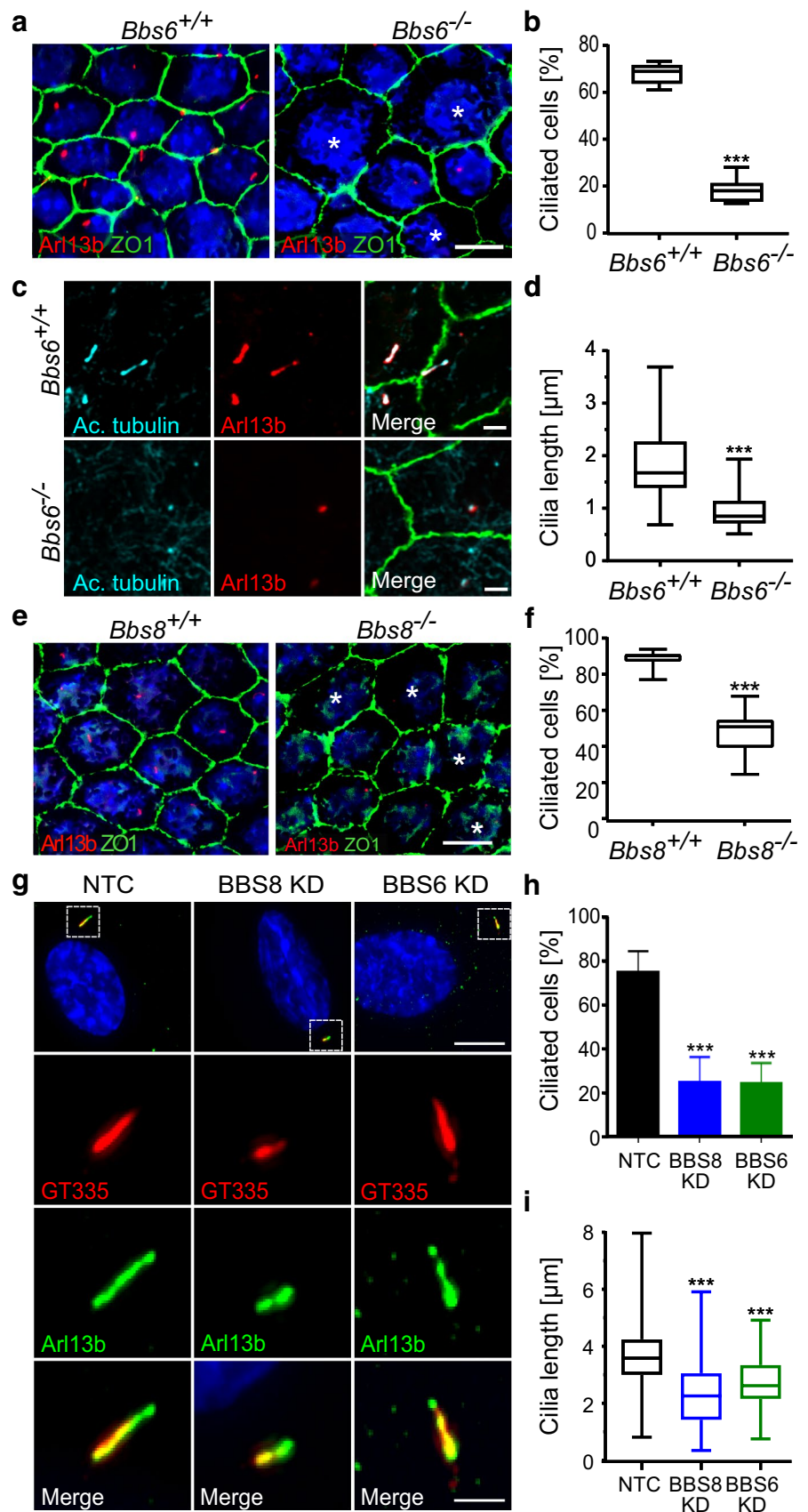
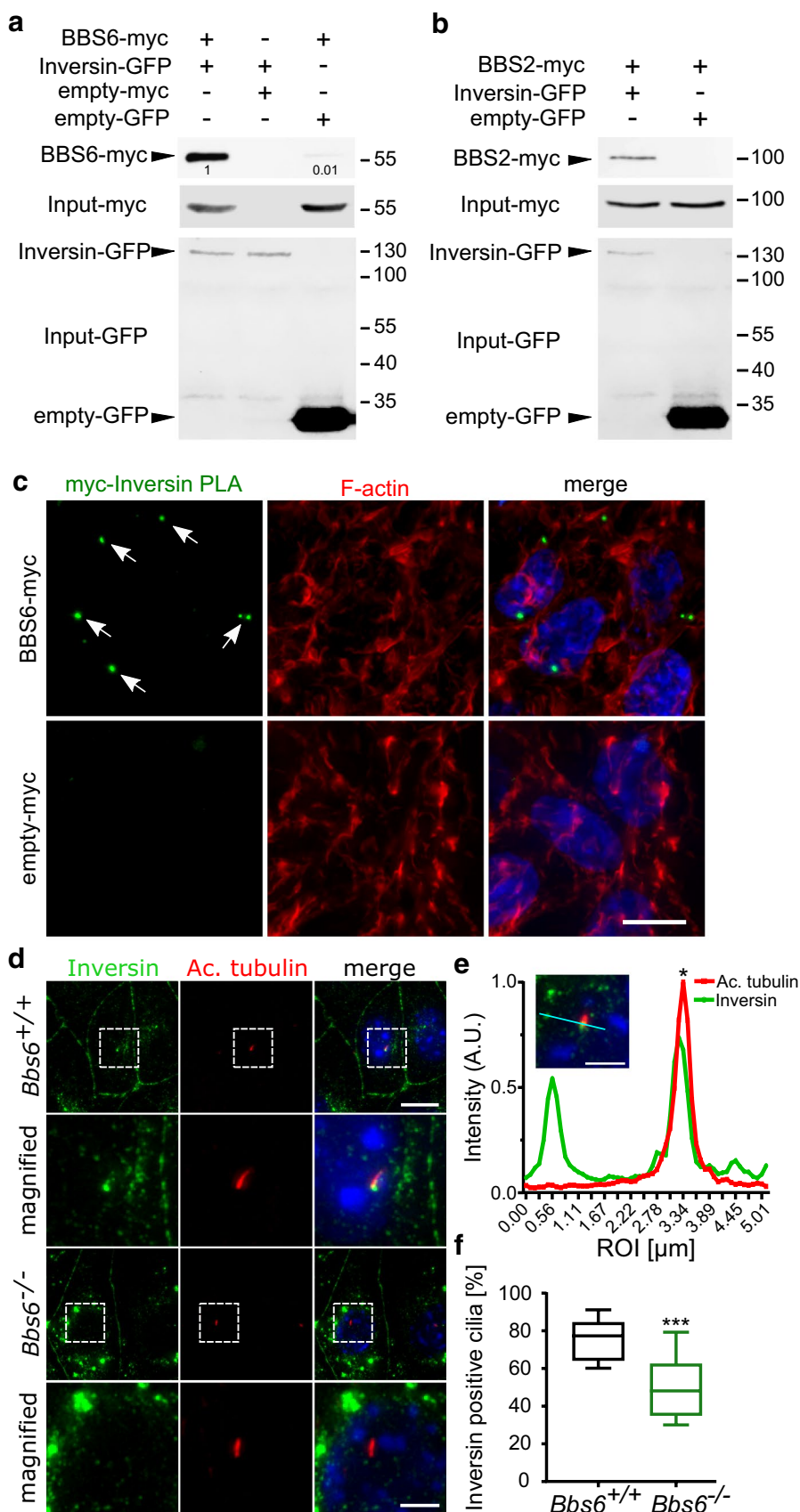
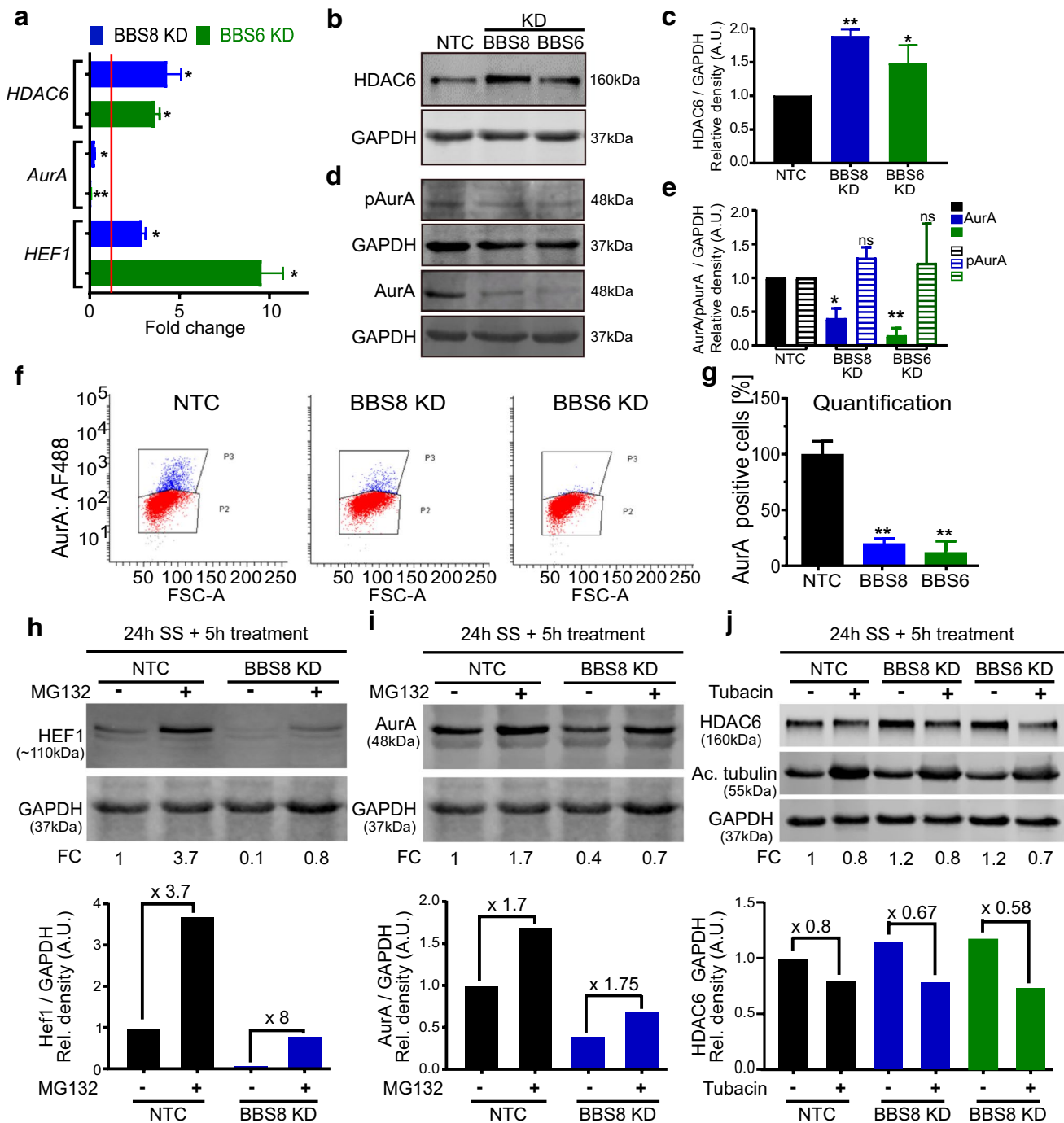


Fig. 4 Mislocalization of Inversin upon loss of BBS proteins. HEK293T cells transiently co-transfected with *myc*-tagged *BBS* and *Inversin-GFP* plasmids. Cell lysates subjected to GFP-TRAP pulldown followed by Western blotting show that Inversin-GFP interacts with *myc*-tagged BBS6 (a) and *myc*-tagged BBS2 (b). Proximity ligation assays (PLA) of HEK cells overexpressing *myc-BBS6* were performed using antibodies against *myc* and endogenous Inversin. Positive PLA foci (green) indicate interaction between Inversin and BBS6. Empty-*myc* transfected control cells did not display positive PLA foci. TRITC-Phalloidin (F-actin, red) was used to visualize cell outlines (c). Representative immunofluorescence images of kidney medullary (KM) cells labeled with antibodies against the primary cilium (acetylated α -tubulin (Ac. tubulin); red) and Inversin (green) show diminished localization of Inversin to the base of the cilium in *Bbs6*^{-/-} cells as compared to the wildtype control (d). ROI linear profile represents fluorescence intensity of corresponding cyan line on the merged image. Peaks indicated by asterisk represent area of co-localization of Inversin and Ac. tubulin in wildtype KM cells (e). *Bbs6*^{+/+} *n* = 215 cilia, *Bbs6*^{-/-} *n* = 140 cilia. Boxplots show a reduction in percentage of Inversin positive Ac. tubulin in *Bbs6*^{-/-} KM cells compared to control cells (f). Statistical analyses in e were performed from three independent experiments using two-tailed Mann-Whitney *U* test, where ****p* < 0.001. Scale bars: c, d 10 μ m





that BBS6 and BBS2 proteins interact with Inversin and regulate its expression at the ciliary base.

BBS proteins regulate key mediators of primary ciliary disassembly

In mammalian cells, ciliary disassembly is mediated by recruitment of HEF1 at the basal body, leading to downstream phosphorylation and activation of AurA and HDAC6,

and subsequent destabilization of ciliary tubulin [22, 48]. We wanted to determine whether BBS proteins are involved in cilia maintenance by protecting the cilium against AurA-HDAC6-mediated disassembly. Gene expression analysis showed an increase of ciliary disassembly genes *HDAC6* and *HEF1* upon knockdown (KD) of BBS8 or BBS6, consistent with reduced ciliary length (Figs. 3 g–i; 5a). Western blot analysis also showed elevated levels of HDAC6 protein expression in hTERT-RPE1 cells (Fig. 5b, c). Expression of

Fig. 5 BBS proteins regulate key mediators of cilia disassembly. Quantitative real-time PCR shows increased gene expression of cilia disassembly components (*HEF1* and *HDAC6*) and decreased expression of *AurA* relative to non-targeting control (NTC, red line) in serum-starved BBS8 or BBS6 knockdown (KD) hTERT-RPE1 cells. *GAPDH* was used as housekeeping control (a). Western blots show a significant increase in protein levels of HDAC6 upon KD of BBS8 and BBS6 in serum-starved hTERT-RPE1 cells (b, c). Conversely, AurA protein levels were decreased upon KD of BBS8 and BBS6 in serum-starved hTERT-RPE1 cells, although pAurA levels were retained (d, e) suggesting an increased ratio of active over total AurA. Flow cytometry analysis was used to further quantify AurA expression in serum-starved BBS8 and BBS6 KD hTERT-RPE1 cells (f, g). Representative flow cytometry dot plots show the AurA-positive cell population (P3, blue) and AurA-negative cell population (P2, red) (f). Quantification of the AurA-positive cell population confirmed a significant decrease in the BBS8 and BBS6 KD cells compared to NTC (g). Western blots show that KD of BBS8 in hTERT-RPE1 cells leads to decreased level of HEF1, which was partially restored by treatment with proteasome inhibitor MG132 (h). An 8-fold increase in HEF1 protein expression was observed upon BBS8 KD compared to 3.7-fold in NTC. Decreased protein levels of AurA in BBS8 KD hTERT-RPE1 cells were also partially restored by treatment with proteasome inhibitor MG132 (i). Increased levels of HDAC6 in BBS8 KD hTERT-RPE1 cells were concomitant with an increase in acetylated α -tubulin and were reduced upon treatment with HDAC6 inhibitor tubacin, as quantified by Western blot (j). Quantification of Western blot data was normalized to GAPDH levels. Bar charts show relative protein expression in arbitrary units (AU). Data are expressed as mean \pm SD, $n=3$ separate experiments for (a–g), while $n=2$ for h–j. Statistical analyses in c, g were done using the Dunnett's multiple comparison test and e using Sidak's multiple comparison test. In c, e and g * $p \leq 0.05$; ** $p \leq 0.01$; *** $p \leq 0.001$; ns not significant. KD Knockdown, NTC non-targeting control, SS serum-starved, FC fold change, FSC-A forward scatter area

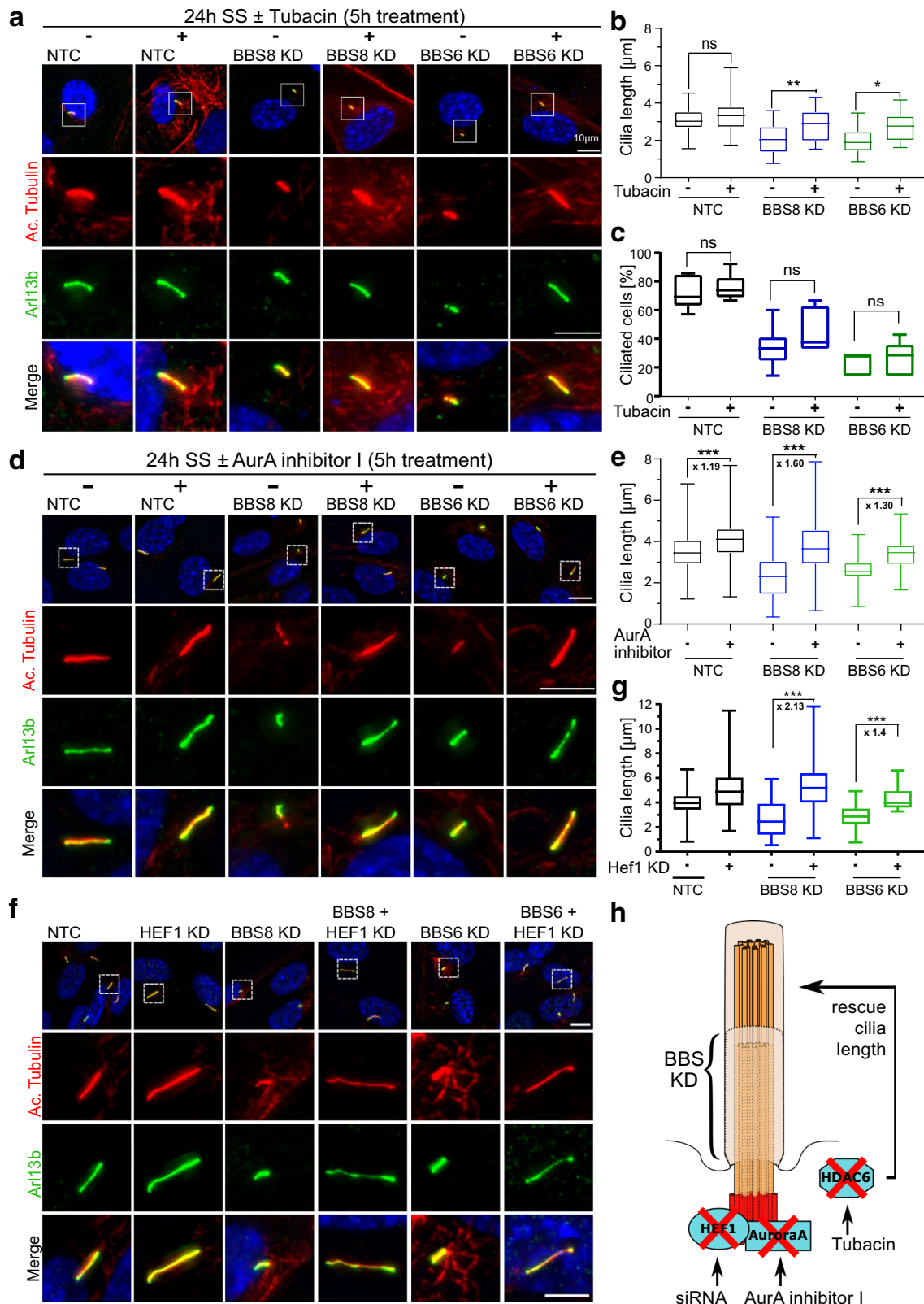
total *AurA* mRNA and AurA protein was decreased in KD cells, as analyzed by qPCR, Western blot and flow cytometry (Fig. 5a, d, e, f, g). In contrast, the level of active phosphorylated AurA (pAurA) was unchanged as shown by Western blot with an antibody specific for pAurA (Thr288) (Fig. 5d, e). Therefore, the ratio of pAurA/AurA was elevated in the KD cells compared to control even without ciliary disassembly via serum activation. Previous reports showed that levels of pAurA peak when cilia disassemble [23]. When we do combined serum activation with BBS KD, we observed a similar trend in that active pAurA is retained upon BBS8 or BBS6 KD (Supp. Figure 5a). As quantified by qPCR, *HEF1* transcript expression was elevated upon both BBS8 and BBS6 KD (Fig. 5a). In an attempt to verify these data in vivo, we analyzed mRNA expression of *Hef1*, *AurA* and *Hdac6* in knockout mouse tissue using unpurified RPE (RPE and choroid). Expression of ciliary disassembly genes *Hef1* and *Hdac6* was increased in *Bbs8*^{-/-} relative to wildtype control littermate tissue. No significant change in expression level could be seen for *AurA*. In *Bbs6*^{-/-} mice, *Hef1* was significantly increased, *AurA* significantly decreased and *Hdac6* remained unchanged (Supp. Figure 3d). These gene expression patterns show a similar trend to the in vitro data.

Although *HEF1* mRNA expression levels were elevated in vitro and in vivo, Western blot analysis showed a reduction in protein upon loss of BBS8 (Supp. Figure 5b). We hypothesized that in the absence of BBS8, HEF1 is actively phosphorylated and targeted for proteasomal degradation. To test this, we treated serum-starved cells with the proteasome inhibitor MG132. This resulted in ~8-fold recovery of HEF1 expression in treated KD cells compared to untreated KD cells which only had a 3.7-fold recovery (Fig. 5h). Therefore, over 50% more HEF1 was recovered in KD cells compared to control (0.1–0.8 vs 1–3.7). Although we saw a mild recovery of total AurA upon inhibiting proteasomal activity in these cells (Fig. 5i), there was little difference between KD and control. Based on these observations, we propose that ciliary disassembly components are differentially regulated by BBS proteins. While loss of BBS8 results in increased levels of HDAC6, it also results in the proteasomal degradation of HEF1 and to some extent of AurA. We wanted to further elucidate whether the ciliary length defect observed in BBS deficient cells could be attributed to dysfunction of ciliary disassembly components.

Ciliary disassembly component inhibition rescues the ciliary length defect caused by BBS knockdown

To confirm that ciliary defects upon BBS KD can be attributed in part to an increase in HDAC6 expression, we treated serum-starved NTC and BBS KD cells with tubacin, a specific HDAC6 inhibitor [22, 49]. Tubacin treatment caused a decrease in HDAC6 and a concomitant increase in the protein level of acetylated tubulin in both NTC and KD cells compared to the vehicle (DMSO) alone, as seen by Western blot (Fig. 5j). This corresponded to a rescue in cilia length (Fig. 6a, b). A significant change in the number of ciliated cells was not observed after treatment with tubacin (Fig. 6c). Next, we used a potent and selective inhibitor of AurA, AurA Inhibitor I [35, 50]. Similarly, this also ameliorated the cilia length defect in BBS8- and BBS6-deficient cells (Fig. 6d, e). To test whether HEF1 activity also underlies the AurA and HDAC6 mediated ciliary disassembly in BBS KD cells, we performed double KD experiments. We observed an appreciable rescue in cilia length in the BBS and HEF1 double KD cells compared to single KD (Fig. 6f, g). We confirmed that double KD did not lead to loss of individual gene KD efficiency (Supp. Figure 4e–g). Recovery of cilia length after inhibition or KD of HEF1, AurA and HDAC6 supports our hypothesis that BBS proteins are involved in the control of ciliary disassembly (Fig. 6h).

To address off-target effects of siRNA we knocked down BBS8 from hTERT-RPE1 cells using single (siRNA 1 or siRNA2) and double siRNAs (siRNA 1 + 2) and looked for levels of HDAC6 via Western blotting. We observed a similar increase in HDAC6 levels in single vs double KD



cells, as quantified using Western blotting analysis (Supp. Figure 5c). Furthermore, using different combinations of siRNA against BBS8 from different companies had the

same effect on AurA expression levels (Supp. Figure 5a). Therefore, we believe that the phenotype we observe is specific. To rule out differences in cell cycle stages, which

Fig. 6 Inhibition of ciliary disassembly components rescues BBS mediated ciliary disassembly. Representative immunofluorescence images of cilia stained with antibodies against acetylated α -tubulin (Ac.tubulin, red) and Arl13b (green), from non-targeting control (NTC), BBS8 and BBS6 knockdown (KD) hTERT-RPE1 cells treated with and without HDAC6 inhibitor, tubacin (a). Quantification of ciliary length show that tubacin treatment did not affect ciliary length in control, yet was able to increase ciliary length in BBS8 and BBS6 KD cells (b). Quantification of ciliated cells showed that treatment with tubacin had no effect on ciliation (c). Treatment with AurA inhibitor I was also able to significantly increase ciliary length in BBS8 and BBS6 KD cells. BBS8 and BBS6 KD tubacin-treated cells show a greater increase in cilia length in comparison to their DMSO mock-treated counterparts, while control cells showed minimal increase (d, e). KD of HEF1 increased ciliary length in control hTERT-RPE1 cells. Double KD of HEF1 and BBS8 or BBS6 was able to reverse the ciliary disassembly phenotype observed in BBS8 or BBS6 KD (f, g). A model showing the inhibition or KD of ciliary disassembly components causes rescue of cilia length in BBS KD hTERT-RPE1 cells (h). Statistical analyses in b, c, e, g were done using the Sidak's multiple comparison test from two independent experiments. The length of at least 1000 cilia from the six different treatment groups (NTC treated, untreated, BBS8/6 KD treated, untreated) in each experiment (Tubacin treatment, AurA treatment and Hef1 KD) were measured. * $p \leq 0.05$; ** $p \leq 0.01$; *** $p \leq 0.001$; *ns* not significant. *KD* Knockdown, *NTC* non-targeting control, *SS* serum-starved

could affect changes in ciliary disassembly components, we performed cell cycle analysis via fluorescence-activated cell sorting (FACS) using propidium iodide (PI). This corroborated that the majority of cells remained in G0/G1 phase in both NTC and KD cells (Supp. Figure 5d), confirming that our results were cell cycle independent.

Loss of BBS proteins regulate HDAC6, thereby influencing post-translational modification of β -catenin

Previous studies have shown that ciliogenesis and ciliary disassembly modulate the switch from β -catenin-dependent canonical to non-canonical Wnt signaling pathways [36, 51]. Therefore, we examined the impact of BBS-regulated ciliary disassembly components on Wnt signaling. β -catenin is a direct substrate of HDAC6, which deacetylates β -catenin at lysine residue (K49), inhibiting downstream phosphorylation [52]. This results in β -catenin stabilization and nuclear accumulation. Although we and others have shown that suppression of *BBS* genes results in stabilization of β -catenin and altered regulation of downstream Wnt targets [18, 38], the mechanisms that cause this stabilization are not yet known. Loss of BBS is not thought to directly affect the core activity of the proteasome [38], which suggests a defect in phosphorylation and subsequent targeting of β -catenin for degradation. Since the stability of β -catenin is mediated by various specific phosphorylation and acetylation events at different sites, we hypothesized that upon loss of BBS, β -catenin becomes differentially modified. Consistent with

this, the level of acetylated β -catenin (Lys49) was reduced after BBS8 or BBS6 KD in hTERT-RPE1 cells as quantified by Western blotting (Fig. 7a). We also sought to identify further downstream phosphorylation events of β -catenin that lead to degradation. Using phospho-specific antibodies, we detected a decrease in phosphorylation at T41/S45 and S33/37/T41 as a result of BBS8 and BBS6 KD (Fig. 7b, c).

To strengthen our findings on Western blot, we performed immunocytochemistry using an antibody against acetylated β -catenin (Lys49) and observed a reduction in nuclear fluorescence intensity upon BBS KD. Treatment with HDAC6 inhibitor tubacin rescued the levels of acetylated β -catenin K49 in BBS-deficient cells (Fig. 7d, e). Previous studies showed that phospho-(S33/37/T41)- β -catenin localizes to the base of the cilium [51, 53]. We observed localization of phospho-(S33/37/T41)- β -catenin not only to the basal body, but also in the nucleus (Fig. 7f). Upon KD of BBS8 and BBS6, this nuclear localization is diminished while localization at the basal body is often absent (Fig. 7f, g).

Reduction of phosphorylation at S33/37/T41 ultimately results in reduced degradation and consequent increase in levels of total β -catenin as observed in Western blot (Fig. 7h, i). This increased level of total β -catenin translated to increased levels of β -catenin activity as measured via luciferase assays (Fig. 7j). Stimulation with Wnt3a conditioned medium significantly increased β -catenin driven TCF/LEF transcription after BBS8 or BBS6 KD. In contrast to phosphorylation at S33/37/T41, phosphorylation at S552 causes stabilization and nuclear accumulation of β -catenin [54]. Consistent with this, and the increased activity of β -catenin, we detected elevated expression and nuclear accumulation of pS552 β -catenin in nonciliated BBS8 KD cells (Fig. 7k, l). Together, these experiments show that loss of BBS molecules influences post-translational modification of β -catenin, which ultimately regulates its signaling activity.

Discussion

In the present work, we demonstrate that ciliary trafficking proteins are required for homeostasis of primary ciliary disassembly components, specific regulation of which is required for ciliary retraction and regulation of signaling pathways. Precise regulation of ciliation is an absolute requirement for tissue differentiation [8, 55]. We focused our attention on BBS proteins known to be required for ciliary trafficking, in particular on a component of the Bosome, BBS8, and a component of the chaperonin complex, BBS6, thought to be required for Bosome assembly [55–58].

The RPE is a ciliated epithelial monolayer essential for visual function. Insights into RPE maturation can be extrapolated to other epithelial tissues for example lung epithelial cells [19]. In mice we showed that as the RPE matures, the

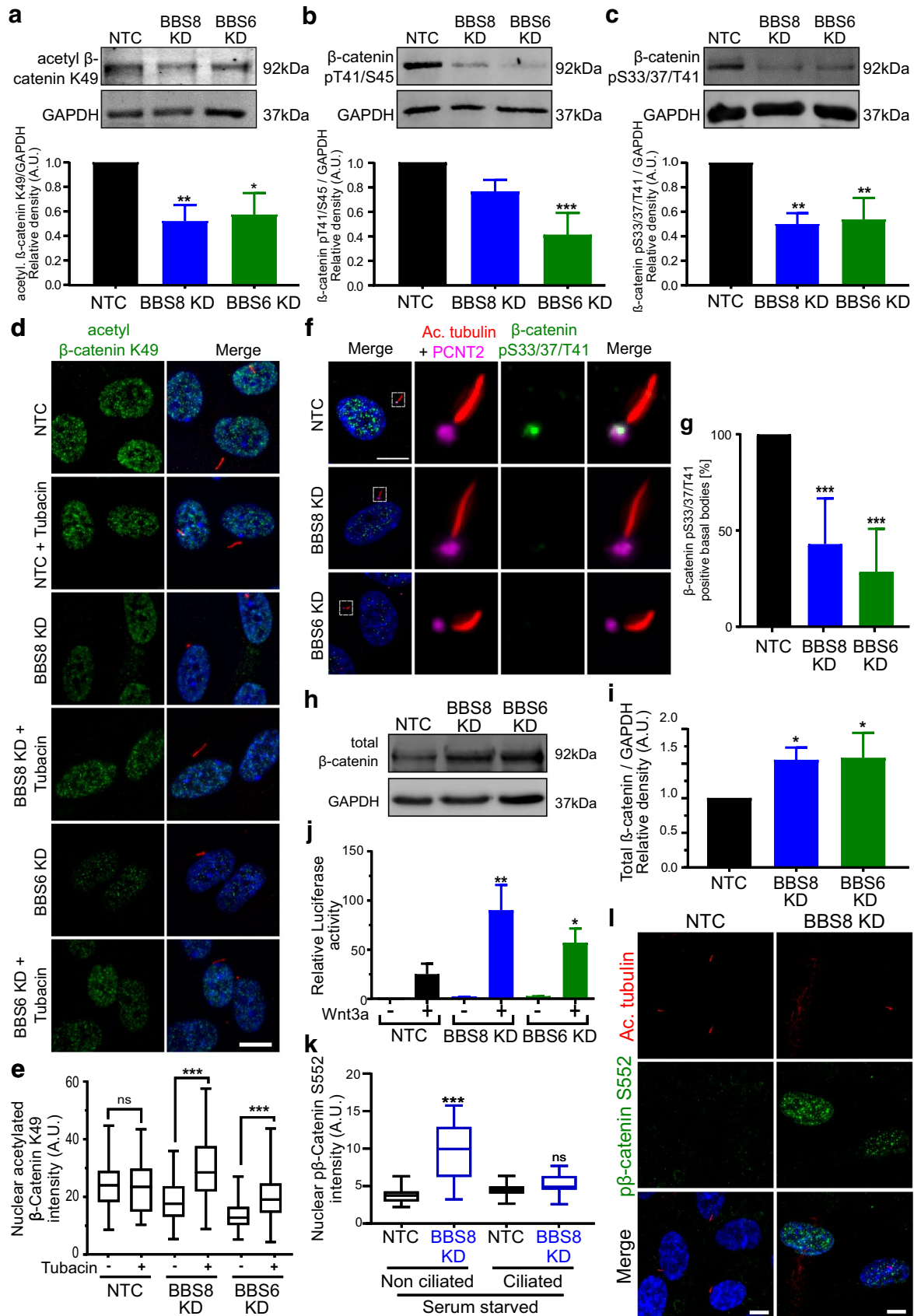


Fig. 7 BBS-mediated regulation of ciliary disassembly components alters post-translational modification of β -catenin. Western blot analysis and quantification show reduced acetylation of β -catenin at K49 (a) and consequently reduced phosphorylation at p41/44 (b) and p33/37/41 (c) upon BBS8 and BBS6 knockdown (KD) in hTERT-RPE1 cells, suggesting an increase in stable and active β -catenin. Immunocytochemistry and quantification using an antibody against acetylated β -catenin K49 (green) show reduced expression in the nucleus upon BBS8 and BBS6 KD compared to non-targeting control (NTC) in hTERT-RPE1 cells (d). Cells were co-labeled with Arl13b (red) to confirm reduction in ciliary length. Reduced β -catenin K49 expression could be rescued by treatment with HDAC6 inhibitor tubacin ($n \geq 100$ for each group) (d, e). Immunocytochemistry using an antibody against β -catenin pS33/37/T41 (green), a target of β -catenin acetylation, shows expression at the base of the cilium and in the nucleus in NTC hTERT-RPE1 cells (f, g). Ciliary axoneme is marked by acetylated α -tubulin (Ac. tubulin, red), and the basal body by Pericentrin 2 (PCNT2, magenta). Quantification confirms reduced localization of β -catenin pS33/37/T41 at the basal body upon BBS8 and BBS6 KD (g). BBS8 and BBS6 KD cause less β -catenin degradation, resulting in increased levels of total β -catenin in hTERT-RPE1 cells, as quantified from Western blot (h, i). This was confirmed by a TCF/LEF luciferase activity assay that measures the transcriptional activity of β -catenin enzymatically. Luciferase activity in Wnt3a-treated non-targeting control HEK cells is upregulated compared to the untreated control. The Wnt response (luciferase activity) is significantly enhanced upon the suppression of BBS8 and BBS6 (j). Immunofluorescence analysis and quantification show increased stability and nuclear translocation of active β -catenin pS552 (green) in non-ciliated hTERT-RPE1 cells after BBS8 KD ($n = 263$ for NTC and 100 for BBS8 KD) (k, l). Cells were co-labeled with Ac. tubulin (green) to confirm reduction in ciliary length. Quantification of Western blot data was normalized to GAPDH levels. Bar charts in a–c show relative protein expression in arbitrary units (A.U.). Data in a, b, c, i, j are expressed as mean \pm SD, $n = 3$ separate experiments. Data in g show mean \pm SD, two independent experiments. Statistical analyses in a, b, c, g, i were done using the Dunnett's multiple comparison test. Data analyses in e, j, k were performed using Sidak's multiple comparison test. $p \leq 0.05$; $**p \leq 0.01$; $***p \leq 0.001$; ns not significant. Scale bars: a, e 10 μ m; b 2 μ m; h 5 μ m

primary cilium retracts with only a few stunted cilia being retained after birth. Cilia dysfunction in knockout mice resulted in abnormal RPE patterning in part due to defective RPE maturation (this and previous study) [19]. Retraction of the primary cilium is accompanied by expression of ciliary disassembly components suggesting that loss of the primary cilium is a tightly controlled cellular event. Interestingly, such mechanisms of ciliary disassembly are also observed in other tissues, such as in the auditory hair cells of the inner ear [6]. Here, the kinocilium plays an important role during development of the Organ of Corti but is reabsorbed by post-natal day 10 [59]. Because cilia are not retained, we suggest that they are less likely to be essential for cellular function in adult RPE, but more likely required for regulating signaling processes during development as we have recently demonstrated [19]. Since retraction of the primary cilium in the RPE is accompanied by the expression of ciliary disassembly components in vivo, we focused our attention on the molecular control of these processes.

The most common pathways that govern ciliary disassembly are through AurA, HEF1 and HDAC6 [10, 22]. Previous reports have shown that BBS proteins regulate cilia length [27] and that BBIP10 (BBS18), an additional subunit of the BBSome, interacts directly with HDAC6 [37], yet the molecular mechanisms underlying this phenomenon have not been elucidated. Here, we observed that the loss of BBS proteins resulted in increased levels of HDAC6 and that inhibition of HDAC6 resulted in a rescue of cilia length in BBS KD cells. Similarly, inhibition of AurA and HEF1 also resulted in rescue of cilia length. Therefore, we propose that BBS proteins maintain cilia length by suppressing HEF1-AurA-HDAC6-mediated disassembly (Fig. 8). Although the total levels of pAurA were not changed upon BBS KD, since inhibition of AurA activity rescued the ciliary length defect in these cells, this suggests a difference in activity.

Because Inversin (NPHP2), a key ciliary protein, influences ciliary disassembly via inhibiting AurA [35, 36] and is also a key mediator of Wnt signaling, we postulated that the role of BBS proteins in ciliary disassembly may in part be mediated via Inversin. We show that BBS proteins are required for Inversin protein expression at the base of the cilium, thereby regulating AurA phosphorylation and subsequent ciliary disassembly. AurA can also be activated by other proteins such as Pitchfork, calmodulin, trichoplein, HIF1 α (Hypoxia-inducible factor 1-alpha) or Plk1 (Polo-like-Kinase 1) [60]. Moreover, some kinesins such as Kif2a (Kinesin family member 2a) might also be involved as they are direct targets of AurA [61]. Therefore, BBS proteins could also be acting upon these regulators. In support of this, some of these proteins have already been shown to interact with other ciliary proteins [62, 63]. BBS proteins may also influence other ciliary length regulating components such as CPAP (Centrobin-mediated Regulation of the Centrosomal Protein 4.1-associated Protein), Nde1 (Nuclear distribution protein nudeE homolog 1) and OFD1 (oral–facial–digital syndrome 1) proteins [64], which remain to be addressed.

Previous studies showed that BBS proteins interact with proteasomal subunits regulating the composition of the centrosomal proteasome [38, 65]. Consequently, loss of BBS proteins results in altered signal transduction due to defects in proteasomal clearance of key signaling proteins including β -catenin [38, 65]. Here, we show that the loss of BBS proteins decreases the stability of HEF1 and AurA proteins. A partial recovery of these proteins is observed upon inhibiting proteasomal function using MG132, suggesting that BBS proteins protect Hef1 and AurA from proteasomal degradation and thus inhibit ciliary disassembly. Increased stability of β -catenin (discussed below) and subsequent upregulation of canonical Wnt signaling upon BBS KD may also in part be ascribable to defects in proteasomal clearance. Similarly, the cilia protein RPGRIP1L (RPGR-Interacting

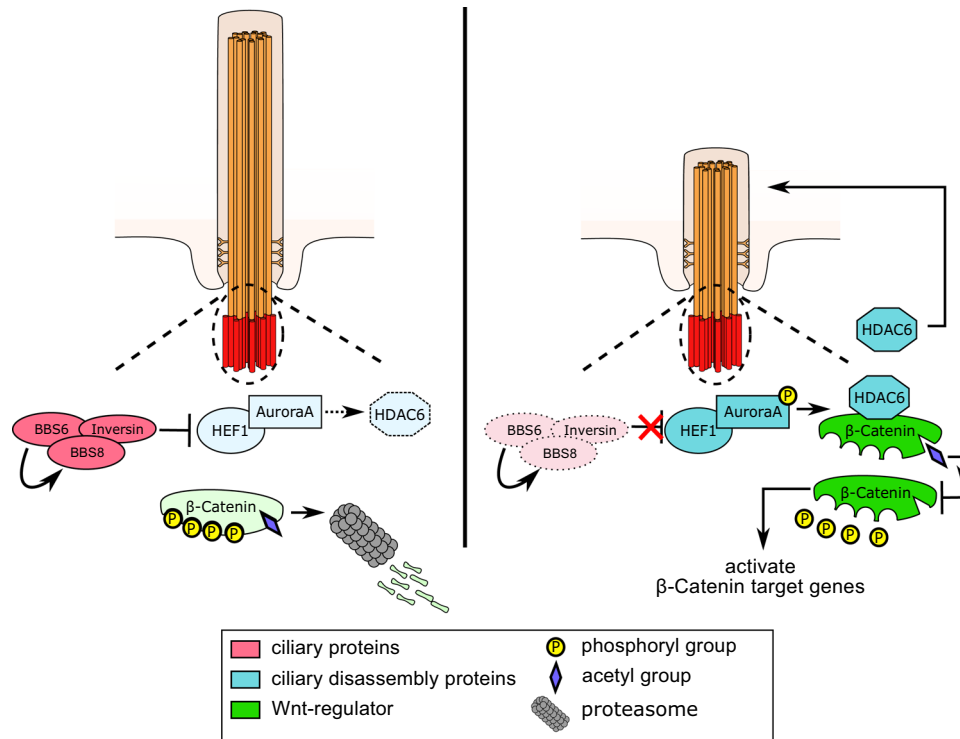


Fig. 8 Model of BBS-mediated regulation of ciliary disassembly. BBS proteins interact with Inversin and regulate its expression at the base of the cilium. Inversin inhibits HEF1/AurA, inactivating histone deacetylase HDAC6 thus preventing ciliary disassembly. As a consequence of dormant HDAC6, β -catenin remains acetylated and phosphorylated, thereby undergoing proteasomal degradation. Upon BBS suppression, Inversin expression decreases at the base of

the cilium. This leads to phosphorylation and activation of AurA via HEF1, resulting in upregulation and activation of HDAC6. HDAC6 deacetylates β -catenin, hence preventing further phosphorylation and degradation. Consequently, β -catenin is stabilized and translocates to the nucleus activating canonical Wnt signaling. This also regulates ciliary length

Protein 1-Like) has been shown to protect canonical Wnt components (dishevelled) from proteasomal degradation at the basal body [53, 66]. Because HEF1 stabilization differed in BBS8 compared to BBS6 KD cells, it suggests differences in the functional role of the BBSome vs. the BBS chaperonins. One explanation for reduced protein levels of HEF1 in serum-starved BBS8 KD cells could be a feedback loop mechanism. Since it is clear from our experiments that BBS8 KD cells experience increased cilia disassembly, these cells may be trying to maintain homeostasis by mediating increased degradation of HEF1, in an effort to maintain cilia length and limit the extent of cilia disassembly. This phenomenon is intriguing, especially considering that we only see this after BBS8 KD and not after BBS6 KD, which warrants more in depth examination in the future.

In an effort to elucidate the underlying mechanisms affecting β -catenin stability upon loss of cilia function, we focused our attention on post-translational modifications (PTMs) of proteins associated with proteasomal degradation [41]. HDAC6 physically interacts and acetylates β -catenin [52] resulting in altered Wnt signaling. Several studies have demonstrated the importance of PTMs such

as ubiquitination, phosphorylation, acetylation and glutamylation in various signaling processes [67]. PTMs such as phosphorylation also actively influence the process of ciliogenesis and maintenance [68]. Targeting β -catenin for degradation is a complex process involving PTMs at various sites [41]. HDAC6 deacetylation of β -catenin at K49 inhibits downstream phosphorylation. Because HDAC6 was increased in the absence of BBS proteins, we observed less acetylation at K49, which results in less β -catenin phosphorylation at T41/S45 and S33/37/T41. Thus, less β -catenin is targeted for degradation. Moreover, upon loss of BBS proteins, β -catenin is actively phosphorylated at S552, a modification that increases its stabilization and nuclear localization (our data and previous data [19]). Together, these dysregulated PTMs result in aberrant canonical-Wnt hyperactivation upon loss of BBS protein function. Although we and others [52] have observed that HDAC6 and AurA can modify β -catenin levels, very little is known about the nature of this regulation which needs further elucidation.

In conclusion, we observed transient expression of the primary cilium in the developing mouse RPE. As the RPE

matures, primary cilia retract, which are accompanied by altered expression of *Hef1*, *AuroraA* and *Hdac6*, key mediators of ciliary disassembly. In control cells, BBS proteins protect against ciliary disassembly whereas the loss of BBS proteins results in altered ciliary disassembly components, including HDAC6, likely via interaction and trafficking of Inversin. This results in HDAC6-mediated downstream cross-talk between ciliary disassembly signaling and canonical-Wnt signaling, leading to PTMs resulting in canonical-Wnt hyperactivation. Taken together, we furthered our understanding into how ciliary proteins modulate cellular signaling pathways and contribute to maturation of epithelial tissues.

Materials and methods

Animals

All mouse experiments had ethical approval from appropriate governing bodies. Experiments were performed in accordance with guidelines provided by ARVO (Association for Research in Vision and Ophthalmology). Animals were housed under a 12 h light–dark cycle. The morning after mating was considered E0.5 and up to 24 h after birth was considered P0. C57BL/6 mice were used for control at embryonic (E14.5, E16.5 and E18.5), and post-natal stages (P1, P7 and adult). *Bbs6* and *Bbs8* knockout mice have been previously described [1, 69].

Cell culture

hTERT-RPE1 and HEK293T cells were obtained from ATCC and cultured in Dulbecco's modified Eagle's medium (DMEM)-F12 (Thermo Fisher) or DMEM (Thermo Fisher) supplemented with heat-inactivated 10% fetal bovine serum (FBS) (LONZA), and 1% penicillin/streptomycin (P/S) (Thermo Fisher) (Referred to as complete media). Immortalized kidney medullary (KM) cells were obtained from P. Beales and cultured as previously described [27].

Antibodies and siRNAs

For immunofluorescence, antibodies used were anti-Arl13b (Rb, 1:1000; Proteintech, 17711-1-AP), anti-acetylated α -tubulin (Mm, 1:800; Sigma, T6793), anti-GT335 (Mm, 1:200; Adipogen, AG-20B-0020), anti- β -catenin (Rb, 1:150; CST, D10A8), anti-acetylated α -tubulin (Rb, 1:1000; Abcam, ab11317), anti-pericentrin2 (Gt, 1:200; SantaCruz, SC28145), and anti-ZO-1 (Mm, 1:150; Thermo Fisher, ZO1-1A12, 339188), anti-GFP (Rb, 1:5000; Clontech, 632592),

anti-Aurora A (D3E4Q) (Rb, 1:100; CST, 14475), anti-phospho-Aurora A (Thr288) (C39D8) (Rb, 1:50; CST, 3079), anti-phospho- β -Catenin (Ser33/37/Thr41) (Rb, 1: 200; CST, 9561), anti-Acetyl- β -Catenin (Lys49) (D7C2) (Rb, 1: 150; CST, 9030), and anti-NPHP2 (Rb, 1:150; Abcam, ab65187). The primary antibodies were detected using Alexa Fluor 488, 555 and 568 (1:400; Molecular Probes) and CFTM640R (1:400; Biotium) conjugated secondary antibodies.

For western blot, antibodies used were anti-myc-Tag (9B11) (Mm, 1:1000, CST, 2276), anti-GFP (Rb, 1:1000; Clontech, 632592), anti-Aurora A (D3E4Q) (Rb, 1:1000; CST, 14475), anti-phospho-Aurora A (Thr288) (C39D8) (Rb, 1:1000; CST, 3079), anti- β -Catenin (D10A8) (Rb, 1: 1000; CST, 8480), anti-phospho- β -Catenin (Ser33/37/Thr41) (Rb, 1: 1000; CST, 9561), anti-phospho- β -Catenin (Thr41/Ser45) (Rb, 1: 1000; CST, 9565), anti-Acetyl- β -Catenin (Lys49) (D7C2) (Rb, 1: 1000; CST, 9030), anti-HEF1/NEDD9 (2G9) (Mm, 1: 1000; CST, 4044), anti-HDAC6 (D2E5) (Rb, 1: 1000; CST 7558). Secondary antibodies used were IRDye 800 and IRDye 680 (Rb, Mm or Gt; 1:10000; Li-cor Bioscience).

For flow cytometry, a primary antibody against Aurora A (D3E4Q) (Rb, 1:100; CST, 14475) and a secondary Alexa Fluor 488-labelled anti-rabbit antibody (1: 250) were used. Propidium iodide (PI, Thermo Fisher, P3566) at 50 μ g/ml was used for cell cycle analysis.

siRNA was used in our study to knockdown (KD) *BBS6* and *BBS8* in hTERT-RPE1 cells. *BBS8* siRNA (HSC.RNAI.N198309.12; IDT), *BBS8* siRNA (L-021417-02-0005; Dharmacon), *BBS6* siRNA (L-013300-00-0005), *HEF1* siRNA (hs.Ri.NEDD9.13; IDT) and non-targeting siRNA (D-001810-10-05) were used.

Transfections and treatments: Plasmid transfections were performed using GeneTrap transfection reagent (made at NEI, NIH, Bethesda, MD, USA). In brief, 6 μ l of GeneTrap transfection reagent was diluted in 90 μ l of DMEM, incubated for 5 min followed by addition of 2 μ g plasmid and then incubated for 20 min at room temperature (RT). The transfection mix was added dropwise to cells in a 6-well plate containing 2 ml complete media. siRNA transfections were performed in 6-well plates with Lipofectamine RNAiMax transfection reagent (Thermo Fisher; 13778150) using a reverse transfection protocol according to the manufacturer's instructions. To induce cilia formation, 24 h post-transfection cells were serum-starved with Opti-MEM (Thermo Scientific) for up to 48 h. For proteasome, AurA or HDAC6 inhibition experiments, 48 h post-transfections cells were serum-starved for 24 h followed by treatment with 10 μ M MG132 (Calbiochem), 1 μ M AurA Inhibitor I (Selleckchem) and 2 μ M tubacin (Sigma), respectively, for the indicated time (5 h) followed by western blot analysis and immunofluorescence. DMSO was taken as vehicle control for treatments.

Tissue preparation and Immunohistochemistry

Mouse eyes were enucleated and immersed in cold phosphate-buffered saline (PBS) and kept on ice for 20 min. Eyes were then placed in 1X PBS and the cornea, lens and retina were removed. The resulting eyecups were then fixed with 4% paraformaldehyde (PFA) in PBS for 1 h at RT, then washed three times with 1X PBS and incubated with 50 mM NH_4Cl for 10 min, followed by incubation with β -Mercaptoethanol for 10 min. Eyecups were permeabilized with PBSTX (0.3% Triton-X) and blocked with blocking buffer (0.1% Ovalbumin, 0.5% Fish gelatine in PBS) at RT for 2 h followed by overnight incubation in primary antibody at 4 °C. Samples were washed three times with 1X PBS followed by incubation in secondary antibody and DAPI for 2 h at RT. Finally, samples were washed with PBS for three times before mounting on glass slides. Cells close to the optic nerve were considered near the center; cells closer to the edge of the eye cup were considered as peripheral. For isolation of pure RPE cells, eyecups were incubated with trypsin at 37 °C for 30–90 min depending on the age of tissue. RPE cells were mechanically removed from underlying choroid and isolated by hand. Choroidal and retinal contamination was checked via qPCR. Contaminated samples were removed from the analysis.

hTERT-RPE1 cells were fixed with 4% PFA for 10 min and permeabilized for 15 min with PBSTX. Immunostaining was performed as described above. KM cells were fixed with 100% methanol for 10 min on ice. Immunostaining was performed as described above.

Specimens were imaged on a Leica DM6000B microscope (Leica, Bensheim, Germany). Images were deconvoluted and co-localization profiles were generated with Leica imaging software (BlindDeblur Algorithm, one iteration step). Images were processed and cilia length measurements were performed using Fiji/ImageJ software (NIH, Bethesda, USA).

PLA assay

Direct in situ protein–protein interactions were investigated by means of a proximity ligation assay (PLA) using Duolink In Situ FarRed Kit Mouse/Rabbit (Sigma) according to the manufacturer's instruction. Cells were incubated with anti-myc and anti-Inversin primary antibodies followed by anti-rabbit PLUS and anti-mouse MINUS secondary PLA probes. The two complementary oligonucleotides were then hybridized, ligated and rolling circle amplified by the provided polymerase, resulting in fluorescence signals when the targeted proteins were closer than 40 nm. TRITC–phalloidin (Sigma) was used for visualization of cells and DAPI for nuclear staining.

Fluorescence-activated cell sorting (FACS) analyses

For FACS, RPE1 cells were stained with an antibody directed against intracellular AurA. Recovered cells were fixed using 4% PFA for 10 min and washed three times with PBS. Cells were permeabilized with 90% ice-cold methanol for 30 min and rinsed three times. Cells were blocked using 0.5% bovine serum albumin (BSA) in PBS and incubated with AurA for 1 h at RT, then washed three times with 0.5% BSA/PBS. After incubation with a secondary antibody (Alexa Fluor 488-labelled anti-rabbit) for 45 min at RT, cells were finally washed with 0.5% BSA/PBS. Cells were acquired using the Invitrogen Attune NxT Flow Cytometer (Thermo Fisher Scientific, Inc., USA), and analyzed using FlowJo (Treestar, CA, USA). For cell cycle analysis, RPE1 cells were detached and fixed with 70% ethanol for 30 min, followed by incubation with 100 $\mu\text{g}/\text{ml}$ RNase A solution and 50 $\mu\text{g}/\text{ml}$ propidium-iodide solution. Samples were acquired and analyzed as described above.

Pulldown and western blotting

For pulldown experiments, HEK cells were transiently co-transfected with Inversin-GFP and pCMV-BBS6/2-myc [27] or empty plasmids. 48 h post-transfections cells were lysed using RIPA buffer supplemented with EDTA-free protease inhibitor cocktail (Halt™ Protease and Phosphatase Inhibitor Cocktail (100X), Thermo Fisher). Pulldown was performed using agarose beads (GFP-Trap-A, ChromoTek) according to the manufacturer's instructions followed by western blot. Proteins were harvested in Laemmli sample buffer and separated on 8–10% SDS–polyacrylamide gel (PAGE), followed by transfer PVDF membrane (Immobilon®-FL PVDF membrane, Sigma, 05317). The blots were blocked with 5% milk or AppliChem blocking buffer (0.2% AppliChem Blocking Reagent, 10 mM TrisHCl, 150 mM NaCl, 0.04% NaN_3 , in ddH₂O; pH 7.4) and probed with antibodies as listed above. The blots were scanned for infrared fluorescence at 680 or 800 nm using the Odyssey Infrared Imaging System (Licor). Densitometry analysis was performed with Fiji/ImageJ software (NIH, Bethesda, MD, USA) and the expression levels were normalized to the input.

Quantitative real-time reverse transcriptase polymerase chain reaction

The total RNA was extracted either from hTERT-RPE1 cells, retina or RPE tissue using TRIzol reagent (Thermo Fisher, 15596026) following manufacturer's instructions. 1 μg of RNA was reverse transcribed to cDNA using GoScript reverse transcription system (Promega, A5000). cDNA was amplified on a StepOnePlus™ Real-Time PCR System

Table 1 Primers

Gene	Species	Forward	Reverse
<i>BBS6</i>	Human	AATGACACTGCCTGGGATG	TCGTTGTGAGTCTTGTGTCTG
<i>BBS8</i>	Human	ATACTCATGTGGAAGCCATCG	ATAGAAGCAACACAGCCCC
<i>HEF1</i>	Human	CATAACCCGCCAGATGCTAAA	CCGGGTGCTGCCTGTACT
<i>AurA</i>	Human	GAATGCTGTGTCTGTCCG	GCCTCTTCTGTATCCCAAGC
<i>HDAC6</i>	Human	CAACTGAGACCGTGGAGAG	CCTGTGCGAGACTGTAGC
<i>NPHP2</i>	Human	GCCTTCAAAATCCAAGCTGTC	CTGTTCTGCCTCTTTTCGTTTG
<i>GAPDH</i>	Human	GAGTCAAGGGATTTGGTCGT	TTGATTTTGAGGGGATCTCG
<i>Hef1</i>	Mouse	GTACCCATCCAGATACCAAAAGG	GGAATGTCATATACCCCTTGAGG
<i>AurA</i>	Mouse	CACACGTACCAGGAGACTTACAGA	AGTCTTGAAATGAGGTCCCTGGCT
<i>Hdac6</i>	Mouse	GGAGACAACCCAGTACATGAATGAA	CGGAGGACAGAGCCTGTAG
<i>Arl13b</i>	Mouse	AGCGGATGTGATTGAGTGTC	ACAAGGTTTCGATCTGACACAG
<i>Ift20</i>	Mouse	AAGGAACCAAAGCATCAAGAATTAG	AG ATGTCATCAGGCAGCTTGAC
<i>Prph2</i>	Mouse	TCTCCTCCAAGGAGGTCAAAG	GAGTCCGGCAGTGATGCTCAC
<i>Rpe65</i>	Mouse	ACTTCCCCTTTCAATCTCTTCC	TTTAACTTCTTCCCAATTCTCACG
<i>Cdh5</i>	Mouse	ACACCTTACCATTGAGACAG	CTGCTCAGGTATTCGTATCGG
<i>Gapdh</i>	Mouse	CGACTTCAACAGCAACTCCCACTCTTCC	TGGGTGGTCCAGGGTTTCTTACTCCTT

(Applied Biosystems, 4376600) using SYBR Green (Thermo Fisher; Platinum™ SYBR™ Green qPCR SuperMix-UDG, 11733046) according to the manufacturer's recommendation. The following cycling conditions were used: 95 °C for 10 min followed by 40 cycles of 95 for 15 s, 60 for 1 min. Specificity of the amplified product was determined by melt curve analysis. Relative target gene expression was normalized to GAPDH and analyzed by comparative Ct or $2^{-\Delta\Delta CT}$ method [70, 71]. For a list of primers used, see Table 1.

Electron microscopy

Electron microscopy was performed as previously described [72].

Luciferase assay

To monitor the activity of the Wnt/ β -catenin signaling pathway characterized by TCF/LEF-dependent target gene transcription, reporter gene assays were performed with the Dual-Glo® Luciferase Assay System (Promega) in a 96-well plate. BBS6 and BBS8 siRNA-mediated KD in HEK293T cells were performed using Lipofectamine RNAiMax transfection reagent (Thermo Fisher) using a reverse transfection protocol according to the manufacturer's instructions. After 24 h cells were transiently transfected with plasmids by X-tremeGENE™ 9 DNA Transfection Reagent (Sigma) according to the manufacturer's protocol. Plasmids used were pRL-TK (Renilla luciferase, 1 ng), TopFlash (5 ng) and the total amount of transfected DNA was equalized to 80 ng by addition of pcDNA3. 24 h post-transfections cells were

stimulated with Wnt3a conditioned media and luciferase activity was measured after 24 h in a Tecan Infinite M200 Pro plate reader. Firefly luciferase activity was normalized to Renilla luciferase activity in each well.

Statistical analysis

Statistical analysis was performed using Graphpad Prism 7.0 software (GraphPad Software Inc., San Diego, CA, USA). For multigroup comparisons, ANOVA followed by Dunnett's multiple comparison test, Tukey's multiple comparison test and Sidak's multiple comparison test was performed depending of the data to be compared. Differences between two groups were compared using a nonparametric Mann–Whitney *U* test. *p* value of 0.05 and below was considered statistically significant. Statistical tests and number of repetitions are described in the legends. Box plots show median (middle line), edge of boxes is top and bottom quartiles (25–75%), and whiskers represent the ranges for the upper 25% and the bottom 25% of data values. Outliers were excluded using the ROUT method (GraphPad Prism). Bar plots show mean \pm standard deviation (SD).

Acknowledgments This work was supported by the Alexander Von Humboldt Foundation and the Johannes Gutenberg University. The authors thank Uwe Wolfrum, Kerstin Nagel-Wolfrum and Anne Régner-Vigouroux for abundant discussion and proofreading. We especially thank Elisabeth Sehn and Gabriele Stern-Schneider for expert technical assistance and Tina Sedmark for providing TEM specimens for analysis.

Author contributions SRP and HLM-S were responsible for conception and experimental design. SRP, VK, LB, A-KV, SS, LRO-C and

HLM-S performed experiments. SRP and VK generated figures. SRP and HLM-S co-wrote the manuscript.

Compliance with ethical standards

Conflict of interest The authors declares that they have no conflict of interest.

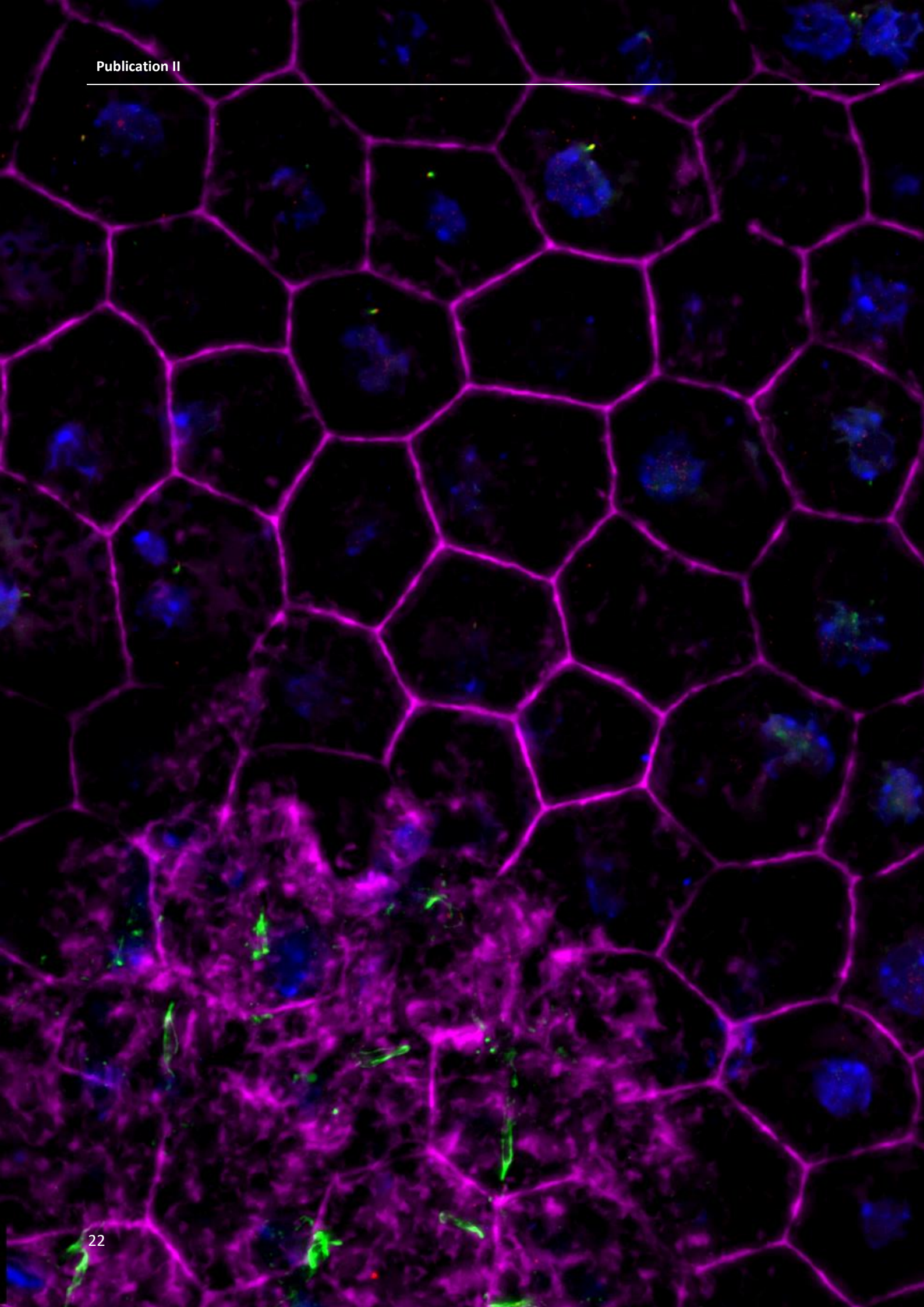
References

- Ross AJ et al (2005) Disruption of Bardet–Biedl syndrome ciliary proteins perturbs planar cell polarity in vertebrates. *Nat Genet* 37:1135–1140
- Schneider L et al (2005) PDGFR α signaling is regulated through the primary cilium in fibroblasts. *Curr Biol* 15:1861–1866
- Goetz SC, Anderson KV (2010) The primary cilium: a signalling centre during vertebrate development. *Nat Rev Genet* 11:331–344
- May-Simera HL, Kelley MW (2012) Cilia, Wnt signaling, and the cytoskeleton. *Cilia* 1:7
- Wheatley DN, Wang AM, Strugnell GE (1996) Expression of primary cilia in mammalian cells. *Cell Biol Int* 20:73–81
- Denman-Johnson K, Forge A (1999) Establishment of hair bundle polarity and orientation in the developing vestibular system of the mouse. *J Neurocytol* 28:821–835
- McDermott KM, Liu BY, Tlsty TD, Pazour GJ (2010) Primary cilia regulate branching morphogenesis during mammary gland development. *Curr Biol* 20:731–737
- Blitzer AL et al (2011) Primary cilia dynamics instruct tissue patterning and repair of corneal endothelium. *Proc Natl Acad Sci* 108:2819–2824
- Iomini C, Tejada K, Mo W, Vaananen H, Piperno G (2004) Primary cilia of human endothelial cells disassemble under laminar shear stress. *J Cell Biol* 164:811–817
- Liang Y, Meng D, Zhu B, Pan J (2016) Mechanism of ciliary disassembly. *Cell Mol Life Sci* 73:1787–1802
- Keeling J, Tsiokas L, Maskey D (2016) Cellular mechanisms of ciliary length control. *Cells* 5:6
- Caspary T, Larkins CE, Anderson KV (2007) The graded response to sonic hedgehog depends on cilia architecture. *Dev Cell* 12:767–778
- Tran PV et al (2008) THM1 negatively modulates mouse sonic hedgehog signal transduction and affects retrograde intraflagellar transport in cilia. *Nat Genet* 40:403–410
- Besschetnova TY et al (2010) Identification of signaling pathways regulating primary cilium length and flow-mediated adaptation. *Curr Biol* 20:182–187
- Thompson CL, Chapple JP, Knight MM (2014) Primary cilia disassembly down-regulates mechanosensitive hedgehog signaling: a feedback mechanism controlling ADAMTS-5 expression in chondrocytes. *Osteoarthr Cartil* 22:490–498
- Sánchez I, Dynlacht BD (2016) Cilium assembly and disassembly. *Nat Cell Biol* 18:711–717
- May-Simera H, Nagel-Wolfrum K, Wolfrum U (2016) Cilia—the sensory antennae in the eye. *Prog Retin. Eye Res.* <https://doi.org/10.1016/j.preteyeres.2017.05.001>
- Wheway G, Parry DA, Johnson CA (2014) The role of primary cilia in the development and disease of the retina. *Organogenesis* 10:69–85
- May-simera HL et al (2018) Primary cilium-mediated retinal pigment epithelium maturation is disrupted in ciliopathy patient cells article primary cilium-mediated retinal pigment epithelium maturation is disrupted in ciliopathy patient cells. *Cell Rep.* 22:189–205
- Plotnikova OV, Pugacheva EN, Golemis EA (2009) Primary cilia and the cell cycle. *Methods Cell Biol* 94:137–160
- Kukic I, Rivera-Molina F, Toomre D (2016) The IN/OUT assay: a new tool to study ciliogenesis. *Cilia* 5:23
- Pugacheva EN, Jablonski SA, Hartman TR, Henske EP, Golemis E (2007) a. HEF1-dependent Aurora A activation induces disassembly of the primary cilium. *Cell* 129:1351–1363
- Kim S, Lee K, Choi J-H, Ringstad N, Dynlacht BD (2015) Nek2 activation of Kif24 ensures cilium disassembly during the cell cycle. *Nat Commun* 6:8087
- Fisher SK, Steinberg RH (1982) Origin and organization of pigment epithelial apical projections to cones in cat retina. *J Comp Neurol* 206:131–145
- Nishiyama K, Sakaguchi H, Hu JG, Bok D, Hollyfield JG (2002) Claudin localization in cilia of the retinal pigment epithelium. *Anat Rec* 267:196–203
- Williams CL et al (2011) MKS and NPHP modules cooperate to establish basal body/transition zone membrane associations and ciliary gate function during ciliogenesis. *J Cell Biol* 192:1023–1041
- Hernandez-Hernandez V et al (2013) Bardet–Biedl syndrome proteins control cilia length through regulation of actin polymerisation. *Hum Mol Genet* 22:3858–3868
- Patzke S et al (2010) CSPP is a ciliary protein interacting with nephrocystin 8 and required for cilia formation. *Mol Biol Cell* 21:2555–2567
- Wei Q et al (2012) The BBSome controls IFT assembly and turnaround in cilia. *Nat Cell Biol* 14:950–957
- Goetz SC, Bangs F, Barrington CL, Katsanis N, Anderson KV (2017) The Meckel syndrome- associated protein MKS1 functionally interacts with components of the BBSome and IFT complexes to mediate ciliary trafficking and hedgehog signaling. *PLoS One* 12:e0173399
- Nachury MV et al (2007) A core complex of BBS proteins cooperates with the GTPase Rab8 to promote ciliary membrane biogenesis. *Cell* 129:1201–1213
- Jin H, Nachury MV (2007) The BBSome. *Curr Biol* 19:472–473
- Otto EA et al (2003) Mutations in INVS encoding inversin cause nephronophthisis type 2, linking renal cystic disease to the function of primary cilia and left-right axis determination. *Nat Genet* 34:413–420
- Plotnikova OV, Golemis EA, Pugacheva EN, Ciliogenesis Cell Cycle-Dependent (2008) Cell cycle-dependent ciliogenesis and cancer. *Cancer Res* 68:2058–2061
- Mergen M et al (2013) The nephronophthisis gene product NPHP2/Inversin interacts with Aurora A and interferes with HDAC6-mediated cilia disassembly. *Nephrol Dial Transpl* 28:2744–2753
- Simons M et al (2005) Inversin, the gene product mutated in nephronophthisis type II, functions as a molecular switch between Wnt signaling pathways. *Nat Genet* 37:537–543
- Loktev AV et al (2008) A BBSome Subunit Links Ciliogenesis, Microtubule Stability, and Acetylation. *Dev Cell* 15:854–865
- Gerdes JM et al (2007) Disruption of the basal body compromises proteasomal function and perturbs intracellular Wnt response. *Nat Genet* 39:1350–1360
- Oh EC, Katsanis N (2013) Context-dependent regulation of Wnt signaling through the primary cilium. *J Am Soc Nephrol* 24:10–18
- Liu C et al (2002) Control of beta-catenin phosphorylation/degradation by a dual-kinase mechanism. *Cell* 108:837–847
- Valenta T, Hausmann G, Basler K (2012) The many faces and functions of β -catenin. *EMBO J* 31:2714–2736

42. Boatright JH et al (2015) Methodologies for analysis of patterning in the mouse RPE sheet. *Mol Vis* 21:40–60
43. Pugacheva EN, Golemis EA (2005) The focal adhesion scaffolding protein HEF1 regulates activation of the Aurora-A and Nek2 kinases at the centrosome. *Nat Cell Biol* 7:937–946
44. Moore FE et al (2010) The WW-HECT protein Smurf2 interacts with the Docking Protein NEDD9/HEF1 for Aurora A activation. *Cell Div* 5:22
45. Konari K et al (1995) Development of the blood-retinal barrier in vitro “ formation of tight junctions as revealed by occludin and ZO-1 Correlates with the barrier function of chick retinal pigment epithelial. *Exp Eye Res* 61:99–108
46. Burke JM, Cao F, Irving PE, Skumatz CMB (1999) Expression of E-Cadherin by human retinal pigment epithelium: delayed expression in vitro. *Invest Ophthalmol Vis Sci* 40:2963–2970
47. Gibbs D et al (2004) Role of myosin VIIa and Rab27a in the motility and localization of RPE melanosomes. *J Cell Sci* 26:6473–6483
48. Hubbert C et al (2002) HDAC6 is a microtubule-associated deacetylase. *Nature* 417:455–458
49. Hideshima T et al (2005) Small-molecule inhibition of proteasome and aggresome function induces synergistic antitumor activity in multiple myeloma. *Proc Natl Acad Sci USA* 102:8567–8572
50. Yuan H et al (2012) Overcoming CML acquired resistance by specific inhibition of Aurora A kinase in the KCL-22 cell model. *Carcinogenesis* 33:285–293
51. Corbit KC et al (2008) Kif3a constrains beta-catenin-dependent Wnt signalling through dual ciliary and non-ciliary mechanisms. *Nat Cell Biol* 10:70–76
52. Li Y, Zhang X, Polakiewicz RD, Yao TP, Comb MJ (2008) HDAC6 is required for epidermal growth factor-induced β -catenin nuclear localization. *J Biol Chem* 283:12686–12690
53. Gerhardt C, Leu T, Lier JM, R  ther U (2016) The cilia-regulated proteasome and its role in the development of ciliopathies and cancer. *Cilia* 5:14
54. Verheyen EM, Gottardi CJ (2010) Regulation of Wnt/ β -catenin signaling by protein kinases. *Dev Dyn* 239:34–44
55. Forcioli-Conti N, Lacas-Gervais S, Dani C, Peraldi P (2015) The primary cilium undergoes dynamic size modifications during adipocyte differentiation of human adipose stem cells. *Biochem Biophys Res Commun* 458:117–122
56. Nachury MV et al (2007) A core complex of BBS proteins cooperates with the GTPase Rab8 to promote ciliary membrane biogenesis. *Cell* 129:1201–1213
57. Jin H, Nachury MV (2009) The BBSome. *Curr Biol* 19:R472–R473
58. Seo S et al (2010) BBS6, BBS10, and BBS12 form a complex with CCT/TRiC family chaperonins and mediate BBSome assembly. *Proc Natl Acad Sci USA* 107:1488–1493
59. Sobkowicz HM, Slapnick SM, August BK (1995) The kinocilium of auditory hair cells and evidence for its morphogenetic role during the regeneration of stereocilia and cuticular plates. *J Neurocytol* 24:633–653
60. Korobeynikov V, Deneka AY, Golemis EA (2017) Mechanisms for nonmitotic activation of Aurora-A at cilia. *Biochem Soc Trans* 45:37–49
61. Jang C, Coppinger JA, Seki A, Yates JR, Fang G (2009) Plk1 and Aurora A regulate the depolymerase activity and the cellular localization of Kif2a. *J Cell Sci* 122:1334–1341
62. Otto EA et al (2005) Nephrocystin-5, a ciliary IQ domain protein, is mutated in Senior-Loken syndrome and interacts with RPGR and calmodulin. *Nat Genet* 37:282–288
63. Kinzel D et al (2010) Pitchfork regulates primary cilia disassembly and left-right asymmetry. *Dev Cell* 19:66–77
64. Gabriel E et al (2016) CPAP promotes timely cilium disassembly to maintain neural progenitor pool. *EMBO J* 35:699–791
65. Liu YP et al (2014) Ciliopathy proteins regulate paracrine signaling by modulating proteasomal degradation of mediators. *J Clin Invest* 124:2059–2070
66. Mahuzier A et al (2012) Dishevelled stabilization by the ciliopathy protein Rpgrip1 l is essential for planar cell polarity. *J Cell Biol* 198:927–940
67. Long H, Wang Q, Huang K (2015) Ciliary/flagellar protein ubiquitination. *Cells* 4:474–482
68. Cao M, Li G, Pan J (2009) Regulation of cilia assembly, disassembly, and length by protein phosphorylation. *Methods Cell Biol* 94:333–346
69. Tadenev ALD et al (2011) Loss of Bardet-Biedl syndrome protein-8 (BBS8) perturbs olfactory function, protein localization, and axon targeting. *Proc Natl Acad Sci USA* 108:10320–10325
70. Livak KJ, Schmittgen TD (2001) Analysis of relative gene expression data using real-time quantitative PCR and. *Methods* 25:402–408
71. Pfaffl MW (2001) A new mathematical model for relative quantification in real-time RT-PCR. *Nucleic Acids Res* 29:45e–45
72. Sedmak T, Wolfrum U (2010) Intraflagellar transport molecules in ciliary and nonciliary cells of the retina. *J Cell Biol* 189:171–186

Publication II – Loss of Ciliary Gene *Bbs8* Results in Physiological Defects in the Retinal Pigment Epithelium (First Author; Published)

In this publication, we show that upon loss of *Bbs8*, the RPE shows changes in gene and protein expression of components initially involved in signaling pathways and developmental processes, and at a later time point, RPE homeostasis and function. We further demonstrated that this led to defective cellular polarization and morphology associated with a possible epithelial-to-mesenchymal transition (EMT)-like phenotype of the RPE cells. For the first time, the importance of ciliary proteins in the RPE and their contribution to visual disorders have been emphasized. All of which must be considered when designing treatment strategies for retinal degeneration. As the *Bbs8* knockout model is a global knockout, we further sought to investigate the effect of ciliary dysfunction only in the RPE.





Loss of Ciliary Gene *Bbs8* Results in Physiological Defects in the Retinal Pigment Epithelium

Sandra Schneider¹, Rossella De Cegli², Jayapriya Nagarajan³, Viola Kretschmer¹, Peter Andreas Matthiessen¹, Daniela Intartaglia², Nathan Hotaling³, Marius Ueffing⁴, Karsten Boldt⁴, Ivan Conte^{2,5} and Helen Louise May-Simera^{1*}

¹ Faculty of Biology, Institute of Molecular Physiology, Johannes Gutenberg-University, Mainz, Germany, ² Telethon Institute of Genetics and Medicine, Pozzuoli, Italy, ³ National Center for Advancing Translational Sciences, National Institutes of Health, Bethesda, MD, United States, ⁴ Medical Bioanalytics, Institute for Ophthalmic Research, Eberhard-Karls University, Tübingen, Germany, ⁵ Department of Biology, University of Naples Federico II, Naples, Italy

OPEN ACCESS

Edited by:

Breandan Kennedy,
University College Dublin, Ireland

Reviewed by:

Silvia C. Finnemann,
Fordham University, United States
Ruxandra Bachmann-Gagescu,
University of Zurich, Switzerland

*Correspondence:

Helen Louise May-Simera
may-simera@uni-mainz.de

Specialty section:

This article was submitted to
Molecular Medicine,
a section of the journal
Frontiers in Cell and Developmental
Biology

Received: 16 September 2020

Accepted: 12 January 2021

Published: 18 February 2021

Citation:

Schneider S, De Cegli R, Nagarajan J, Kretschmer V, Matthiessen PA, Intartaglia D, Hotaling N, Ueffing M, Boldt K, Conte I and May-Simera HL (2021) Loss of Ciliary Gene *Bbs8* Results in Physiological Defects in the Retinal Pigment Epithelium. *Front. Cell Dev. Biol.* 9:607121. doi: 10.3389/fcell.2021.607121

Primary cilia are sensory organelles vital for developmental and physiological processes. Their dysfunction causes a range of phenotypes including retinopathies. Although primary cilia have been described in the retinal pigment epithelium (RPE), little is known about their contribution to biological processes within this tissue. Ciliary proteins are increasingly being identified in non-ciliary locations and might carry out additional functions, disruption of which possibly contributes to pathology. The RPE is essential for maintaining photoreceptor cells and visual function. We demonstrate that upon loss of *Bbs8*, predominantly thought to be a ciliary gene, the RPE shows changes in gene and protein expression initially involved in signaling pathways and developmental processes, and at a later time point RPE homeostasis and function. Differentially regulated molecules affecting the cytoskeleton and cellular adhesion, led to defective cellular polarization and morphology associated with a possible epithelial-to-mesenchymal transition (EMT)-like phenotype. Our data highlights the benefit of combinatorial “omics” approaches with *in vivo* data for investigating the function of ciliopathy proteins. It also emphasizes the importance of ciliary proteins in the RPE and their contribution to visual disorders, which must be considered when designing treatment strategies for retinal degeneration.

Keywords: cilia, ciliopathy, retinal pigment epithelium, genetic disease, molecular medicine, RPE, Epithelial-to-Mesenchymal Transition (EMT)

INTRODUCTION

Primary cilia are microtubule-based sensory organelles extending from the cell membrane and are indispensable for a variety of developmental and physiological processes. As such, they are considered as signaling hubs that transmit extracellular signals, and are involved in regulating many signaling pathways, including Wnt, hedgehog, and transforming growth factor β (Tgf- β) (Fliegau et al., 2007; Ishikawa and Marshall, 2011; May-Simera et al., 2017, 2018; Pala et al., 2017). Defects in primary cilia function or assembly lead to a wide range of diseases, collectively termed ciliopathies. Since nearly every cell exhibits a primary cilium, ciliary dysfunction leads to a multitude of different phenotypes, with retinopathy being the most common (Waters and Beales, 2011; May-Simera et al., 2017). The Bardet-Biedl syndrome (BBS) was one of the first ciliopathies described. *BBS* genes encode proteins required for ciliary trafficking, making them essential for maintenance and

function of primary cilia and as such for development and homeostasis of various tissues and organs (Goetz and Anderson, 2010; Waters and Beales, 2011; Forsythe and Beales, 2013; Valverde et al., 2015). Ciliary proteins are increasingly being identified in non-ciliary locations and might carry out additional functions, disruption of which possibly contributes to pathology (Novas et al., 2015; Marchese et al., 2020).

Most research on the retinal aspect of ciliopathies has mainly focused on the photoreceptor, whose outer segment (POS) is a highly specialized primary cilium with the so-called connecting cilium akin to the ciliary transition zone. To date, there is limited information on the contribution of primary cilia in other ocular cell types. Probably, the most relevant ciliated tissue in addition to the photoreceptor cells is the retinal pigment epithelium (RPE). Our recent discoveries did indeed reveal an indispensable role for primary cilia in maturation and functional polarization of this tissue (May-Simera et al., 2018; Patnaik et al., 2019). The RPE is a monolayer of pigmented epithelial cells intercalated between the neural retina and the choriocapillaris of the eye and forms part of the blood-retinal barrier (BRB). With their long apical microvilli, RPE cells ensheath the light-sensitive POS leading to the functional interaction between both tissues (Strauss, 2005; Willoughby et al., 2010). The RPE has additional roles which are critically dependent on maintaining its epithelial phenotype: absorption of scattered photons, regeneration of 11-*cis* retinal in the visual cycle, phagocytosis of shed POS, secretion of various growth factors, transepithelial transport of nutrients and ions, and the maintenance of photoreceptor cells. Therefore, RPE dysfunction and associated failure of one or more of its functional processes are often linked with retinal degeneration and vision impairment (Strauss, 2005; Bharti et al., 2011; Chen et al., 2019).

We have previously shown that primary cilia are crucial for maturation and polarization of induced pluripotent stem cells (iPSC)-RPE *in vitro* (May-Simera et al., 2018). As a consequence of inefficient ciliogenesis and therefore of incomplete RPE maturation, the RPE cells showed reduced expression of adult RPE-specific genes, defective apical microvilli morphology, as well as reduced functionality. Confirming this, we demonstrated that primary cilia dysfunction *in vivo* leads to changes in RPE cell morphology, including underdeveloped tight junctions and apical microvilli in newborn (P0) cilia mutant mice (May-Simera et al., 2018). However, to date, long-term consequences of primary cilia dysfunction in the RPE remain to be investigated. The present study was aimed at elucidating these effects *in vivo* on the maturation and homeostasis of the RPE as the tissue ages. To do so, we again turned to the *Bardet-Biedl syndrome protein* (*Bbs*)-deficient mouse model, as *Bbs* knockouts display significantly reduced and dysfunctional primary cilia (Ross et al., 2005; Tadenev et al., 2011). The *Bbs8/Ttc8* gene encodes a component of the “BBSome,” a protein complex required for ciliary trafficking (Tadenev et al., 2011). We used a *Bbs8*-knock out model since loss of *Bbs8* has one of the most pronounced ciliopathy phenotypes particularly with regard to visual dysfunction (Tadenev et al., 2011; Dilan et al., 2018; May-Simera et al., 2018; Kretschmer et al., 2019; Patnaik et al., 2019).

Our data provides evidence of how loss of ciliary gene/protein *Bbs8* results in physiological defects affecting RPE homeostasis

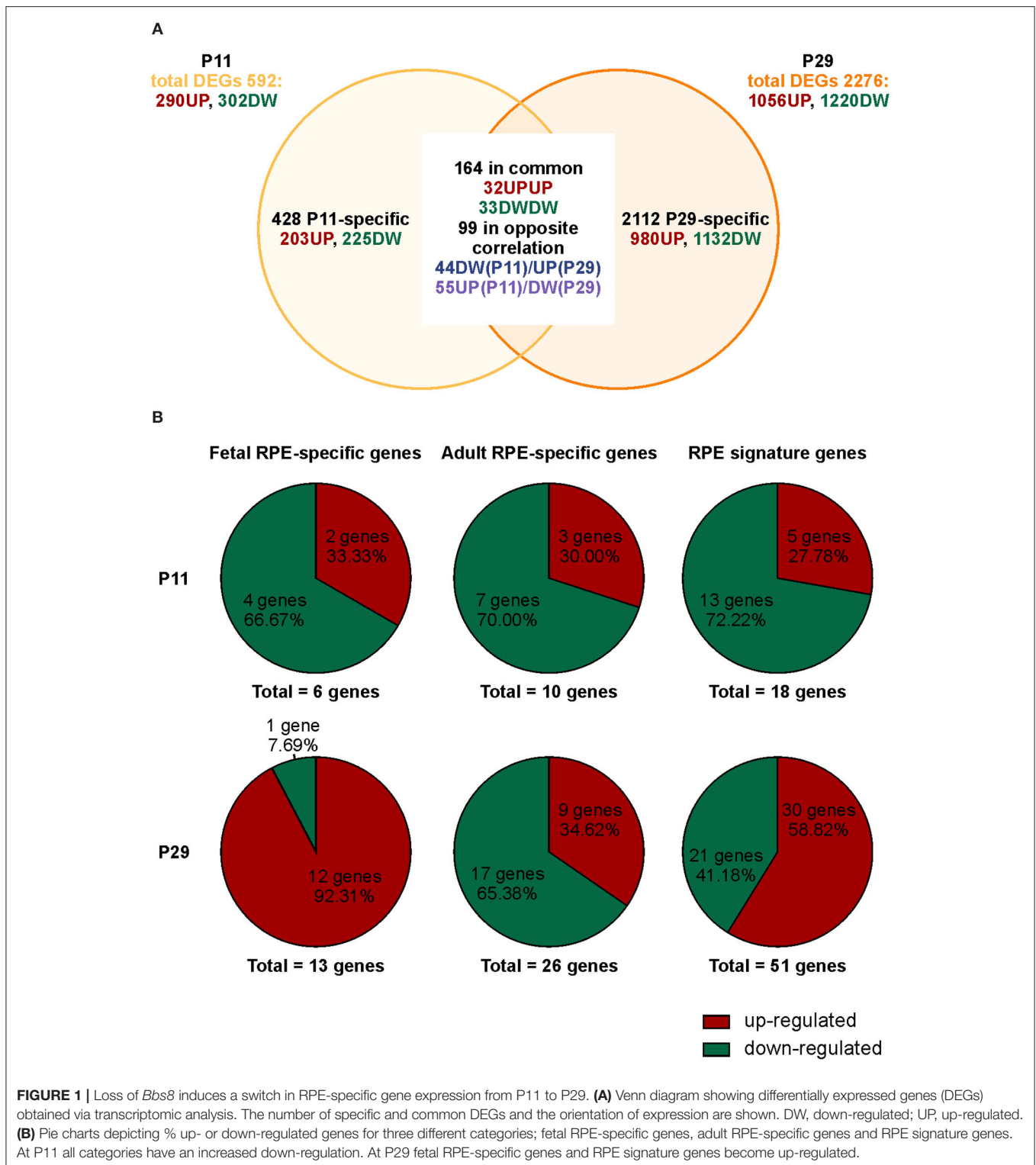
and function, characterized by alteration in both gene and protein expression profiles.

RESULTS

Transcriptomic Analysis of *Bbs8*-Deficient RPE Reveals Mis-regulation of Genes Involved in Numerous RPE-Essential Processes

We previously demonstrated that *Bbs8*^{-/-} mice show incomplete maturation of the RPE at postnatal day 0 (P0) prior to development of the POS, due in part to over-activation of canonical Wnt signaling (May-Simera et al., 2018). However, whether and how ablation of *Bbs8* caused other developmental defects, including alterations of RPE maturation and its crosstalk with adjacent photoreceptor cells has been not been investigated. We first explored the phenotypic consequences caused by loss of *Bbs8* in the RPE by focusing on patterns of gene expression. We investigated the effect of *Bbs8* deletion in the RPE by carrying out an unbiased QuantSeq 3' mRNA sequencing analysis of P11 and P29 RPE specimens isolated from *Bbs8*^{-/-} and *Bbs8*^{+/+} mouse eyes. At both time points, this analysis yielded differentially expressed transcripts in *Bbs8*^{-/-} RPE compared to littermate controls. At P11, we observed up-regulation of 290 transcripts and down-regulation of 302 transcripts (Figure 1A, Supplementary Tables 1, 3). At P29, 1,056 transcripts were up-regulated, and 1220 transcripts were down-regulated (Figure 1A, Supplementary Tables 2, 4). This raised the possibility that loss of *Bbs8* may directly or indirectly influence expression of a large number of genes and alter RPE maturation and function. To better investigate this possibility, we compared the mis-regulated genes with lists of RPE-specific genes, divided into fetal RPE-specific, adult RPE-specific and RPE signature genes published in Strunnikova et al. (2010) (Figure 1B, Supplementary Table 5). Across all three categories a similar trend was observed at P11, namely that ~70% differentially expressed genes (DEGs) were down-regulated and ~30% were up-regulated (Fetal RPE-specific *n* = 6 genes, Adult RPE-specific *n* = 10 genes, RPE signature *n* = 18 genes). However, at P29 ~90% of the fetal RPE-specific genes were up-regulated, whereas ~65% of the adult RPE-specific genes were down-regulated (Fetal RPE-specific *n* = 13 genes, Adult RPE-specific *n* = 26 genes, RPE signature *n* = 51 genes). Suggesting a delay in RPE maturation in the mutants.

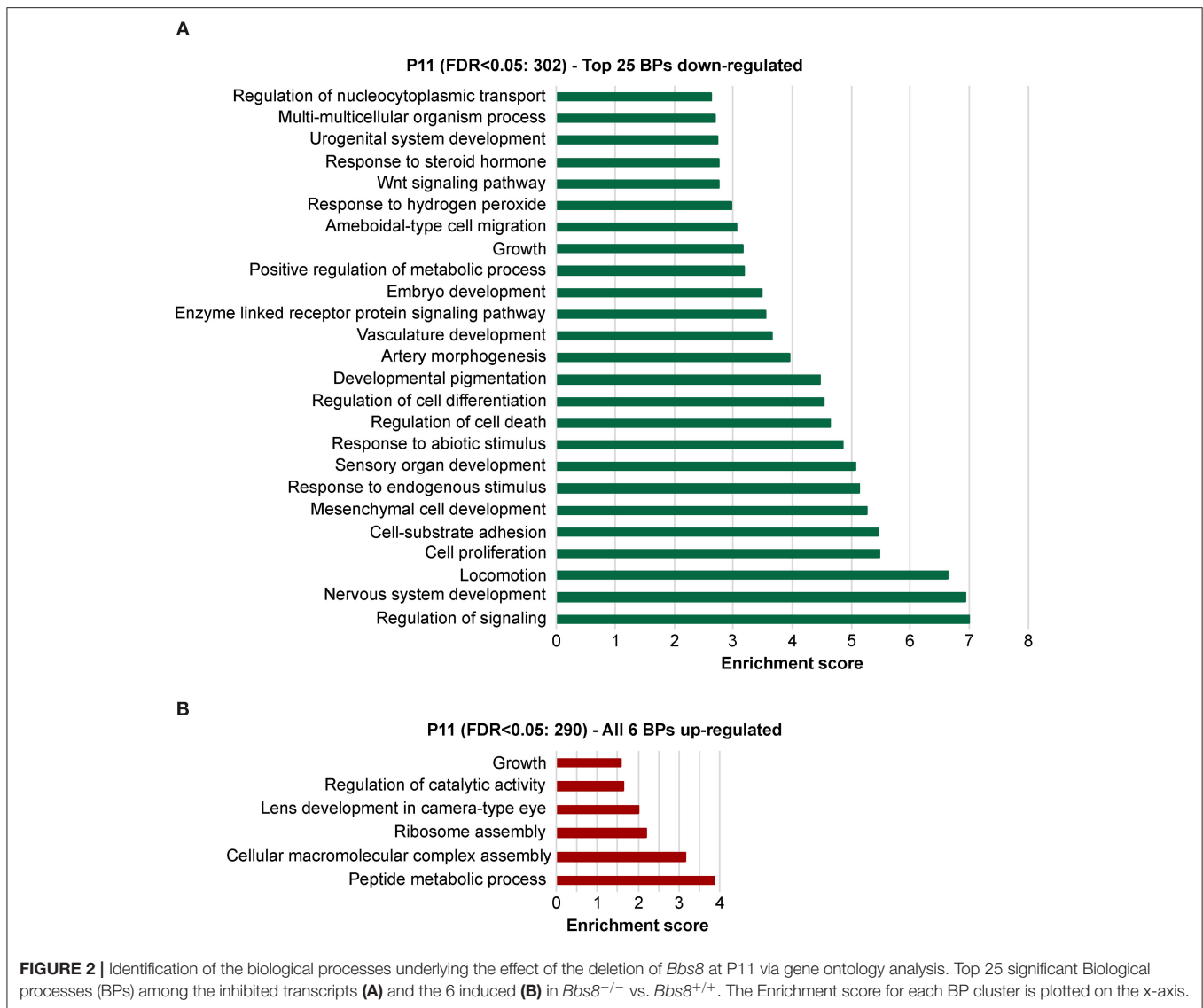
To explore the biological significances of these transcriptomes, we performed a gene ontology enrichment analysis (GOEA) restricting the output to biological process (BP) terms at each time point (see Figure 2 and Supplementary Table 6 for P11, and Figure 3 and Supplementary Table 7 for P29). Figure 2 shows the top 25 most significant down-regulated and all six up-regulated BP-clusters in which the inhibited and induced transcripts, respectively, were mainly functionally enriched. The Enrichment score (ES) represents the amount to which genes in a gene ontology cluster are over-represented. The ES scale can vary dependent on how genes cluster in a given term. At P11 most of the DEGs involved signaling and developmental processes (Figure 2, Supplementary Table 6),



while at P29 they involved RPE homeostasis and function (Figure 3, Supplementary Table 7).

A comparison of DEGs in *Bbs8*^{-/-} vs. control RPE at two timepoints, P11 and P29, identified 65 mis-regulated

genes as shown in the Venn diagram in Figure 1A. Of these 32 were up-regulated and 33 down-regulated at both time points. We again performed GOEA analysis to identify common biological processes. We identified three clusters of

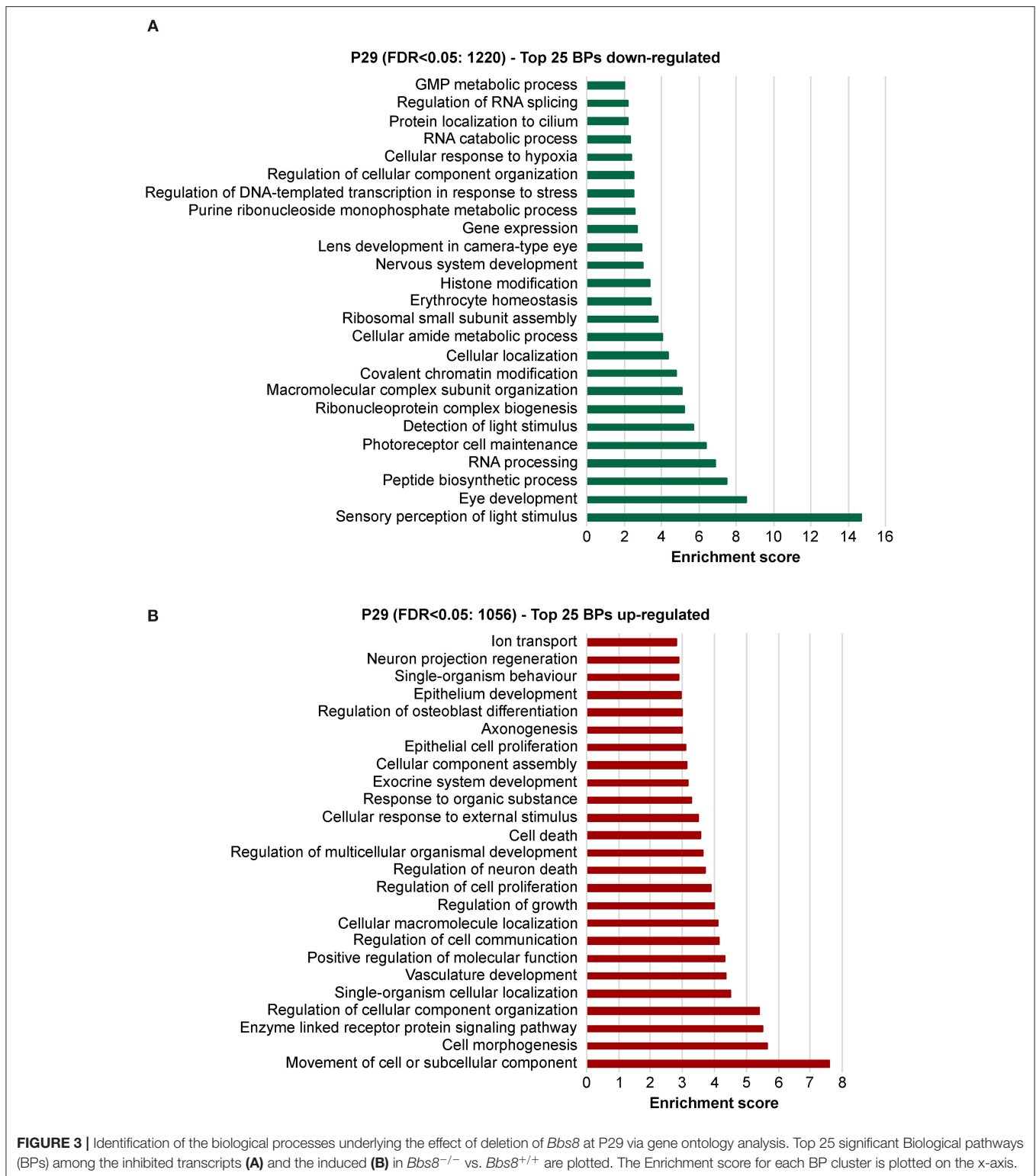


biological processes that were significantly up-regulated and three that were significantly down-regulated. Up-regulated processes included responses to metal ions (albeit only four genes), processes involving cellular organization and apoptotic processes (Figure 4A, Supplementary Table 8). Down-regulated processes included responses to endogenous stimuli, processes involving signal transduction and visual perception (Figure 4A, Supplementary Table 8). Since the genes involved in visual perception included several photoreceptor-specific genes, we attributed this cluster to contamination of adjacent tissues (see discussion). The heatmap in Figure 4B visualizes differentially regulated genes associated with these processes. Many mis-regulated genes are involved in RPE polarization and function, receptors and channel proteins (*Trpm3*, *Drd4*, *Mt1*), cytokines (*Vegfa*, *S100B*) and genes encoding proteins involved in phagocytosis and cellular metabolism (*Anxa2*, *Ctsd*, *Ezr*, *Trf*). Moreover, we detected an up-regulation of genes associated with

apoptotic processes suggesting possible pathological changes in the *Bbs8* knockout RPE as early as P11, not necessarily just associated with a delay in maturation.

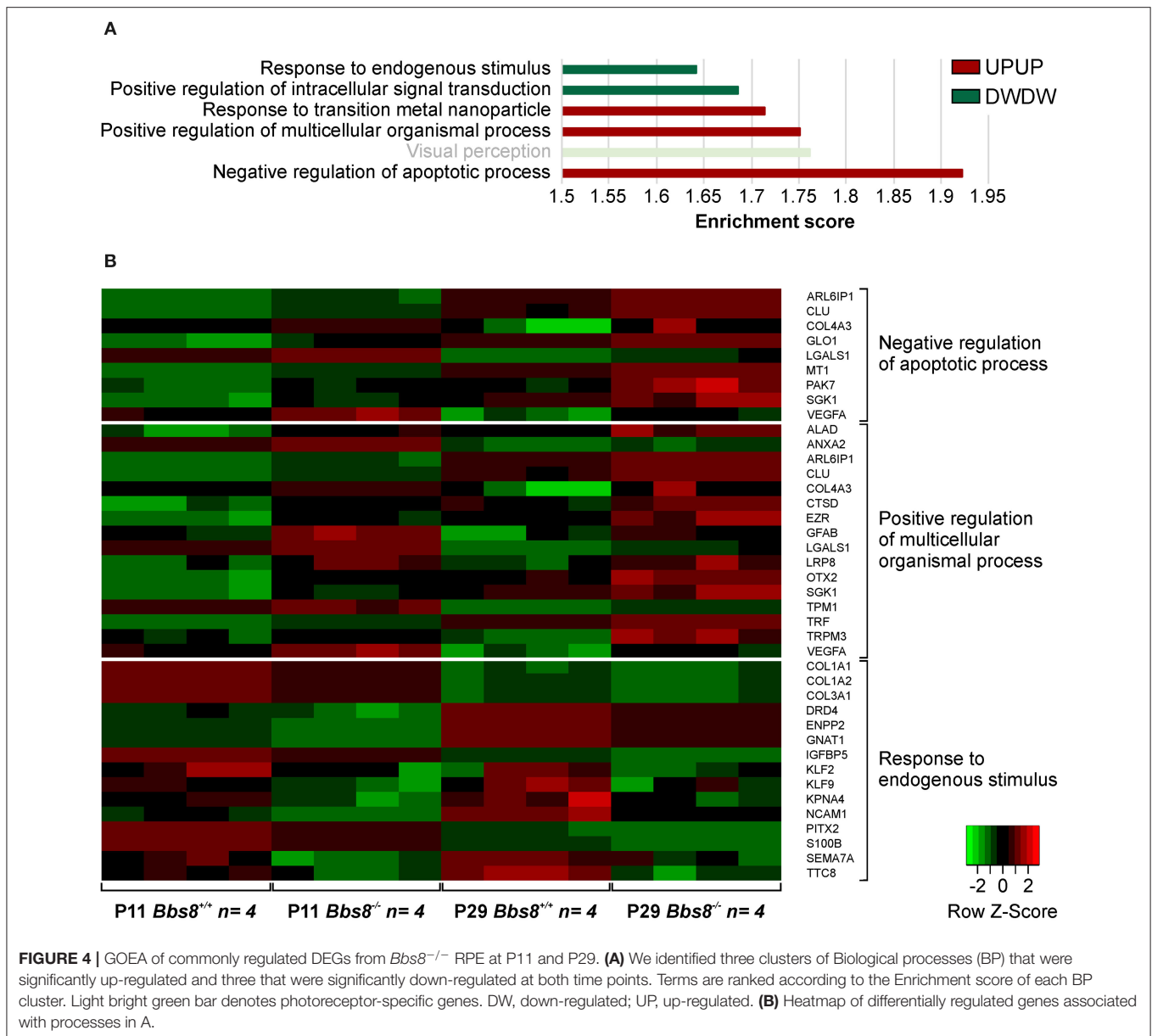
Proteomic Analysis of *Bbs8*-Deficient RPE Suggests Loss of Functionality

To better investigate the phenotypic consequences associated with *Bbs8* depletion, we performed mass spectrometry-based quantitative proteomics. We analyzed RPE cells isolated from *Bbs8*^{-/-} and *Bbs8*^{+/+} mice at P11 and P29. At both time points, a significant mis-regulation of the proteome was observed. In agreement with the transcriptomic analysis, we observed more mis-regulation in P29 *Bbs8*^{-/-} RPE even at protein level. In *Bbs8*^{-/-} at P11 we detected ten proteins down-regulated and only one up-regulated (Figure 5A, Supplementary Table 9). Several of these down-regulated proteins were associated with



photoreceptor outer segment (POS) processes. Since many of these proteins are not significantly changed at the transcript level it suggests that they might come from POS. Their down-regulation in the mutant might be due to alteration in POS

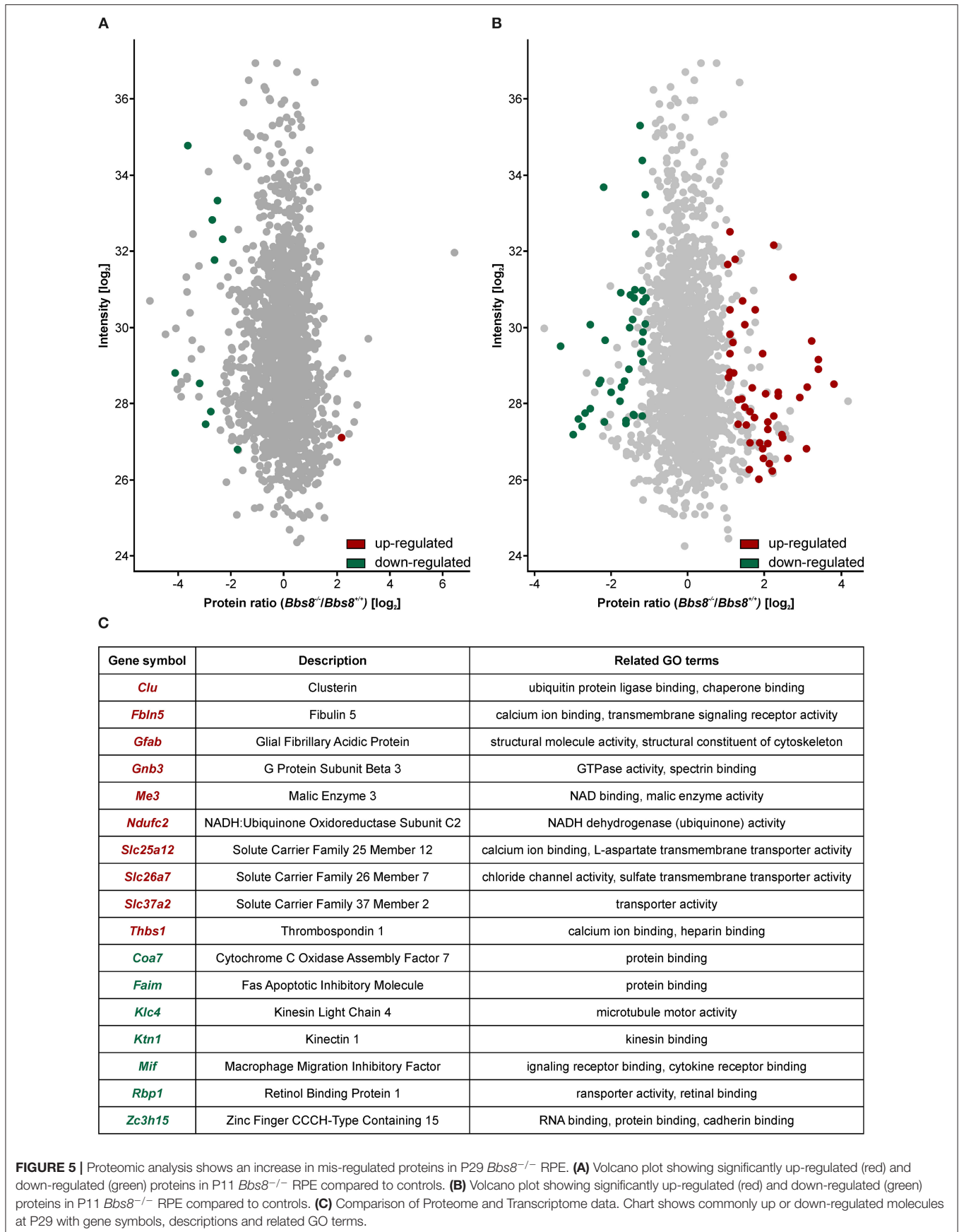
processing in the RPE, in defects in the POS phagocytosis or both cellular processes. This last possibility is particularly attractive, because RPE cells begin to extend their microvilli by P5 to phagocytize shed POS around P11 (Mazzoni et al.,



2014). Concordantly, our data also showed an increase in the protein expression of mitochondrial transcription factor A (Tfam). This data further indicated that *Bbs8*^{-/-} RPE showed a defect in the differentiation since, previous reports have highlighted the relevance of Tfam up-regulation in modulating cell differentiation (Collu-Marchese et al., 2015; Agostini et al., 2016).

At P29, 50 proteins were up-regulated and 40 down-regulated (Figure 5B, Supplementary Table 9). To gain insight into differentially regulated processes, we performed an enrichment analysis of the significantly dysregulated proteins. At P11 there were not enough molecules to perform enrichment analysis. At P29 we found integrin binding (GO:0005178) significantly mis-regulated, including adhesion proteins such as Paxillin,

Thrombospondin, and Vitronectin. This data may suggest defects in cellular adhesion. In an attempt to consolidate our transcriptomic and proteomic datasets, we looked for overlapping molecules (transcripts/proteins). At P11 only one molecule (Gnat) was down-regulated in both data sets. At P29, ten molecules were up-regulated in both data sets whilst seven were down-regulated (Figure 5C). These include molecules involved in metabolism and cytoskeletal components. The proteomic data set at P29 contained at least eight other up-regulated proteins involved in metabolism (Atp5j, Cox5b, Slc25a11, Ndufa9, Timm9, Mtch1, Isca2, Timm8a1). It also contained other down-regulated cytoskeletal proteins associated with adhesion (Paxillin, Palmd, Limch1, Pdlim2, Ernm, Ctnn). The mis-regulation of this subset of proteins is indicative of



significant metabolic or physiologic changes likely affecting function and not just a delay in maturation in the RPE upon loss of *Bbs8*.

Loss of *Bbs8* Results in Defective RPE-Cell Morphology

Since several dys-regulated molecules were involved in adhesion, and RPE function is critically dependent on a tightly connected monolayer epithelium, we examined RPE cellular morphology and patterning in RPE flatmount preparations from *Bbs8*^{-/-} and *Bbs8*^{+/+} mice. We stained for F-actin, a cytoskeletal marker, and zonula occludens-1 (ZO-1), a tight junction protein, at different time points (P0, P11, P29, and P81) (Figure 6A). From P11 onwards, we observed a progressive loss of the typical hexagonal, honeycomb-like structure in *Bbs8*^{-/-} RPE cells compared to control. This morphological phenotype was accompanied by discontinuous staining of both F-actin and ZO-1 markers (arrowheads). Morphology of the RPE cells was significantly impaired and culminated in evident distortion or complete disruption of cytoplasmic membranes (asterisks) at P81. In contrast to this, cellular morphology in the control flatmounts remained consistent as the tissue aged (Figure 6A).

To investigate this further we assessed cellular morphology changes via high-content image analysis. Due to the nature of the disrupted morphology encountered in the mutant samples, damaged areas could not be included in the automatic software analysis (for an example see Supplementary Figure 1G). Epithelial parameters included area, perimeter, hexagonality, polygonality, eccentricity, and number of neighbors (Figures 6B–F, Supplementary Figures 1A–F). Even without the damaged regions, quantification of area revealed that *Bbs8*^{-/-} RPE cells were significantly larger compared to controls at P29, and the variance in cell area was significantly increased at P29 and at P81 (Figure 6B). P29 *Bbs8*^{-/-} RPE also showed a significant increase in cell perimeter and in the variance of cell perimeter (Figure 6C). Although not statistically significant, we observed that *Bbs8*^{-/-} RPE cells were becoming less hexagonal with age, which is opposite to normal *Bbs8*^{+/+} RPE (Figure 6D). A similar trend was observed with the Hexagonality SD (standard deviation) (Figure 6E). Although the majority of RPE cells lose their cilium as the tissue matures, these findings indicate that either ciliary function, even in just a small percentage of cells, is continuously required for maintenance of epithelial morphology. Alternatively, a subset of ciliary proteins (in particular the BBS proteins) may have additional alternative functions affecting cellular morphology.

Loss of *Bbs8* Leads to Functional RPE Defects

Disrupted morphology can consequently lead to a loss of polarization, which is essential for RPE functionality. In the RPE, apical microvilli are intricately connected to the adjacent POS and are indispensable for retinal homeostasis. Ezrin, a member of the Ezrin/Radixin/Moesin (ERM) family, is a key marker for microvilli, found in epithelial microvilli, where it bridges the actin cytoskeletal filaments and the cell membrane (Bonilha et al.,

2006; Ohana et al., 2015). With *Bbs8* deletion *Ezrin* transcripts were significantly up-regulated, in contrast to down-regulation at the proteomic level at both ages. This might suggest a possible compensatory regulatory effect due to dysfunctional protein, in which the absence of a functional protein stimulates the cell to increase transcription (negative feedback). We stained *Bbs8*-deficient RPE flatmounts with anti-phospho-Ezrin(Thr567)/Radixin(Thr564)/Moesin(Thr558) (p-ERM), which marks functional Ezrin at apical microvilli (Ohana et al., 2015). In P11 *Bbs8*^{-/-} RPE, we observed decreased p-ERM staining compared to control, although occasionally there was irregular accumulation at the apical surface (Figure 7A arrowheads, Supplementary Figure 2 arrowheads). At a later time point (P81) p-ERM was predominantly absent (Figure 7A) which suggests a worsening of apical microvilli formation in *Bbs8*-deficient RPE as already described at P0 (May-Simera et al., 2018).

Defective apical microvilli undoubtedly have a consequent effect on the functional connection between RPE and POS. To verify this, we assessed the retinal adhesion between RPE and adjacent retina at P16. We quantified the amount of melanin in RPE apical microvilli still attached to the retina after it is mechanically separated from the RPE. Compared to controls, *Bbs8*^{-/-} retina showed higher concentration of melanin, this could mean that despite apical microvilli abnormalities, retinal adhesion was stronger or that there was defective directional movement of melanosomes back to the cell body (Figure 7B). To further investigate RPE function upon loss of *Bbs8*, we performed a phagocytosis assay on *BBS8* KD ARPE-19 cells using siRNA. Due to the volume of material required and difficulty in obtaining *Bbs8*^{-/-} material, it was not possible to perform this assay in primary RPE cultures. We adapted a protocol previously described by Nandrot et al. (2007). *BBS8* knockdown was optimized and validated using qPCR (Supplementary Figure 3A) and assay conditions were tested prior to performing the experiments (Supplementary Figure 3B). *BBS8* KD ARPE-19 cells showed significant up-regulation of bound POS compared to control, although the internalization, or more specifically the phagocytosis, of POS was significantly decreased in *BBS8* KD cells (Figure 7C). Combined this data shows that loss of *Bbs8* disrupts processes involving functional apical processes.

Loss of *Bbs8* Induces EMT-Like Traits in the RPE

Previous studies have shown that ciliary mutations induce epithelial-to-mesenchymal transition (EMT) in other organs and tissues, including epicardial tissue, kidney epithelial cells, and pancreatic β -cells (Guen et al., 2017; Blom and Feng, 2018; Han et al., 2018; Volta et al., 2019). EMT denotes the trans-differentiation of epithelial cells into mesenchymal cells and is manifested by loss of cell junctions and apical-basal polarity, as well as reorganization of the cytoskeleton and changes in signaling and gene expression associated with cell shape (Lamouille et al., 2014). Since our omics data showed differential expression of molecules involved in

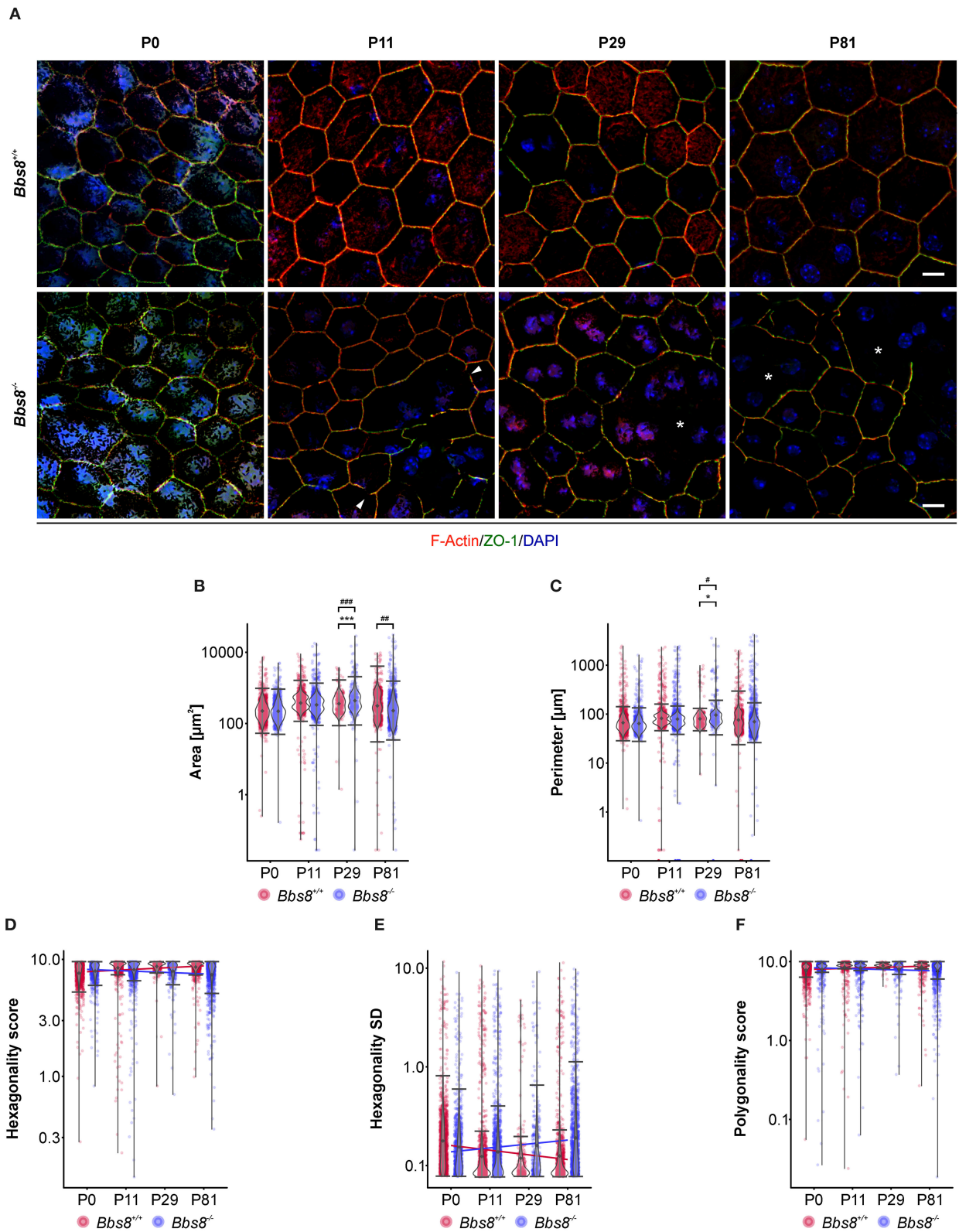


FIGURE 6 | Cell morphological defects are seen in *Bbs8*-deficient RPE. **(A)** Representative images of RPE flatmounts stained for F-actin (red) and ZO-1 (green) to visualize cytoskeleton and cell membrane. DAPI was used to stain nuclear DNA. P11 *Bbs8*^{-/-} RPE shows discontinuous membrane staining (arrowheads). Starting in *(Continued)*

FIGURE 6 | P29 *Bbs8*^{-/-} RPE shows larger areas of RPE cells with distorted or even completely disrupted cell membranes (asterisks). Scale bars: 10 μ m. **(B-F)** Quantification of cell morphology parameters. Statistical analysis is described in methods. **(B)** Comparison of cell area of *Bbs8*^{-/-} and *Bbs8*^{+/+} RPE cells reveals an increase of the mean ($p = 6.43 \times 10^{-45}$) and the variance ($p = 5.28 \times 10^{-52}$) of P29 *Bbs8*^{-/-} RPE cells and an increase of variance ($p = 0.0013$) of P81 *Bbs8*^{-/-} RPE cells. **(C)** Comparison of cell perimeter of *Bbs8*^{-/-} and *Bbs8*^{+/+} RPE cells reveals an increase of the mean ($p = 0.0342$) and the variance ($p = 0.0272$) of P29 *Bbs8*^{-/-} RPE cells. **(D)** Comparison of hexagonality score of *Bbs8*^{-/-} and *Bbs8*^{+/+} RPE cells. The blue line depicts a trend toward cells being less hexagonal in the mutant over time. The opposite trend (red line) is observed in *Bbs8*^{+/+} RPE. **(E)** The standard deviation of the hexagonality score trends upwards in the mutant (blue line). The opposite trend is observed in *Bbs8*^{+/+} RPE (red line). **(F)** Comparison of polygonality score of *Bbs8*^{-/-} and *Bbs8*^{+/+} RPE cells reveals a trend to more polygonal cells in *Bbs8*^{-/-} RPE with higher age (blue line). The opposite trend is observed in *Bbs8*^{+/+} RPE (red line). (n : P0 *Bbs8*^{+/+} = 1,492 cells, P0 *Bbs8*^{-/-} = 1,030 cells, P11 *Bbs8*^{+/+} = 1,536 cells, P11 *Bbs8*^{-/-} = 1,755 cells, P29 *Bbs8*^{+/+} = 331 cells, P29 *Bbs8*^{-/-} = 383 cells, P81 *Bbs8*^{+/+} = 1,128 cells, P81 *Bbs8*^{-/-} = 1,315 cells) Significance levels: mean: > 0.05 not significant (ns), $\leq 0.05^*$, $\leq 0.01^{**}$, $\leq 0.001^{***}$; variance: > 0.05 not significant (ns), $\leq 0.05^\#$, $\leq 0.01^{\#\#}$, $\leq 0.001^{\#\#\#}$.

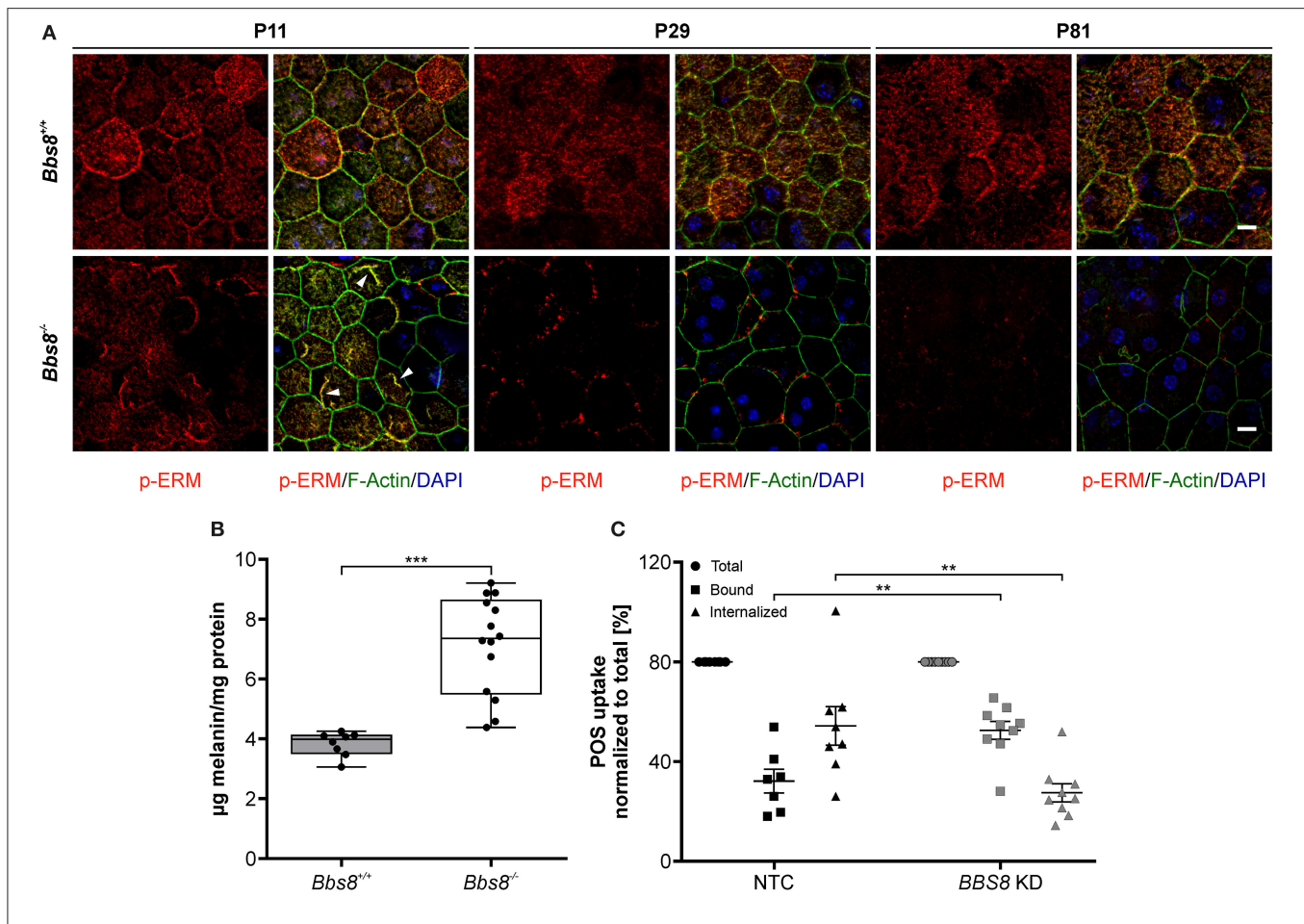


FIGURE 7 | Deletion of *Bbs8* leads to defects in RPE function. **(A)** Representative images of RPE flatmounts stained for p-ERM (red) and F-actin (green) to visualize apical microvilli and the cytoskeleton. DAPI was used to stain nuclear DNA. P11 *Bbs8*^{-/-} RPE shows abnormal accumulations of p-ERM staining (arrowheads). Staining of p-ERM is dramatically reduced as the tissue ages. *Bbs8*^{+/+} RPE shows consistent staining at all ages. Scale bars: 10 μ m. **(B)** Retinal adhesion assay. Quantification of melanin attached to the retina is significantly increased in P16 *Bbs8*^{-/-} compared to controls ($p < 0.0001$). Statistical analysis was performed using ROUT test (Q = 0.1 %) identified 2 outliers before using unpaired t -test (n : *Bbs8*^{-/-} = 14, *Bbs8*^{+/+} = 8). **(C)** Phagocytosis assay. Quantification of photoreceptor outer segments (POS) uptake reveals a significant increase in bound POS ($p = 0.0025$) and a significant down-regulation in internalized POS ($p = 0.0025$) in *BBS8* KD ARPE-19 cells compared to controls. Statistical analysis was performed using ROUT test (Q = 10%) identified 1 outlier before doing a one-way ANOVA and Tukey $post-hoc$ test (n : *BBS8* KD = 9, NTC = 7-8). Significance levels: $\leq 0.01^{**}$, $\leq 0.001^{***}$.

adhesion and polarization and our patterning data identified changes in cell morphology, we looked specifically for EMT-related changes upon loss of *Bbs8*. Virtually all GO terms associated with differentially expressed genes that were initially down-regulated at P11 and then up-regulated at P29 were associated with EMT-related processes (Figure 8A). Similarly, a

heatmap visualizing genes involved specifically in EMT revealed an up-regulation at P29, although not at P11 (Figure 8B). To support our transcriptomic data, we performed qPCR of EMT hallmark genes in *Bbs8*^{-/-} eyecups. Changes in the gene expression of the EMT transcription factor Snail have previously been detected in RPE cells undergoing EMT

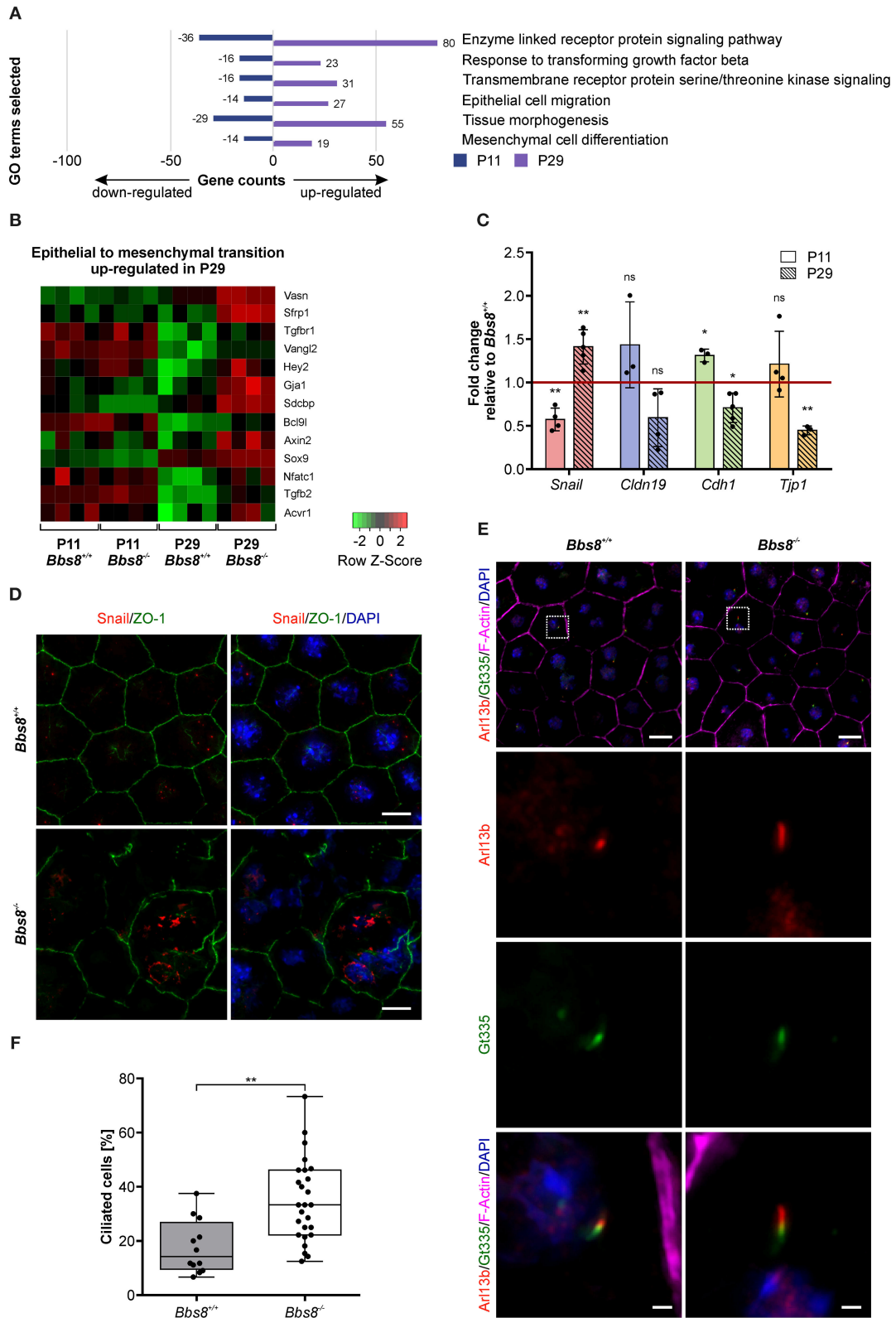


FIGURE 8 | Loss of *Bbs8* induces EMT-like traits in the RPE. **(A)** GO terms associated with differentially expressed genes that were initially down-regulated at P11 and then up-regulated at P29. **(B)** Heatmap showing DEGs associated with epithelial-to-mesenchymal transition in the four experimental groups. *shi* **(C)** Quantitative (Continued)

FIGURE 8 | gene expression shows a shift toward EMT-like associated gene expression profiles between P11 and P29. *Snail* expression shifts from down-regulation at P11 ($p = 0.0073$) toward up-regulation at P29 ($p = 0.0096$). Expression of *Cldn19*, *Cdh1*, and *Tjp1* shifts from an up-regulation (*Cldn19*: $p = 0.2681$, *Cdh1*: $p = 0.0180$ and *Tjp1*: $p = 0.3439$) at P11 toward a down-regulation at P29 (*Cldn19*: $p = 0.0919$, *Cdh1*: $p = 0.0189$ and *Tjp1*: $p = 0.0028$) (P11 n: *Bbs8*^{-/-} = 3–4, *Bbs8*^{+/+} = 4; P29 n: *Bbs8*^{-/-} = 3–5, *Bbs8*^{+/+} = 3–5). Statistical analysis was performed using one sample *t*-test. *Cdh1*: E-cadherin, *Cldn19*: Claudin 19, *Snail*: *Snail*, *Tjp1*: tight-junction protein 1. **(D)** Representative images of P11 RPE flatmounts stained for Snail (red) and ZO-1 (green). DAPI was used to stain nuclear DNA. P11 *Bbs8*^{-/-} RPE shows an increase in Snail expression especially in cells with disrupted morphology. Scale bars: 10 μ m. **(E)** Representative images of RPE flatmounts at P29, stained for primary cilia using Arl13b (red) and Gt335 (green). F-Actin (magenta) was stained to visualize the cytoskeleton and DAPI was used to stain nuclear DNA. Higher magnifications are indicated in the image by a square. Scale bars: 10 μ m, higher magnifications 1 μ m. **(F)** Quantification of ciliated cells in P29 *Bbs8* RPE showing a significant increase in ciliation in *Bbs8*-deficient RPE compared to control ($p = 0.0011$) (n: *Bbs8*^{-/-} = 4 eyes, 340 cells, *Bbs8*^{+/+} = 2 eyes, 157 cells). Statistical analysis was performed using unpaired *t*-test. Significance levels: > 0.05 not significant (ns), $\leq 0.05^*$, $\leq 0.01^{**}$, $\leq 0.001^{***}$.

(Tamiya and Kaplan, 2016). Increased Snail is known to repress expression of E-cadherin and claudins (Lamouille et al., 2014). Furthermore, ZO-1 expression has been shown to be reduced upon EMT (Lamouille et al., 2014). In agreement with these observations, our qPCR data showed a shift toward an EMT-like state between P11 and P29 (Figure 8C). At P11 we saw a significant down-regulation of *Snail*, which accompanied a trend toward up-regulation of *Cldn19* and *Tjp1* and a significant induction of *Cdh1* compared to controls. In contrast, at P29 we detected a significant induction of *Snail* correlated to the significant down-regulation of *Cdh1* and *Tjp1*, together with a trend toward a down-regulation of *Cldn19* compared to controls. These opposite effects of EMT hallmark gene expression between P11 and P29 further supports the possibility that these alterations are mediated by the development of EMT-like characteristics over time. This finding is consistent with the observed progression of disrupted RPE cell morphology (Figure 6). In further demonstration that disrupted regions in the RPE could be linked to EMT, we stained P11 RPE flatmounts for Snail and observed an increase in Snail expression in mutant cells with disrupted morphology (Figure 8D, Supplementary Figure 4A). Snail expression was mostly localized to the nucleus in damaged areas and was not detected in control tissue.

EMT denotes the trans-differentiation from an epithelial to a mesenchymal cell (Ohlmann et al., 2016). This process includes de-differentiation, as well as *de novo* differentiation of cells of an epithelial cell layer. EMT has been linked to primary ciliogenesis as a mechanism of EMT programs (Guen et al., 2017) therefore, we examined ciliation in our mutant tissue. Primary cilia were identified via co-localization of ciliary membrane marker Arl13b and transition zone marker Gt335. To denote a true primary cilium, Arl13b staining must extend beyond Gt335 staining (Figure 8E). We had previously shown that the percentage of ciliated cells in mouse RPE is transient and reduces to under 20% in mature RPE. Similarly, we found that at P29 around 15% of control RPE cells were ciliated. In *Bbs8*^{-/-} RPE we observed a significant increase with almost twice as many ciliated cells (Figure 8F). In *Bbs8*^{-/-} RPE we also observed cilia at P81, whereas these were never detected in controls (Supplementary Figure 4B). This increase in ciliation in *Bbs8*^{-/-} RPE might be consistent with a failure of ciliary disassembly since we had previously seen a similar level of ciliation in in *Bbs8*^{-/-} RPE at E16.5, and could contribute to the development of a possible EMT-like phenotype observed at P29.

DISCUSSION

Ciliary mutations lead to a range of pathological phenotypes with retinal dystrophy being one of the most common. Not only do they cause syndromic retinal disorders, but they also underlie numerous non-syndromic retinal dystrophies and a large proportion of genes associated with vision loss directly encode ciliary proteins (<https://sph.uth.edu/Retnet/>). So far, most research on these retinopathies has focused on the highly specialized primary cilium of the photoreceptors, which undoubtedly plays a significant role in disease progression. However, there is little information available on the contribution of dysfunctional ciliary proteins in other ocular cell types (May-Simera et al., 2017, 2018). The RPE is a ciliated epithelial monolayer intercalated between the choriocapillaris and the retina and is indispensable for photoreceptor health and function (Strauss, 2005; May-Simera et al., 2018). Due to the close interaction between the RPE and the photoreceptors of the retina, they are often considered as a functional unit. We recently showed that primary cilia in the RPE are required for its maturation (May-Simera et al., 2018; Patnaik et al., 2019). Here we demonstrate that, upon ciliary disruption via deletion of *Bbs8*, the RPE never fully matures and exhibits phenotypic defects that affect RPE function even before adjacent photoreceptors have differentiated. This developmental defect is supported by a number of observations. Deletion of *Bbs8* leads to changes in gene and protein expression not only involving signaling pathways and developmental processes, but also at a later time point RPE homeostasis and function. Differentially regulated molecules affecting the cytoskeleton and cellular adhesion led to defective cellular polarization and morphology consequently disrupting phagocytic functions. Our combinatorial “omics” approach (QuantSeq 3' mRNA sequencing and Mass spectrometry) strongly supported our *in vivo* data and highlights the value of multi-omic approaches in identifying *in vivo* molecular mechanisms in the RPE.

Importantly, as RPE and photoreceptor cells are in close physical contact to each other, we noticed contamination of photoreceptor tissue. The latter may arise from an alteration of extracellular matrix between photoreceptor and RPE and/or precocious degeneration events in the outer segments of *Bbs8*^{-/-} photoreceptors. In particular, at P29 we found changes involved in sensory perception of light stimulus in the RPE in the *Bbs8*^{-/-} mouse. Although this might be attributable to contamination events, it is also in accordance with recent data published by Liu et al. (2019), which highlighted the capacity of not completely

differentiated RPE to produce essential visual cycle genes (Liu et al., 2019). Interestingly, in the proteomic data at P11 we found several photoreceptor outer segment (POS) proteins to be down-regulated compared to control. Since most of these are not significantly changed at the transcript level, it suggests that these do indeed come from POS in the control. This might be due to alteration in POS processing in the RPE or due to defects in the POS phagocytosis. It could also suggest a technical difference in that the preparations from control animals had closer attachment to the outer segments, thereby leaving more contamination upon separation. This in turn could represent a defect in the OS, but also a loss of attachment between the RPE and OS in the mutant animals.

Extrapolating from these, it would suggest that the P11 transcript changes are mostly RPE specific and strongly support an alteration in RPE differentiation and function. Furthermore, the availability of comparable gene expression level for a large number of RPE-specific genes rendered our results robust with regard to contaminant variation. Moreover, the majority of mis-regulated genes were exclusively involved in RPE polarization and function, rather than to a generic RPE gene expression changes.

An important point to consider is that our mouse model is not an RPE conditional knockout, meaning that adjacent photoreceptors also lacked *Bbs8*. We and others have already shown that loss of *Bbs8* results in early onset retinal degeneration with significant photoreceptor outer segment disruption (Dilan et al., 2018; Kretschmer et al., 2019). Although substantial photoreceptor outer segment defects can cause a secondary effect in the RPE, photoreceptor-dependent degeneration does not necessarily go hand in hand with early RPE cell loss or gross RPE morphology. This can be seen in other mouse models with photoreceptor specific mutations (such as peripherin and rhodopsin), which do not have an early RPE phenotype despite retinal degeneration (Cheng et al., 1997; Liu et al., 2010). Since we observed changes in the RPE as early as P11, a time point at which the photoreceptor outer segments are still forming, we hypothesize that loss of *Bbs8* in the RPE intrinsically leads to abnormalities, which likely become amplified when interacting with defective photoreceptors. Ideally this could be answered by generating RPE-specific *Bbs8* mutant mice. However, since retinopathy patients inevitably have mutations affecting all ocular tissues, there is still value in understanding the mechanisms of disease progression in global mouse mutants.

Bbs8 is an integral component of the BBSome required for ciliary trafficking, and countless studies have shown that loss of *Bbs8* compromises ciliary function (Ansley et al., 2003; Blacque et al., 2004; Tadenev et al., 2011; Hernandez-Hernandez et al., 2013; May-Simera et al., 2015; Goyal et al., 2016). As primary cilia are essential for early developmental and physiological processes, their dysfunction may have long-term effects on the RPE (Fliegauf et al., 2007; Ishikawa and Marshall, 2011; May-Simera et al., 2017, 2018; Pala et al., 2017). However, the percentage of ciliated cells in the RPE varies over time from over 70% between embryonic day (E) 14.5 and E16.5 to around 10% after birth and in adult (May-Simera et al., 2018; Patnaik et al., 2019). If we consider *Bbs8* function to be restricted to ciliary

processes, then this either means that the changes we describe in this study are a consequence of earlier ciliary dysfunction, or that residual ciliated cells in some way contribute to RPE homeostasis. In this case, the increase in ciliation in *Bbs8* mutant RPE at P29 and beyond might be contributing to the phenotype. Alternatively, *Bbs8* might also exert other functional roles, not directly associated with the primary cilium.

Additional roles for “traditional” ciliary proteins have recently been identified for numerous classes of ciliary proteins, in particularly the BBS proteins (Novas et al., 2015; Marchese et al., 2020). These might include membrane trafficking, cytoskeletal organization, or transcriptional regulation (Gascue et al., 2012; Hernandez-Hernandez et al., 2013; Patnaik et al., 2020). Interestingly, the transcriptomic data at P29 identified several biological processes associated with the nucleus, such as many RNA-related processes, transcription, histone/chromatin modification, and gene expression. Addressing this question will require the generation and comparison of various different cilia/*Bbs*-specific conditional mutant mice, as well as a more detailed elucidation of *Bbs* function in epithelial tissues.

Although *Bbs8* has the potential to regulate multiple cellular processes, our omics data identified specific processes associated with a change in RPE phenotype. At P11 we identified mis-regulation of genes/proteins particularly associated with signaling and developmental processes, while at P29, we observed mis-regulation of gene/protein expression associated with functional processes. These changes were reflected upon assessment of cellular morphology *in vivo*, in that we observed a loss of cellular epithelial morphology, as well as progressive disruption of cell membranes. Since RPE function is critically dependent on the maintenance of its epithelial phenotype, it was not surprising to find loss of RPE functionality upon loss of ciliary function (Strauss, 2005; Bharti et al., 2011; Adijanto et al., 2012; Chen et al., 2019). Maintenance of an epithelial phenotype is crucial for apical-basal polarization of the tissue. This facilitates ezrin-rich apical microvilli to extend from the apical surface and engulf the POS. These microvilli (also referred to as apical processes) are required for the phagocytosis of shed POS and the high level of cross talk between RPE and photoreceptor cells. Loss of apical microvilli upon depletion of *Ezrin* causes photoreceptor degeneration *in vivo* (Bonilha et al., 2006). We saw that loss of *Bbs8* leads to abnormal accumulation of p-ERM early on, with almost complete absence at a later time point (P81). This observation suggests a loss of polarization or inability to form apical microvilli. Previous reports have proposed that apical microvilli are indispensable for the functional connection between RPE cells and the POS, yet defects in apical microvilli undoubtedly lead to RPE dysfunction (Bonilha et al., 2006; Nandrot et al., 2007). In line with this, we observed that *Bbs8*^{-/-} RPE displayed an increase in retinal adhesion *in vivo*, and knockdown of *Bbs8* resulted in decreased phagocytosis of POS *in vitro*.

EMT denotes the trans-differentiation from epithelial cells into mesenchymal cells and loss of an epithelial phenotype. Key processes in this include changes in signaling, reorganization of the cytoskeleton, as well as loss of cell junctions and apical-basal polarity (Lamouille et al., 2014; Ohlmann et al., 2016). In our

data we found three GO terms (mesenchymal cell differentiation, epithelial cell migration, and membrane organization) associated with these processes, that were significantly down-regulated at P11, but significantly up-regulated by P29. This, coupled with the recent findings that dys-regulation of primary cilia signaling has already been shown to induce EMT in other tissues and organs, including epicardial tissue, basal mammary stem cells, and kidney epithelial cells (Lamouille et al., 2014; Ohlmann et al., 2016; Guen et al., 2017; Blom and Feng, 2018; Han et al., 2018), makes us believe that a loss of *Bbs8* might induce an EMT-like phenotype. In support of this the downstream EMT-transcription factor Snail was only found in the nuclei of *Bbs8* mutant tissue.

RPE dysfunction can lead to retinal degeneration and blindness (Strauss, 2005; Bharti et al., 2011; Adijanto et al., 2012; Chen et al., 2019). So far, most research on retinal degeneration in ciliopathy patients has targeted photoreceptors. Our findings highlight that the contribution of defective cilia or ciliary proteins may be more complex than initially envisaged, and that their function in the biological processes within in the RPE must also be taken into consideration. This is relevant for syndromic ciliopathy patients and also for others affected by non-syndromic retinal degeneration as a consequence of mutations in a ciliary disease gene. These considerations warrant attention when designing treatment strategies for retinal degeneration.

MATERIALS AND METHODS

Animals

All experiments had ethical approval from the Landesuntersuchungsamt Rheinland-Pfalz and were performed in accordance with the guidelines given by the ARVO Statement for the Use of Animals in Ophthalmic and Vision Research. Animal maintenance and handling were performed in line with the Federation for Laboratory Animal Science Associations (FELASA) recommendations. Animals were housed in a 12-h (h) light/dark cycle. The morning after mating was considered as embryonic day (E) 0.5 and up to 24 h after birth was considered as postnatal day (P) 0. Animals were sacrificed by cervical dislocation. Generation of *Bbs8*^{-/-} mice and genotyping was previously described (Tadenev et al., 2011). Tissues and samples were collected from two groups, namely age-matched control (*Bbs8*^{+/+}) and mutant (*Bbs8*^{-/-}) littermates. Each individual animal was considered a biological replicate. A minimum of three biological replicates were used for each experiment. For RNA sequencing a minimum of four biological replicates was used.

Antibodies

For immunofluorescence, the following primary antibodies were used: anti-phospho-Ezrin (Thr567)/Radixin(Thr564)/Moesin(Thr558) (p-ERM) (rb, 1:100, Cell Signaling Technology, #3141), anti-snail (rb, 1:100, Cell Signaling Technology, #3879), anti-Arl13b (rb, 1:800, Proteintech, #17711-1-AP), and anti-Gt335 (mM, 1:800, Adipogen, #AG-20B-0020). These antibodies were detected using the appropriate Alexa Fluor (AF)-488, -555, and -647 (1:400; Molecular Probes) conjugated secondary antibodies.

Anti-Zonula Occludens-1 (ZO-1) was directly conjugated with AF-488 (1:100, ZO-1-1A12, Invitrogen, 339188) and Phalloidin was directly conjugated with AF-647 (1:40, Cell Signaling Technology, #8940).

Fluorescence Staining and RPE Flatmount Preparation

Mice were sacrificed, eyes were enucleated and adjacent tissues, such as muscle and fat, cornea, lens, and retina were removed. Remaining eyecups were fixed with 4% paraformaldehyde (PFA) in 1× phosphate-buffered saline (PBS) for 1 h. Following fixation, the eyecups were washed three times with 1× PBS, incubated with 50 mM NH₄Cl for 10 min and permeabilized with 1× PBS 0.1% Tween-20 (PBST) with 0.3% Triton-X (TX) (PBST-TX) for 1 h and blocked with blocking buffer (0.1% ovalbumin, 0.5% fish gelatin in 1× PBS) for 1 h. Following this, eyecups were incubated with primary antibodies over night at 4°C. Eyecups were washed three times with 1× PBS and incubated with secondary antibodies, directly conjugated antibodies, and DAPI (Carl Roth) for 2 h in the dark. Post staining, two washing steps with PBST-TX and one with 1× PBS for 20 min were performed, followed by mounting on microscope slides using Fluoromount-G (SouthernBiotech). Flatmounts were imaged using a Leica DM6000B microscope. Deconvolution (BlindDeblur Algorithm, one iteration step) and maximum projection were performed using Leica imaging software (Leica, Bensheim, Germany). Images were processed via Fiji using color correction and contrast adjustment (Schindelin et al., 2012).

RPE Cell Isolation

For RPE cell isolation, we adapted a protocol previously described (Nandrot et al., 2004). Mice were sacrificed, eyes were enucleated and placed in ice-cold 1× Hank's balanced salt solution (Ca²⁺-Mg²⁺-free) (HBSS-) (Gibco, #14175-095) with 0.01 M Hepes (Gibco, #15630-080) (HBSS-H-). Adjacent tissues, such as muscle and fat, cornea, lens, and retina were removed and eyecups were placed in 1.5 ml trypsin (2 mg/ml) (Difco trypsin 250, BD #215240) in 1× Hank's balanced salt solution (with Ca²⁺ and Mg²⁺) (HBSS+) (Gibco, #14025-092) with 0.01 M Hepes (HBSS+)-H and incubated for 5 min (P11) or 30 min (adult) respectively at 37°C. Following this, the eyecups were transferred into ice-cold (HBSS+)-H and RPE sheets were peeled off the choroid. In case of P11, eyecups were then again incubated in trypsin for 2 min in 37°C and remaining RPE sheets were peeled off. RPE sheets were transferred to a microfuge tube and washed three times with ice-cold (HBSS+)-H (9391 rcf, 1.5 min, 4°C). RPE cells were then pelleted (9391 rcf, 1.5 min, 4°C), supernatant was removed and the RPE pellet was snap-frozen in liquid nitrogen. RPE pellets were kept at -80°C.

RNA Isolation From Murine Eyecups

Mice were sacrificed and the eyes were enucleated. Adjacent tissues, such as muscle and fat, were removed and the cornea, lens, retina, and optic nerve were discarded. Remaining eyecups were homogenized in TRIzol Reagent (Invitrogen) using a pestle. For RNA extraction, TRIzol Reagent was used according to

manufacturer's recommendations and RNA was stored at -80°C until usage.

QuantSeq 3' mRNA Sequencing Library Preparation

Preparation of libraries was performed with a total of 30 ng of RNA from each sample using QuantSeq 3' mRNA-Seq Library prep kit (Lexogen, Vienna, Austria) according to manufacturer's instructions. Total RNA was quantified using the Qubit 2.0 fluorimetric Assay (Thermo Fisher Scientific). Libraries were prepared from 30 ng of total RNA using the QuantSeq 3' mRNA-Seq Library Prep Kit FWD for Illumina (Lexogen GmbH). Quality of libraries was assessed by using High Sensitivity DNA D1000 ScreenTape system (Agilent Technologies). Libraries were sequenced on a NovaSeq 6000 sequencing system using an S1, 100 cycles flow cell (Illumina Inc.). Amplified fragmented cDNA of 300 bp in size were sequenced in single-end mode with a read length of 100 bp. Illumina NovaSeq base call (BCL) files are converted in fastq file through bcl2fastq (version v2.20.0.422).

QuantSeq 3' mRNA Sequencing Data Processing and Analysis

For analysis, sequence reads were trimmed using BDduk software (<https://jgi.doe.gov/data-and-tools/bbtools/bb-tools-user-guide/usage-guide/>) (BBMap suite 37.31) to remove adapter sequences, poly-A tails and low-quality end bases (regions with average quality below 6). Alignment was performed with STAR 2.6.0a3 (Dobin et al., 2013) on mm10 reference assembly obtained from Cell Ranger website ([https://support.10xgenomics.com/single-cell-gene-expression/software/release-notes/build#mm10_3.0.0;Ensembl assembly release 93](https://support.10xgenomics.com/single-cell-gene-expression/software/release-notes/build#mm10_3.0.0;Ensembl%20assembly%20release%2093)). Expression levels of genes were determined with htseq-count (Anders et al., 2015) using Gencode/Ensembl gene model. All genes having < 1 cpm in less than n_{min} samples and Perc MM reads $> 20\%$ simultaneously were filtered out. Differential expression analysis was performed using edgeR (Robinson et al., 2009), a statistical package based on generalized linear models, suitable for multifactorial experiments. A minimum of 3 biological replicates were used for statistics. The threshold for statistical significance chosen was False Discovery Rate (FDR) < 0.05 : in detail, 592 genes were differentially expressed (290 genes induced and 302 inhibited) in the P11 dataset (GSE144845) while 2,276 genes were differentially expressed (1,056 genes induced and 1,220 inhibited) in the P29 dataset (GSE144846). Gene Ontology (GOEA) and Functional Annotation Clustering analyses were performed using DAVID Bioinformatic Resources (Huang et al., 2009a,b) restricting the output to Biological Process terms (BP_FAT). The threshold for statistical significance of GOEA was FDR < 0.1 and Enrichment score (ES) ≥ 1.5 . The Enrichment score (ES) represents the amount to which genes in a gene ontology cluster are over-represented. We then compared the two datasets. The VENN diagram in Figure 1 summarizes the results after the comparison: we found 33 down-regulated and 32 up-regulated genes, respectively, in common in the two datasets genes and over 90 regulated in opposite correlation (44

down-regulated in P11 and up-regulated in P21; 55 up-regulated in P11 and down-regulated genes in P29).

Data Visualization

Heatmaps (Figures 4B, 8B) were generated using custom annotated scripts.

Quantitative Real-Time PCR (qPCR)

RNA was reverse transcribed to cDNA using GoTaq Probe 2-Step RT-qPCR System (Promega) and cDNA was stored at -20°C until usage. qPCR was performed via the StepOne-Plus Real-Time PCR System (Applied Biosystems) using Platinum SYBR Green (Invitrogen).

The following cycling conditions were used: 95°C for 10 min followed by 40 cycles of 95°C for 15 s, 60°C for 1 min. Relative target gene expression was normalized to *Tbp*. The primer sequences used are listed in Table 1. A minimum of 3 biological replicates were used for statistics.

Proteomics

For tissue lysis, RPE cells were transferred to 1.4 mm ceramic beads containing 0.5 ml Precellys[®] tubes and 100 μl lysis buffer per mg tissue was added. For lysis, samples were shaken in the Precellys[®] 24 system three times at 5,500 rpm for 20 s with 30 s of cooling on ice between each step. All lysates were incubated for 30 min at 4°C in an end-over-end shaker, centrifuged 10 min at 4°C with 10,000 g and supernatant was transferred to a new tube. The protein concentration was determined by a Bradford assay.

Affinity purified eluates were precipitated with chloroform and methanol followed by trypsin digestion as described before (Gloeckner et al., 2009). LC-MS/MS analysis was performed on Ultimate3000 RSLCnano systems (Thermo Scientific) coupled to an Orbitrap Fusion Tribrid mass spectrometer (Thermo Scientific) by a nano spray ion source. Tryptic peptide mixtures were injected automatically and loaded at a flow rate of 10 $\mu\text{l}/\text{min}$ in 0.1% trifluoroacetic acid in HPLC-grade water onto a nano trap column (Thermo Scientific; Orbitrap Fusion: 2 mm x 10 mm, μPAC Trapping column, 300 nm, 100–200 \AA , PharmaFluidics). After 3 min, peptides were eluted and separated on the analytical column (Orbitrap Fusion: 315 μm x 50 cm, μPACTM nano-LC columns—50 cm μPACTM C18, 300 nm, 100–200 \AA , PharmaFluidics) by a linear gradient from 2 to 30%

TABLE 1 | Sequences of used primers.

Gene	Forward (5'-3')	Reverse (5'-3')
Cdh1	ACTGTGAAGGGACGGTCAAC	GGAGCAGCAGGATCAGAATC
Cldn19	TCCTCTTGGCAGGTCTCT GT	GTGCAGCAGAGAAAGGAAC C
Snail	TCCAAACCCACTCGGATG TGAAGA	TTGGTGCTTGTGGAGCAAGG ACAT
Tbp	CTTCGTGCAAGAAATGCT GAAT	CAGTTGTCCGTGGCTCTCTT ATT
Tjp1	GACCAATAGCTGATGTTG CCAGAG	TGCAGGCGAATAATGCCAGA

of buffer B (80% acetonitrile and 0.08% formic acid in HPLC-grade water) in buffer A (2% acetonitrile and 0.1% formic acid in HPLC-grade water) at a flow rate of 300 nl/min over 95 min. Remaining peptides were eluted by a short gradient from 30 to 95% buffer B in 5 min. From the high-resolution MS pre-scan with a mass range of 335 to 1,500. The Orbitrap Fusion was run in top speed mode with a cycle time of 3 s. The normalized collision energy for HCD was set to a value of 30 and the resulting fragments were detected in the ion trap. The lock mass option was activated; the background signal with a mass of 445.12003 was used as lock mass (Olsen et al., 2005). Every ion selected for fragmentation was excluded for 20 s by dynamic exclusion.

MS/MS data were analyzed using the MaxQuant software (version 1.6.1.09) (Cox and Mann, 2008; Cox et al., 2009). As a digesting enzyme, Trypsin/P was selected with maximal 2 missed cleavages. Cysteine carbamidomethylation was set for fixed modifications, and oxidation of methionine and N-terminal acetylation were specified as variable modifications. The data were analyzed by label-free quantification (no fast LFQ) with the minimum ratio count of 2. The first search peptide tolerance was set to 20, the main search peptide tolerance to 4.5 ppm and the re-quantify option was selected. For peptide and protein identification, the following subset of the SwissProt database was used: mouse release 2019_08, #17,027 entries, contaminants were detected using the MaxQuant contaminant search. A minimum peptide number of 2 and a minimum length of 7 amino acids were tolerated. Unique and razor peptides were used for quantification. The match between run options was enabled with a match time window of 0.7 min and an alignment time window of 20 min. The statistical analysis was done using the Perseus software (version 1.6.2.3) (Tyanova et al., 2016). A minimum of 3 biological replicates were used for statistics. Potential contaminants, peptides only identified by side or reverse sequence were removed. Minimum half of the samples must have valid values. Based on the median value, significance A (Benjamini-Hochberg FDR) was calculated. The stability of protein ratios within groups was determined using the student's *t*-test. Only proteins with a significance A < 0.05 and a student's *t*-test *p* < 0.05 were taken as being significantly altered.

Gene enrichment analysis was performed using GetGo (<http://getgo.russelllab.org/>) (Boltdt et al., 2016). Only gene names of proteins that showed a significance A < 0.05 and a student's *t*-test *p* < 0.05 for this analysis.

Cell Morphology Assessment

After image acquisition the images were processed using a previously published trained neural network that can accurately identify cell borders in fluorescent images (Schaub et al., 2020). After the algorithm identified cell borders, the segmentation was manually validated for each image. If borders were incorrect, segmentations were manually corrected. Once validated, the images with the identified borders were then analyzed using the methodology outlined by Sharma et al. (2019). Cells in each image were assessed for area, perimeter, number of neighbors, elongation of the cell (Aspect ratio), how like regular convex polygons (Polygonality Score—Equations 1–3) cells were, how hexagonal (Hexagonality Score—Equations 4–6) cells were

(Sharma et al., 2019), the standard deviation of the hexagonality of cells, Feret's Max diameter, Feret's minimum diameter, and the solidity of the cells.

$$PSR = \frac{P_{Cell}}{P_{Hull}} * \left[1 - \left| 1 - \frac{P_{Cell}}{N_{Neighbors} \sqrt{\frac{4 * A_{Cell}}{N_{Neighbors} * \cot \frac{\pi}{N_{Neighbors}}}}} \right| \right] \quad (1)$$

$$PAR = \frac{A_{Cell}}{A_{Hull}} * \left[1 - \left| 1 - \frac{4 * A_{Cell}}{N_{Neighbors} \left(\frac{P_{Cell}}{N_{Neighbors}} \right)^2 * \cot \frac{\pi}{N_{Neighbors}}} \right| \right] \quad (2)$$

$$Polygonality_{Score} = 10 * \left(\frac{PSR + PAR}{2} \right) \quad (3)$$

$$HSR = \frac{P_{Cell}}{P_{Hull}} * \left[1 - \left| 1 - \frac{P_{Cell}}{6 * \sqrt{\frac{4 * A_{Cell}}{6 * \cot \frac{\pi}{6}}}} \right| \right] \quad (4)$$

$$HAR = \frac{A_{Cell}}{A_{Hull}} * \left[1 - \left| 1 - \frac{4 * A_{Cell}}{6 * \left(\frac{P_{Cell}}{6} \right)^2 * \cot \frac{\pi}{6}} \right| \right] \quad (5)$$

$$Hexagonality_{Score} = 10 * \left(\frac{HSR + HAR}{2} \right) \quad (6)$$

To calculate the above the python package SciPy 1.2.2 was used (Virtanen et al., 2020), with the addition of the polygonality score, hexagonality score, standard deviation of the hexagonality score, and number of neighbors. The calculations were validated on digitally created synthetic images of shapes and cells to ensure that the values that it produces were accurate.

All statistical analysis was performed using R (R. Foundation for Statistical Computing, 2017), the lme4 package (Bates et al., 2015), and the emmeans package (Searle et al., 1980). Data was first assessed for normality by determining data skewness, kurtosis, and q-q plots. All differences between *Bbs8*^{+/+} and *Bbs8*^{-/-} were assessed using linear mixed effects models controlling for repeated measures from each mouse. Linear marginal means rather than least squared means were used to determine the magnitude of differences. Differences in variance of the data was determined by taking the residual of all measures from their median and running the linear mixed effect model using residual values rather than raw data. A Bonferroni-Dunn correction was used to correct for the additional assessment of residuals, as well as raw data. All pair-wise comparisons were controlled for using Tukey's post test and an adjusted alpha of 0.05 was used for significance. All plots for shape/morphological measurements were done using the ggplot2 package (Wickham, 2009).

Retinal Adhesion Assay

For the retinal adhesion assay, we adapted a protocol previously described (Nandrot et al., 2006). Mice were sacrificed, eyes were enucleated and transferred into 1× Hank's balanced salt solution containing Ca²⁺ and Mg²⁺ (HBSS+) (Gibco, #14025-092). Adjacent tissues, cornea and lens were removed. One eyecup at a time was transferred into a dry, empty dish and cut radially toward the optic nerve. The eyecup was then flattened, and the neural retina peeled off using forceps. Retinae were lysed individually in 50 mM Tris (pH 7.5), 2 mM EDTA, 150 mM NaCl,

1% Triton X-100, 0.1% SDS, and 1% NP-40, freshly supplemented with 1% protease and phosphatase inhibitors via sonication for 10 s on ice. After centrifugation (5 min, 21130 rcf, 4°C) lysates and pellets were kept separate on ice and protein content of the lysates were quantified using bicinchoninic acid (BCA) assay. For melanin dissolution, the pellets were washed in 100 μ l 50% ethanol and 50% diethylether (10 min, 21130 rcf). Supernatant was discarded, pellets were dissolved in 150 μ l 20% DMSO, 2 M NaOH and incubated for 30 min at 60°C. To quantify melanin concentration, absorbance of samples and commercially available melanin (Sigma-Aldrich, #M0418) dissolved in 20% DMSO, 2 M NaOH at defined concentrations were measured at 490 nm. Individual melanin concentrations were normalized to the corresponding protein concentration to calculate the concentration of melanin per milligram of protein.

Cell Culture

ARPE-19 cells were kindly provided from Karsten Boldt (Tübingen) and cultured in DMEM/F-12 + GlutaMax (Gibco, #31331028) supplemented with 10% fetal bovine serum (FBS) (LONZA), and 1% penicillin/streptomycin (Thermo Fischer, #10378016) (referred to as complete medium). *BBS8* siRNA (Dharmacon, #L-021417-02-0005) and non-targeting siRNA (IDT, TriFECTa) were used to generate *BBS8 KD* and *Non-targeting control (NTC)* cells. Transfections were performed using antibiotic-free medium in 96-well plates using Lipofectamine RNAiMAX reagent (Invitrogen, #113778150) according to manufacturer's recommendations for reverse transfections. Post transfection, the cells were cultured in complete medium. The phagocytosis assay was performed 48 h post-transfection.

Phagocytosis Assay

Isolation and preparation of bovine POS were described previously (Nandrot et al., 2007). For phagocytosis assay, we adapted a protocol previously described (Nandrot et al., 2007). Confluent *BBS8 KD* and *NTC* cells were preincubated for 1 h in serum- and antibiotic-free DMEM/F-12 + GlutaMax followed by incubation with POS for 7 h at 37°C in the dark. To remove excess POS, three washing steps with PBS supplemented with 0.2 mM Ca^{2+} and 1 mM Mg^{2+} (PBS-CM) were performed. In order to differentiate between bound and internalized POS, parallel wells were incubated with 4% trypan blue for 10 min followed by two washing steps with PBS-CM. Addition of trypan blue quenches surface fluorescence and therefore the two populations (internalized vs. bound) can be distinguished (bound = total – internalized). All wells were fixed in ice-cold methanol for 10 min, rehydrated in PBS-CM for 10 min at room temperature and incubated with DAPI (1:400) for 15 min. Following this, two washing steps with PBS-CM were performed and an equal volume of PBS-CM was added to all wells. FITC-POS and DAPI-labeled cells were quantified using the Infinite M1000 Pro microplate reader and associated Magellan software (Tecan).

Statistics

Unless indicated differently, statistical analysis was performed using GraphPad Prism 6.0. ROUT test ($Q = 0.1\%$) was performed prior to statistical analysis. Used statistical tests are stated in

corresponding figure legends. For qPCR data a one sample *t*-test with a theoretical mean set as 1 (WT = *Bbs8*^{+/+} value) was performed. For the retinal adhesion analysis, a D'Agostino & Pearson omnibus normality test was performed to check that the results are normally distributed. Following this, an unpaired *t*-test was performed. For the phagocytosis assay, a one-way ANOVA and Tukey *post-hoc* test was performed. Images and data were analyzed blinded to genotype. See sections Cell morphology assessment, QuantSeq 3' mRNA sequencing data processing and analysis and Proteomics for more details. Sample size was determined by availability of tissue with a minimum of three biological replicates.

DATA AVAILABILITY STATEMENT

The datasets presented in this study can be found in online repositories. The names of the repository/repositories and accession number(s) can be found in the article/**Supplementary Material**.

ETHICS STATEMENT

The animal study was reviewed and approved by the Landesuntersuchungsamt Rheinland-Pfalz and were performed in accordance with the guidelines given by the ARVO Statement for the Use of Animals in Ophthalmic and Vision Research. Animal maintenance and handling were performed in line with the Federation for Laboratory Animal Science Associations (FELASA) recommendations..

AUTHOR CONTRIBUTIONS

SS, RD, NH, KB, IC, and HLM-S designed experiments. SS, RD, JN, VK, PAM DI, NH, and KB performed experiments and analyzed data. SS and HLM-S wrote the paper, and conceived and directed the study. All authors revised the manuscript.

FUNDING

This work was funded by the Alexander von Humboldt Foundation (Sofja Kovalevskaja Award) and the Deutsche Forschungsgemeinschaft (DFG) SPP 2127 (MA 6139/3-1).

ACKNOWLEDGMENTS

The authors would like to thank Petra Gottlöber, Sonja Boxhorn, Jana Kurpinski, and Rike Hähnel for their technical assistance. We would also like to thank Kapil Bharti for helpful discussion and Jessica Gumerson for assistance in analyzing flatmount images. Finally, the authors are grateful to Diego Carrella and Lucio di Filippo (TIGEM Bioinformatics Core) for bioinformatics assistance.

SUPPLEMENTARY MATERIAL

The Supplementary Material for this article can be found online at: <https://www.frontiersin.org/articles/10.3389/fcell.2021.607121/full#supplementary-material>

Supplementary Figure 1 | *Bbs8*-deficient RPE show changes in cell morphological parameters. **(A–F)** Quantification of cell morphology parameters. Statistical analysis is described in methods. Comparison of **(A)** eccentricity, **(B)** minFerret, **(C)** maxFerret, **(D)** solidity, **(E)** equivalent diameter, and **(F)** number of neighbors of *Bbs8*^{-/-} and *Bbs8*^{+/+} RPE cells show no significant changes (*n*: P0 = 6 eyes, P11 = 9 eyes, P29 = 4 eyes, P81 = 3 eyes). Significance levels: mean: > 0.05 not significant (ns), ≤ 0.05*, ≤ 0.01**, ≤ 0.001***; variance: > 0.05 not significant (ns), ≤ 0.05#, ≤ 0.01##, ≤ 0.001###. **(G)** Representative images of RPE flatmounts stained for ZO-1 (green) to visualize the cell membrane and DAPI for nuclear DNA. In *Bbs8*^{-/-} RPE we identified discontinuous membrane staining at all ages. These areas were excluded from cell morphology assessment. Scale bar: 25 μm.

Supplementary Figure 2 | Deletion of *Bbs8* leads to changes in apical microvilli. Representative images of RPE flatmounts (Z-stack) stained for p-ERM (orange) and F-actin (red) to visualize apical microvilli and the cytoskeleton. DAPI was used to stain nuclear DNA. P11 *Bbs8*^{-/-} RPE shows abnormal accumulations of p-ERM staining (arrowheads). Images were taken using a Confocal Zeiss LSM 9 with Airyscan 9. Scale bars: 10 μm.

Supplementary Figure 3 | Optimization of phagocytosis assays using ARPE-19 cells. **(A)** Quantification of *BBS8* expression after knockdown using *BBS8* siRNA from Dharmacon (dh) and IDT compared to non-targeting control (NTC) (*n* = 3). Due to higher efficacy of the siRNA from Dharmacon, further experiments were performed using this. Statistical analysis was performed using one-way ANOVA and Dunnett's test *post-hoc* test. Significance levels: > 0.05 not significant (ns), ≤ 0.05*, ≤ 0.01**, ≤ 0.001***. **(B)** Comparison of total, bound and internalized fluorescently labeled photoreceptor outer segments (POS). FITC/DAPI ratio measured after incubation of ARPE19 cells for 5 and 7 h, respectively.

Supplementary Figure 4 | Deletion of *Bbs8* leads to increased expression of Snail and changes ciliation in the RPE. **(A)** Representative images of P11 RPE flatmounts stained for Snail (red) and ZO-1 (green). DAPI was used to stain nuclear DNA. P11 *Bbs8*^{-/-} RPE shows an increase in Snail expression in the nuclear region, particularly in cells with disrupted morphology. Scale bars: 25 μm. **(B)** Representative images of P81 RPE flatmounts (Z-stack) stained for primary cilia

(arrowheads) using Ar113b (red) and Gt335 (green). F-Actin (magenta) was stained to visualize the cytoskeleton and DAPI was used to stain nuclear DNA. Co localization of Ar113b and transition zone marker Gt335 is required to determine a true primary cilium, which is more readily identified in the mutant (white arrows). Scale bars: 10 μm. Images were taken using a Leica DM6000B microscope.

Supplementary Table 1 | Differentially expressed genes (DEGs) significantly regulated at P11. Significance defined by using False Discovery Rate (FDR) < 0.05 as threshold. 290 genes induced in red, and 302 inhibited in green.

Supplementary Table 2 | Differentially expressed genes (DEGs) significantly regulated at P29. Significance defined by using False Discovery Rate (FDR) < 0.05 as threshold. 1,056 genes induced in red; and 1220 inhibited in green.

Supplementary Table 3 | Comparison of differentially expressed genes (DEGs) between *Bbs8*^{-/-} and control with RPE-specific gene lists.

Supplementary Table 4 | Gene Ontology enrichment analysis of the differentially expressed genes (DEGs) between *Bbs8*^{-/-} and control at P11. The Biological Process (BP_FAT) terms enriched among the down-regulated (*n* = 302) and up-regulated (*n* = 290) genes are highlighted in green (A) and red (B), respectively. For each BP annotation cluster, the GO identifier ("GO:"), associated term ("Term") and Enrichment score are provided. The genes belonging to each term are listed in column D (and their total number in column C under "count"). False Discovery Rate score (FDR) is shown in column E.

Supplementary Table 5 | Gene Ontology enrichment analysis of the differentially expressed genes (DEGs) between *Bbs8*^{-/-} and control at P29. The Biological Process (BP_FAT) terms enriched among the down-regulated (*n* = 1,220) and up-regulated (*n* = 1,056) genes are highlighted in green (A) and red (B), respectively. For each BP annotation cluster, the GO identifier ("GO:"), associated term ("Term") and Enrichment score are provided. The genes belonging to each term are listed in column D (and their total number in column C under "count"). False Discovery Rate score (FDR) is shown in column E.

Supplementary Table 6 | Gene Ontology enrichment analysis of the differentially expressed genes (DEGs) resulting from the comparison of the two datasets at P11 and P29. The Biological Process (BP_FAT) terms enriched among the down-regulated genes in both datasets (*n* = 33) and up-regulated in both datasets (*n* = 32) genes are highlighted in green (A) and red (B), respectively. For each BP annotation cluster, the GO identifier ("GO:"), associated term ("Term") and Enrichment score are provided. The genes belonging to each term are listed in column D (and their total number in column C under "count"). False Discovery Rate score (FDR) is shown in column E.

REFERENCES

- Adjianto, J., Castorino, J. J., Wang, Z. X., Maminishkis, A., Grunwald, G. B., and Philp, N. J. (2012). Microphthalmia-associated transcription factor (MITF) promotes differentiation of human retinal pigment epithelium (RPE) by regulating microRNAs-204/211 expression. *J. Biol. Chem.* 287, 20491–20503. doi: 10.1074/jbc.M112.354761
- Agostini, M., Romeo, F., Inoue, S., Niklison-Chirou, M. V., Elia, A. J., Dinsdale, D., et al. (2016). Metabolic reprogramming during neuronal differentiation. *Cell Death Differ.* 23, 1502–1514. doi: 10.1038/cdd.2016.36
- Anders, S., Pyl, P. T., and Huber, W. (2015). HTSeq-A Python framework to work with high-throughput sequencing data. *Bioinformatics* 31, 166–169. doi: 10.1093/bioinformatics/btu638
- Ansley, S. J., Badano, J. L., Blacque, O. E., Hill, J., Hoskins, B. E., Leitch, C. C., et al. (2003). Basal body dysfunction is a likely cause of pleiotropic Bardet-Biedl syndrome. *Nature* 425, 628–633. doi: 10.1038/nature02030
- Bates, D., Mächler, M., Bolker, B., and Walker, S. (2015). Fitting linear mixed-effects models using lme4. *J. Stat. Softw.* 67, 201–210. doi: 10.18637/jss.v067.i01
- Bharti, K., Miller, S. S., and Arnheiter, H. (2011). The new paradigm: retinal pigment epithelium cells generated from embryonic or induced pluripotent stem cells. *Pigment Cell Melanoma Res.* 24, 21–34. doi: 10.1111/j.1755-148X.2010.00772.x
- Blacque, O. E., Reardon, M. J., Li, C., McCarthy, J., Mahjoub, M. R., Ansley, S. J., et al. (2004). Loss of *C. elegans* BBS-7 and BBS-8 protein function results in cilia defects and compromised intraflagellar transport. *Genes Dev.* 18, 1630–1642. doi: 10.1101/gad.1194004
- Blom, J. N., and Feng, Q. (2018). Cardiac repair by epicardial EMT: current targets and a potential role for the primary cilium. *Pharmacol. Ther.* 186, 114–129. doi: 10.1016/j.pharmthera.2018.01.002
- Boldt, K., Van Rееuwijk, J., Lu, Q., Koutroumpas, K., Nguyen, T. M. T., Texier, Y., et al. (2016). An organelle-specific protein landscape identifies novel diseases and molecular mechanisms. *Nat. Commun.* 7, 1–13. doi: 10.1038/ncomms11491
- Bonilha, V. L., Rayborn, M. E., Saotome, I., McClatchey, A. I., and Hollyfield, J. G. (2006). Microvilli defects in retinas of ezrin knockout mice. *Exp. Eye Res.* 82, 720–729. doi: 10.1016/j.exer.2005.09.013
- Chen, Y., Yang, J., Geng, H., Li, L., Li, J., Cheng, B., et al. (2019). Photoreceptor degeneration in microphthalmia (Mitf) mice: Partial rescue by pigment epithelium-derived factor. *DMM Dis. Model. Mech.* 12:dmm035642. doi: 10.1242/dmm.035642
- Cheng, T., Peachey, N. S., Li, S., Goto, Y., Cao, Y., and Naash, M. I. (1997). The effect of peripherin/rds haploinsufficiency on rod and cone photoreceptors. *J. Neurosci.* 17, 8118–8128. doi: 10.1523/JNEUROSCI.17-21-08118.1997
- Collu-Marchese, M., Shuen, M., Pauly, M., Saleem, A., and Hood, D. A. (2015). The regulation of mitochondrial transcription factor A (Tfam) expression during skeletal muscle cell differentiation. *Biosci. Rep.* 35:e00221. doi: 10.1042/BSR20150073

- Cox, J., and Mann, M. (2008). MaxQuant enables high peptide identification rates, individualized p.p.b.-range mass accuracies and proteome-wide protein quantification. *Nat. Biotechnol.* 26, 1367–1372. doi: 10.1038/nbt1511
- Cox, J., Matic, I., Hilger, M., Nagaraj, N., Selbach, M., Olsen, J. V., et al. (2009). A practical guide to the maxquant computational platform for silac-based quantitative proteomics. *Nat. Protoc.* 4, 698–705. doi: 10.1038/nprot.2009.36
- Dilan, T. L., Singh, R. K., Saravanan, T., Moye, A., Goldberg, A. F. X., Stoilov, P., et al. (2018). Bardet-Biedl syndrome-8 (BBS8) protein is crucial for the development of outer segments in photoreceptor neurons. *Hum. Mol. Genet.* 27, 283–294. doi: 10.1093/hmg/ddx399
- Dobin, A., Davis, C. A., Schlesinger, F., Drenkow, J., Zaleski, C., Jha, S., et al. (2013). STAR: ultrafast universal RNA-seq aligner. *Bioinformatics* 29, 15–21. doi: 10.1093/bioinformatics/bts635
- Fliegauf, M., Benzing, T., and Omran, H. (2007). When cilia go bad: cilia defects and ciliopathies. *Nat. Rev. Mol. Cell Biol.* 8, 880–893. doi: 10.1038/nrm2278
- Forsythe, E., and Beales, P. L. (2013). Bardet-Biedl syndrome. *Eur. J. Hum. Genet.* 21, 8–13. doi: 10.1038/ejhg.2012.115
- Gascue, C., Tan, P. L., Cardenas-Rodriguez, M., Libisch, G., Fernandez-Calero, T., Liu, Y. P., et al. (2012). Direct role of Bardet-Biedl syndrome proteins in transcriptional regulation. *J. Cell Sci.* 125, 362–375. doi: 10.1242/jcs.089375
- Gloeckner, C. J., Boldt, K., and Ueffing, M. (2009). Strep/FLAG tandem affinity purification (SF-TAP) to study protein interactions. *Curr. Protoc. Protein Sci.* 1–19. doi: 10.1002/0471140864.ps1920s57
- Goetz, S. C., and Anderson, K. V. (2010). The primary cilium: a signalling centre during vertebrate development. *Nat. Rev. Genet.* 11, 331–344. doi: 10.1038/nrg2774
- Goyal, S., Jäger, M., Robinson, P. N., and Vanita, V. (2016). Confirmation of TTC8 as a disease gene for nonsyndromic autosomal recessive retinitis pigmentosa (RP51). *Clin. Genet.* 89, 454–460. doi: 10.1111/cge.12644
- Guen, V. J., Chavarria, T. E., Kröger, C., Ye, X., Weinberg, R. A., and Lees, J. A. (2017). EMT programs promote basal mammary stem cell and tumor-initiating cell stemness by inducing primary ciliogenesis and Hedgehog signaling. *Proc. Natl. Acad. Sci. U.S.A.* 114, E10532–E10539. doi: 10.1073/pnas.1711534114
- Han, S. J., Jung, J. K., Im, S. S., Lee, S. R., Jang, B. C., Park, K. M., et al. (2018). Deficiency of primary cilia in kidney epithelial cells induces epithelial to mesenchymal transition. *Biochem. Biophys. Res. Commun.* 496, 450–454. doi: 10.1016/j.bbrc.2018.01.079
- Hernandez-Hernandez, V., Pravincumar, P., Diaz-Font, A., May-Simera, H., Jenkins, D., Knight, M., et al. (2013). Bardet-biedl syndrome proteins control the cilia length through regulation of actin polymerization. *Hum. Mol. Genet.* 22, 3858–3868. doi: 10.1093/hmg/ddt241
- Huang, D. W., Sherman, B. T., and Lempicki, R. A. (2009a). Bioinformatics enrichment tools: paths toward the comprehensive functional analysis of large gene lists. *Nucleic Acids Res.* 37, 1–13. doi: 10.1093/nar/gkn923
- Huang, D. W., Sherman, B. T., and Lempicki, R. A. (2009b). Systematic and integrative analysis of large gene lists using DAVID bioinformatics resources. *Nat. Protoc.* 4, 44–57. doi: 10.1038/nprot.2008.211
- Ishikawa, H., and Marshall, W. F. (2011). Ciliogenesis: building the cell's antenna. *Nat. Rev. Mol. Cell Biol.* 12, 222–234. doi: 10.1038/nrm3085
- Kretschmer, V., Patnaik, S. R., Kretschmer, F., Chawda, M. M., Hernandez-Hernandez, V., and May-Simera, H. L. (2019). Progressive characterization of visual phenotype in bardet-biedl syndrome mutant mice. *Investig. Ophthalmol. Vis. Sci.* 60, 1132–1143. doi: 10.1167/iovs.18-25210
- Lamouille, S., Xu, J., and Derynck, R. (2014). Molecular mechanisms of epithelial-mesenchymal transition. *Nat. Rev. Mol. Cell Biol.* 15, 178–196. doi: 10.1038/nrm3758
- Liu, B., Calton, M. A., Abell, N. S., Benchorin, G., Gloudemans, M. J., Chen, M., et al. (2019). Genetic analyses of human fetal retinal pigment epithelium gene expression suggest ocular disease mechanisms. *Commun. Biol.* 2:186. doi: 10.1038/s42003-019-0430-6
- Liu, H., Wang, M., Xia, C. H., Du, X., Flannery, J. G., Ridge, K. D., et al. (2010). Severe retinal degeneration caused by a novel rhodopsin mutation. *Investig. Ophthalmol. Vis. Sci.* 51, 1059–1065. doi: 10.1167/iovs.09-3585
- Marchese, E., Ruoppolo, M., Perna, A., Capasso, G., and Zaccchia, M. (2020). Exploring key challenges of understanding the pathogenesis of kidney disease in bardet-biedl syndrome. *Kidney Int. Rep.* 5, 1403–1415. doi: 10.1016/j.ekir.2020.06.017
- May-Simera, H., Nagel-Wolfrum, K., and Wolfrum, U. (2017). Cilia - The sensory antennae in the eye. *Prog. Retin. Eye Res.* 60, 144–180. doi: 10.1016/j.preteyeres.2017.05.001
- May-Simera, H. L., Petralia, R. S., Montcouquiol, M., Wang, Y. X., Szarama, K. B., Liu, Y., et al. (2015). Ciliary proteins bbs8 and ift20 promote planar cell polarity in the cochlea. *Development* 142, 555–566. doi: 10.1242/dev.113696
- May-Simera, H. L., Wan, Q., Jha, B. S., Hartford, J., Khristov, V., Dejene, R., et al. (2018). Primary cilium mediated retinal pigment epithelium maturation is retarded in ciliopathy patient cells. *Cell Rep.* 22, 189–205. doi: 10.1016/j.celrep.2017.12.038
- Mazzoni, F., Safa, H., and Finnemann, S. C. (2014). Advanced analysis of photoreceptor outer segment phagocytosis by RPE cells in culture. *Exp. Eye Res.* 126, 51–60. doi: 10.1016/j.exer.2014.01.010
- Nandrot, E. F., Anand, M., Almeida, D., Atabai, K., Sheppard, D., and Finnemann, S. C. (2007). Essential role for MFG-E8 as ligand for alphavbeta5 integrin in diurnal retinal phagocytosis. *Proc. Natl. Acad. Sci. U.S.A.* 104, 12005–12010. doi: 10.1073/pnas.0704756104
- Nandrot, E. F., Anand, M., Mousumi, S., and Finnemann, S. C. (2006). Novel role for avbeta5-integrin in retinal adhesion and its diurnal peak. *Am. J. Physiol. Cell Physiol.* 290, C1256–C1262. doi: 10.1152/ajpcell.00480.2005
- Nandrot, E. F., Kim, Y., Brodie, S. E., Huang, X., Sheppard, D., and Finnemann, S. C. (2004). Loss of synchronized retinal phagocytosis and age-related blindness in mice lacking avβ5 integrin. *J. Exp. Med.* 200, 1539–1545. doi: 10.1084/jem.20041447
- Novas, R., Cardenas-Rodriguez, M., Irigoín, F., and Badano, J. L. (2015). Bardet-Biedl syndrome: is it only cilia dysfunction? *FEBS Lett.* 589, 3479–3491. doi: 10.1016/j.febslet.2015.07.031
- Ohana, R., Weiman-Kelman, B., Raviv, S., Tamm, E. R., Pasmanik-Chor, M., Rinon, A., et al. (2015). MicroRNAs are essential for differentiation of the retinal pigmented epithelium and maturation of adjacent photoreceptors. *Development* 142, 2487–2498. doi: 10.1242/dev.121533
- Ohlmann, A., Scholz, M., Koch, M., and Tamm, E. R. (2016). Epithelial-mesenchymal transition of the retinal pigment epithelium causes choriocapillaris atrophy. *Histochem. Cell Biol.* 146, 769–780. doi: 10.1007/s00418-016-1461-4
- Olsen, J. V., de Godoy, L. M. F., Li, G., Macek, B., Mortensen, P., Pesch, R., et al. (2005). Parts per million mass accuracy on an orbitrap mass spectrometer via lock mass injection into a C-trap. *Mol. Cell. Proteomics* 4, 2010–2021. doi: 10.1074/mcp.T500030-MCP200
- Pala, R., Alomari, N., and Nauli, S. M. (2017). Primary cilium-dependent signaling mechanisms. *Int. J. Mol. Sci.* 18:2272. doi: 10.3390/ijms18112272
- Patnaik, S. R., Farag, A., Brücker, L., Volz, A. K., Schneider, S., Kretschmer, V., et al. (2020). Tissue-dependent differences in Bardet-Biedl syndrome gene expression. *Biol. Cell* 112, 39–52. doi: 10.1111/boc.201900077
- Patnaik, S. R., Kretschmer, V., Brücker, L., Schneider, S., Volz, A.-K., Oancea-Castillo, L., et al. (2019). Bardet-Biedl Syndrome proteins regulate cilia disassembly during tissue maturation. *Cell. Mol. Life Sci.* 76, 757–775. doi: 10.1007/s00018-018-2966-x
- R. Foundation for Statistical Computing (2017). *R: A Language and Environment for Statistical Computing* (Vienna).
- Robinson, M. D., McCarthy, D. J., and Smyth, G. K. (2009). edgeR: a Bioconductor package for differential expression analysis of digital gene expression data. *Bioinformatics* 26, 139–140. doi: 10.1093/bioinformatics/btp616
- Ross, A. J., May-Simera, H., Eichers, E. R., Kai, M., Hill, J., Jagger, D. J., et al. (2005). Disruption of Bardet-Biedl syndrome ciliary proteins perturbs planar cell polarity in vertebrates. *Nat. Genet.* 37, 1135–1140. doi: 10.1038/ng1644
- Schaub, N. J., Hotaling, N. A., Manescu, P., Padi, S., Wan, Q., Sharma, R., et al. (2020). Deep learning predicts function of live retinal pigment epithelium from quantitative microscopy. *J. Clin. Invest.* 130, 1010–1023. doi: 10.1172/JCI131187
- Schindelin, J., Arganda-Carreras, I., Frise, E., Kaynig, V., Longair, M., Pietzsch, T., et al. (2012). Fiji: an open-source platform for biological-image analysis. *Nat. Methods* 9, 676–682. doi: 10.1038/nmeth.2019
- Searle, S. R., Speed, F. M., and Milliken, G. A. (1980). Population marginal means in the linear model: an alternative to least squares means. *Am. Stat.* 34:216. doi: 10.2307/2684063
- Sharma, R., Khristov, V., Rising, A., Jha, B. S., Dejene, R., Hotaling, N., et al. (2019). Clinical-grade stem cell-derived retinal pigment epithelium patch

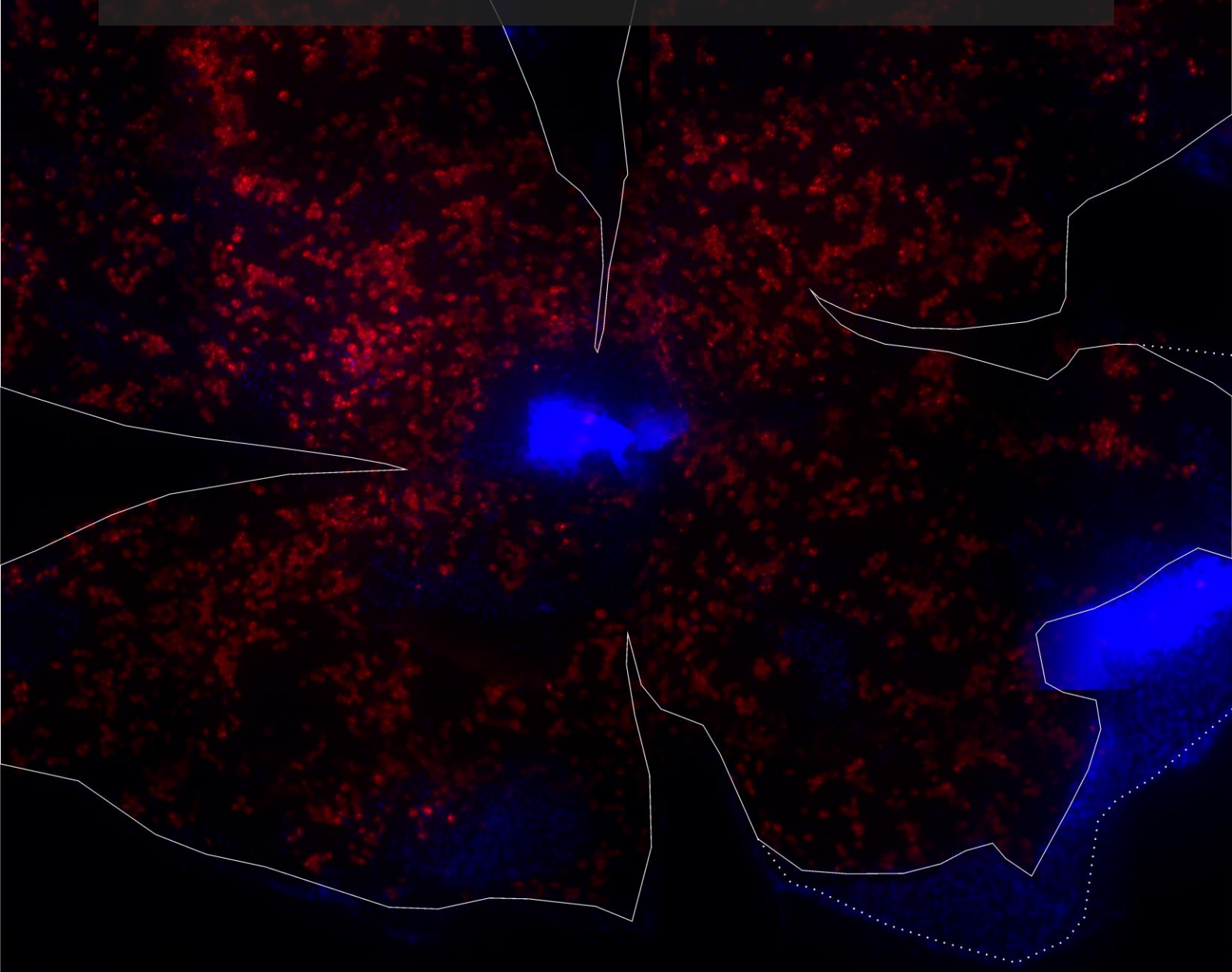
- rescues retinal degeneration in rodents and pigs. *Sci. Transl. Med.* 11:eaat5580. doi: 10.1126/scitranslmed.aat5580
- Strauss, O. (2005). The retinal pigment epithelium in visual function. *Physiol. Rev.* 85, 845–881. doi: 10.1152/physrev.00021.2004
- Strunnikova, N. V., Maminishkis, A., Barb, J. J., Wang, F., Zhi, C., Sergeev, Y., et al. (2010). Transcriptome analysis and molecular signature of human retinal pigment epithelium. *Hum. Mol. Genet.* 19, 2468–2486. doi: 10.1093/hmg/ddq129
- Tadenev, A. L. D., Kulaga, H. M., May-Simera, H. L., Kelley, M. W., Katsanis, N., and Reed, R. R. (2011). Loss of Bardet-Biedl syndrome protein-8 (BBS8) perturbs olfactory function, protein localization, and axon targeting. *Proc. Natl. Acad. Sci. U.S.A.* 108, 10320–10325. doi: 10.1073/pnas.1016531108
- Tamiya, S., and Kaplan, H. J. (2016). Role of epithelial - mesenchymal transition in proliferative vitreoretinopathy. *Exp. Eye Res.* 142, 26–31. doi: 10.1016/j.exer.2015.02.008
- Tyanova, S., Temu, T., Sinitcyn, P., Carlson, A., Hein, M. Y., Geiger, T., et al. (2016). The Perseus computational platform for comprehensive analysis of (prote)omics data. *Nat. Methods* 13, 731–740. doi: 10.1038/nmeth.3901
- Valverde, D., Castro-Sánchez, S., and Álvarez-Satta, M. (2015). Bardet-Biedl syndrome: a rare genetic disease. *J. Pediatr. Genet.* 2, 77–83. doi: 10.3233/PGE-13051
- Virtanen, P., Gommers, R., Oliphant, T. E., Haberland, M., Reddy, T., Cournapeau, D., et al. (2020). SciPy 1.0: fundamental algorithms for scientific computing in Python. *Nat. Methods* 17, 261–272. doi: 10.1038/s41592-019-0686-2
- Volta, F., Scerbo, M. J., Seelig, A., Wagner, R., O'Brien, N., Gerst, F., et al. (2019). Glucose homeostasis is regulated by pancreatic β -cell cilia via endosomal EphA-processing. *Nat. Commun.* 10, 1–17. doi: 10.1038/s41467-019-12953-5
- Waters, A. M., and Beales, P. L. (2011). Ciliopathies: an expanding disease spectrum. *Pediatr. Nephrol.* 26, 1039–1056. doi: 10.1007/s00467-010-1731-7
- Wickham, H. (2009). *ggplot2*. New York, NY: Springer. doi: 10.1007/978-0-387-98141-3
- Willoughby, C. E., Ponzin, D., Ferrari, S., Lobo, A., Landau, K., and Omid, Y. (2010). Anatomy and physiology of the human eye: effects of mucopolysaccharidosis disease on structure and function - a review. *Clin. Exp. Ophthalmol.* 38, 2–11. doi: 10.1111/j.1442-9071.2010.02363.x

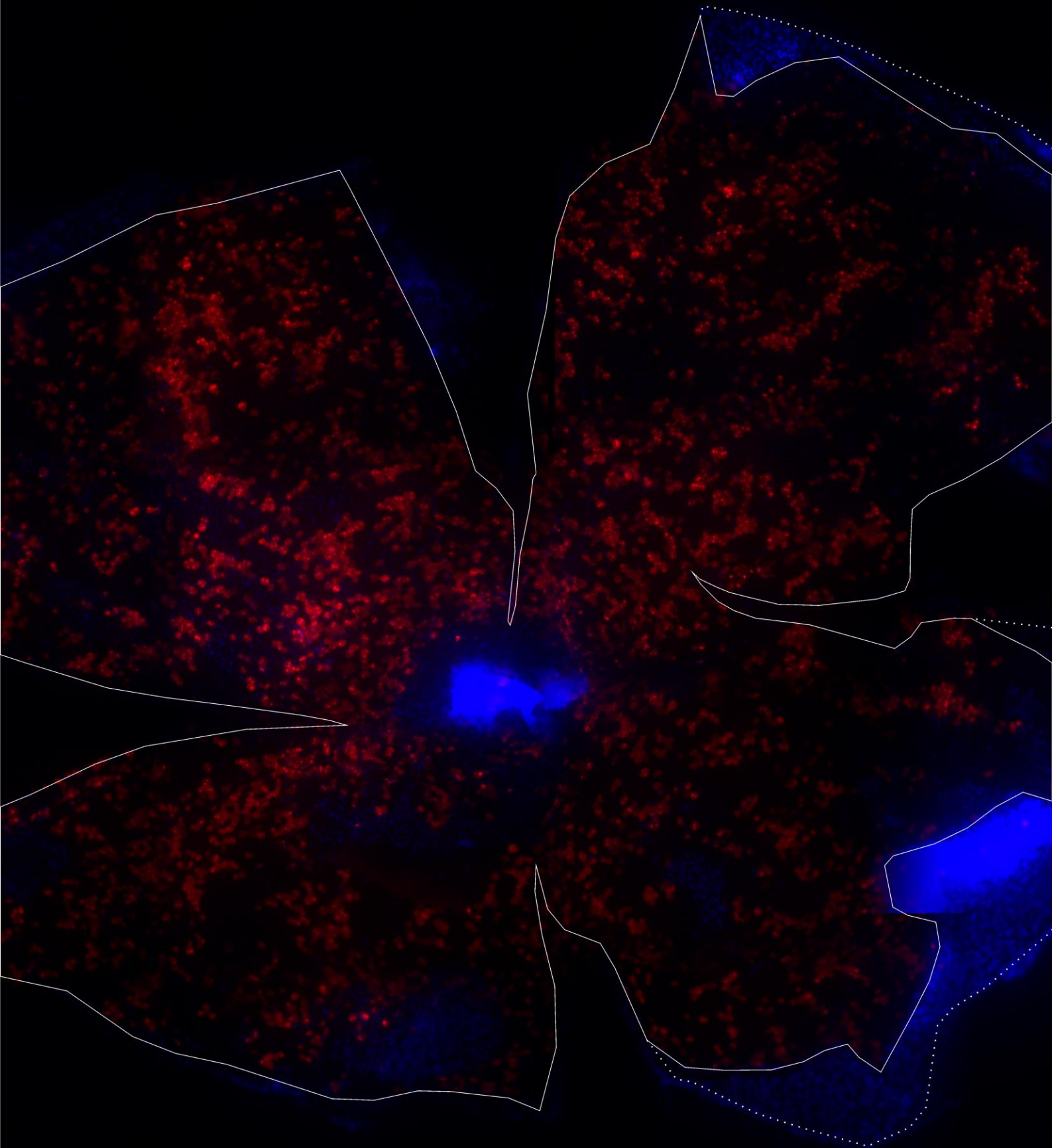
Conflict of Interest: The authors declare that the research was conducted in the absence of any commercial or financial relationships that could be construed as a potential conflict of interest.

Copyright © 2021 Schneider, De Cegli, Nagarajan, Kretschmer, Matthiessen, Intartaglia, Hotaling, Ueffing, Boldt, Conte and May-Simera. This is an open-access article distributed under the terms of the Creative Commons Attribution License (CC BY). The use, distribution or reproduction in other forums is permitted, provided the original author(s) and the copyright owner(s) are credited and that the original publication in this journal is cited, in accordance with accepted academic practice. No use, distribution or reproduction is permitted which does not comply with these terms.

Publication III – Generation of an inducible RPE-specific Cre transgenic-mouse line (First Author; Published)

Due to lack of specificity or poor recombination of the currently available inducible RPE-specific Cre recombinases, we generated and characterized a tamoxifen-inducible RPE-specific Cre transgenic mouse line under transcriptional control of an RPE-specific Tyrosinase enhancer. This inducible RPE-specific Cre transgenic-mouse line shows a high level of recombination in adult mice (47.25-69.48%), as well as in embryonic RPE (~83%). Compared to other inducible RPE-specific Cre transgenic mouse lines, this newly generated *RPE-Tyrosinase-Cre^{ERT2}* line shows a more uniformly distributed and more effective recombination.





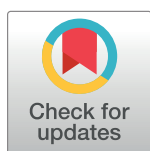
RESEARCH ARTICLE

Generation of an inducible RPE-specific *Cre* transgenic-mouse line

Sandra Schneider¹, Nathan Hotaling², Maria Campos², Sarita Rani Patnaik¹, Kapil Bharti², Helen Louise May-Simera^{1*}

1 Institute of Molecular Physiology, Johannes-Gutenberg University, Mainz, Germany, **2** National Eye Institute, NIH, Bethesda, MD, United States of America

* hmaysime@uni-mainz.de



Abstract

The retinal pigment epithelium (RPE) is an epithelial monolayer in the back of the vertebrate eye. RPE dysfunction is associated with retinal degeneration and blindness. In order to fully understand how dysregulation affects visual function, RPE-specific gene knockouts are indispensable. Since the currently available RPE-specific *Cre* recombinases show lack of specificity or poor recombination, we sought to generate an alternative. We generated a tamoxifen-inducible RPE-specific *Cre* transgenic mouse line under transcriptional control of an RPE-specific *Tyrosinase* enhancer. We characterized the *Cre*-mediated recombinant expression by crossing our *RPE-Tyrosinase-CreEr^{T2}* mouse line with the *tdTomato* reporter line, *Ai14*. Detected fluorescence was quantified via high-content image analysis. Recombination was predominantly observed in the RPE and adjacent ciliary body. RPE flatmount preparations revealed a high level of recombination in adult mice (47.25–69.48%). Regional analysis of dorsal, ventral, nasal and temporal areas did not show significant changes in recombination. However, recombination was higher in the central RPE compared to the periphery. Higher levels of *Cre*-mediated recombinant expression was observed in embryonic RPE (~83%). Compared to other RPE-specific *Cre* transgenic mouse lines, this newly generated *RPE-Tyrosinase-CreEr^{T2}* line shows a more uniform and higher level of recombination with the advantage to initiate recombination in both, prenatal and postnatal animals. This line can serve as a valuable tool for researches exploring the role of individual gene functions, in both developing and differentiated RPE.

OPEN ACCESS

Citation: Schneider S, Hotaling N, Campos M, Patnaik SR, Bharti K, May-Simera HL (2018) Generation of an inducible RPE-specific *Cre* transgenic-mouse line. PLoS ONE 13(11): e0207222. <https://doi.org/10.1371/journal.pone.0207222>

Editor: Alfred S. Lewin, University of Florida, UNITED STATES

Received: May 18, 2018

Accepted: October 26, 2018

Published: November 15, 2018

Copyright: This is an open access article, free of all copyright, and may be freely reproduced, distributed, transmitted, modified, built upon, or otherwise used by anyone for any lawful purpose. The work is made available under the [Creative Commons CC0](https://creativecommons.org/licenses/by/4.0/) public domain dedication.

Data Availability Statement: All relevant data are within the paper and its Supporting Information files.

Funding: HMS, SS, SRP were funded by the Alexander Von Humboldt Foundation (Sofia Kovalevskaja award 2014). MC, NH, KB are all funded by the NEI, Intramural program.

Competing interests: The authors have declared that no competing interests exist.

Introduction

The retinal pigment epithelium (RPE) is a monolayer of pigmented epithelial cells intercalated between the neural retina and the choriocapillaris. With their long apical microvilli, RPE cells surround the light-sensitive outer segments of the retinal photoreceptors [1]. Due to its numerous functional roles, the RPE is essential for vision [2]. On the basal side, the RPE is in contact with the Bruch's membrane and together they control ion, nutrient, water and metabolite transport between the retina and the retinal vascular network, the choriocapillaris [2,3]. Additionally, the RPE is important for re-isomerization of all-*trans*-retinol to 11-*cis*-retinal,

phagocytosis of the shed photoreceptor outer segments, and absorption of incident light, all of which are essential for health and function of the photoreceptor cells [2–5]. RPE dysfunction and associated failure of one or more of these processes can lead to retinal degeneration and blindness [2]. Furthermore, dysfunction of the RPE has been associated with age-related macular degeneration (AMD), the most common cause of irreversible blindness in the elderly population [4]. In order to fully understand the molecular development and function of the RPE, and how dysregulation can affect visual function, RPE-specific gene knockouts are indispensable.

Homozygous germline knockout of widely expressed genes often leads to embryonic or neonatal lethality. Therefore, a tissue-specific gene-knockout strategy is required to determine tissue-specific effects of gene function. For this, the Cre/LoxP-system has emerged as the most commonly used method to introduce somatic mutations exclusively in the tissue of interest in mice [6,7]. In this system, a Cre recombinase is driven by a tissue-specific promoter and enables precise excision of a DNA sequence in the tissue of interest [4,5,7]. This technique enables either recombination-activated gene expression or conditional gene inactivation [6–8]. The site-specific Cre recombinase, derived from the P1 bacteriophage, is able to bind to a 34 bp recognition site (*loxP site*) and excise the DNA flanked between two *loxP* sites (floxed), leaving a single *loxP site* remaining [4,8–10]. Furthermore, conditional knockout of a gene in early development may have differing effects compared to ablation of gene function at a later time point [4,5,9]. Therefore, temporal gene expression also needs to be taken into account. To add a temporal dimension to the study of gene function, an inducible component can be added to the activation of the Cre [5,11]. The two most commonly used are the tetracycline-inducible Cre recombinase and the ligand-dependent 4-hydroxytamoxifen (4-OHT)-inducible Cre recombinase [4,7,11,12]. Due to its faster rate of induction, the 4-OHT-inducible Cre recombinase is more highly recommended [13]. Here, the Cre recombinase is fused to a ligand-binding domain (LBD) of the human estrogen receptor (ER) resulting in a CreER^{T2} construct, which is only activated upon addition of 4-OHT [6,11]. Taken together, a combination of a ligand-dependent tissue-specific promoter-driven Cre expression facilitates spatial and temporal control of Cre recombinase activity [7,11]. For this a mouse must inherit both, the gene for Cre and a floxed gene of interest, and be treated with tamoxifen, which will then be metabolized to its active form 4-OHT, at required time points [6,12].

Important considerations for choosing the Cre mouse lines are the level of expression in desired tissue of interest, and the level of ectopic expression. To date, few RPE-specific Cre mouse lines have been reported. Four non-inducible RPE-specific Cre lines include the *dopa-chrome tautomerase (Dct)*-Cre [8], the *tyrosinase related protein-1 (Tyrp1)*-Cre [9], the *Melanoma-associated antigen recognized by T cells (MART1)*-Cre [14], and the *bestrophin-1 (BEST1)*-Cre [4]. All of these Cre recombinases lead to ectopic Cre recombination. The *Dct*-Cre line causes additional recombination in the telencephalon, the *MART1*-Cre line in the skin, and the *BEST1*-Cre line leads to ectopic Cre expression in the testis. However, in all, the expression in the eye is restricted to the RPE [4,8,14]. In contrast, the widely used *Tyrp1*-Cre line leads to ectopic Cre expression in the neuroretina, which might affect interpretations when studying retinal phenotypes caused by loss-of-function mutations in the RPE [9]. Thus far, two inducible RPE-specific Cre lines have been reported, the *monocarboxylate transporter 3 (Mct3)*-Cre [15] and the Tet-on *VMD2*-Cre [5]. Depending on the genetic background of the mice and the timing of induction, the *Mct*-Cre line only leads to low levels of recombination (5–20%) [4,15]. For the *VMD2*-Cre line, the level of recombination has not been reported. However, at P4 it shows the greatest activity [4,5], suggesting that it might be less efficient for manipulation of genes expressed at earlier time points.

To address the above shortcomings, we generated an inducible RPE-specific transgenic mouse line with uniform recombination efficiency. Since the 4-OHT-inducible *CreEr^{T2}* is considered the most efficient driver for inducible genetic recombination [6], we generated a transgenic mouse line using this *Cre* recombinase under transcriptional control of a previously published and validated RPE-specific enhancer of the *Tyrosinase* gene [16,17]. *Tyrosinase* (*Tyr*) is expressed in all pigmented cells. However, it is differentially regulated between the RPE and melanocytes due to a novel tissue-specific distal regulatory element (*Cns-2*), which is located at -47 kb from the transcription start site [17]. *Cns-2* is responsible for *Tyrosinase* gene expression in the RPE, but not in melanocytes. In this study, we characterize our inducible RPE-specific *Cre* mouse line and evaluate its level of recombination efficiency by crossing it with a commonly used reporter mouse line.

Material and methods

Generation of a transgenic RPE-Tyrosinase-*CreEr^{T2}* mouse line

A RPE-*Tyrosinase-CreEr^{T2}* transgenic mouse line (strain C57BL/6N) was generated by insertion of a (5'-3') construct containing a RPE-specific *Tyr enhancer* (*Cns-2*) (4721 bp) [17], a *hsp70 minimal promoter* (985 bp) and a construct for the inducible *Cre-ER^{T2}* recombinase [11] (1983 bp). *Cre-ER^{T2}* was amplified from the pCAG-*CreERT2* vector (Addgene) and cloned into the *Tyr-Hsp70* vector using *XhoI/SalI* enzymes. Generation of the *Tyr-GFP* mouse line was previously reported [16].

Animals

All experiments had ethical approval from the Landesuntersuchungsamt Rheinland-Pfalz and were performed in accordance with the guidelines given by ARVO Statement for the Use of Animals in Ophthalmic and Vision Research. Animal maintenance and handling were performed in line with Federation for Laboratory Animal Science Associations (FELASA) recommendations. Mice were housed in a 12 h light/dark cycle. Animals were sacrificed by cervical dislocation. The morning after mating was considered as E0.5. From the time at which the mice were six weeks old, they were considered adult.

B6.Cg-Gt(ROSA)26Sor^{tm14(CAG-tdTomato)Hze/J} reporter mice (JAX stock #007914; [18]; referred to as *Ai14*) were crossed with RPE-*Tyrosinase-CreEr^{T2}* mice to visualize *Cre* expression. *Ai14* mice possess a floxed stop cassette upstream of the CAG promoter-driven red fluorescent protein *tdTomato*. Following *Cre*-mediated recombination the stop cassette is excised, allowing expression of *tdTomato*.

Genotyping

For DNA isolation the tissue samples were incubated in tissue digestion buffer (10 mM Tris-HCl pH 8.0, 10 mM EDTA, 200 mM NaCl, 0.5% SDS, 0.1 mg/ml Proteinase K) overnight at 55 °C. Afterwards the samples are vortexed and centrifuged at 21,130 rcf for 10 min. The supernatant was transferred carefully into a new tube and incubated with double the volume of 95% Ethanol for at least 10 min at room temperature. After centrifugation at 21,130 rcf for 15 min, the DNA pellet was air dried at room temperature and dissolved in Milli-Q water to a concentration between 100 and 200 µg/ml. PCR of genomic DNA was performed using GoTaq G2 Hot Start Polymerase (Promega). For detection of the *Cre* construct, the following primers were used *Cre-F* (5' -GAGTGAACGAACCTGGTTCGAAATCAGTGCG-3') and *Cre-R* (5' -GCATTACCGGTCGATGCAACGAGTGATGAG-3'). To detect a ~300-bp product using the following cycling conditions: 90 s at 94 °C for initial denaturation, followed by 40 cycles of

30 s at 94 °C for denaturation, 30 s at 55 °C for annealing, 60 s at 72 °C for extension, and finally 5 min at 72 °C for final extension. To detect the *Ai14* construct, the Jackson Laboratory (www.jax.org) provided primer sequences and thermocycling conditions. All PCR products were separated on a 2% agarose gel and visualized using GelRed Nucleic Acid Gel Stain.

Cre recombinase activity in transgenic mice

To induce Cre recombination activity in the mice, 1.6 mg Tamoxifen (Sigma-Aldrich, T5648) and 1.6 µg β-Estradiol (Sigma-Aldrich, E8875) were administered on five consecutive days via intraperitoneal injection (IP) or oral gavage (OG). Tamoxifen was prepared as a 10 mg/ml stock solution in flax seed oil. The solution was incubated at 37 °C and vortexed occasionally until dissolved. β-Estradiol was added to the tamoxifen solution at a concentration of 10 mg/ml. Treatment of pregnant dams was started at E9.5 and embryos were harvested at E17.5. For treatment in adults, eyes were harvested on the fifth day after the last application. For short-term (ST) analyses of Cre activity eyes were harvested five days after the last treatment application. For long-term (LT) Cre activity eyes were harvested three months after the last treatment application.

Quantitative real-time PCR (qRT-PCR)

Tissues of adult mice were harvested on the fifth day (ST) or three months (LT) after the last application and homogenized in TRIzol Reagent (Invitrogen) using a pestle. For RNA extraction, the TRIzol Reagent was used according to manufacturer’s recommendations. RNA was stored at -80 °C. RNA was reverse transcribed to cDNA using GoTaq Probe 2-Step RT-qPCR System (Promega) and cDNA was stored at -20 °C. qRT-PCR was performed via a StepOne-Plus Real-Time PCR System (Applied Biosystems) using Platinum SYBR Green (Invitrogen). The following cycling conditions were used: 95 °C for 10 min followed by 40 cycles of 95 °C for 15 sec, 60 °C for 1 min. Relative target gene expression was normalized to *TBP*. Primer sequences are listed in [Table 1](#).

Fluorescence staining and mounting of flatmount RPE and retina

For RPE or retina staining, mice were sacrificed, eyes were enucleated and the retina was removed. The tissue was fixed with 4% paraformaldehyde (PFA) in 1× phosphate-buffered saline (PBS) for 1 h and washed three times with 1× PBS. To reduce auto-fluorescence from the PFA, the tissue was incubated with 50 mM NH₄Cl for 10 min before permeabilizing with 1× PBS 0.1% Tween-20 (PBST) with 0.3% Triton-X (TX) (PBST-TX) for 1 h and blocked with blocking buffer (0.1% ovalbumin, 0.5% fish gelatin in 1× PBS) over night at 4 °C. Eyecups were incubated with DAPI (Carl Roth) and a directly conjugated Zonula Occludens-1 (ZO-1) antibody, conjugated to Alexa Fluor 488 (ZO-1-1A12, Invitrogen, 339188) in blocking buffer for 2 h in dark conditions at room temperature. Post staining, two washing steps with PBST-TX and one with 1× PBS for 20 min each were performed. Eyecups or retina were flat mounted with Fluoromount-G (SouthernBiotech) and examined using a fluorescence

Table 1. Primers used for qRT-PCR.

Gene	Species	Forward	Reverse
<i>Lrat</i>	Mouse	TTCAAGCTCTTTAGCGTGAGC	TTTCATAGGGACGGTTCTTCC
<i>Rpe65</i>	Mouse	TTGAAACTGTGGAGGAAGTCTGTC	GACTGCCAGTGAGCCAGAG
<i>Ttr</i>	Mouse	CCTCGCTGGACTGGTATTTG	GACCATCAGAGGACATTTGG
<i>Tbp</i>	Mouse	CTTCGTGCAAGAAATGCTGAAT	CAGTTGTCCGTGGCTCTCTTATT

<https://doi.org/10.1371/journal.pone.0207222.t001>

microscope (ZEISS Axio Scan.Z1, Leica DM6000 B). Entire optic cup imaging was performed at either 10× or 20× magnification across three channels (red: tdTomato, green: ZO-1, and blue: DAPI). Exposure times were kept consistent at each magnification with scaling of the exposure time between magnifications to adjust for the decreased numerical aperture of the 10× objective.

Fluorescent staining and transmission electron microscopy of eye and embryo sections

For RPE or retina staining, mice were sacrificed, eyes were enucleated and immediately fixed with 4% paraformaldehyde (PFA) in 1× phosphate-buffered saline (PBS). After 5 min of fixation a hole was poked through the middle of the cornea and the eyes were incubated again in 4% PFA for another 15 min. Following this, the eyes were cut along the ora serrata and the anterior segment was removed, leaving the lens intact. The resulting eyes were fixed in 4% PFA for another hour. Post fixation, four washing steps with 1× PBS for 15 min each were performed. Afterwards the eyes were incubated in following sucrose solutions, each made with 1× PBS: once in 10% sucrose solution for 30 min, twice in 20% sucrose solution for 20 min each and once in 30% sucrose solution overnight. The next day the eyes were again incubated in 30% sucrose solution for 1 h. Afterwards the eyes were cryofixed in isopentane, cryosectioned and immunostained as previously described [19]. For immunostaining, the sections were placed on poly-L-lysine coverslips and permeabilized with 0.5% PBS-TX for 10 min before incubation with 50 mM NH₄Cl for 10 min. After a washing step with 1× PBS for 5 min, the sections were blocked with blocking buffer for 30 min at room temperature and then incubated with monoclonal primary antibodies against ADP-ribosylation factor-like protein 13B (Arl13b) (Sigma-Aldrich), Calbindin (Millipore), Calretinin (Millipore), Protein kinase C α (PKC α) (Sigma) or Glutamine synthetase (GS) (Abcam), diluted in blocking buffer, overnight at 4 °C. Three washing steps with 1× PBS, 10 min each, were performed before incubation with secondary antibodies conjugated to Alexa-488 (Invitrogen) and DAPI, diluted in blocking buffer, for 2 h in dark conditions at room temperature. Post staining, three washing steps with 1× PBS and one with Milli-Q water, 10 min each, were performed and the sections were mounted using Mowiol 4–88. The sections were examined using a fluorescence microscope (Leica DM6000 B) and the images were processed via FIJI using color correction and contrast adjustment. Whole E16.5 embryos were fixed in 4% paraformaldehyde overnight at 4 °C, then washed in 1× PBS and transferred to 30% sucrose/1× PBS until the embryos sank. Embryos were then incubated in a 1:1 mixture of OCT and 30% sucrose/1× PBS for 30 min on a rocking platform. After transferring embryos to an embedding mold containing OCT, they were oriented as desired and frozen on dry ice. Frozen blocks were cut on a microtome, stained with DAPI and imaged using fluorescence microscope (ZEISS Axio Scan.Z1). For transmission electron microscopy (TEM), dissected eyecups were fixed in 2.5% glutaraldehyde in 0.1M cacodylate buffer with 0.1M sucrose for 1 h at room temperature. Post fixation they were placed in 2% osmium tetroxide (in 0.1M cacodylate buffer) for 1 h and then dehydrated through an ethanol series. After embedding in epoxy resin, eyes were cut and processed for TEM using standard EM procedures.

Image analysis

Images were processed using a custom FIJI plugin. Areas of expression in all regions were assessed for all cells across all 15 eyes. Areas of coverage were then aggregated across Male IP, Female IP, and Female OG and a statistical analysis was performed to determine if expression was heterogeneous. Whole optic cup images were separated into their respective channels.

Background subtraction and intensity scaling was performed in each channel so that 99% of the signal obtained in the image fell within the dynamic range of the image (16-bit image). Background subtraction and scaling was done to transform pixel intensity histograms between all images into similar distributions. After scaling, images were converted to 8-bit images. Images whose initial intensity distribution took less than 5% of the dynamic range of the image were removed from analysis due to the lack of signal to noise. Images were then duplicated into a “Foreground” image and a “Background” image. The Foreground images were used to quantify expression levels and thus were not further edited. The Background images were used to identify areas in the images that could not be measured (bubbles or tissue damage) or that did not contain tissue (background). No expression quantification was done on Background images.

In Background images, all pixels first had one intensity unit added to them. Then, areas in images that contained artifacts (bubbles or damaged tissue) or no tissue were manually removed (given a 0-value). After giving a 0-value to all non-measurable/background areas in an image a background mask was created in which the location of all 0-value pixels was identified. This mask was overlaid onto the Foreground image and all background pixels were given a 0-value in the Foreground Image. The total area of the background pixels was subtracted from the total image area to identify the total possible area of expression (A_{Tot}). All Foreground images were then segmented using a manually validated threshold. The area segmented as expressing (A_{Exp}) was then divided by A_{Tot} to determine the total percent of expression (A_{Per}). Representative image processing is shown in supplementary information (S5 Fig).

$$\frac{A_{Exp}}{A_{Tot}} = A_{Per} \quad \text{Eq 1}$$

In adult mice, nasal, temporal, dorsal, ventral, central, and peripheral areas were then manually cropped in each image and Eq 1 was used to determine the percent expressing in each cropped image. The central region was determined as an ellipsoid region that was half the diameter of the total butterfly eye cup in each orthogonal direction (nasal/temporal and dorsal/ventral). All area outside this region was defined as the periphery.

In fetal eyes, Cre activity was predominately found in the nucleus and little tdTomato expression after Cre mediated recombination was seen in the cytoplasm. Thus, expression in these eyes was performed using two methodologies: (1) by assessing the total area of nuclear expression and total area of Cre/tdTomato expression and dividing the respective areas as shown in Eq 1. (2). Across seven fetal eyes 73,499 cell nuclei were measured. To ensure the robustness of this method the total count of nuclei (N_{Nuc}) was also determined as well as the total count of nuclei that expressed Cre/tdTomato (N_{Exp}). The ratio of these was then taken to determine the total percent expressing (N_{Per}). Eq 2 shows this formula below.

$$\frac{N_{Exp}}{N_{Nuc}} = N_{Per} \quad \text{Eq 2}$$

Statistics

All comparisons between treatments were performed with a linear mixed effect (LME) model controlling for the repeated measures performed on each eye (Total expression and regional expression) as well as for multiple eyes coming from each mouse (2 eyes per mouse). An LME model was used because several eyes were removed due to lack of staining (intensity histogram represented less than 5% of the dynamic range of the image) and thus modeling approaches that could allow for “missing” data were necessary. Multiple comparisons were controlled for using Tukey’s Post-Test. Normality was tested for using the Kolmogorov-Smirnov (KS)

normality test. All statistical analysis was performed using R [20] with the “nlme” package [21] and the “multcomp” package [22]. Significance was set as less than 0.05.

Results

Generation of *Cre* transgenic mice

To generate an RPE-specific *Cre* transgene, a *hsp70* promoter was placed downstream of a RPE-specific *Tyr* enhancer *Cns-2* [17], as previously described [23]. To verify the expression of this combined construct containing both, the *Tyr* enhancer *Cns-2* and *hsp70* promoter, a *GFP* cassette was fused downstream (*Tyr-GFP*) (Fig 1A) [16]. As previously observed in embryonic tissue, this *Tyr-GFP* construct was also spatially restricted to the RPE in the adult eye. We observed GFP expression distributed throughout the whole RPE in adult mice (Fig 1B, S1 Fig). To obtain a tamoxifen-inducible *RPE-Tyrosinase-CreEr^{T2}* transgene, the *GFP* cassette was replaced by a *CreEr^{T2}* cassette [11] (Fig 1C). In order to characterize the specificity and efficiency of this inducible RPE specific *Cre* recombinase, we crossed the *RPE-Tyrosinase-CreEr^{T2}* mouse line with a *tdTomato* reporter line, namely *Ai14*. This mouse line contains a floxed *Stop* cassette upstream of the gene for the red fluorescent protein *tdTomato* [18], and is therefore able to express *tdTomato* after tamoxifen treatment (Fig 1C).

Analysis of *Cre*-mediated recombination in *Ai14;RPE-Tyrosinase-CreEr^{T2}* mice

To evaluate recombinant expression of our generated transgene, we analyzed the expression of *tdTomato* in *Ai14;RPE-Tyrosinase-CreEr^{T2}* mice RPE. After five days of consecutive tamoxifen treatment, the mouse eyes were harvested on the fifth day after the last dose, and prepared for flatmount preparations or cryosections. Recombinant expression of *tdTomato* was detected via fluorescence microscopy (Fig 2). In longitudinal cross-sections, we predominantly observed recombination in the RPE (Fig 2A and 2B, S3 Fig) as well as in the ciliary body (Fig 2A, white arrowheads). Quantification showed relatively low recombinant expression in the ciliary body (~10.71%) (Fig 3C and 3D). In contrast, retina flatmounts from treated animals showed virtually no *tdTomato* expression (Panel A in S2 Fig). Longitudinal cross-sections revealed occasionally weak ectopic expression in the inner plexiform layer (IPL) of the retina (S3 Fig). To identify any possible cell type specificity of the occasional ectopic expression in the inner retina, we performed immunohistochemistry with a variety of inner retina markers (Calbindin, Calretinin, Protein kinase C alpha (PKC α), Glutamine synthetase (GS)). In the rare event of red fluorescence in the retina, we never found any co-expression with these inner retina markers, suggesting that ectopic expression was not observed in horizontal cells, amacrine cells, rod bipolar cells or Müller glia cells. Therefore, this expression is not in any of the dominant retinal cell types. To confirm that *tdTomato* expression was not detected in any other tissue types outside of the eye, we prepared whole mouse embryo sections at E16.5. Whole body imaging confirmed that recombination was only restricted to the eye (Fig 3A), and higher magnification of the eye also showed specificity for the RPE and absence of recombination in the retina (Fig 3B). To test for leakiness of *Cre* expression, we generated flatmount preparations from a variety of control mice, and looked for any unspecific activation of *Cre* (Fig 4). In contrast to a treated *Ai14;RPE-Tyrosinase-CreEr^{T2}* mouse, we never detected any *Cre* activity in untreated *Ai14;RPE-Tyrosinase-CreEr^{T2}* mice. We confirmed this in both male and female mice. To exclude any preparation artifact that might lead to fluorescent detection, we also prepared a RPE flatmount from an untreated *Ai14* mouse that did not contain the *RPE-Tyrosinase-CreEr^{T2}* construct. No fluorescent signal could ever be detected. Since

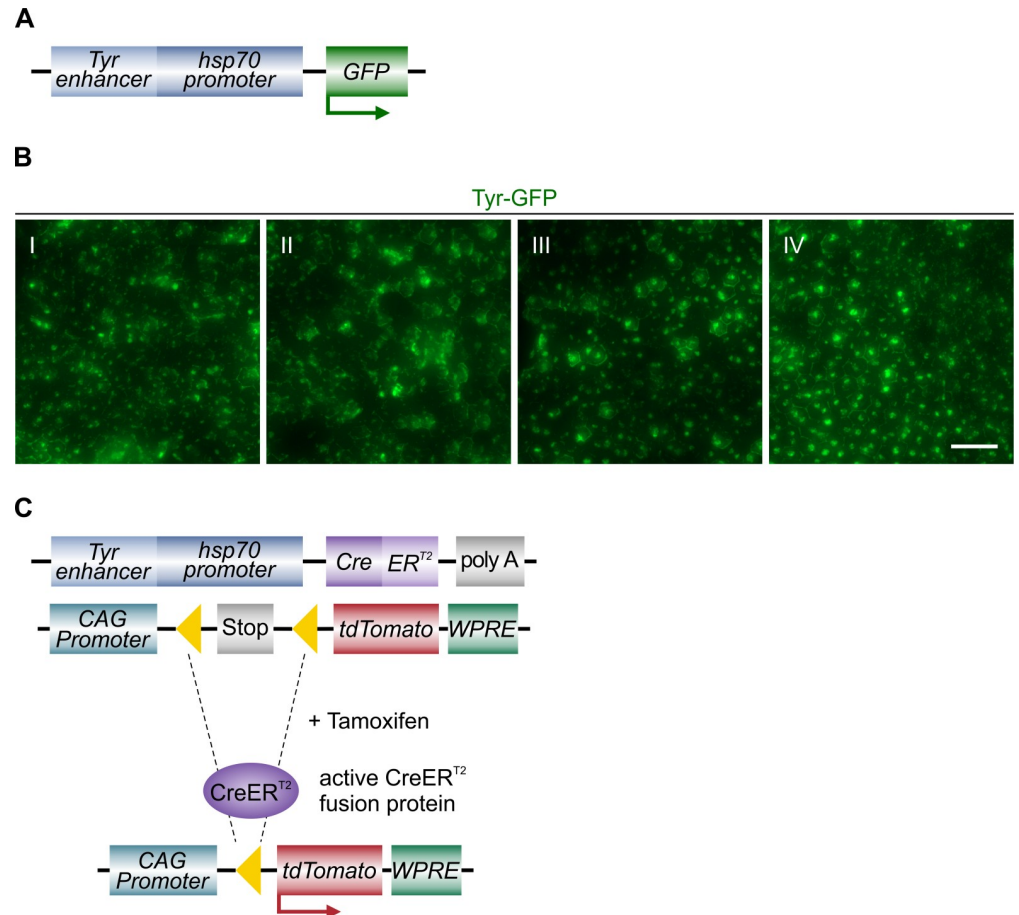


Fig 1. Generation of tamoxifen-inducible Cre transgenic mice. A: Schematic of the RPE-specific *Tyr-GFP* construct used for generation of *Tyr-GFP* mice. B: Regional examples (I-IV) of *Tyr-GFP* expression showing comprehensive expression of GFP under control of the *Tyr* promoter. Images taken from the flatmount shown in S1 Fig. C: Schematic of the induction of Cre activity in double transgenic mice. Mice harboring the *RPE-Tyrosinase-CreEr^{T2}* cassette and the *Ai14* cassette are treated with tamoxifen to induce Cre activity. Following recombination, the floxed exons (yellow triangles) are excised. In the case of the *Ai14* cassette, recombination removes a stop sequence allowing for expression of tdTomato. Scale bar: (B) 50 μ m.

<https://doi.org/10.1371/journal.pone.0207222.g001>

application of β -Estradiol assists late stages of gestation and initiation of pup delivery, [24], we added β -Estradiol to our treatment solutions in both pregnant (see below) and non-pregnant mice. To exclude unintended activation of the Cre recombinase via addition of β -Estradiol, we treated animals with β -Estradiol alone, dissolved in flax seed oil at the same concentration as in the tamoxifen solution (Panel B in S2 Fig). Our data showed that β -Estradiol alone was not able to drive recombination via Cre-ER^{T2}.

Efficacy and assessment of homogeneity of Cre-mediated recombination in adult mice

To quantify the efficiency of the recombinant expression of our generated transgene, we analyzed the expression of tdTomato via software analysis in *Ai14;RPE-Tyrosinase-CreEr^{T2}* mice. Mice were treated as mentioned above and recombinant expression of tdTomato was detected via fluorescence microscopy. Flatmounts of the RPE showed a uniform distribution of tdTomato expression throughout the entire RPE (Fig 5A). Depending on gender, we observed

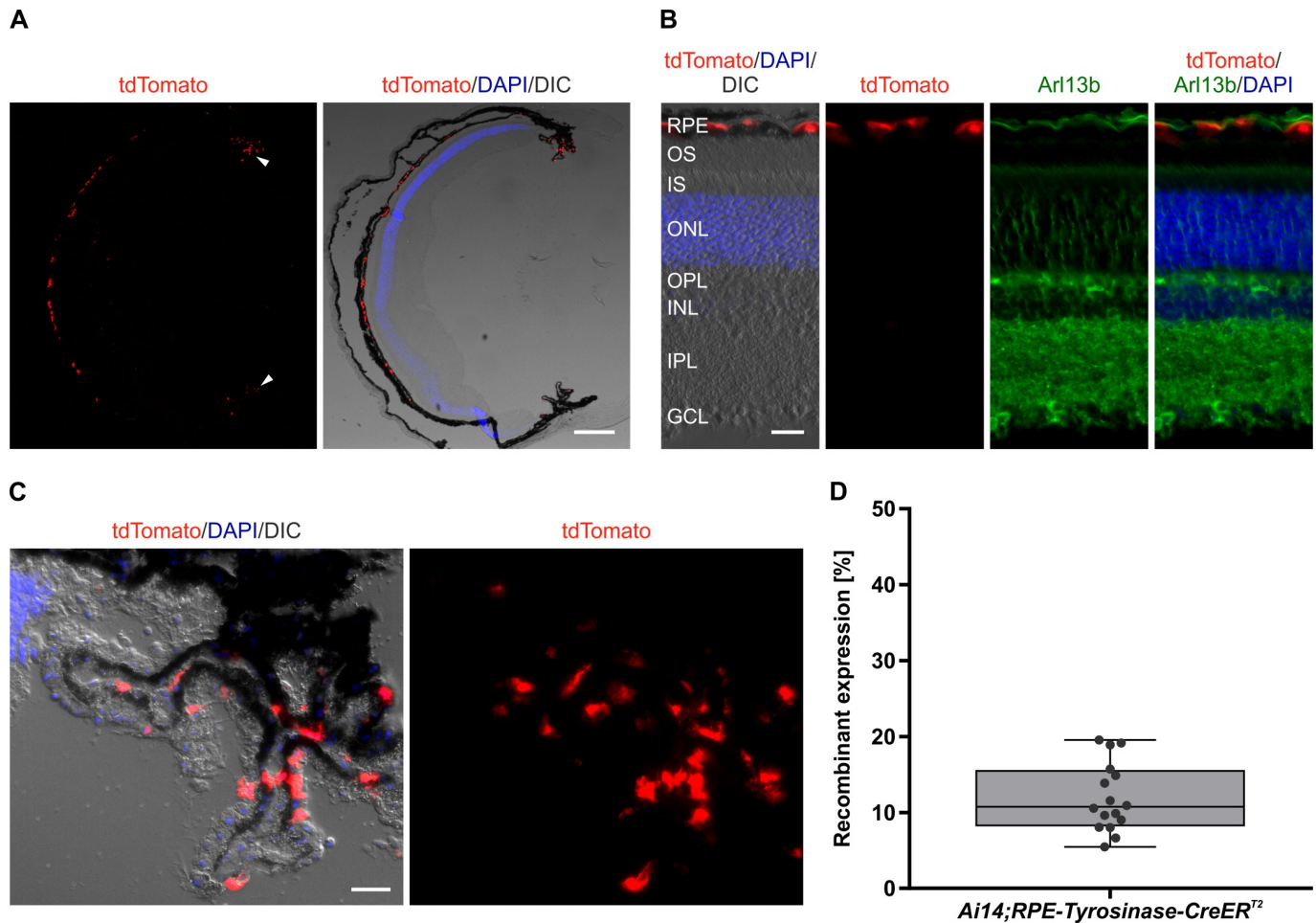


Fig 2. Cre-mediated recombinant expression in the RPE of adult *Ai14;RPE-Tyrosinase-CreEr^{T2}* mice. A, B: Localization of tdTomato expression in an adult eye upon Cre activity in longitudinal cryosections stained with DAPI (blue) and Arl13b (green) to visualize the connecting cilium (B), respectively. Differential interference contrast (DIC) image was overlaid with the DAPI staining and red fluorescent tdTomato expression. Cre activity resulted in tdTomato expression, which is seen in the RPE and to a lesser extent in the ciliary body (white arrowheads). C: Cre activity resulted in simultaneous tdTomato expression in the ciliary body. D: Quantification of tdTomato expression in the ciliary body. n = 16 ciliary bodies from three individual animals. RPE: Retinal pigment epithelium, OS: Outer segments, IS: Inner segments, ONL: Outer nuclear layer, OPL: Outer plexiform layer, INL: Inner nuclear layer, IPL: Inner plexiform layer, GCL: Ganglion cell layer. Scale bars: (A) 250 μ m, (B) 25 μ m, (C) 25 μ m.

<https://doi.org/10.1371/journal.pone.0207222.g002>

between 47.25% and 69.48% recombinant expression in adult mice (Fig 5B). In female mice, application via oral gavage (OG) did not show any significant differences compared to intraperitoneal injection (IP) ($p = 0.949$). Whereas, IP injections was significantly more efficient in male mice compared to female mice ($p = 0.0029$).

Additionally, we quantified the homogeneity of recombinant expression across the entire RPE monolayer. In order to determine any spatial differences in the level of tdTomato expression and recombination, we divided the RPE flatmounts into dorsal, ventral, nasal and temporal regions (Panel A in S5 Fig) and quantified the level of tdTomato via high-content image analysis (Fig 5C). We saw no significant differences between nasal-temporal and dorsal-ventral expression in any of the treatment conditions tested, thereby confirming that that our newly generated *RPE-Tyrosinase-CreEr^{T2}* driver can be used to target the entire RPE in adult animals. Similarly, we analyzed the distribution of tdTomato expression in center versus peripheral areas of the RPE flatmounts (Panel B in S5 Fig). The center was defined on the RPE flatmount

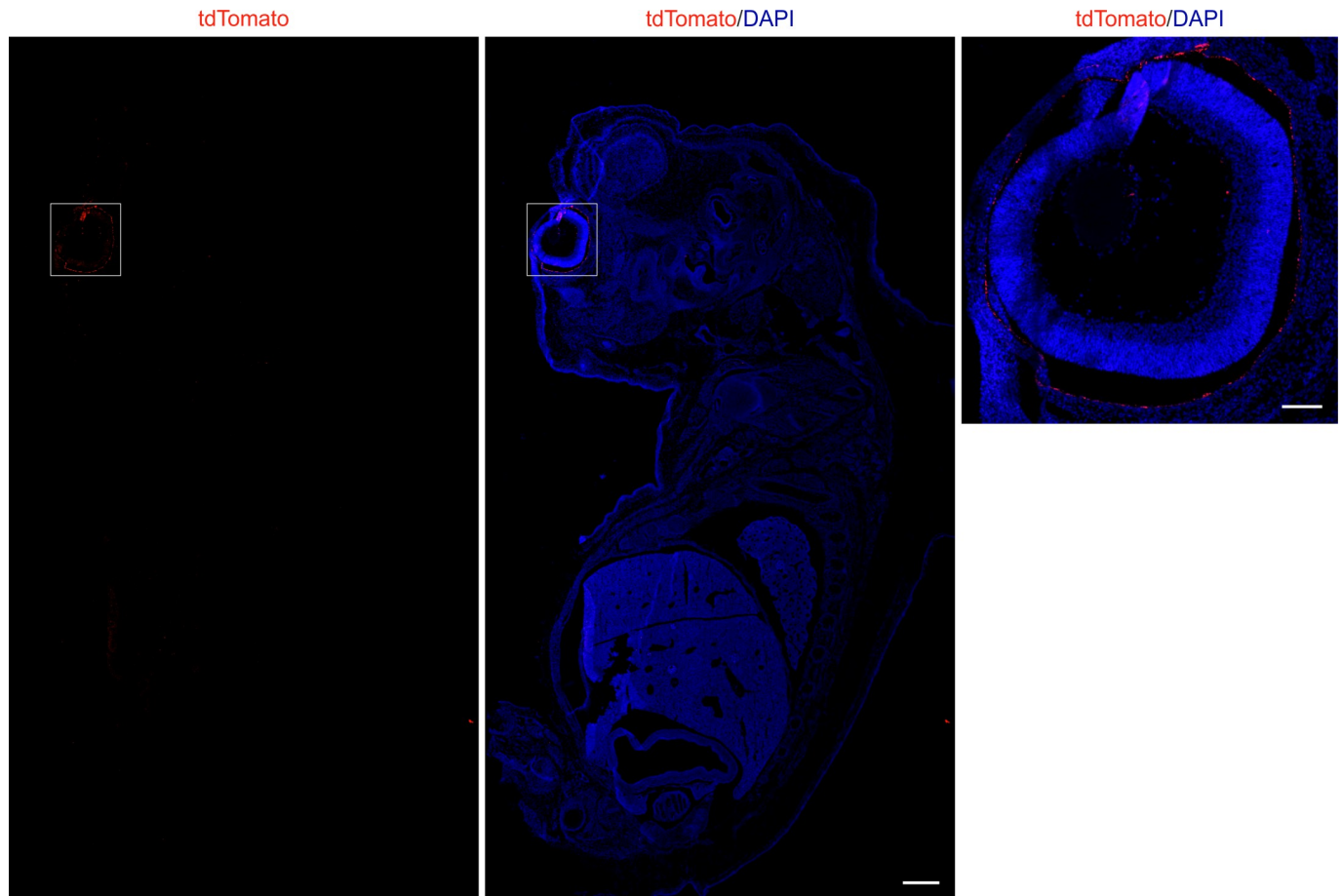


Fig 3. Cre-mediated recombinant expression in an *Ai14;RPE-Tyrosinase-CreEr^{T2}* embryo section. A: Fluorescent image of tdTomato expression in longitudinal embryo sections stained with DAPI (blue) showing that Cre activity is restricted to the eye. B: Higher magnification of the eye region in A shows high specificity for the RPE. Scale bar: (A) 500 μ m, (B) 100 μ m.

<https://doi.org/10.1371/journal.pone.0207222.g003>

at the optical nerve. As seen in Fig 5D, there was only a mean difference of 12% expression between center (64.80%) and periphery (52.71%; $p = 8.60E-07$) across all treatment groups despite the area ratio between center and periphery being 25%.

Efficacy of Cre-mediated recombination in embryonic mice

Since many developmental studies address the role of gene expression during RPE development, we wanted to determine the level of *Cre* recombination driven by our *RPE-Tyrosinase-CreEr^{T2}* construct achieved in embryonic tissue. For this, timed pregnant *Ai14;RPE-Tyrosinase-CreEr^{T2}* mice were treated with tamoxifen in order to trigger Cre-mediated recombination embryonically. Since *Tyr* expression starts at E10.5 [17], we began treatment at E9.5. Following five days of treatment, embryos were collected at E17.5, the RPE was dissected for flatmount preparations, stained and mounted for analysis of recombinant expression of tdTomato via fluorescence microscopy (Fig 6). RPE flatmounts showed a uniform distribution of tdTomato throughout the whole RPE monolayer (Fig 6A). Two separate methods for quantification (described in the methods) revealed similar levels of recombinant expression, namely 82.50% (Area) vs. 83.51% (Cell Count) (Fig 6B). For the Cell Count method, two values over 100% were obtained. This was caused by detection of more tdTomato positive cells than DAPI

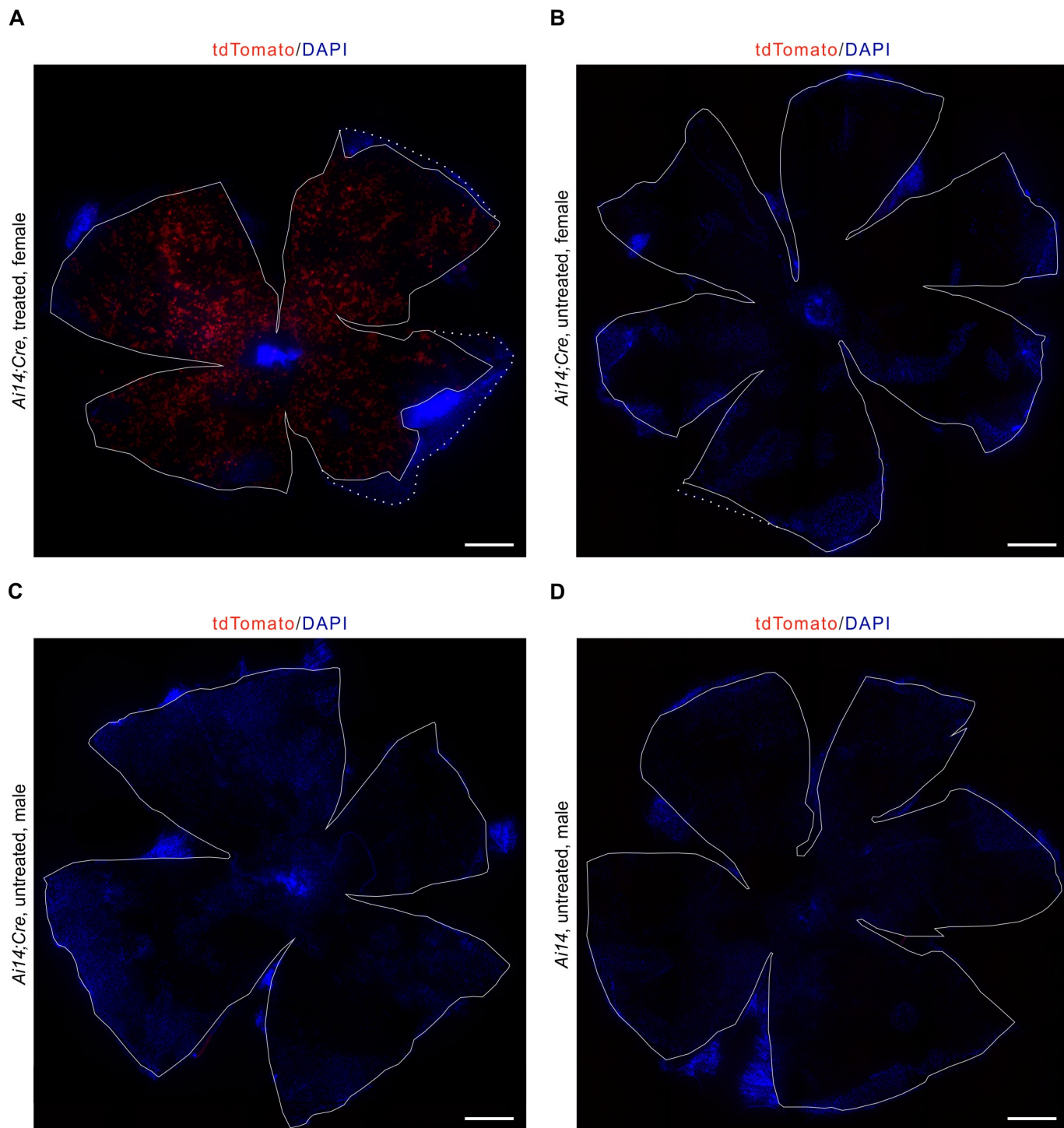


Fig 4. Representative RPE flatmount preparations from control animals. A: RPE flatmount of a treated female adult *Ai14;RPE-Tyrosinase-CreEr^{T2}* mouse showing tdTomato expression throughout the whole RPE. B: RPE flatmount of an untreated female adult *Ai14;RPE-Tyrosinase-CreEr^{T2}* mouse showing no red fluorescence, thus tdTomato expression. C: RPE flatmount of an untreated male adult *Ai14;RPE-Tyrosinase-CreEr^{T2}* mouse showing no red fluorescence, thus tdTomato expression. D: RPE flatmount of an untreated male adult *Ai14* mouse, being *Cre* negative. No red fluorescence, thus tdTomato expression, was observed. All flatmounts were counterstained with DAPI (blue). Scale bar: (A-D) 500 μ m.

<https://doi.org/10.1371/journal.pone.0207222.g004>

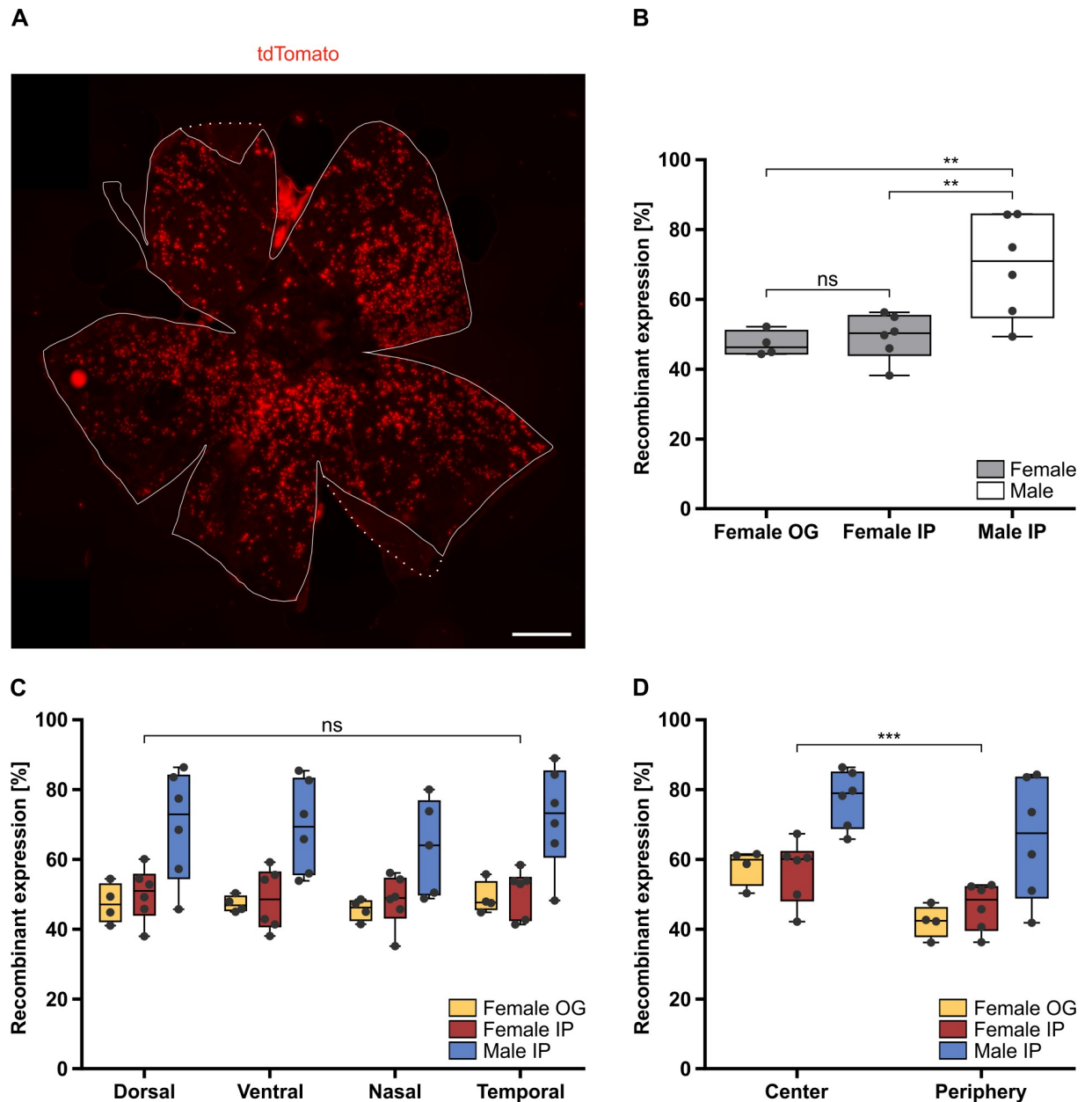


Fig 5. Analysis of Cre-mediated recombinant expression and its overall distribution in the adult *Ail4;RPE-Tyrosinase-CreEr^{T2}* RPE. A: Fluorescent image showing the uniform distribution of tdTomato expressing cells throughout an adult RPE flatmount preparation. Outline of the RPE indicated by the solid line, dotted line represents inverted choroidal tissue. B: Quantification of recombinant expression in RPE of female mice, treated via oral gavage (OG) (47.25%) (n = 4 eyes) compared to female mice treated via intraperitoneal injection (IP) (49.35%) (n = 6 eyes) showed similar levels of recombinant expression (p = 0.949). The difference between male (69.48%) (n = 6 eyes) and female mice, both treated via IP, is statistically significant (p = 0.0029). C: Quantification of the recombinant expression in dorsal, ventral, nasal and temporal areas of the RPE in three different treatment conditions (Female OG, Female IP and Male IP) showed no significant regional differences (p = 0.9995, p = 0.5315). D: Quantification of the recombinant expression in central vs. peripheral areas of the RPE in the three different treatment conditions (Female OG, Female IP and Male IP) showed a significant difference (p = 8.60E-07). Significance levels: > 0.05 not significant (ns), ≤ 0.05 *, ≤ 0.01 **, ≤ 0.001 ***. Scale bar: (A) 500 μm.

<https://doi.org/10.1371/journal.pone.0207222.g005>

positive cells. Representative higher magnified images of a RPE flatmount are shown in Fig 6C. Manual counting of this smaller region revealed 77.87% recombinant expression (Nuclei: 235, tdTomato: 183). Manual counting of additional regions from different RPE flatmounts

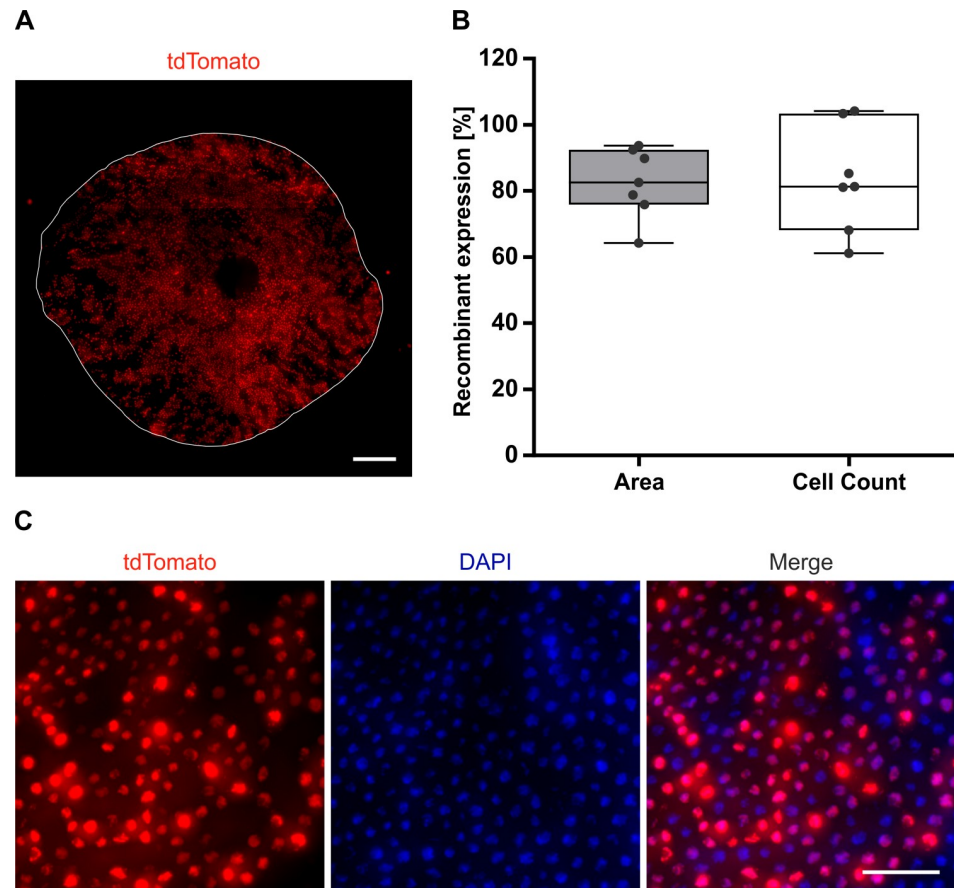


Fig 6. Analysis of the Cre-mediated recombinant expression in embryonic *Ai14;RPE-Tyrosinase-CreEr^{T2}* mice. A: Fluorescent flatmount image showing the uniform distribution of tdTomato expressing cells throughout the RPE of an E17.5 *Ai14;RPE-Tyrosinase-CreEr^{T2}* embryo. Outline of the RPE indicated by the solid line. B: Upon quantification method, recombinant expression in embryonic mice was 82.5% (Area) and 83.5% (Cell Count), respectively ($n = 7$ eyes). C: Representative fluorescent flatmount images showing tdTomato expression and DAPI staining of an E17.5 *Ai14;RPE-Tyrosinase-CreEr^{T2}* RPE. Scale bar: (A) 200 μm , (C) 50 μm .

<https://doi.org/10.1371/journal.pone.0207222.g006>

resulted in 82.35% recombinant expression ($82.35\% \pm 2.97\%$ SD, 2735 nuclei counted), suggesting that our automated software was reliable. These results demonstrate that our newly generated *Tyr-CreER^{T2}* mouse line can also be employed as a tool for developmental studies.

Analysis of toxicity after Cre activation

Since Cre expression can sometimes lead to cellular toxicity, we checked for pathological phenotypes in the RPE of treated mice [12]. High-resolution histological preparations, imaged via transmission electron microscopy (TEM), showed no morphological changes of the RPE and surrounding structures (Bruch's Membrane), either after short-term (up to five days) or long-term (up to three months) Cre activity (Fig 7A). Higher magnification of fluorescently labeled RPE flatmounts, also showed no morphological changes in tdTomato expressing cells, based on cellular morphology and epithelial patterning, either after short-term or long-term Cre activity (Fig 7B). Again, suggesting that Cre expression is not detrimental to cellular homeostasis. Gene expression of mature RPE markers (*Lecithin retinol acyltransferase (Lrat)*, *Retinal pigment epithelium-specific 65 kDa protein (Rpe65)*, *Transthyretin (Ttr)*), as measured by quantitative real-time PCR (qRT-PCR), showed no differential expression between treated and

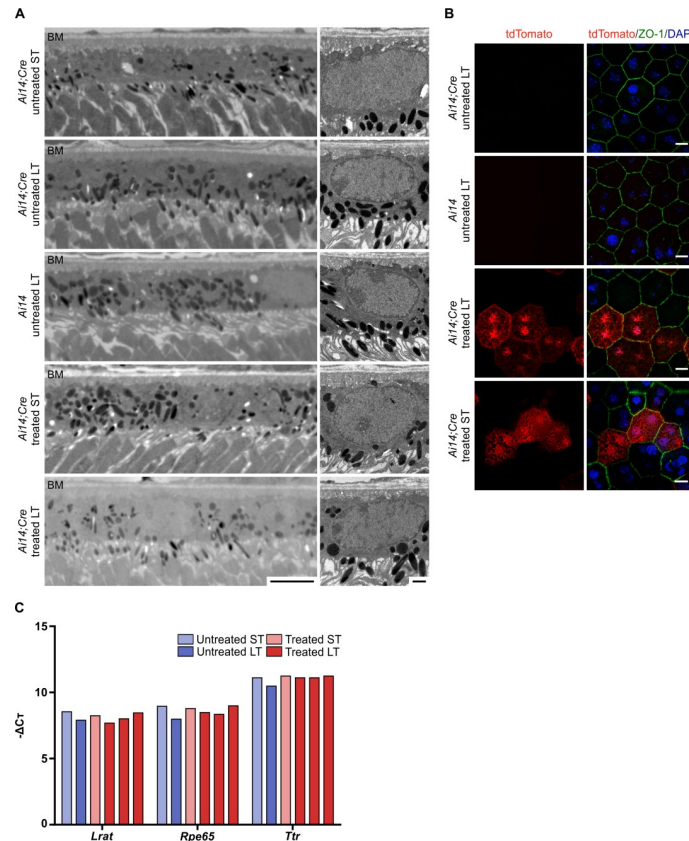


Fig 7. Analysis of the long-term effect of Cre activity on RPE cells of adult *Ai14;RPE-Tyrosinase-CreEr^{T2}* mice. A: Electron micrographs of adult RPE at lower (left) and higher magnification (right), showing no phenotypical abnormalities after short- and long-term Cre activity. B: Flatmount preparations of adult RPE after short-term and long-term Cre activity, showing no morphological changes in cells expressing TdTomato expression (red) and no expression in untreated mice. The tight junction-associated protein ZO-1 (green) was labeled to visualize the cell borders. C: qRT-PCR shows no difference in expression of mature RPE markers (*Lrat*, *Rpe65* and *Ttr*) relative to housekeeping gene (*Tbp*). *Ai14;Cre: Ai14;RPE-Tyrosinase-CreEr^{T2}*. ST: short-term effect of tamoxifen-treatment. LT: long-term effect of tamoxifen-treatment. BM: Bruch's membrane. Scale bars: (A) right: 5 μm, left: 1 μm, (B) 10 μm.

<https://doi.org/10.1371/journal.pone.0207222.g007>

untreated mice of the same age (Fig 7C). Furthermore, no difference in gene expression was observed between RPE tissues exposed to short- vs. long-term Cre activity.

Discussion

With its numerous functions, the RPE is unconditionally essential for the health and function of the retina and thereby for visual processes. Since RPE dysfunction is associated with retinal degeneration and blindness [2], it is essential to understand molecular development and function of the RPE. Currently available RPE Cre recombinases show lack of specificity or poor recombination. Therefore, we sought to generate an alternative. Here we show that our *RPE-Tyrosinase-CreEr^{T2}* transgenic mouse line will be a valuable tool for spatially and temporally controlled Cre activation in both, embryonic and adult mouse RPE.

Crossing our *RPE-Tyrosinase-CreEr^{T2}* transgenic mouse line with a reporter mouse line (*Ai14*) enabled us to evaluate the recombination efficiency and specificity. Embryo sections revealed a specificity for ocular tissues. As shown in the immunostained eye sections, activity of the *RPE-Tyrosinase-CreEr^{T2}* is mainly restricted to the RPE. Minimal ectopic expression was detected in the INL of the retina, where no cell type-specificity was observed. Also retina

flatmounts revealed that this level of ectopic expression is negligible. Additionally, relatively low expression was also observed in the pigmented cells of the ciliary body. Since the RPE extends into the pigmented parts of the ciliary body and iris during development [25], this finding was not unexpected. Importantly, analysis of the recombinant expression of tdTomato in the RPE revealed that Cre recombinase activity did not lead to any morphological changes in cell morphology, proving that Cre recombinase activity did not lead to cellular toxicity and thereby to pathological phenotypes of RPE cells. Flatmount preparations of a variety of control mice showed a high specificity of Cre recombinase activation. Cre recombinase was only activated upon tamoxifen-treatment, confirming that the observed red fluorescence was due to recombinant expression and not a preparation artefact.

Analysis of the recombinant expression of tdTomato in the RPE revealed between 47.25% and 69.48% recombination in adult mice and 83.0% recombination in embryonic mice. Nonetheless, a percentage of unaffected cells may serve as internal controls and thus be beneficial in some circumstances. The difference of recombinant expression in adults vs. embryos could reflect differential dosing in the target tissue. Furthermore, recombination in the embryos may be more efficient, and effective since the RPE is actively developing as opposed to an already differentiated adult eye. Other studies have also observed differences when treating female vs. male mice with tamoxifen [26,27]. Therefore, it was unsurprising, that our treatment also led to different recombination levels in female (49.35%) vs. male (69.48%) mice. This is most likely caused by differences in the homeostasis of sex hormones, e.g. estrogens, especially considering that tamoxifen is an estrogen antagonist. We showed that Cre-mediated recombination in the *RPE-Tyrosinase-CreEr^{T2}* mice led to uniform distributions of expression patterns throughout the RPE monolayer as can be seen on the RPE flatmounts. This was statistically verified and analysis of the local distribution found no differences in expression between dorsal/ventral/nasal/temporal regions. However, we do see a difference in expression levels between the central vs. peripheral regions of adult RPE. This might reflect regional differences in the level of *Tyrosinase* gene expression. Since we still do not achieve a fully penetrant recombination, this may lie in the induction via tamoxifen and inefficient excision of the floxed exons. Expression of the *Tyr-GFP* construct shows virtually complete coverage, suggesting that the chosen promoter targets most cells in the RPE.

Compared to the existing non-inducible RPE-specific *Cre* mouse lines, *Dct-Cre* [8], *Tyrp1-Cre* [9], *MART1-Cre* [14], and *BEST1-Cre* [4], our *RPE-Tyrosinase-CreEr^{T2}* line has the benefit that it is possible to start recombination in both, embryonic and postnatal stages and thereby adds a temporal dimension for establishing gene control of RPE development and function. Since the onset of expression in those lines is at set time points (E12.5, E10.5, E12.5, and P10, respectively) having the flexibility of choosing the onset of gene recombination in embryos, neonates and adult mice will be of interest for studying the role of gene function in both, development and adulthood [4,14]. Furthermore, all other existing lines show ectopic expression. For gene knockout of widely expressed genes, knockout in the telencephalon (*Dct-Cre*), the skin (*MART1-Cre*) or testis (*BEST1-Cre*), could result in unintended side effects [4,8,14]. More relevant may be the ectopic expression in the neuroretina when using the *Tyrp1-Cre* line, which might be problematic when analyzing retinal phenotypes caused by loss-of-function mutations in the RPE [9]. In this regard, our newly generated *Cre* line had minimal ectopic expression. The expression in the retina was negligible (below the limit of quantification), confined to the INL, and was not cell type specific. In contrast to the reported inducible RPE-specific *Cre* lines, *Mct3-Cre* [15] and *VMD2-Cre* [5], our *RPE-Tyrosinase-CreEr^{T2}* mice show a higher level of recombination and an earlier possible onset of expression since the other genes are expressed later in RPE development. The *Mct3-Cre* line exhibits relatively low levels of recombination in adults (5–20%), whereas the recombination level in

embryos was not reported [4,15]. The *VMD2-Cre* line shows the highest enzymatic activity at P4, whereas the level of recombination has not been reported so far [4,5].

Taken together, we generated a tamoxifen-inducible RPE-specific *Cre* transgenic mouse line, with high levels of uniformly distributed recombination in embryos and postnatal mice. This mouse line will serve as a valuable tool for those, who are interested in studying the functional role of gene expression in the RPE. This may ultimately be advantageous for development of new therapeutic targets to prevent RPE causative visual dysfunction.

Supporting information

S1 Fig. *Tyr-GFP* expression *in vivo*. Fluorescent image showing the high expression of GFP throughout an RPE flatmount of an adult *Tyr-GFP* mouse. Roman numerals and corresponding boxes indicate the regions which were taken for Fig 1B. Scale bar: 500 μ m.

(TIF)

S2 Fig. Absent Cre-mediated recombinant expression in control tissue. A: Representative image of an adult *Ai14;RPE-Tyrosinase-CreEr^{T2}* retina flatmount showing minimal tdTomato expression. Differential interference contrast (DIC) image was overlaid with the red fluorescent tdTomato expression image. B: Representative image of an adult *Ai14;RPE-Tyrosinase-CreEr^{T2}* RPE flatmount treated with β -Estradiol only. Outline of the RPE indicated by the solid line, dotted line represents inverted choroidal tissue. Scale bars: (A,B) 500 μ m.

(TIF)

S3 Fig. Cre-mediated ectopic expression in the retina is not cell type-specific. Representative immunofluorescence images of retina sections from treated adult *Ai14;RPE-Tyrosinase-CreEr^{T2}* mice, stained with antibodies against (A) Calbindin, (B) Calretinin, (C) PKC α , and (D) GS. Ectopic expression never co-localized with any of the inner retina specific markers. RPE: Retinal pigment epithelium, OS: Outer segments, IS: Inner segments, ONL: Outer nuclear layer, OPL: Outer plexiform layer, INL: Inner nuclear layer, IPL: Inner plexiform layer, GCL: Ganglion cell layer. PKC α : Protein kinase C α , GS: Glutamine synthetase. Scale bars: (A) 50 μ m, (B-D) 75 μ m.

(TIF)

S4 Fig. Validation montage image as generated by the analysis program. After microscopy, the raw image was processed using color correction, contrast adjustment, and the background was manually removed, resulting in the processed image. Using this image, the program measured first the total area in pixels and afterwards the fluorescent cells in pixels. On the far right panel, the images for total area and measured cells were merged.

(TIF)

S5 Fig. Representation of RPE locations used for regional comparisons. A: Example of RPE flatmount divided into dorsal (magenta) vs. ventral (cyan) and nasal (magenta) vs. temporal (cyan) areas. B: Example of RPE flatmount divided into central (cyan) vs. peripheral (magenta) areas.

(TIF)

Acknowledgments

The authors would like to thank Petra Gottlöber, Sophie Schröder and Viola Kretschmer for their technical assistance and intellectual input. They would also like to acknowledge the unwavering commitment of the animal care teams at the JGU, Mainz and the NEI, Bethesda

that made this research possible. Finally, they would also like to thank the NEI transgenic mouse core and histology core.

Author Contributions

Conceptualization: Sandra Schneider, Nathan Hotaling, Kapil Bharti, Helen Louise May-Simera.

Data curation: Sandra Schneider, Helen Louise May-Simera.

Formal analysis: Sandra Schneider, Nathan Hotaling, Helen Louise May-Simera.

Funding acquisition: Sarita Rani Patnaik, Kapil Bharti, Helen Louise May-Simera.

Investigation: Sandra Schneider, Helen Louise May-Simera.

Methodology: Sandra Schneider, Nathan Hotaling, Maria Campos, Sarita Rani Patnaik, Helen Louise May-Simera.

Resources: Kapil Bharti, Helen Louise May-Simera.

Software: Nathan Hotaling.

Supervision: Sarita Rani Patnaik, Kapil Bharti, Helen Louise May-Simera.

Validation: Nathan Hotaling.

Writing – original draft: Sandra Schneider, Helen Louise May-Simera.

Writing – review & editing: Nathan Hotaling, Kapil Bharti.

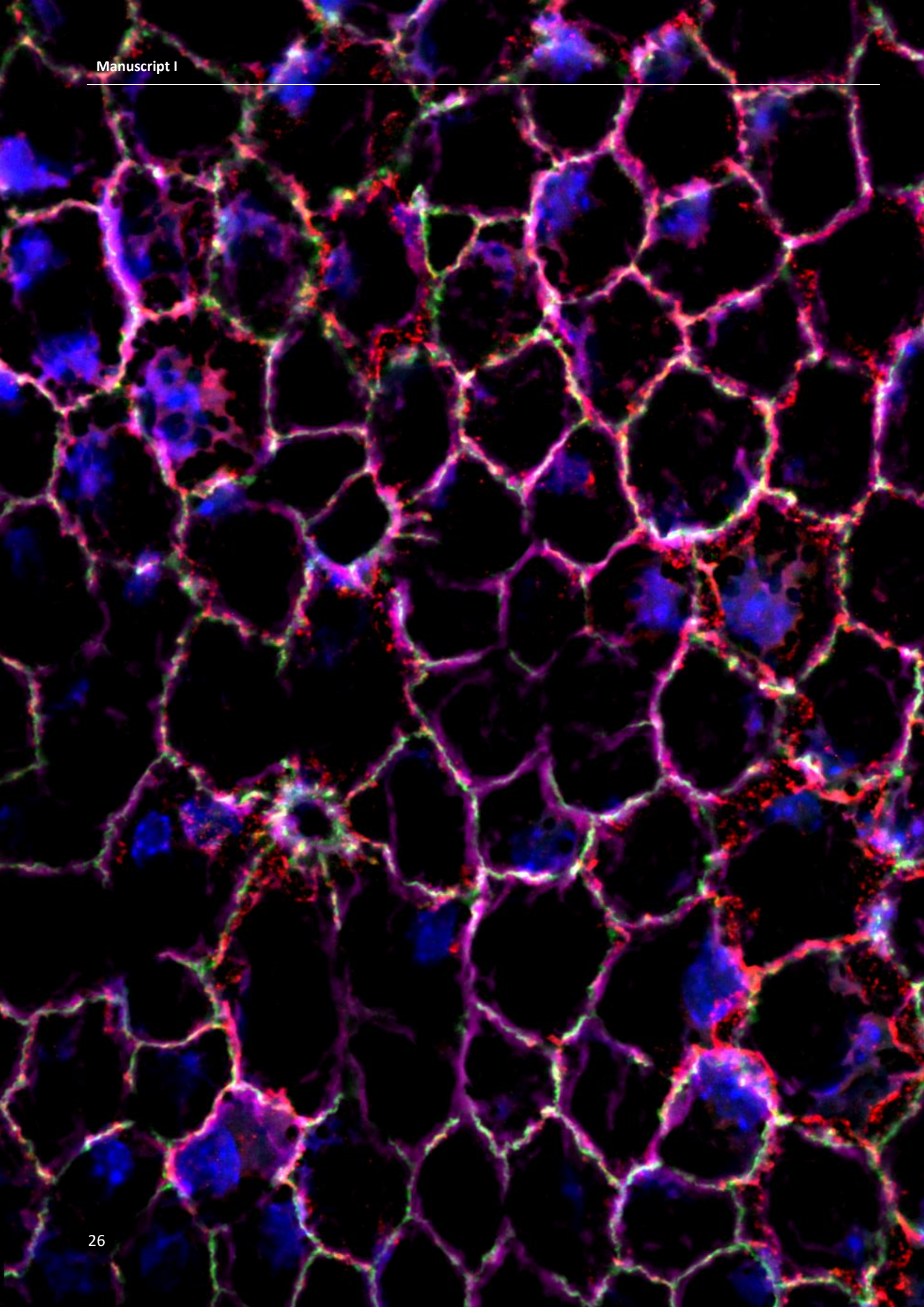
References

1. Willoughby CE, Ponzin D, Ferrari S, Lobo A, Landau K, Omid Y. Anatomy and physiology of the human eye: Effects of mucopolysaccharidoses disease on structure and function—a review. *Clin Exp Ophthalmol*. 2010; 38: 2–11. <https://doi.org/10.1111/j.1442-9071.2009.02223.x>
2. Strauss O. The Retinal Pigment Epithelium in Visual Function. *Physiol Rev*. 2005; 85: 845–881. <https://doi.org/10.1152/physrev.00021.2004> PMID: 15987797
3. Bharti K, Miller SS, Arnheiter H. The new paradigm: retinal pigment epithelium cells generated from embryonic or induced pluripotent stem cells. *Pigment Cell Melanoma Res*. 2011; 24: 21–34. <https://doi.org/10.1111/j.1755-148X.2010.00772.x> PMID: 20846177
4. Iacovelli J, Zhao C, Wolkow N, Veldman P, Gollomp K, Ojha P, et al. Generation of Cre transgenic mice with postnatal RPE-specific ocular expression. *Investig Ophthalmol Vis Sci*. 2011; 52: 1378–1383. <https://doi.org/10.1167/iovs.10-6347> PMID: 21212186
5. Le YZ, Zheng W, Rao PC, Zheng L, Anderson RE, Esumi N, et al. Inducible expression of Cre recombinase in the retinal pigmented epithelium. *Investig Ophthalmol Vis Sci*. 2008; 49: 1248–1253. <https://doi.org/10.1167/iovs.07-1105> PMID: 18326755
6. Feil S, Valtcheva N, Feil R. Inducible Cre Mice. In: Kühn R, Wurst W, editors. *Gene Knockout Protocols*. 2nd ed. Human Press; 2009. pp. 343–363. https://doi.org/10.1007/978-1-59745-471-1_18
7. Bosenberg M, Muthusamy V, Curley DP, Wang Z, Hobbs C, Nelson B, et al. Characterization of melanocyte-specific inducible Cre recombinase transgenic mice. *Genesis*. 2006; 44: 262–267. <https://doi.org/10.1002/dvg.20205> PMID: 16676322
8. Guyonneau L, Rossier A, Richard C, Hummler E, Beermann F. Expression of cre recombinase in pigment cells. *Pigment Cell Res*. 2002; 15: 305–309. <https://doi.org/10.1034/j.1600-0749.2002.02039.x> PMID: 12100497
9. Mori M, Metzger D, Garnier JM, Chambon P, Mark M. Site-specific somatic mutagenesis in the retinal pigment epithelium. *Investig Ophthalmol Vis Sci*. 2002; 43: 1384–1388.
10. Nagy A. Cre recombinase: The universal reagent for genome tailoring. *Genesis*. 2000; 26: 99–109. [https://doi.org/10.1002/\(SICI\)1526-968X\(200002\)26:2<99::AID-GENE1>3.0.CO;2-B](https://doi.org/10.1002/(SICI)1526-968X(200002)26:2<99::AID-GENE1>3.0.CO;2-B) PMID: 10686599

11. Feil R, Wagner J, Metzger D, Chambon P. Regulation of Cre recombinase activity by mutated estrogen receptor ligand-binding domains. *Biochem Biophys Res Commun*. 1997; 237: 752–757. <https://doi.org/10.1006/bbrc.1997.7124> PMID: 9299439
12. Saunders TL. Inducible Transgenic Mouse Models. In: Hofker MH, van Deursen JM, editors. *Transgenic Mouse Methods and Protocols*. 2nd ed. Human Press; 2011. pp. 103–115. https://doi.org/10.1007/978-1-60761-974-1_7
13. Ledbetter DJ, Thomson JG, Piedrahita JA, Rucker EB III. Gene Targeting in Embryonic Stem Cells, II: Conditional Technologies. In: Pinkert CA, editor. *Transgenic Animal Technology*. 3rd ed. Elsevier; 2014. pp. 141–165. Available: <http://linkinghub.elsevier.com/retrieve/pii/B9780124104907000220>
14. Aydin IT, Beermann F. A *mart-1::Cre* transgenic line induces recombination in melanocytes and retinal pigment epithelium. *Genesis*. 2011; 49: 403–409. <https://doi.org/10.1002/dvg.20725> PMID: 21309074
15. Longbottom R, Fruttiger M, Douglas RH, Martinez-Barbera JP, Greenwood J, Moss SE. Genetic ablation of retinal pigment epithelial cells reveals the adaptive response of the epithelium and impact on photoreceptors. *Proc Natl Acad Sci*. 2009; 106: 18728–18733. <https://doi.org/10.1073/pnas.0902593106> PMID: 19850870
16. Maruotti J, Sripathi SR, Bharti K, Fuller J, Wahlin KJ, Ranganathan V, et al. Small-molecule-directed, efficient generation of retinal pigment epithelium from human pluripotent stem cells. *Proc Natl Acad Sci*. 2015; 112: 10950–10955. <https://doi.org/10.1073/pnas.1422818112> PMID: 26269569
17. Murisier F, Guichard S, Beermann F. Distinct distal regulatory elements control tyrosinase expression in melanocytes and the retinal pigment epithelium. *Dev Biol*. 2007; 303: 838–847. <https://doi.org/10.1016/j.ydbio.2006.11.038> PMID: 17196956
18. Madisen L, Zwingman TA, Sunkin SM, Oh SW, Zariwala HA, Gu H, et al. A robust and high-throughput Cre reporting and characterization system for the whole mouse brain. *Nat Neurosci*. Nature Publishing Group; 2010; 13: 133–140. <https://doi.org/10.1038/nn.2467> PMID: 20023653
19. Overlack N, Kilic D, Bauß K, Märker T, Kremer H, van Wijk E, et al. Direct interaction of the Usher syndrome 1G protein SANS and myomegalin in the retina. *Biochim Biophys Acta—Mol Cell Res*. Elsevier B.V.; 2011; 1813: 1883–1892. <https://doi.org/10.1016/j.bbamcr.2011.05.015> PMID: 21767579
20. R Foundation for Statistical Computing. R: A language and environment for statistical computing. [Internet]. Vienna; 2017. Available: <https://www.r-project.org/>
21. Pinheiro J, Bates D, DebRoy S, Sarkar D, R Core Team. *nlme: Linear and Nonlinear Mixed Effects Models*. [Internet]. 2018. Available: <https://cran.r-project.org/package=nlme>
22. Hothorn T, Bretz F, Westfall P. Simultaneous inference in general parametric models. *Biometrical J*. 2008; 50: 346–363. <https://doi.org/10.1002/bimj.200810425> PMID: 18481363
23. Bharti K, Gasper M, Ou J, Brucato M, Clore-Gronenborn K, Pickel J, et al. A regulatory loop involving PAX6, MITF, and WNT signaling controls retinal pigment epithelium development. *PLoS Genet*. 2012; 8: 1–17. <https://doi.org/10.1371/journal.pgen.1002757> PMID: 22792072
24. Lizen B, Claus M, Jeannotte L, Rijji FM, Gofflot F. Perinatal induction of Cre recombination with tamoxifen. *Transgenic Res*. 2015; 24: 1065–1077. <https://doi.org/10.1007/s11248-015-9905-5> PMID: 26395370
25. Bharti K, Nguyen MTT, Skuntz S, Bertuzzi S, Arnheiter H. The other pigment cell: Specification and development of the pigmented epithelium of the vertebrate eye. *Pigment Cell Res*. 2006; 19: 380–394. <https://doi.org/10.1111/j.1600-0749.2006.00318.x> PMID: 16965267
26. Hemieda FAKES. Influence of gender on tamoxifen-induced biochemical changes in serum of rats. *Mol Cell Biochem*. 2007; 301: 137–142. <https://doi.org/10.1007/s11010-006-9405-2> PMID: 17279326
27. Dluzen DE, Mickley KR. Gender differences in modulatory effects of tamoxifen upon the nigrostriatal dopaminergic system. *Pharmacol Biochem Behav*. 2005; 80: 27–33. <https://doi.org/10.1016/j.pbb.2004.10.007> PMID: 15652377

Manuscript I – Ablation of primary cilia exclusively in the RPE leads to retinal degeneration and visual impairment in mice (Co-First Author; submitted)

In this publication, we show that ablation of primary cilia exclusively in the RPE results in a progressive ocular pathogenicity leading to visual impairment. For the first time, it could be demonstrated that cilia defects in the RPE, which precede retinal defects, contribute to retinal degeneration. This is caused by initially affecting RPE homeostasis and function, ultimately leading to photoreceptor degeneration and vision loss.



1 Ablation of primary cilia exclusively in the RPE leads 2 to retinal degeneration and visual impairment.

3 Viola Kretschmer^{1*}, Sandra Schneider^{1*}, Peter A. Matthiessen^{1#}, Dominik Reichert^{1,2#}, Nathan
4 Hotaling², Gunnar Glasßer³, Ingo Lieberwirth³, Kapil Bharti⁴, Rossella De Cegli⁵, Ivan Conte^{5,6},
5 Emeline F. Nandrot⁷, Helen L. May-Simera¹

6 ¹ Faculty of Biology, Institute of Molecular Physiology, Johannes Gutenberg-University, Mainz, Germany. ² National Center for Ad-
7 vancing Translational Sciences, National Institutes of Health, Bethesda, MD, United States. ³ Max Planck Institute for Polymer Re-
8 search, Mainz, Germany. ⁴ National Eye Institute, NIH, Bethesda, MD, USA. ⁵ Telethon Institute of Genetics and Medicine, Pozzuoli,
9 Italy. ⁶ University of Naples "Federico II", Naples, Italy. ⁷ INSERM, CNRS, Institut de la Vision, Sorbonne Université, Paris, France. *
10 Contributed Equally, # Contributed Equally

11

12 Abstract

13 Vision impairment places a serious burden on the aging society, affecting the lives of mil-
14 lions of people. Many retinal diseases are of genetic origin, of which over 50% are due to mutations
15 in cilia-associated genes. Most research on retinal degeneration has focused on the ciliated pho-
16 toreceptor cells of the retina. However, the contribution of primary cilia in other ocular cell types
17 has largely been ignored. The retinal pigment epithelium (RPE) is a monolayer epithelium at the
18 back of the eye intricately associated with photoreceptors and essential for visual function. It is
19 already known that primary cilia in the RPE are critical for its development and maturation, how-
20 ever whether this affects RPE function and retinal tissue homeostasis is unclear. By generating a
21 conditional knockout mouse model in which primary cilia were exclusively ablated in the RPE we
22 could for the first time show that cilia disruption in the RPE results in defective RPE function. This
23 results in photoreceptor degeneration and ultimately leads to vision impairment. Transcriptomic
24 analysis offers insights into mechanisms underlying pathogenic changes which include transcripts
25 related to epithelial homeostasis, the visual cycle and phagocytosis. This mouse model enables
26 us to tease out the functional role of cilia in the RPE and their contribution to retinal degeneration,
27 providing a powerful tool for basic and translational research in syndromic and non-syndromic
28 retinal degeneration. Our findings that cilia defects in the RPE precede and contribute to retinal
29 degeneration should be considered when designing treatment strategies for retinal degeneration.

30 Introduction

31 Vision loss affects more than 200 million people globally and with an aging population it is set to
32 increase exponentially. A multitude of retinal diseases responsible for vision loss are genetically
33 inherited, with 300 retinal disease-causing genes identified so far. Strikingly, at least 50% of these
34 genes encode cilia-associated genes. Primary cilia are microtubule-based sensory organelles
35 found on almost every eukaryotic cell type and are crucial for many developmental and physiolog-
36 ical processes. They are comprised of an axoneme, composed of nine microtubule doublets ex-
37 tending from the basal body, and a ciliary membrane, which is continuous with the cell membrane.
38 Due to an accumulation of receptors in the ciliary membrane, primary cilia coordinate several
39 signaling pathways such as Wnt, Hedgehog (Hh), and transforming growth factor- β (Tgf- β), all
40 indispensable for cell differentiation, organogenesis and tissue homeostasis (1–5).

41 Defects in primary cilia function or assembly are responsible for a wide range of diseases,
42 collectively termed ciliopathies. Retinal degeneration is one of the most common phenotypes as-
43 sociated with all syndromic ciliopathies. Furthermore, primary cilia dysfunction has been associ-
44 ated with a growing number of non-syndromic retinal dystrophies, such as retinitis pigmentosa
45 (RP) (2,6). In the vertebrate eye, primary cilia are present in a variety of different cell types (2). So
46 far, most research on retinal degeneration in ciliopathies has predominantly focused on the highly
47 specialized primary cilium of the retinal photoreceptor cell, which elaborates in a connecting cilium
48 followed by a sensory photoreceptor outer segment (POS), constituted of stacked membranous
49 discs enriched for components of the phototransduction machinery. However, the contribution of
50 defective primary cilia in other ocular cell types has not yet been comprehensively studied (2,7).

51 We have recently shown that primary cilia in the retinal pigment epithelium (RPE) are cru-
52 cial for its development and maturation. Furthermore, ciliary defects impair RPE functions that are
53 essential for photoreceptor health and activity (7,8). The RPE is a monolayer of pigmented epi-

54 thelial cells located between the neural retina and the choriocapillaris. With their long apical mi-
55 crovilli, RPE cells closely interact with photoreceptors in order to maintain visual function and en-
56 gulf the oxidized extremities of light-sensitive POS continuously (9–11). Due to its diverse roles,
57 the RPE is indispensable for health, maintenance, and function of the photoreceptor cells and,
58 therefore, for vision. RPE dysfunction can lead to retinal degeneration and blindness, and has
59 been associated with inherited rod-cone dystrophies and age-related macular degeneration
60 (AMD), the most common cause of irreversible blindness in the elderly population (10–13).

61 Whether ciliary dysfunction in the RPE disrupts RPE function, and how this might contrib-
62 ute to vision loss or retinal degeneration is not known. Therefore, we sought to generate a condi-
63 tional targeted ciliopathy in the RPE. To do this we analyzed a conditional *Intraflagellar transport*
64 *protein 20 homolog (Ift20)* knockout mouse model, in which primary cilia were exclusively ablated
65 in the RPE (14,15). The *Ift20* gene encodes an intraflagellar transport (IFT) protein essential for
66 assembly, maintenance, and function of primary cilia. Defects in IFT have been shown to impair
67 ciliogenesis (2,16,17) and loss of IFT20 is seen as a good model for loss of ciliary function.

68 Our data provide evidence that loss of primary cilia exclusively in the RPE results in phys-
69 iological defects affecting RPE homeostasis and function and demonstrates that disruption of this
70 process may contribute to aberrant retinal abnormalities. For the first time, we could show that
71 ciliary defects in the RPE can precede retinal degeneration and subsequent visual impairment.

72 **Results**

73 **Deletion of *Ift20* in the RPE ablates primary cilia in the RPE** 74 **without affecting retinal development**

75 In order to abolish primary cilia exclusively in the RPE, conditional *Ift20* knockout mice
76 (*Ift20^{null};Tyrp2-Cre*) were generated by crossing *Ift20^{fllox}* mice with a Tyrosinase-related protein-2
77 (*Tyrp2*)-Cre transgenic mouse line, in which Cre activity in the eye was observed from mouse

78 embryonic day E9.5 onwards (18). Consistent with the gradual *Tyrp2* expression in the developing
79 RPE at E11.5, Cre activity was observed mainly in the dorsal RPE with a ‘patchy’ activity in the
80 ventral RPE. At E13.5, most of the RPE cells showed Cre activity (14,15). This results in a re-
81 mediated deletion of exons 2 and 3, leading to the loss of the start codon and thus producing a null
82 allele for *Ift20* (15). Ablation of *Ift20* eliminates the complete ciliary structure since IFT20 assists
83 in the transport of ciliary membrane proteins from the Golgi complex to the cilium (17), essential
84 for assembly, maintenance and function of primary cilia (16,17).

85 To determine the efficiency of recombination, we stained RPE flatmounts of E16.5-old mice
86 for IFT20 and for the cis-Golgi matrix protein GM130 (**Figure 1a**) (17). Quantification, wherein only
87 cells positive for GM130 were considered, revealed that *Ift20^{null};Tyrp2-Cre* mice showed a signifi-
88 cant reduction in IFT20 expression in the RPE (5.3%) compared to controls (98.5%) (**Figure 1b**).
89 To determine whether this reduction of IFT20 expression in the RPE leads to a loss of cilia, we
90 identified primary cilia via co-localization of ciliary membrane marker ARL13b and transition zone
91 marker GT335 at E16.5 when RPE primary cilia are longest and most abundant (**Figure 1c**) (19).
92 Quantification confirmed a significant decrease in ciliation in *Ift20^{null};Tyrp2-Cre* RPE (total ciliation
93 = 12.5%) compared to controls (total ciliation = 84.3%) (**Figure 1d**).

94 Despite loss of primary cilia in the RPE, adjacent photoreceptor primary cilia and the retina
95 developed normally. Histological sections and transmission electron microscopy (TEM) of eye
96 sections from 1-month-old mice showed that deletion of *Ift20* specifically in the RPE does not
97 affect the development and maturation of the neural retina (**Figure 1e**). Furthermore, in
98 *Ift20^{null};Tyrp2-Cre* mice, we were able to observe fully matured photoreceptors, exhibiting a typical
99 photoreceptor primary cilium with a basal body, transition zone (connecting cilium) and axoneme,
100 extending into the outer segment (**Figure 1f,g**). To confirm that our Cre driver activity was re-
101 stricted to the RPE, we crossed the *Tyrp2-Cre* line with a tdTomato reporter mouse, namely Ai14.
102 This mouse line contains a floxed Stop cassette upstream of the gene for the red fluorescent

103 protein tdTomato (20), and only expresses tdTomato in cells with Cre activity. Fluorescent analysis
104 of ocular sections confirmed that *Tyrp2-Cre* activity was only found in the RPE (**Figure 1h**).

105 **Loss of primary cilia in the RPE results in defective RPE func-** 106 **tion**

107 To examine the functional effect of primary cilia loss exclusively in the RPE, we measured
108 the RPE response by direct current ERG (dcERG) in P25 mice (**Figure 2a-c**). In *Ift20^{null};Tyrp2-*
109 *Cre* mice we observed significant differences compared to control mice in the c-wave response (p
110 = 0.045). The c-wave mainly comes from sub retinal K^+ changes leading to K^+ signaling in the
111 RPE and reflects functional integrity of photoreceptors and RPE (21,22). We also observed a
112 significant difference in fast oscillation (FO, $p = 0.029$), which suggests delayed hyperpolarization
113 of the basolateral membrane of the RPE, probably as a delayed consequence of light-evoked
114 subretinal K^+ decrease that leads to a decreased potential across the RPE (effectively causing
115 the c-Wave) (**Figure 2b,c**) (23). Similarly, the Light Peak response (LP) was significantly reduced
116 in *Ift20^{null};Tyrp2-Cre* mice ($p = 0.0056$), indicating a possible defect in Cl^- channel activity, causing
117 depolarization of the basal membrane (24). The off-response (Off) showed a reduced trend, how-
118 ever, this was not statistically significant.

119 RPE-photoreceptor interaction was also examined by analysis of retinal adhesion between
120 RPE cells and adjacent photoreceptors. Normally, RPE apical microvilli form a functional connec-
121 tion between the RPE and POS (10,11). Melanin synthesized by the RPE can be found in the
122 apical processes that wrap around the photoreceptor outer segments of the retina. This makes it
123 a good marker for assessing the attachment of the RPE to the retina upon separation. We as-
124 sessed retinal adhesion in P16 and 3-month-old mice by quantifying the amount of melanin, found
125 in RPE-derived microvilli, attached to the retina after mechanical separation from the RPE (**Figure**
126 **2d**) (25). We observed a significantly reduced amount of melanin attached to the retina in
127 *Ift20^{null};Tyrp2-Cre* mice compared to control as early as P16, suggesting a decrease in retinal

128 adhesion (**Figure 2e**). At the age of P30, this reduction is even more pronounced. In contrast, the
129 melanin concentration in *Ift20^{+/+};Tyrp2-Cre* retinas remained stable between these two time points.

130 To determine whether the RPE from *Ift20^{null};Tyrp2-Cre* mice had a phagocytosis defect,
131 we cultured RPE cells from *Ift20^{null};Tyrp2-Cre* and *Ift20^{+/+};Tyrp2-Cre* mice and performed phago-
132 cytosis assays *in vitro* (26). After being exposed to POS, we found that mutant RPE cultures were
133 less able to phagocytose POS as compared to the control RPE (**Figure 2f,g**).

134 Combined, these results suggest that the loss of primary cilia in the RPE affected several
135 aspects of RPE function and homeostasis. To determine whether this was enough to influence
136 retinal health and visual function, we sought to further characterize the visual phenotype in
137 *Ift20^{null};Tyrp2-Cre* mice.

138 **Ablation of primary cilia exclusively in the RPE leads to visual** 139 **impairment in mice**

140 Despite changes in RPE functionality that were observed as early as P25, retinal health
141 as observed via electroretinogram (ERG), and visual function as measured via the optomotoric
142 reflex (OMR), was initially unaffected. ERG responses were measured under both scotopic (dark-
143 adapted, 10 cd.s/m²) and photopic (light-adapted, 100 cd s/m²) conditions over a period of 12
144 months (**Figure 3a-e**). Representative ERG traces of *Ift20^{null};Tyrp2-Cre* and *Ift20^{+/+};Tyrp2-Cre*
145 mice at 1 -month, 6 -months and 12 -months of age are shown in **Figure 3a**. In control mice, the
146 amplitudes for both the scotopic and photopic a-waves, which reflect photoreceptor responses,
147 and the scotopic and photopic b-waves that mirror the response of secondary neurons remained
148 constant over a period of 12 months. At 1-month of age no significant differences could be ob-
149 served between *Ift20^{null};Tyrp2-Cre* mice compared to controls. However, starting at 2-months of
150 age the amplitude of the scotopic a-wave was significantly lower at around -330μV and declined
151 to approximately 50% (~160μV) over the course of a year (**Figure 3b**). In agreement with our

152 observations, by the age of three months scotopic b-wave response in the mutants was also sig-
153 nificantly lower and declined to approximately 50% at 1-year of age (**Figure 3c**). Similarly, in pho-
154 topic conditions significant changes in a- and b-wave amplitudes compared to controls were ob-
155 served from 3-months of age onwards and declined by approximately 50% over the course of a
156 year (**Figure 3d,e**).

157 These findings were consistent with the morphology of the retinal layers as observed via
158 optical coherence tomography (OCT) (**Figure 3f,g,h**)(27). Highly significant changes in the thick-
159 ness of the retina in *Ift20^{null};Tyrp2-Cre* mice, compared to controls, were only observed from 6-
160 months of age. This was predominantly driven by the loss of photoreceptor cells, noticeable by a
161 significant reduction of the outer nuclear layer, consistently declining from the age of five months
162 onwards (**Figure 3h**, black significance levels). This was accompanied by thinning of the POS
163 layer, while inner segment thickness did not significantly decline until 10-months of age. Collec-
164 tively, these measurements show the subsequent reduction of outer retinal layers over time. De-
165 spite these changes, visual acuity did not seem to be affected as measured via the OMR. Visual
166 acuity thresholds remained stable at around 0.38 cyc/° in *Ift20^{null};Tyrp2-Cre*, as well as in control
167 *Ift20^{+/+};Tyrp2-Cre* (**Supplementary Figure 1**).

168 Combined, these data suggest a normally developing retina with relatively stable morphology and
169 function in the first 2-months of age, after which we observe a progressive retinal degeneration
170 and a decline in ERG responses, although global vision, as seen by the OMR response, remains
171 intact.

172 **Loss of primary cilia in the RPE leads to defective RPE ultra-**
173 **structure resulting in increased macrophage accumulation**
174 **over time.**

175 To gain insight into the mechanism underlying RPE dysfunction and corresponding retinal
176 degeneration, we examined RPE morphology more closely. Using histology and TEM, we ana-
177 lyzed the ultrastructure of the RPE and adjacent POS in 1- and 4-months-old mice (**Figure 4**). In
178 the mutant at 1-month of age, we observed an increased number of subretinal vacuoles, which
179 appeared to be membrane bound and filled with small particles (**Figure 4a,b**). Despite these struc-
180 tures occasionally being found in the control, they were more commonly observed in *Ift20^{null};Tyrp2-*
181 *Cre* RPE (**Figure 4c**) and had never been seen in preparations from ciliopathy mutant mice before.
182 Surprisingly, at 4-months of age vacuoles were no longer present.

183 In contrast, at 4-months of age, we observed numerous abnormalities in mutant RPE cells.
184 These include regions of multilayered cells (**Figure 4d top right panel**) and abnormal accumula-
185 tion of material, possibly detached microvilli or un-phagocytosed POS, in the subretinal space
186 (**Figure 4d bottom right panel**). Closer inspection revealed that the microvilli-like structures in
187 the mutant were often not as closely attached to the RPE and were less likely to engulf POS
188 compared to control. This observation is consistent with the loss of retinal adhesion as seen by
189 the retinal adhesion assay (**Figure 2d,e**) and suggests a defect in physiological processes. De-
190 spite seeing changes of the microvilli structures upon TEM, scanning electron microscopy (SEM)
191 at an earlier time point (**Supplementary Figure 2a**) did not show any differences. However, these
192 studies could only be done at P0, since the close association between the RPE and POS prohibits
193 a clean separation between the two tissues at later stages.

194 In an attempt to quantify these ultrastructural changes, we measured the thickness of the
195 RPE, the width of the Bruch's membrane, as well as the 'depth' of the microvilli (in terms of dis-
196 tance between the apical RPE membrane and end of the POS (**Figure 4e,f**). Although there was
197 no significant difference in RPE thickness between control and mutant at either of the two time
198 points measured (**Figure 4g**), the microvilli 'depth' was significantly increased at both stages (**Fig-**
199 **ure 4h**). The thickness of the Bruch's membrane was only slightly increased in the mutant at one

200 month of age (**Figure 4i**). We also noticed that the centered elastin layer of the Bruch's membrane
201 became increasingly discontinuous in the mutant (**Figure 4j**).

202 RPE cells from *Ift20^{null};Tyrp2-Cre* mice also displayed abnormal pigmentation at both time
203 points examined (**Supplementary Figure 2b**). Examples include two 'normal' RPE cells flanking
204 a cell almost completely devoid of melanosomes at 1-month of age. In addition, at 4-months of
205 age we observed an RPE cell that appeared devoid of melanosomes in the cell body, which was
206 flanked by an RPE cell with an excessive accumulation of melanosomes.

207 The increasing pathogenicity of the RPE in *Ift20^{null};Tyrp2-Cre* mice over time led us to
208 examine macrophage/microglia in the subretinal space in older mice (1-2 years). We fluorescently
209 labeled RPE flat mounts with the macrophage/microglia markers IBA1 and F4/80 (**Figure 5a**). We
210 imaged the entire RPE flat mount and quantified the number of macrophages per mm² (**Figure**
211 **5b**). Combining all ages reveals significantly more macrophages in *Ift20^{null};Tyrp2-Cre* animals
212 (**Figure 5c**). These findings were confirmed in a separate experiment with a different cohort of
213 mice (**Supplementary Figure 3**). Increased expression of these markers is a sign of elevated
214 inflammatory and degenerative processes as a result of and possible contributing to continued
215 pathogenesis.

216 Taken together with our previous data, it appears as if defects in RPE homeostasis and
217 physiological processes might underly RPE malfunction, ultimately affecting photoreceptors and
218 leading to their demise.

219

220 **Single-cell analysis of RPE flatmounts revealed minor** 221 **changes to cellular morphology**

222 To further probe the phenotype of *Ift20^{null};Tyrp2-Cre* mice we examined epithelial patterning at
223 P11, P29 and P90. For this we assessed changes in cellular morphology via high-content image
224 analysis of fluorescently labelled images of entire RPE flatmounts from both *Ift20^{+/+};Tyrp2-Cre* and

225 *Ift20^{null};Tyrrp2-Cre* mice at P11, P29 and P90. Each RPE flat mount was stained with phalloidin
226 and imaged in tiled panels at 20x magnification. Cell borders were recognized and segmented
227 using REShAPE, a machine learning based segmentation tool for RPE monolayer (28). The re-
228 sultant images outlining the cell borders were used to calculate cell morphometry for individual
229 RPE cell (**Figure 6a**). We analyzed four morphometric features, namely cell area, aspect ratio
230 (AR), number of neighbors and hexagonality, which have previously been shown to define the
231 compact packing of RPE cells and change in degenerating RPE cells (28).

232 Upon analysis of all cells across the whole flat mount, we observed a modest increase in cell size
233 in the mutant starting from P29 onwards (**Figure 6b,c**). This was accompanied by a small but
234 significant decrease in the aspect ratio at the same ages, which refers to the elongation of the
235 cells (**Figure 6c**). The number of neighbors and hexagonality score was not significantly different
236 at any stage (**Figure 6c**).

237 Despite seeing minor changes in cellular morphology by three months of age, this was not
238 accompanied by an increase in RPE cell death as measured by apoptotic markers Caspase 3 and
239 8 (**Figure 6d-f**). This suggests that the mild defects we see in epithelial patterning at this age is
240 not due to RPE cell loss.

241

242 **Transcriptomic analysis reveals maturation defects in mutant**

243 **RPE**

244 To further investigate the effect of primary cilia ablation specifically in the RPE, we per-
245 formed an unbiased RNA-seq analysis of RPE cells isolated from *Ift20^{null};Tyrrp2-Cre* and
246 *Ift20^{+/+};Tyrrp2-Cre* mice at P11, P29 and 3-months of age. At all three time-points we observed a
247 significant mis-regulation of the transcriptome compared to controls (**Figure 7**). More specifically,
248 at P11 we observed an up-regulation of 853 transcripts and a down-regulation of 724 transcripts.

249 At P29, we observed an up-regulation of 403 transcripts and a down-regulation of 300 transcripts.
250 At 3 months, we observed an up-regulation of 454 transcripts and a down-regulation of 145 tran-
251 scripts (**Figure 7a, Supplementary Table 1**). We compared the differentially expressed genes
252 (DEGs) with a list of RPE signature genes published in Strunnikova et al. (2010) (**Figure 7b,**
253 **Supplementary Table 2**). The number of differentially expressed RPE signature genes de-
254 creased as the tissue matured, however, across all ages more genes were down-regulated than
255 up-regulated compared to controls, suggesting a less robust RPE transcriptome (**Figure 7a**).

256 In an attempt to further determine the biological consequences of these differentially ex-
257 pressed transcripts, we performed a gene ontology enrichment analysis (GOEA), restricting the
258 output to biological process (BP) terms at each time point (**Figure 7c,d, Supplementary Table**
259 **3**). At P11, many of the down-regulated transcripts correlated with BPs associated with develop-
260 ment, differentiation, and maturation. These include 'epithelial cell proliferation', 'regulation of sig-
261 nal transduction' and 'regulation of multicellular organismal development'. At P29, we found more
262 changes in transcripts related to RPE function, with BPs including 'visual perception', 'ion trans-
263 membrane transport' and 'response to cAMP'. In contrast to P11, we found many more BPs up-
264 regulated than down-regulated at 3-months of age. Since the retina had begun to deteriorate by
265 this stage, many of these changes are likely to be secondary, as a consequence of a loss of
266 cellular homeostasis between RPE and PRs.

267 Although all three time points reflect different stages of RPE maturation and pathogenic
268 processes, it is still interesting to compare differentially expressed transcripts common across all
269 three data points as these might reflect possible underlying mechanisms (**Supplementary Table**
270 **4**): we identified 50 genes that were consistently up-regulated, whilst only 16 genes were consist-
271 ently down-regulated. Consistently down-regulated genes included *Rpe65*, a key component of
272 the visual cycle (10,11). More importantly, consistent with our morphological and functional data,
273 we observed that the expression of *Nog* (Noggin) was most strongly inhibited (refer to **Supple-**
274 **mentary Table 4**). *Nog* has been described as an anti-EMT (epithelial-to-mesenchymal transition)

275 gene, as its overexpression suppresses EMT (30–32). Moreover, the four most highly up-regu-
276 lated genes were all keratins (*Krt15*, *Krt4*, *Krt5* and *Krt6a*) (**Supplementary Table 4**). Mis-regula-
277 tion of keratins have been shown to contribute to EMT, of which specifically *Krt6a* overexpression
278 has been found to induce EMT in lung carcinoma (33). This data is in line with our previous findings
279 that loss of ciliary protein *Bbs8* in the RPE leads to a pathological phenotype involving EMT (8)
280 and is consistent with the increased aspect ratio of *Ift20^{null};Tyrrp2-Cre* RPE.

281 Furthermore, among the common DEGs we observed significant changes in DEGs asso-
282 ciated with epithelial characteristics (**Figure 8, Supplementary Table 5**). Genes that are associ-
283 ated with transmembrane transport (**Figure 8a**) were down-regulated in P29 *Ift20^{null};Tyrrp2-Cre*
284 RPE but up-regulated at 3 months of age. Furthermore, in P29 and 3 month-old *Ift20^{null};Tyrrp2-Cre*
285 RPE we found genes associated with cytoskeletal reorganization that are mis-regulated (**Figure**
286 **8b**), and genes that are associated with tissue remodeling, which were down-regulated (**Figure**
287 **8c**). These results show a switch in gene expression of genes associated with the epithelial char-
288 acteristics of the RPE.

289 Since many of our phenotypic findings had shown functional disruption, we specifically
290 identified differentially expressed transcripts associated with the visual cycle and phagocytosis
291 (**Figure 8d,e**). As already highlighted, *RPE65* a key component of the visual cycle was consist-
292 ently down regulated across all three ages. Furthermore, there was an increase in differential
293 regulation of other visual cycle transcripts as the tissue matures and ages. The opposite could be
294 said for transcripts associated with phagocytosis.

295 As a proof of concept, we validated RNA seq results via qPCR and Immunohistochemistry.
296 qPCR confirmed upregulation of *Mfge8* expression at P29 and immunohistochemistry showed a
297 reduction of RPE65 levels at 3 months.

298

299 Collectively, all these observations strongly suggest that the ablation of primary cilia exclusively
300 in the RPE results in a progressive ocular pathogenicity that leads to visual impairment. Loss of

301 primary cilia only in the RPE causes defects in RPE maturation and RPE function, both of which
302 ultimately affects photoreceptor health and cause their degeneration. Along with the progressive
303 demise of retinal photoreceptors, we could show that ERG responses in *Ift20^{null};Tyrp2-Cre* mice
304 declined, leading to visual impairments of those mice.

305 **Discussion**

306 Primary cilia dysfunction leads to a wide range of pathological phenotypes, collectively termed
307 ciliopathies, with retinal degeneration being one of the most common. Ciliary mutations do not
308 only cause syndromic retinal disorders, but they also underlie numerous non-syndromic retinal
309 dystrophies (<https://sph.uth.edu/Retnet/>). So far, most research on retinal ciliopathies has focused
310 on the highly specialized primary cilium of the photoreceptors, which undoubtedly contribute sig-
311 nificantly to disease progression. However, the contribution of dysfunctional primary cilia in other
312 ocular cell types has not yet been comprehensively studied (2,6,7).

313 We recently showed that loss of *Bbs8*, a gene encoding for a component of the “BBSome”,
314 which is required for ciliary trafficking, results in defects in RPE homeostasis and function (8).
315 Although it could be shown that defective cilia in the RPE affect RPE function, it must be consid-
316 ered that interaction with defective photoreceptors might be a leading driver to this effect. Thus,
317 distinguishing whether defects in the RPE precede or contribute to retinal defects is difficult. To
318 be able to delineate the mutual influence of these two tissues, we aimed at dissecting the role of
319 ciliary defects in the RPE by ablating primary cilia exclusively in the RPE for which we used an
320 RPE-specific *Ift20* conditional knockout mouse model (14,15).

321 Here, we demonstrate for the first time that loss of ciliation in the RPE leads to defects in
322 RPE homeostasis and functionality that ultimately lead to retinal degeneration along with visual
323 impairment. Importantly, adjacent retina was not affected since the morphology of the retina in
324 TEM sections looked comparable to control, and ERG function was not significantly altered until
325 2-months of age. This suggests that our Cre driver is not leaky and that any subsequent loss in

326 retinal function is a secondary consequence of disruption in the RPE. From the data we show, we
327 conclude that the RPE phenotype precedes photoreceptor degeneration, as can be seen by a
328 combination of ERG and OCT data. The RPE displays a significant phenotype (already evident at
329 1 month (Figure 2a-c)) much earlier on than the photoreceptors of the retina (becoming significant
330 from 3 month onwards- Figure 3 b,d,f-h (ONL-thickness)).

331 The choice of Cre driver is an important factor to consider. Many RPE-specific Cre drivers
332 are under the control of late RPE genes, which only become active once the RPE has matured.
333 However, since the cilium is expressed as early as E14.5 (7,19), we chose a Cre driver with early
334 RPE Cre activity starting at E11.5 (15). The majority of RPE cells retract their cilium post birth,
335 with only 5-10% remaining ciliated in adult (19). Since our Cre driver is already active during em-
336 bryonic development, we are not able to address the question of what these remaining ciliated
337 RPE cells are doing and how they might be contributing to RPE function post development. For
338 this we would need to use an inducible Cre driver to ablate ciliation only in the RPE at later time
339 points such as the *Tyrosinase-CreEr^{T2}* mouse line that we recently characterized (34). What we
340 could show here is that developmental defects in the RPE lead to it a pathological degeneration
341 which precedes retinal degeneration.

342 We decided to use the *Ift20* floxed mouse line to ensure that all aspects of ciliation would
343 be ablated. In addition to IFT, which is essential for trafficking along the ciliary axoneme, IFT20 is
344 also required for trafficking from the Golgi to the base of the cilium (17), thereby influencing very
345 early stages of ciliogenesis. In contrast, floxed *mouse* lines with many other *IFT* genes still retain
346 some residual ciliary machinery. It is also important to consider that ciliary proteins have also been
347 shown to exert non ciliary functions, disruptions of which likely contribute to a cellular phenotype
348 (35–38). By careful examination and comparison of different RPE-specific cilia mutants, one might
349 be able to tease out the role of the cilium vs. ciliary proteins in other cellular functions.

350 Of particular interest is the role of cilia in relation with the actin cytoskeleton. Ciliary signal-
351 ing and ciliary proteins regulate various aspects of actin dynamics (39). The RPE cannot be

352 viewed alone but as a functional unit closely associated with the POS. This interaction is mediated
353 via the actin-based apical processes, modified microvilli, extending from the RPE apical surface.
354 In our data we have seen numerous indications that this close connection is disrupted. We ob-
355 served changes in the retinal adhesion, decreased rates of phagocytosis, as well as structural
356 changes (vacuoles at 1-month of age and excess material at 3-months of age) in the subretinal
357 space (Figure 4a-f). The accumulated debris seen at 3-months of age might be excess microvilli-
358 like structures or possibly non-phagocytosed POS, both of which could be a consequence of dis-
359 rupted interaction between the RPE and retina. The question remains whether the dysfunctional
360 apical processes are a consequence of ciliary signaling and secondary cytoskeletal rearrange-
361 ments, or whether ciliary proteins have a direct effect on these actin networks. The modest
362 changes in RPE cellular morphology as seen via REShAPE analysis might also be a consequence
363 of cytoskeletal aberrations. Further examination of cellular morphology at later stages would be of
364 interest, however the older the tissue becomes the higher the likelihood of secondary conse-
365 quences due to retinal degeneration.

366 We were encouraged to see that the stimulus related response of the RPE reflected
367 by the different dcERG components was significantly reduced in our mutant mice as early as 1-
368 month of age, which indicates reduced or mal-function of the RPE. Light causes a hyperpolariza-
369 tion in the photoreceptors resulting in a reduction in subretinal K^+ . This leads to a hyperpolarization
370 in the RPE apical membrane and a decrease in intracellular K^+ as the RPE tries to compensate
371 the loss of K^+ in subretinal space. This leads to a delayed hyperpolarization of the basal mem-
372 brane. The RPE response is consequently not directly induced by light but reflects the responses
373 to photoreceptor light response (40). A decrease in the c-wave response suggests changes in
374 inward rectifying K^+ conductance. The positive c-wave, which peaks several seconds after the
375 light onset, consists of two underlying potentials, both involving inward rectifying K^+ conductance
376 (41–43). It is firstly comprised of a negative potential caused by the Müller cells and secondly of a
377 much larger positive potential caused by the apical membrane of the RPE when measured at the

378 cornea surface. Furthermore, a significant change in Fast Oscillation (FO) represents defects in
379 the delayed basolateral membrane hyperpolarization (44). The most significant change was ob-
380 served in the Light Peak (LP) response which represents the activities of Cl⁻ channels depolarizing
381 the basal membrane (24,45).

382 The transcriptomic data offers first insights into mechanisms underlying pathogenic
383 changes. Perhaps unsurprisingly, at the earliest time point examined (P11) many of the differen-
384 tially expressed transcripts were related to development, differentiation, and maturation. As the
385 tissue ages we found more changes in transcripts related to RPE function, which reflect an im-
386 paired apical membrane structure, possibly initiating EMT. There is mounting evidence that abla-
387 tion of primary cilia triggers EMT (46,47). Moreover, the association between loss of ciliation in
388 the RPE and EMT is in keeping with our previous findings in congenital *Bbs8* knockout mice, in
389 which we showed that loss of BBS8 induces EMT-like traits in the RPE and is consistent with
390 higher aspect ratio in mutant RPE cells (8). Our data, suggesting that lack of cilia might underly a
391 possible EMT phenotype which precedes and is possibly the cause of photoreceptor degenera-
392 tion, is in line with other recent findings that EMT in the RPE underlies retinal degeneration (48–
393 50). This might offer a valuable entry point into therapeutic interventions. Since these initial find-
394 ings had not been done in a conditional RPE-specific knockout, it had been difficult to attribute the
395 phenotype with ciliation in the RPE alone, yet our current findings support a direct link between
396 these two. Additional mouse models using alternative floxed drivers for various cilia related genes,
397 as well as different RPE-specific Cre drivers that ablate ciliary proteins at various time points in
398 RPE development and maturation, would be helpful to pinpoint more precise roles for cilia and
399 cilia proteins in all aspects of RPE biology.

400 It was also interesting to observe several differentially expressed transcripts associated
401 with the visual cycle and phagocytosis. Since we could see an increase in differential regulation
402 of visual cycle transcripts as the tissue matured it suggests a worsening phenotype over time.

403 Intriguingly, the opposite could be said for transcripts associated with phagocytosis. The reason
404 for this is as yet unclear and further proteomic examination of these targets is required. Since cilia
405 have also been shown to be involved in autophagy (51), we also looked for expression of autoph-
406 agy transcripts. Out of a curated list of 179 genes we found less and less differentially regulated
407 autophagy genes as the tissue matured (with just six at 3 months) (Supplementary Table 6). This
408 suggested that autophagy is less affected in these mutants and is in line with our TEM analysis in
409 which we did not observe any accumulation of autophagosomes and autophagolysosomes struc-
410 tures in the RPE.

411 In summary, we could demonstrate that loss of cilia in the RPE leads to a pathogenic
412 phenotype that has a significant impact on retinal degeneration leading to visual impairment. This
413 shows that cilia defects in the RPE precede and contribute to retinal degeneration, which must be
414 considered when designing treatment strategies for retinal degeneration. These findings are rele-
415 vant for both syndromic ciliopathy patients, as well as for patients suffering from non-syndromic
416 retinal degeneration as a consequence of mutations in ciliary genes.

417 **Materials and Methods**

418 **Animals**

419 All animal experiments had ethical approval from the Landesuntersuchungsamt Rhein-
420 land-Pfalz and were performed in accordance with the institutional guidance for care and use of
421 laboratory animals. Animal maintenance and handling was performed in line with Federation for
422 Laboratory Animal Science Associations (FELASA) recommendations. Mice were housed in a 12-
423 hr light/dark cycle. The morning after mating was considered as embryonic day (E) 0.5 and up to
424 24 hrs after birth was considered as postnatal day (P) 0. Animals were sacrificed by cervical dis-
425 location.

426 Mice with RPE-specific depletion of *Ift20* (*Ift20^{null};Tyrp2-Cre*) were generated by crossing *Ift20^{flox/flox}*
427 mice with *tyrosinase-related protein-2 (Tyrp2)-Cre* mice (14,15). *Ift20^{flox/flox}* mice possess LoxP
428 sites in introns 1 and 3. Crossing these mice with *Tyrp2-Cre* mice leads to deletion of exons 2 and
429 3 and creates the *Ift20^{null}* allele (14). Homozygous *Ift20^{null};Tyrp2-Cre* mice were viable after birth.
430 Genotyping for the *Ift20* alleles was done by PCR using following primers (14): (A) 5'-ACTCAG-
431 TATGCAGCC-CAGGT-3', (B) 5'-GCTAGATGCTGGGCGTAAAG-3'. To detect the *Cre* allele, fol-
432 lowing primers were used: (Cre-F) 5'-CAATGCTGTTTCACTGGTTATG-3', (Cre-R) 5'-CATT-
433 GCCCCTGTTTC-ACTACT-3'.

434 *B6.Cg-Gt(ROSA)26Sor^{tm14(CAG-tdTomato)Hze}/J* reporter mice (JAX stock #007914; (52) referred
435 to as *Ai14*) were crossed with *tyrosinase-related protein-2 (Tyrp2)-Cre* mice to visualize *Cre*
436 expression. *Ai14* mice possess a floxed stop cassette upstream of the CAG promoter-driven red
437 fluorescent protein tdTomato. Following Cre-mediated recombination the stop cassette is excised,
438 allowing expression of tdTomato.

439 **Antibodies**

440 For immunofluorescence, the following primary antibodies were used: anti-ARL13B (rb,
441 1:800, Proteintech, #17711-1-AP), anti-GM130 (mMAb, 1:100, BD Biosciences, #610822), anti-
442 GT335 (mMAb, 1:800, Adipogen, #AG-20B-0020), anti-IFT20 (53), anti-Iba1(rb, 1:100, FUJIFILM
443 Wako Pure Chemical Corporation, #019-19741) or anti-Iba1(1:300, Abcam, #ab153696), anti-
444 F4/80 [Cl:A3-1] (mMAb, 1:100 Abcam, #ab6640) or anti-F4/80 (1:150, AbD Serotec, #
445 MCA497GA). These antibodies were detected using the appropriate AlexaFluor (AF) -488-, and -
446 555-conjugated (1:400; Molecular Probes) secondary antibodies. Anti-Zonula Occludens-1 (ZO-
447 1) was directly conjugated with AF-488 (1:100, ZO-1-1A12, Invitrogen, 339188) and Phalloidin
448 was directly conjugated with AF-647 (1:40, Cell Signaling Technology, #8940).

449 **RPE flatmount preparation and immunohistochemistry**

450 Mice were sacrificed and the eyes were enucleated. Anterior segment, lens and retina
451 were removed, and eyecups were fixed with 4% paraformaldehyde (PFA) in 1× phosphate-buff-
452 ered saline (PBS) for 1 hr, followed by three washing steps with 1× PBS. To reduce PFA-induced
453 auto-fluorescence, eyecups were incubated with 50 mM NH₄Cl for 10 min, before permeabilizing
454 with 1× PBS 0.1% Tween-20 (PBST) with 0.3% Triton-X (TX) (PBST-TX) for 1 hr and blocking
455 with blocking buffer (0.1% ovalbumin, 0.5% fish gelatin in 1× PBS) for 1 hr. Following this, eyecups
456 were incubated with primary antibodies overnight at 4°C. Eyecups were washed three times with
457 1× PBS, followed by incubation with secondary antibodies, directly conjugated antibodies, and
458 DAPI (Carl Roth) for 2 hrs in dark conditions. Post staining, two washing steps with PBST-TX and
459 one with 1× PBS for 20 min each were performed, and eyecups were mounted with Fluoromount-
460 G (SouthernBiotech) and examined using a Leica DM6000 B microscope. Deconvolution
461 (BlindDeblur Algorithm, one iteration step) and maximum projection were performed using Leica
462 imaging software (Leica, Bensheim, Germany). Images were processed via Fiji using colour cor-
463 rection and contrast adjustment (54).

464 For Microglia/Macrophage analysis, RPE flatmounts were co-stained for IBA1 and F4/80
465 and scanned using the Zeiss Axioscan. IBA1 and F4/80 positive cells were manually counted
466 across the whole flatmount using ImageJ. Values are represented as mean of total cells counted
467 by three individuals.

468 **Cell morphology assessment**

469 RPE flatmounts were stained for F-actin or ZO-1 and scanned using the Zeiss Axios-
470 can. Cells were segmented using RESHAPE analysis, a machine learning based software previ-
471 ously published by Ortolan et al. 2022 (28). Data for cell size, aspect ratio (AR) and hexagonality
472 is displayed as Median ± SD, number of neighbors as Mean ± SD .

473 **Retinal adhesion assay**

474 Retinal adhesion assay was performed as described in Schneider et al. (2021).

475 **Transmission electron microscopy (TEM)**

476 Mouse eyes were fixed in 0.1 M cacodylate-buffered fixative containing 2.5% glutaralde-
477 hyde and 0.1 M sucrose for 1 hr at room temperature. After 10 min of fixation, the anterior segment
478 was removed. The eyecups were then postfixed in 2% osmium tetroxide (in 0.1 M cacodylate
479 buffer) for 1 hr at room temperature followed by dehydrating steps using a graded ethanol series
480 (30-100%). After embedding in epoxy resin, eyes were cut and processed for TEM using standard
481 EM procedures and analyzed using a FEI Tecnai 12 BioTwin transmission electron microscope.

482 **Scanning electron microscopy (SEM) of embryonic eyecups**

483 Pregnant dams were sacrificed, and the gravid uteri were removed and placed into 1× PBS
484 (room temperature). To expose the embryos, the uterine wall and fetal membranes were dissected
485 carefully in order not to harm the embryos. Following this, the embryos were sacrificed, and eye
486 dissection was performed in 1× Hank's balanced salt solution (HBSS) supplemented with 0.1 M
487 HEPES (HBSS-H). Anterior segment, lens and retina were removed, and eyecups were fixed with
488 HBSS-H containing 4% PFA, 2.5% glutaraldehyde and 10 mM CaCl₂ overnight at 4°C. Following
489 this, three washing steps with 1× PBS supplemented with 0.1 M HEPES (1× PBS-H) were per-
490 formed. The eyecups were then postfixed in 1% osmium tetroxide (in 1× PBS-H) for 1 hr at room
491 temperature, followed by three washing steps of 5 min each using distilled water. Next, dehydrat-
492 ing steps using a graded ethanol series (30-100%) were performed. Following dehydration, the
493 eyecups were dried using a critical point dryer (Bal-Tec CPD 030). Dried eyecups were mounted
494 carefully onto conductive carbon adhesive on top of SEM studs under a stereo microscope care-
495 fully using a fine brush and forceps, and sputter coated with gold (115 sec). Samples were stored
496 in a desiccator until microscopy.

497 **RPE cell isolation**

498 For RPE cell isolation was performed as described in Schneider et al. (2021). RPE
499 pellets were dissolved in 100 µL TRIzol Reagent (Invitrogen), snap-frozen in liquid nitrogen and
500 kept at -80°C.

501 **RNA isolation**

502 RPE cells were homogenized in TRIzol Reagent (Invitrogen) using a pestle and TRIzol
503 Reagent was added to a final volume of 500 µL. For RNA extraction, TRIzol Reagent was used
504 according to manufacturer's recommendations and RNA was stored at -80°C until usage.

505 **QuantSeq 3' mRNA sequencing library preparation**

506 Preparation of libraries, QuantSeq 3' mRNA sequencing data processing and analysis
507 were performed as described in Schneider et al. (2021).

508 **Data visualization**

509 Heatmaps (**Figure 6**) were generated using custom annotated scripts.

510 **Accession codes**

511 The whole set of results is available in the GEO database (GSE144724). The title of the series is
512 "Transcriptome profile of IFT20 Floxed mouse RPE cells all positive for DCT Cre".

513 **qPCR validation of QuantSeq 3' mRNA sequencing**

514 qPCR was performed as described in Schneider et al. (2021) using iTaq Universal SYBR
515 Green Supermix (Bio Rad, #1725121) on the QuantStudio™ 3 Real-Time PCR System.

516 Primers: Housekeeping Tbp_Fwd: TGTATCTACCGTGAATCTTGGC, Tbp_Rev:
517 CCAGAACTGAAAATCAACGCAG, Mfge8 F: AGACATGGAACCTGCGTG, Mfge8 R:
518 ATTCCTGTCACTTGCCTCTG.

519 **Primary mouse RPE cell culture**

520 RPE cells from 9- to 12-day-old animals were sequentially isolated as previously de-
521 scribed and adapted as described below (55). Briefly, eyecups without their lens were digested
522 for 45 min at 37°C with 1.5 mg/mL hyaluronidase (Sigma), and neural retina was gently peeled
523 from the eyecup. RPE sheets were peeled from the Bruch's membrane after a 45 min digestion
524 step at 37°C with 1 mg/mL trypsin (Invitrogen) and seeded into the wells of a 384-well plate after
525 a last trypsin digestion step. Cells were grown to confluence for 5 to 10 days in MEM α modification
526 (Sigma), supplemented with 5% fetal bovine serum (FBS, HyClone, GE Healthcare Life Sciences),
527 1% N1 medium supplement (Sigma), 0.5 mM glutamine, 1% non-essential amino acids (Gibco),
528 1% penicillin/streptomycin (Gibco), 250 mg/L taurine, 20 μ g/L hydrocortisone and 0.0130 μ g/L
529 triiodo-thyronin at 37°C, 5% CO₂ (56).

530 ***In vitro* phagocytosis assay**

531 POS were isolated from porcine eyes, obtained fresh from the slaughterhouse, and cova-
532 lently labelled with fluorescein isothiocyanate (FITC) dye (Invitrogen) for *in vitro* phagocytosis as-
533 says as previously described (26). Cultured primary mouse RPE cells were challenged with ap-
534 proximately 10 FITC-POS per cell for 1.5 hrs. Great care was taken to load the same amount of
535 POS in each well. For this 1.1x10E7 POS were resuspended into 300 μ L medium and 14 μ L (i.e.
536 5.13x10E5 POS/well) were applied in each well of a 384-well plate containing either control or
537 mutant RPE primary cells. Non-specifically tethered POS were removed with three thorough
538 washes in 1x PBS containing 1 mM MgCl₂ and 0.2 mM CaCl₂ (PBS-CM). Cells were fixed with
539 4% PFA, PFA was quenched with 50 mM NH₄Cl, and non-specific sites were blocked using 1%
540 BSA in PBS-CM. Tight junctions were labelled using an anti-ZO-1 antibody (rb, Invitrogen), fol-
541 lowed by an incubation with a mixture of the appropriate AF-594 secondary antibody and Phal-
542 loidin, directly conjugated with FluoProbes 647H (Interchim, #FP-BZ9630), to label the actin cyto-
543 skeleton. Nuclei were counter-stained with Hoechst 33258 (Invitrogen). FITC-POS and Hoechst-
544 labelled nuclei were quantified by fluorescence plate reading using the Morphology v9 plug-in to

545 identify nuclei and delimitate cell boundaries (HCS Studio Cell Analysis Software, Cellomics Ar-
546 rayscan VTI HCS reader, Thermo Scientific). Quantification: Cell junction markers were used to
547 delineate cell borders. When the labeling was not clear enough cells were not counted. POS were
548 counted per identified cells and ratios of numbers of POS/cell were calculated. This was performed
549 on three independent assays of 4-9 wells each, and significance was assessed with the Welch-
550 corrected parametric unpaired Student t-test ($P < 0.05$ *).

551 **Electroretinography (ERG)**

552 Full-field ERGs were recorded in mice at the age of 1 to 12 months. Mice were dark
553 adapted for >12 hrs. Mice were anesthetized by intraperitoneal (i.p.) injection of a ketamine
554 (87.5 mg/kg) / xylazine (12.5 mg/kg) cocktail and pupil dilator was applied (1% tropicamide/2.5%
555 phenylephrine). ERG responses of the outer retina were recorded on a full-field stimulator (Espion
556 E3 ColorDome; Diagnosys, LLC, Lowell, MA, USA) with a Gold electrode attached to the corneal
557 surface of both eyes referenced to needle electrodes (Diagnosys) between the ears and in the
558 tail. For electrical contact and corneal integrity, a drop of 2% methylcellulose was applied to each
559 eye. Mice were placed on a heating pad (37°C) under the ColorDome (Diagnosys) and subjected
560 to six steps of strobe flashes of increasing stimulus intensities (dark adapted: 0.0001, 0.001, 0.01,
561 0.1, 1 and 10 cd s/m²) followed by 2 min of light adaptation and flashes of 0.3, 1, 3, 10, 30, and
562 100 cd s/m², concluded by a 10-Hz flicker stimulus of 100 cd s/m². The a-wave was determined
563 by measuring the peak of the first negative wave. The b-wave was calculated from the trough of
564 the a-wave to the peak of the first positive wave or from baseline if no a-wave was present.

565 **Optical coherence tomography (OCT)**

566 OCT (Bioptigen, Research Triangle Park, NC, USA) was performed subsequent to full-field
567 ERG measurement in order to reduce burdens caused by anesthesia. The OCT image was cap-
568 tured using a rectangular volume scan (20 B-scan 1 frame). Images were imported as stacks in
569 ImageJ (National Institutes of Health, Bethesda, MD, USA). The StackReg plugin was used to

570 remove image distortion due to respiration of the animal (57). Slices were then merged using 'Z
571 project' and 'Sum Slices'. Retinal layers were measured manually 500 μm from the center of the
572 optic nerve (58). Data processing was done using Matlab. Statistical comparisons of *Ift20^{null};Tyrp2-*
573 *Cre* versus *Ift20^{+/+};Tyrp2-Cre* mice were done using the Holm-Sidak test (59,60) and statistical
574 comparison of P25 versus other ages was performed using the Dunnet's multiple comparison (61),
575 both followed with a One-way ANOVA (significance levels: > 0.05 not significant (ns), < 0.05 *, <
576 0.01 **, < 0.001 ***).

577 **Optomotor response (OMR)**

578 OMR was recorded using the quantitative OMR setup (qOMR, Phenosys, Berlin, Ger-
579 many), which allows for measurement and analysis of the behavior of freely moving mice. Vertical
580 stripes of 13 different spatial frequencies between 0.0125 and 0.5 cyc/deg were presented on a
581 rotating virtual sphere surrounding the animal. To keep the spatial frequency constant, the mouse
582 was video tracked to automatically maintain the distance between the animal and the virtual
583 sphere. Therefore, the perceived spatial frequency was maintained (62,63). Each stimulus was
584 presented for 60 sec. The automated tracking was used to quantitatively evaluate all experiments.
585 Stimulus-correlated head movements were determined and the ratio of movements within a ve-
586 locity range of 2 to 14 deg/s in the correct direction, divided by movements in the same range in
587 the incorrect direction, were calculated and defined as the OMR (OMRindex). Each set of stimuli
588 was presented three times in a pseudo-randomized order with resting time of a minimum of 1 hr
589 between trials. Data analysis was done using the quantitative OMR software and Matlab. To de-
590 termine the range of stimulus uncorrelated activity of all animals (baseline), we calculated the
591 interquartile interval for the OMR for all mice at 0.5 cyc/deg, a spatial frequency not perceivable
592 by the animals. (OMRindex, 1.15; **Supplementary Figure 2**, yellow areas) (64). Thus, the spatial
593 frequency threshold was calculated as the intersection of polynomial fit (third degree) with this
594 baseline interval.

595 **Direct-coupled electroretinography (DC-ERG)**

596 DC-ERGs were recorded in anesthetized (same conditions as in “Electroretinography”)
597 P25 mice using microelectrode holder half-cells (holder/pellet) (MEH34515, WPI) with borosilicate
598 glass capillary tubes OD: 1.5mm ID: 0.84mm (1B150F-3, WPI) filled with Hank’s buffered salt
599 solution (15266355, Gibco). Electrodes remained in direct contact with the cornea through 2 %
600 methylcellulose. Electric contact was monitored for 10 min prior to the recording to facilitate
601 steady-state conditions. Data was analyzed, smoothed using a moving average filter spanning
602 100 ms and displayed using Matlab (The MathWorks Inc., Natick, MA, USA). The linear drift was
603 corrected by subtracting the best fit line through the 300 ms preceding light onset. DC-ERG com-
604 ponents were then measured as follows: c-wave: maximum in the 500 ms after light onset, FO:
605 peak of c-wave to minimum in 1500 ms after stimulus onset, LP: Difference between FO and
606 response at stimulus offset (4500 ms), Off: minimum after stimulus offset. Statistical analysis was
607 done using the unpaired two-tailed t-test (significance levels: > 0.05 not significant (ns), < 0.05 *,
608 < 0.01 **, < 0.001 ***).

609 **Figure legends**

610 **Figure 1: Conditional knockout of *Ift20* ablates primary cilia in the RPE without affecting**
611 **other retinal layers. a.** Representative fluorescent images of E16.5 RPE flatmounts stained for
612 IFT20 (red) and cis-Golgi matrix protein GM130 (green). Staining for F-Actin (magenta) was used
613 to visualize the cytoskeleton, whereas DAPI was used to stain nuclear DNA. E16.5 *Ift20^{null};Tyrp2-*
614 *Cre* RPE showed less IFT20 staining compared to controls. Scale bars: 10 μ m. **b.** Quantification
615 of IFT20 positive cells in E16.5 RPE revealed that *Ift20^{null};Tyrp2-Cre* RPE showed near to no IFT20
616 staining (5.3%) compared to control (98.5%) confirming the knockout. Statistical analysis was
617 performed using ROUT test (Q = 0.1%) before using unpaired t-test (p < 0.001). **c.** Representative
618 fluorescent images of E16.5 RPE flatmounts stained for ARL13B (red) and GT335 (green) to

619 visualize primary cilia. Staining for F-Actin (magenta) was used to visualize the cytoskeleton, DAPI
620 to stain nuclear DNA. E16.5 *Ift20^{null};Tyrp2-Cre* RPE showed less ciliary staining compared to
621 controls. Scale bars: 10 μ m. **d.** Quantification of primary cilia in E16.5 RPE revealed that
622 *Ift20^{null};Tyrp2-Cre* RPE showed significantly less ciliated cells (12.5%) compared to controls
623 (84.3%). Statistical analysis was performed using ROUT test (Q = 0.1%) before using unpaired t-
624 test ($p < 0.001$). **e.** Representative images of histological eye sections from 1-month-old mice. In
625 both *Ift20^{null};Tyrp2-Cre* and control RPE, no differences in retinal layers could be observed. Scale
626 bar: 25 μ m. **f.** Representative image of a TEM image showing a morphological intact *Ift20^{null};Tyrp2-
627 Cre* photoreceptor cell displaying an intact photoreceptor primary cilium. Scale bar: 1 μ m. **g.**
628 Scheme showing a typical photoreceptor primary cilium. **h.** Representative retina cross section of
629 *Ift20^{null};Tyrp2-Cre* crossed with a tdTomato reporter mouse with F-Actin staining visualized by
630 Phalloidin staining (light blue) and DAPI for nuclei (blue). tdTomato expression (red) representing
631 Cre activity is detectable only in RPE. Scale bar: 20 μ m.

632 RPE: Retinal pigment epithelium, OS: Outer segments, IS: Inner segments, ONL: Outer nuclear
633 layer, OPL: Outer plexiform layer, INL: Inner nuclear layer, IPL: Inner plexiform layer, Ce: Centriole.
634 CC: Connecting cilium, Ax: Axoneme, TZ: Transition zone, BB: Basal body Significance levels: >
635 0.05 not significant (ns), < 0.05 *, < 0.01 **, < 0.001 ***.

636 **Figure 2: Ablation of primary cilia in the RPE affects RPE function.** **a.** Representative DC-
637 ERG trace showing all components of a DC-ERG response (c-wave, FO, LP, Off). **b.** Averaged
638 trace of DC-ERG response from P25 *Ift20^{null};Tyrp2-Cre* mice (red) versus *Ift20^{+/+};Tyrp2-Cre* mice
639 (black). Traces were drift-corrected and smoothed by a moving average filter (see Material and
640 Methods). Stimulus = 10 cd/cm^2 . **c.** Quantification of DC-ERG responses. Significant differences
641 were observed in c-wave ($p = 0.045$), FO ($p = 0.029$) and LP ($p = 0.0056$). The off-response
642 showed no significance ($p = 0.15$). Statistical analysis was performed using the unpaired two-
643 tailed *t*-test (n: *Ift20^{+/+};Tyrp2-Cre*, *Ift20^{null};Tyrp2-Cre* = 14 eyes, 8 mice). **d.** Schematic of

644 experimental procedure of Retinal Adhesion Assay. After enucleation and removal of the lense the
645 retina was separated from eyecup ripping of melanin containing apical microvilli. After lysis the
646 Melanin can be quantified. **e.** Quantification of melanin attached to the retina was significantly
647 increased in P16 *Ift20^{null};Tyrp2-Cre* compared to controls ($p < 0.05$). This effect increased over
648 time (3 months of age, $p < 0.001$). In contrast, the melanin concentration in *Ift20^{+/+};Tyrp2-Cre*
649 retinas remained stable between both ages ($p > 0.05$). **f.** Representative fluorescent images of *in*
650 *vitro* phagocytosis assay. Scale bar: 30 μm . **g.** *In vitro* phagocytosis assay. Quantification of POS
651 uptake revealed a significant decrease in POS phagocytosis ($p = 0.0025$) in isolated and cultured
652 *Ift20^{null};Tyrp2-Cre* RPE primary cells compared to controls. Statistical analysis was performed
653 using the Welch-corrected parametric unpaired t-test ($P < 0.05$).

654 POS: Photoreceptor outer segments, FO: fast oscillation, LP: light peak, Off: off-response.
655 Significance levels: > 0.05 not significant (ns), < 0.05 *, < 0.01 **, < 0.001 ***.

656 **Figure 3: Loss of primary cilia in the RPE affects visual function in mice.** **a.** Representative
657 traces of the electric responses upon light stimulation of photoreceptors and downstream cells of
658 *Ift20^{+/+};Tyrp2-Cre* (black) and *Ift20^{null};Tyrp2-Cre* (red) mice in photopic (100 cd s/m^2) and scotopic
659 (10 cd s/m^2) conditions. From 1-month of age until 12-months of age a degression of the
660 responses was seen. **b.** The scotopic a-wave of *Ift20^{null};Tyrp2-Cre* cones was significantly lower
661 compared to controls. Over the course of a year the scotopic a-wave declined to approximately
662 50%. **c.** By the age of 3-months, the scotopic b-wave response of the secondary neurons was
663 significantly lower in *Ift20^{null};Tyrp2-Cre* mice compared to controls. The scotopic b-wave also
664 declined to approximately 50% within one year. **d.** From 3-month of age, the photopic a-wave
665 response of *Ift20^{null};Tyrp2-Cre* cones was significantly lower and declined by approximately 50%
666 over the course of a year. **e.** From 3-month of age, the photopic b-wave response of *Ift20^{null};Tyrp2-*
667 *Cre* secondary neurons was significantly lower and declined by approximately 50% within one
668 year. Statistical analysis was performed using unpaired t-test. Significance levels: > 0.05 not

669 significant (ns), < 0.05*, < 0.01**, < 0.001***. **f.** Representative Images of *In vivo* OCT scans of
670 *Ift20^{null};Tyrp2-Cre* mice from 1 to 12 months compared to 1 month old *Ift20^{+/+};Tyrp2-Cre*. **g.** Retinal
671 thickness (RET), as well as outer nuclear layer (ONL) and photoreceptor inner (IS) and outer
672 segments (OS) were measured 500 μm off the center of the optic nerve. *Ift20^{null};Tyrp2-Cre* retina
673 thickness was reduced at 6-months of age and continuously declined until 12-months of age. **h.**
674 Quantification revealed that the RPE thickness in *Ift20^{null};Tyrp2-Cre* mice was significantly lower
675 already at 1-month of age and the subsequent reduction of the retina was accompanied by
676 thinning of the photoreceptor outer segments, while inner segment thickness did not significantly
677 decline until 10-months of age. Statistical analysis was performed using Holm-Sidak test
678 (*Ift20^{null};Tyrp2-Cre* versus *Ift20^{+/+};Tyrp2-Cre*) and Dunnet's multiple comparison (age comparison),
679 both followed by a One-way ANOVA. BM: Bruch's membrane, RPE: Retinal pigment epithelium,
680 OS: Outer segments, IS: Inner segments, OLM: outer limiting membrane, ONL: Outer nuclear
681 layer, OPL: Outer plexiform layer, INL: Inner nuclear layer, IPL: Inner plexiform layer, GCL:
682 Ganglion cell layer. Significance levels: > 0.05 not significant (ns), < 0.05*, < 0.01**, < 0.001***.

683 **Figure 4: Deletion of *Ift20* in the RPE results in defective RPE morphology.** **a.** H&E-stained
684 cross section through the mouse eyes reveals disrupted structures and vacuoles in the outer
685 layers of *Ift20^{null};Tyrp2-Cre* retinae compared to *Ift20^{+/+};Tyrp2-Cre*. **b.** Representative TEM images
686 of eye sections from 1-month-old mice showing subretinal vacuoles in *Ift20^{null};Tyrp2-Cre* mice.
687 Scale bars: top: 10 μm , I: 5 μm , II: 5 μm . **c.** Quantification of subretinal vacuoles revealed a total
688 of 13 vacuoles in *Ift20^{+/+};Tyrp2-Cre* mice and 113 subretinal vacuoles in *Ift20^{null};Tyrp2-Cre* mice.
689 In both, the same number of sections were examined (n: *Ift20^{+/+};Tyrp2-Cre*, *Ift20^{null};Tyrp2-Cre* = 9
690 sections, 4 eyes, 3 mice). **d.** Representative TEM images of eye sections from 4-month-old mice
691 showing multilayered RPE cells (top) as well as the absence of microilli and accumulation of debris
692 (bottom, red arrow) in *Ift20^{null};Tyrp2-Cre* mice. Scale bars: 10 μm . **e.** Measurements taken from
693 TEM images: Bruch's membrane, RPE thickness and Microvilli 'depth'. **f.** Representative TEM
694 images of eye sections showing vacuoles and disruptions in the Bruch's membrane in

695 *Ift20^{null};Tyrp2-Cre* mice at 1 months of age, while they appear less at 4 month. At 4 months defects
696 in pigmentation are showing. Scale bars: 10 μ m. **g.** Quantification of RPE thickness measured in
697 *Ift20^{+/+};Tyrp2-Cre* and *Ift20^{null};Tyrp2-Cre* reveals significant differences between 1 and 4 months,
698 but no differences between control and knockout. **h.** Quantification of microvilli 'depth' measured
699 in *Ift20^{+/+};Tyrp2-Cre* and *Ift20^{null};Tyrp2-Cre* shows highly significant differences between control
700 and knockout. **i.** Quantification of Bruch's membrane thickness measured in *Ift20^{+/+};Tyrp2-Cre*
701 and *Ift20^{null};Tyrp2-Cre* reveals only slightly increases in the mutant at one month of age. Statistical
702 analysis was performed using the unpaired two-tailed t-test (*Ift20^{+/+};Tyrp2-Cre* n= 96)
703 *Ift20^{null};Tyrp2-Cre* n= 120). Significance levels: > 0.05 not significant (ns), < 0.05 *, < 0.01 **, <
704 0.001 ***. **j.** Representative TEM images of eye sections from 1-month-old mice showing a
705 discontinuous and malformed Bruch's membrane at *Ift20^{null};Tyrp2-Cre* RPE cells. Scale bar: 2 μ m.

706 **Figure 5: Analysis of morphology by Reshape analysis of RPE flatmounts.** **a.** *Ift20^{+/+};Tyrp2-*
707 *Cre* and *Ift20^{null};Tyrp2-Cre* RPE flatmounts stained with Phalloidin (red), Cell borders were
708 automatically analysed, segmented and visualized by Color-Coded Images. **b.** Representative
709 images showing Phalloidin staining (red) at P11, P29 and P90 of *Ift20^{+/+};Tyrp2-Cre* and
710 *Ift20^{null};Tyrp2-Cre* RPE flatmounts. Scale bar: 20 μ m. **c.** Quantification of the cell size, aspect ratio
711 (AR), number of neighbors and hexagonality *Ift20^{+/+};Tyrp2-Cre* and *Ift20^{null};Tyrp2-Cre* RPE
712 flatmounts. Analysis of Cell size reveals a modest increase in cell size in the mutant starting from
713 P29 onwards while aspect ratio was decreasing. No changes were detected in number of
714 neighbors and hexagonality. **d+e.** Analysis of Apoptosis markers Caspase-3 (**d**) and Caspase-8
715 (**e**) revealed no significant difference between *Ift20^{+/+};Tyrp2-Cre* and *Ift20^{null};Tyrp2-Cre* at 3
716 months although there seems to be slightly higher levels of Caspase-3 in *Ift20^{null};Tyrp2-Cre*. Scale
717 bar: 10 μ m.

718 **Figure 6: Macrophages in RPE flatmount.** **a.** Representative images of RPE flatmounts of
719 *Ift20^{+/+};Tyrp2-Cre* and *Ift20^{null};Tyrp2-Cre* at 24 months. Macrophages were stained by markers

720 IBA1 (green) and F4/80 (red). **b.** Quantification of macrophage numbers per mm² separated by
721 age. **c.** Combining all ages reveals significantly more macrophages in *Ift20^{null};Tyrp2-Cre*. Statistical
722 analysis was performed using the unpaired two-tailed t-test (*Ift20^{+/+};Tyrp2-Cre* n= 10,
723 *Ift20^{null};Tyrp2-Cre* n= 10). Significance levels: > 0.05 not significant (ns), < 0.05 *, < 0.01 **, <
724 0.001 ***. Scale bar: 20µm

725 **Figure 7: Deletion of *Ift20* in the RPE leads to changes in RPE-specific gene expression. a.**
726 Bar chart showing differentially expressed genes (DEGs) obtained via transcriptomic analysis. The
727 number of specific and common DEGs and the orientation of expression are shown. **b.** Bar chart
728 depicting the number up- and down-regulated genes for RPE signature genes. At all ages, the
729 number of differentially expressed RPE signature genes decreased, however, across all ages
730 more genes were down-regulated than up-regulated compared to controls. **c.** Identification of the
731 biological processes underlying the effect of the deletion of *Ift20* via gene ontology analysis. The
732 top 10 down-regulated significant biological processes (BPs) in *Ift20^{null};Tyrp2-Cre* vs.
733 *Ift20^{+/+};Tyrp2-Cre* are shown. The Enrichment score for each BP cluster is plotted on the x-axis. **d.**
734 Identification of the biological processes underlying the effect of the deletion of *Ift20* via gene
735 ontology analysis. The top 10 up-regulated significant biological processes (BPs) in *Ift20^{null};Tyrp2-*
736 *Cre* vs. *Ift20^{+/+};Tyrp2-Cre* are shown. The Enrichment score for each BP cluster is plotted on the
737 x-axis.

738 **Figure 8: GOEA of commonly regulated DEGs from in *Ift20^{null};Tyrp2-Cre* RPE.** Heatmaps
739 showing DEGs associated with transmembrane transport (**a.**), cytoskeleton organization (**b.**) and
740 tissue remodeling (**c.**). **d.** Table of up- (green) and downregulated (red) visual cycle associated
741 RNA in P11, P29 and P90 RPE in *Ift20^{null};Tyrp2-Cre* compared to *Ift20^{+/+};Tyrp2-Cre*. **e.** Table of up-
742 (green) and downregulated (red) phagocytosis associated RNA in P11, P29 and P90 RPE in
743 *Ift20^{null};Tyrp2-Cre* compared to *Ift20^{+/+};Tyrp2-Cre*. **f:** Validation of RNA levels by qPCR of P29
744 *Ift20^{null};Tyrp2-Cre* vs *Ift20^{+/+};Tyrp2-Cre* RPE (red line). Data confirms upregulation of *Mfge8*

745 upregulated. **g.** Western blot analysis of 3months old *Ift20^{null};Tyrp2-Cre* RPE lysate with RPE65-
746 staining confirms reduced RPE65 levels in mutant compared to control. Scale bars= 20µm

747 **Supplementary Figure 1: Loss of primary cilia in the RPE does not affect the optomotoric**
748 **reflex in mice.** Optomotor response curves of *Ift20^{+/+};Tyrp2-Cre* and *Ift20^{null};Tyrp2-Cre* mice.
749 Single measurements (purple dots) show a normal flicker. Visual acuity thresholds remained
750 stable at around 0.38 cyc/° (dashed line, spatial frequency threshold) in both, *Ift20^{+/+};Tyrp2-Cre*
751 and *Ift20^{null};Tyrp2-Cre* mice over the time of 12 months.

752 **Supplementary Figure 2: Deletion of *Ift20* in the RPE does not affect apical microvilli in P0**
753 **mice. a.** Representative SEM images of P0 RPE flatmounts. No differences in microvilli
754 morphology were observed between P0 *Ift20^{null};Tyrp2-Cre* and *Ift20^{+/+}Tyrp2-Cre* RPE. Scale bar:
755 5 µm. **b.** Representative TEM images of *Ift20^{null};Tyrp2-Cre* show abnormal pigmentation at one
756 month and 4 months. Two pigmented RPE cells flank a cell almost completely devoid of
757 melanosomes at one month. At 4-months of age we observed an RPE cell that appeared devoid
758 of melanosomes in the cell body, which was flanked by an RPE cell with an excessive
759 accumulation of melanosomes. Scale bar = 10 µm.

760 **Supplementary Figure 3: Macrophages in RPE flatmount. a.** Representative images of RPE
761 flatmounts of *Ift20^{+/+};Tyrp2-Cre* and *Ift20^{null};Tyrp2-Cre* at 22 and 24 months. Macrophages were
762 stained by markers IBA1 (green) and F4/80 (red). **b.** Quantification of macrophage numbers per
763 mm² separated by age shows a trend towards more macrophages in *Ift20^{null};Tyrp2-Cre*.

764 **Supplementary Figure 4: a.** Specificity of the amplified product was determined by the analysis
765 of the melt curves and amplification plots. **b.** Visualization of amplification product via Agarose gel
766 electrophoresis shows clear bands at the expected size for *Mfge8* and *Tbp* and no signal in control
767 samples (H₂O).

768 **Acknowledgments**

769 The authors wish to thank Petra Gottlöber and Elisabeth Sehn for their technical assistance. The
770 authors would also like to thank A. Potey from the high-throughput screening platform of the Institut
771 de la Vision (Paris) for her technical assistance in phagocytosis assays quantification. Finally, the
772 authors are grateful to Diego Carrella (TIGEM Bioinformatics Core) for Heatmaps generation. The
773 authors would also like to acknowledge their funding sources, the Alexander von Humboldt Foun-
774 dation, the Deutsche Forschungsgemeinschaft SPP2127 (DFG Grant MA 6139/3-1) and the
775 Studienstiftung des Deutschen Volkes.

776 Author Contributions: S.S., V.K. N.H., I.C., E.N., and H.L.M-S., designed the study; V.K.,S.S.,
777 P.A.M., D.R., G G., I.L. R.D.C, acquired the data; I.C. and R.D.C.analyzed and interpreted the
778 RNA sequencing data; V.K., S.S., P.A.M., D.R. and E.N. analysed and interpreted the remaining
779 data. S.S., H.L.M-S. and V.K. wrote and/or revised the manuscript.

780 **References**

- 781 1. May-Simera HL, Kelley MW. Cilia, Wnt signaling, and the cytoskeleton. *Cilia*. 2012;1(1):7.
- 782 2. May-Simera H, Nagel-Wolfrum K, Wolfrum U. Cilia - The sensory antennae in the eye.
783 *Prog Retin Eye Res*. 2017;60:144–80.
- 784 3. Ishikawa H, Marshall WF. Ciliogenesis: building the cell's antenna. *Nat Rev Mol Cell Biol*.
785 2011;12(4):222–34.
- 786 4. Pala R, Alomari N, Nauli SM. Primary cilium-dependent signaling mechanisms. *Int J Mol*
787 *Sci*. 2017;18(11).
- 788 5. Fliegau M, Benzing T, Omran H. When cilia go bad: cilia defects and ciliopathies. *Nat*
789 *Rev Mol Cell Biol*. 2007;8(11):880–93.

- 790 6. Waters AM, Beales PL. Ciliopathies: An expanding disease spectrum. *Pediatric Nephrol-*
791 *ogy*. 2011;26(7):1039–56.
- 792 7. May-Simera HL, Wan Q, Jha BS, Hartford J, Khristov V, Dejene R, et al. Primary Cilium
793 Mediated Retinal Pigment Epithelium Maturation is Retarded in Ciliopathy Patient Cells.
794 *CellReports*. 2018;22(1).
- 795 8. Schneider S, De Cegli R, Nagarajan J, Kretschmer V, Matthiessen PA, Intartaglia D, et al.
796 Loss of Ciliary Gene *Bbs8* Results in Physiological Defects in the Retinal Pigment Epithe-
797 lium. *Front Cell Dev Biol*. 2021;9(February):1–20.
- 798 9. Willoughby CE, Ponzin D, Ferrari S, Lobo A, Landau K, Omid Y. Anatomy and physiology
799 of the human eye: Effects of mucopolysaccharidoses disease on structure and function -
800 a review. *Clin Exp Ophthalmol*. 2010;38(SUPPL. 1):2–11.
- 801 10. Strauss O. The Retinal Pigment Epithelium in Visual Function. *Physiol Rev*. 2005;85:845–
802 81.
- 803 11. Lakkaraju A, Umopathy A, Tan LX, Daniele L, Philp NJ, Boesze-Battaglia K, et al. The cell
804 biology of the retinal pigment epithelium. *Prog Retin Eye Res*. 2020;78(February):100846.
- 805 12. Bharti K, Miller SS, Arnheiter H. The new paradigm: retinal pigment epithelium cells gen-
806 erated from embryonic or induced pluripotent stem cells. *Pigment Cell Melanoma Res*.
807 2011;24(1):21–34.
- 808 13. Chen Y, Yang J, Geng H, Li L, Li J, Cheng B, et al. Photoreceptor degeneration in mi-
809 crophthalmia (*Mitf*) mice: Partial rescue by pigment epithelium-derived factor. *DMM Dis-*
810 *ease Models and Mechanisms*. 2019;12(1).
- 811 14. Jonassen JA, Agustin JS, Follit JA, Pazour GJ. Deletion of *IFT20* in the mouse kidney
812 causes misorientation of the mitotic spindle and cystic kidney disease. *Journal of Cell Bi-*
813 *ology*. 2008;183(3):377–84.

- 814 15. Davis N, Yoffe C, Raviv S, Antes R, Berger J, Holzmann S, et al. Pax6 dosage require-
815 ments in iris and ciliary body differentiation. *Dev Biol.* 2009;333(1):132–42.
- 816 16. Hao L, Scholey JM. Intraflagellar transport at a glance. *J Cell Sci.* 2009;122(7):889–92.
- 817 17. Follit JA, Tuft RA, Fogarty KE, Pazour GJ. The Intraflagellar Transport Protein IFT20 Is
818 Associated with the Golgi Complex and Is Required for Cilia Assembly. Margolis B, editor.
819 *Mol Biol Cell.* 2006 Sep;17(9):3781–92.
- 820 18. Davis N, Yoffe C, Raviv S, Antes R, Berger J, Holzmann S, et al. Pax6 dosage require-
821 ments in iris and ciliary body differentiation. *Dev Biol.* 2009;333(1):132–42.
- 822 19. Patnaik SR, Kretschmer V, Brücker L, Schneider S, Volz AK, Oancea-Castillo L del R, et
823 al. Bardet–Biedl Syndrome proteins regulate cilia disassembly during tissue maturation.
824 *Cellular and Molecular Life Sciences.* 2019 Feb 16;76(4):757–75.
- 825 20. Madisen L, Zwingman TA, Sunkin SM, Oh SW, Zariwala HA, Gu H, et al. A robust and
826 high-throughput Cre reporting and characterization system for the whole mouse brain. *Nat*
827 *Neurosci [Internet].* 2010 Jan 17 [cited 2022 Apr 24];13(1):133–40. Available from:
828 <https://pubmed.ncbi.nlm.nih.gov/20023653/>
- 829 21. Yu M, Peachey NS. Use of Direct Current Electroretinography for Analysis of Retinal Pig-
830 ment Epithelium Function in Mouse Models. *Methods Mol Biol [Internet].* 2018 [cited 2022
831 Oct 26];1753:103–13. Available from: <https://pubmed.ncbi.nlm.nih.gov/29564784/>
- 832 22. Wu J, Peachey NS, Marmorstein AD. Light-evoked responses of the mouse retinal pig-
833 ment epithelium. *J Neurophysiol [Internet].* 2004 Mar [cited 2022 Oct 26];91(3):1134–42.
834 Available from: <https://pubmed.ncbi.nlm.nih.gov/14614107/>
- 835 23. Griff ER, Linsenmeier RA, Steinberg RH. The Cellular Origin of the Fast Oscillation. In
836 1983. p. 13–20.

- 837 24. Gallemore RP, Steinberg RH. Light-evoked modulation of basolateral membrane Cl⁻ con-
838 ductance in chick retinal pigment epithelium: The light peak and fast oscillation. *J*
839 *Neurophysiol.* 1993;70(4):1669–80.
- 840 25. Nandrot EF, Anand M, Sircar M, Finnemann SC. Novel role for $\alpha\beta 5$ -integrin in retinal ad-
841 hesion and its diurnal peak. *Am J Physiol Cell Physiol.* 2006;290(4):1256–62.
- 842 26. Parinot C, Rieu Q, Chatagnon J, Finnemann SC, Nandrot EF. Large-scale purification of
843 porcine or bovine photoreceptor outer segments for phagocytosis assays on retinal pig-
844 ment epithelial cells. *Journal of Visualized Experiments.* 2014;(94):1–8.
- 845 27. Berger A, Cavallero S, Dominguez E, Barbe P, Simonutti M, Sahel JA, et al. Spectral-do-
846 main optical coherence tomography of the rodent eye: highlighting layers of the outer ret-
847 ina using signal averaging and comparison with histology. *PLoS One* [Internet]. 2014 May
848 2 [cited 2022 Oct 26];9(5). Available from: <https://pubmed.ncbi.nlm.nih.gov/24788712/>
- 849 28. Ortolan D, Sharma R, Volkov A, Maminishkis A, Hotaling NA, Hury LA, et al. Single-cell-
850 resolution map of human retinal pigment epithelium helps discover subpopulations with
851 differential disease sensitivity. *Proc Natl Acad Sci U S A* [Internet]. 2022 May 10 [cited
852 2022 Oct 26];119(19). Available from: <https://pubmed.ncbi.nlm.nih.gov/35522714/>
- 853 29. Strunnikova N V., Maminishkis A, Barb JJ, Wang F, Zhi C, Sergeev Y, et al. Transcrip-
854 tome analysis and molecular signature of human retinal pigment epithelium. *Hum Mol*
855 *Genet.* 2010;19(12):2468–86.
- 856 30. Choi S, Yu J, Park A, Dubon MJ, Do J, Kim Y, et al. BMP-4 enhances epithelial mesen-
857 chymal transition and cancer stem cell properties of breast cancer cells via Notch signal-
858 ing. *Sci Rep.* 2019;9(1):1–14.

- 859 31. Kim BR, Oh SC, Lee DH, Kim JL, Lee SY, Kang MH, et al. BMP-2 induces motility and
860 invasiveness by promoting colon cancer stemness through STAT3 activation. *Tumor Biol-*
861 *ogy*. 2015;36(12):9475–86.
- 862 32. Ohta S, Suzuki K, Tachibana K, Tanaka H, Yamada G. Cessation of gastrulation is medi-
863 ated by suppression of epithelial-mesenchymal transition at the ventral ectodermal ridge.
864 *Development*. 2007;134(24):4315–24.
- 865 33. Yang B, Zhang W, Zhang M, Wang X, Peng S, Zhang R. KRT6A Promotes EMT and
866 Cancer Stem Cell Transformation in Lung Adenocarcinoma. *Technol Cancer Res Treat*.
867 2020;19(11):1–8.
- 868 34. Schneider S, Hotaling N, Campos M, Patnaik SR, Bharti K, May-Simera HL. Generation
869 of an inducible RPE-specific Cre transgenic-mouse line. Lewin AS, editor. *PLoS One*.
870 2018 Nov 15;13(11):e0207222.
- 871 35. Hua K, Ferland RJ. Primary cilia proteins: ciliary and extraciliary sites and functions. *Cel-*
872 *lular and Molecular Life Sciences*. 2018;75(9):1521–40.
- 873 36. Kim JC, Badano JL, Sibold S, Esmail MA, Hill J, Hoskins BE, et al. The Bardet-Biedl pro-
874 tein BBS4 targets cargo to the pericentriolar region and is required for microtubule an-
875 choring and cell cycle progression. *Nat Genet*. 2004;36(5):462–70.
- 876 37. Scott CA, Marsden AN, Rebagliati MR, Zhang Q, Chamling X, Searby CC, et al. Nu-
877 clear/cytoplasmic transport defects in BBS6 underlie congenital heart disease through
878 perturbation of a chromatin remodeling protein. *PLoS Genet*. 2017;13(7):1–26.
- 879 38. Gascue C, Tan PL, Cardenas-Rodriguez M, Libisch G, Fernandez-Calero T, Liu YP, et al.
880 Direct role of Bardet-Biedl syndrome proteins in transcriptional regulation. *J Cell Sci*.
881 2012;125(2):362–75.

- 882 39. Brücker L, Kretschmer V, May-Simera HL. The entangled relationship between cilia and
883 actin. *International Journal of Biochemistry and Cell Biology*. 2020;129(August):105877.
- 884 40. Yu M, Peachey NS. Use of direct current electroretinography for analysis of retinal pig-
885 ment epithelium function in mouse models. *Methods in Molecular Biology*.
886 2018;1753:103–13.
- 887 41. Wu J, Peachey NS, Marmorstein AD. Light-Evoked Responses of the Mouse Retinal Pig-
888 ment Epithelium. *J Neurophysiol*. 2004 Mar;91(3):1134–42.
- 889 42. Yuan Y, Shimura M, Hughes BA. Regulation of inwardly rectifying K⁺ channels in retinal
890 pigment epithelial cells by intracellular pH. *Journal of Physiology*. 2003;549(2):429–38.
- 891 43. Hughes BA, Swaminathan A. Modulation of the Kir7.1 potassium channel by extracellular
892 and intracellular pH. *Am J Physiol Cell Physiol*. 2008;294(2):423–31.
- 893 44. Linsenmeier RA, Steinberg RH. Delayed basal hyperpolarization of cat retinal pigment ep-
894 ithelium and its relation to the fast oscillation of the DC electroretinogram. *Journal of Gen-
895 eral Physiology*. 1984;83(2):213–32.
- 896 45. Steinberg RH. Interactions between the retinal pigment epithelium and the neural retina.
897 *Documenta Ophthalmologica*. 1985 Oct;60(4):327–46.
- 898 46. Han SJ, Jung JK, Im SS, Lee SR, Jang BC, Park KM, et al. Deficiency of primary cilia in
899 kidney epithelial cells induces epithelial to mesenchymal transition. *Biochem Biophys Res
900 Commun*. 2018;496(2):450–4.
- 901 47. Iruzubieta P, Castiella T, Monleón E, Berga C, Muñoz G, Junquera C. Primary cilia pres-
902 ence and implications in bladder cancer progression and invasiveness. *Histochem Cell
903 Biol*. 2021;155(5):547–60.

- 904 48. Zhou M, Geathers JS, Grillo SL, Weber SR, Wang W, Zhao Y, et al. Role of Epithelial-
905 Mesenchymal Transition in Retinal Pigment Epithelium Dysfunction. *Front Cell Dev Biol.*
906 2020;8(June):1–13.
- 907 49. Rosales MAB, Shu DY, Iacovelli J, Saint-Geniez M. Loss of PGC-1 α in RPE induces mes-
908 enchymal transition and promotes retinal degeneration. *Life Sci Alliance.* 2019 Jun
909 17;2(3):e201800212.
- 910 50. Jin WK, Kyung HK, Burrola P, Mak TW, Lemke G. Retinal degeneration triggered by inac-
911 tivation of PTEN in the retinal pigment epithelium. *Genes Dev.* 2008;22(22):3147–57.
- 912 51. Morleo M, Franco B. The Autophagy-Cilia Axis: An Intricate Relationship. *Cells [Internet].*
913 2019 Aug 1 [cited 2022 Oct 26];8(8). Available from: [https://pub-](https://pub-med.ncbi.nlm.nih.gov/31443299/)
914 [med.ncbi.nlm.nih.gov/31443299/](https://pub-med.ncbi.nlm.nih.gov/31443299/)
- 915 52. Madisen L, Zwingman TA, Sunkin SM, Oh SW, Zariwala HA, Gu H, et al. A robust and
916 high-throughput Cre reporting and characterization system for the whole mouse brain. *Nat*
917 *Neurosci.* 2010;13(1):133–40.
- 918 53. Pazour GJ, Baker SA, Deane JA, Cole DG, Dickert BL, Rosenbaum JL, et al. The intrafla-
919 gellar transport protein, IFT88, is essential for vertebrate photoreceptor assembly and
920 maintenance. *Journal of Cell Biology.* 2002;157(1):103–13.
- 921 54. Schindelin J, Arganda-Carreras I, Frise E, Kaynig V, Longair M, Pietzsch T, et al. Fiji: An
922 open-source platform for biological-image analysis. *Nat Methods.* 2012;9(7):676–82.
- 923 55. Nandrot EF, Kim Y, Brodie SE, Huang X, Sheppard D, Finnemann SC. Loss of synchro-
924 nized retinal phagocytosis and age-related blindness in mice lacking $\alpha\beta 5$ integrin. *Jour-*
925 *nal of Experimental Medicine.* 2004;200(12):1539–45.

- 926 56. Maminishkis A, Chen S, Jalickee S, Banzon T, Shi G, Wang FE, et al. Confluent monolay-
927 ers of cultured human fetal retinal pigment epithelium exhibit morphology and physiology
928 of native tissue. *Invest Ophthalmol Vis Sci.* 2006;47(8):3612–24.
- 929 57. Thévenaz P, Ruttimann UE, Unser M. A pyramid approach to subpixel registration based
930 on intensity. *IEEE Transactions on Image Processing.* 1998;7(1):27–41.
- 931 58. Berger A, Cavallero S, Dominguez E, Barbe P, Simonutti M, Sahel JA, et al. Spectral-do-
932 main optical coherence tomography of the rodent eye: Highlighting layers of the outer ret-
933 ina using signal averaging and comparison with histology. *PLoS One.* 2014;9(5).
- 934 59. Holm S. A simple sequentially rejective multiple test procedure. *Scandinavian journal of*
935 *statistics.* 1979;6(2):65–70.
- 936 60. Seidler J, Vondráček J, Saxl I. The life and work of Zbyněk Šidák (1933–1999). *Applica-*
937 *tions of Mathematics.* 2000 Oct;45(5):321–36.
- 938 61. Dunlap WP, Marx MS, Agamy GJ. FORTRAN IV functions for calculating probabilities as-
939 sociated with Dunnett's test. *Behavior Research Methods & Instrumentation.* 1981
940 May;13(3):363–6.
- 941 62. Kretschmer F, Sajgo S, Kretschmer V, Badea TC. A system to measure the Optokinetic
942 and Optomotor response in mice. *J Neurosci Methods.* 2015;256:91–105.
- 943 63. Kretschmer F, Kretschmer V, Kunze VP, Kretzberg J. OMR-arena: Automated measure-
944 ment and stimulation system to determine mouse visual thresholds based on optomotor
945 responses. *PLoS One.* 2013;8(11):1–12.
- 946 64. Kretschmer F, Tariq M, Chatila W, Wu B, Badea TC. Comparison of optomotor and opto-
947 kinetic reflexes in mice. *J Neurophysiol.* 2017;118(1):300–16.

Figure 1

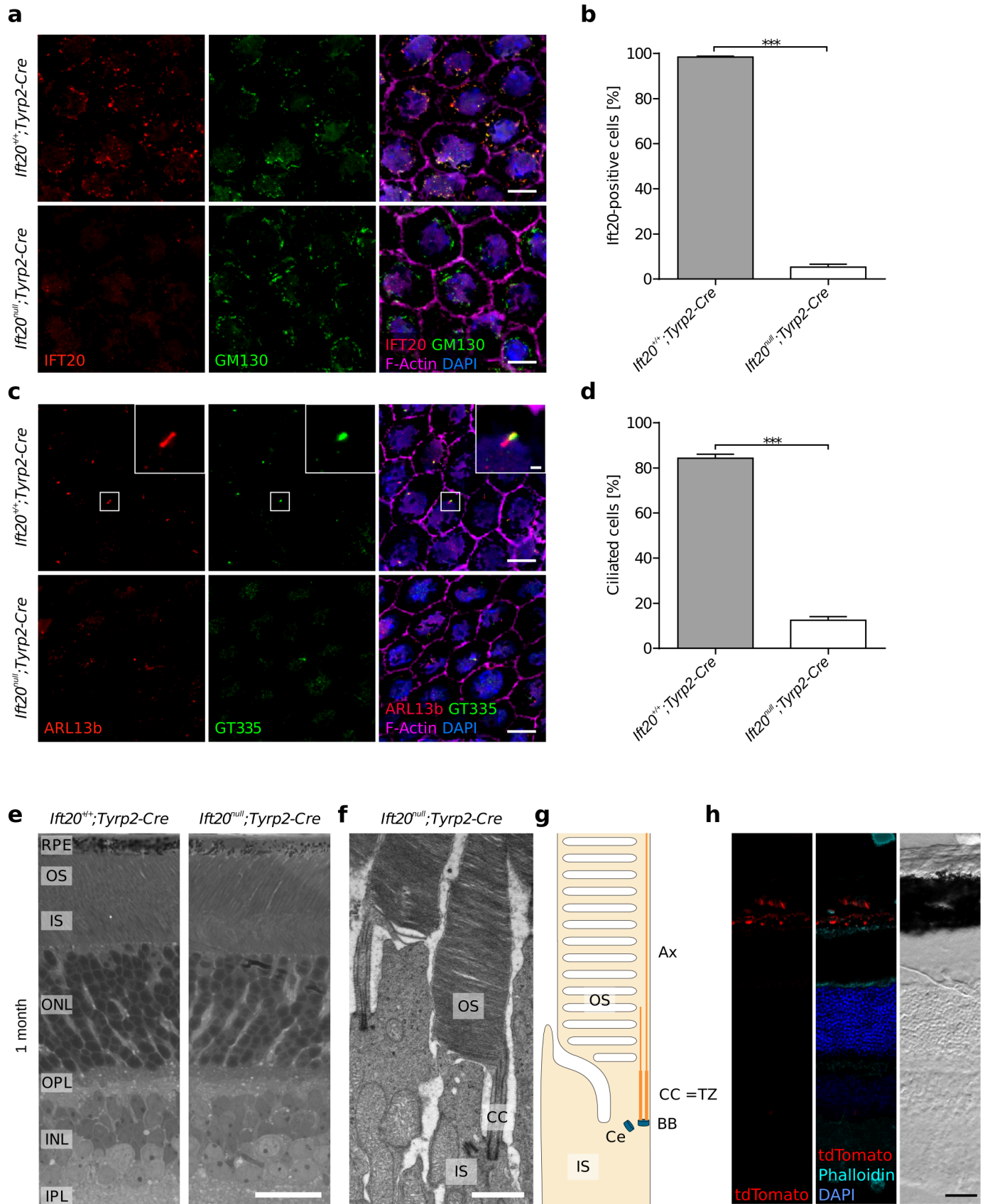


Figure 2

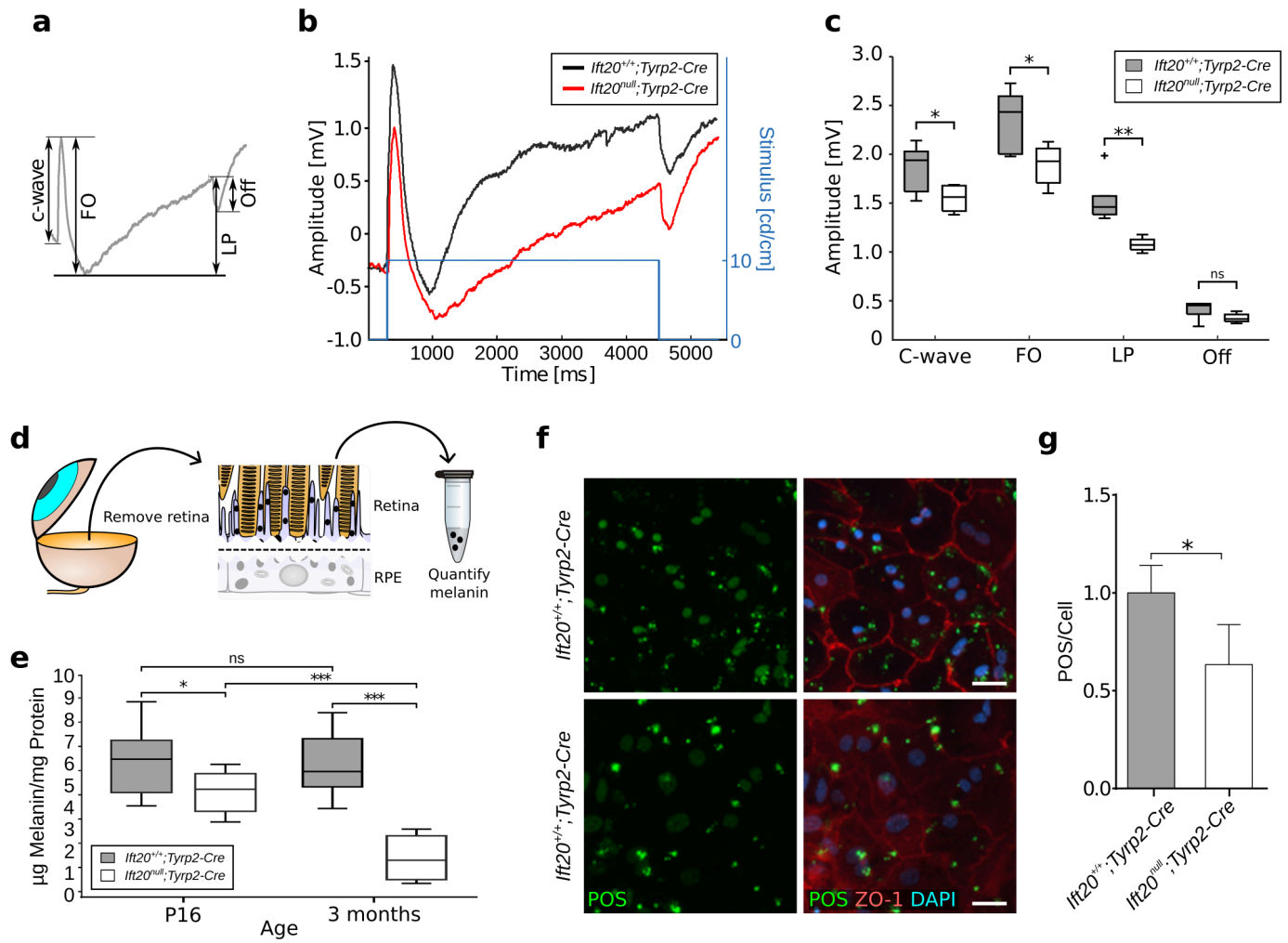


Figure 3

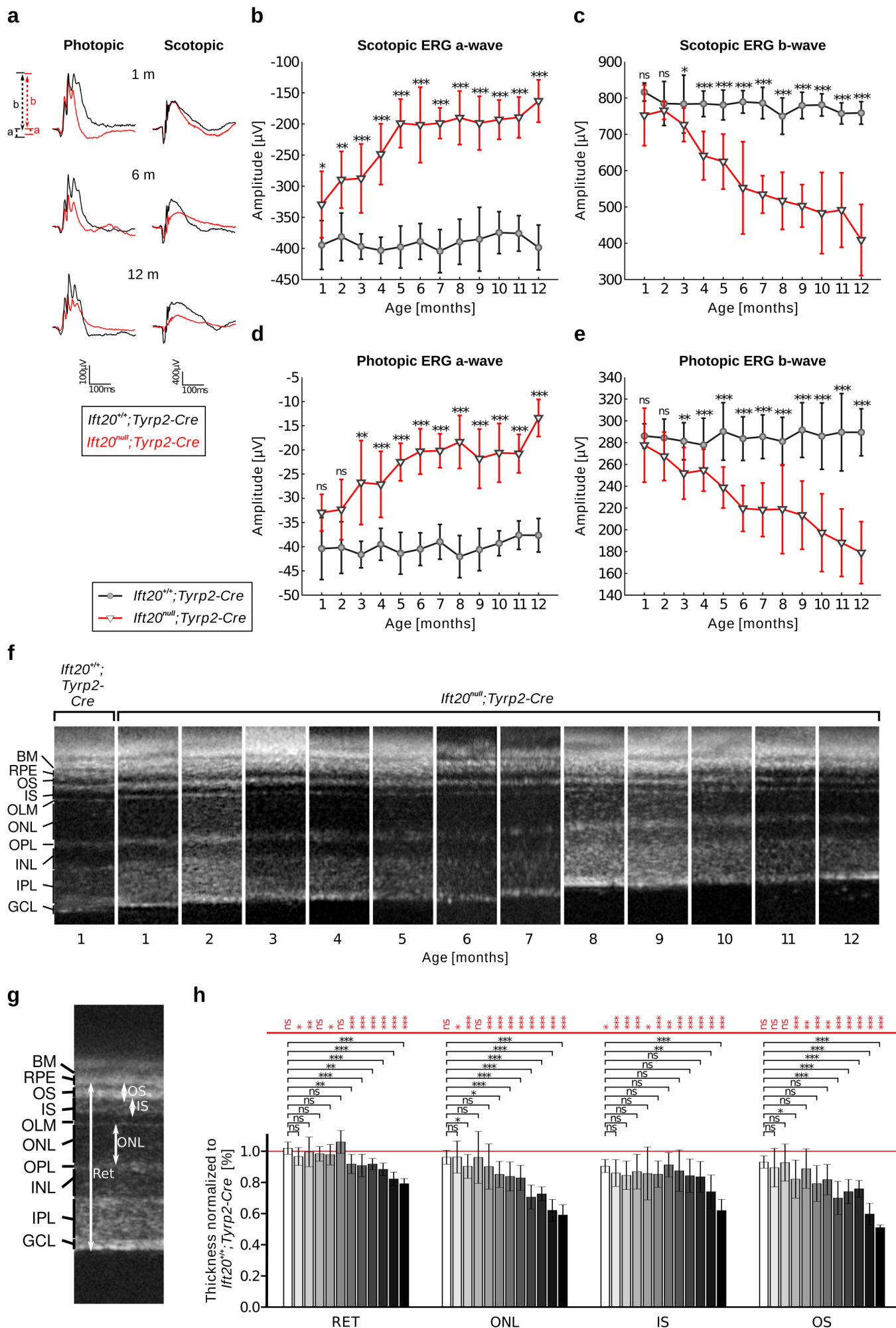


Figure 4

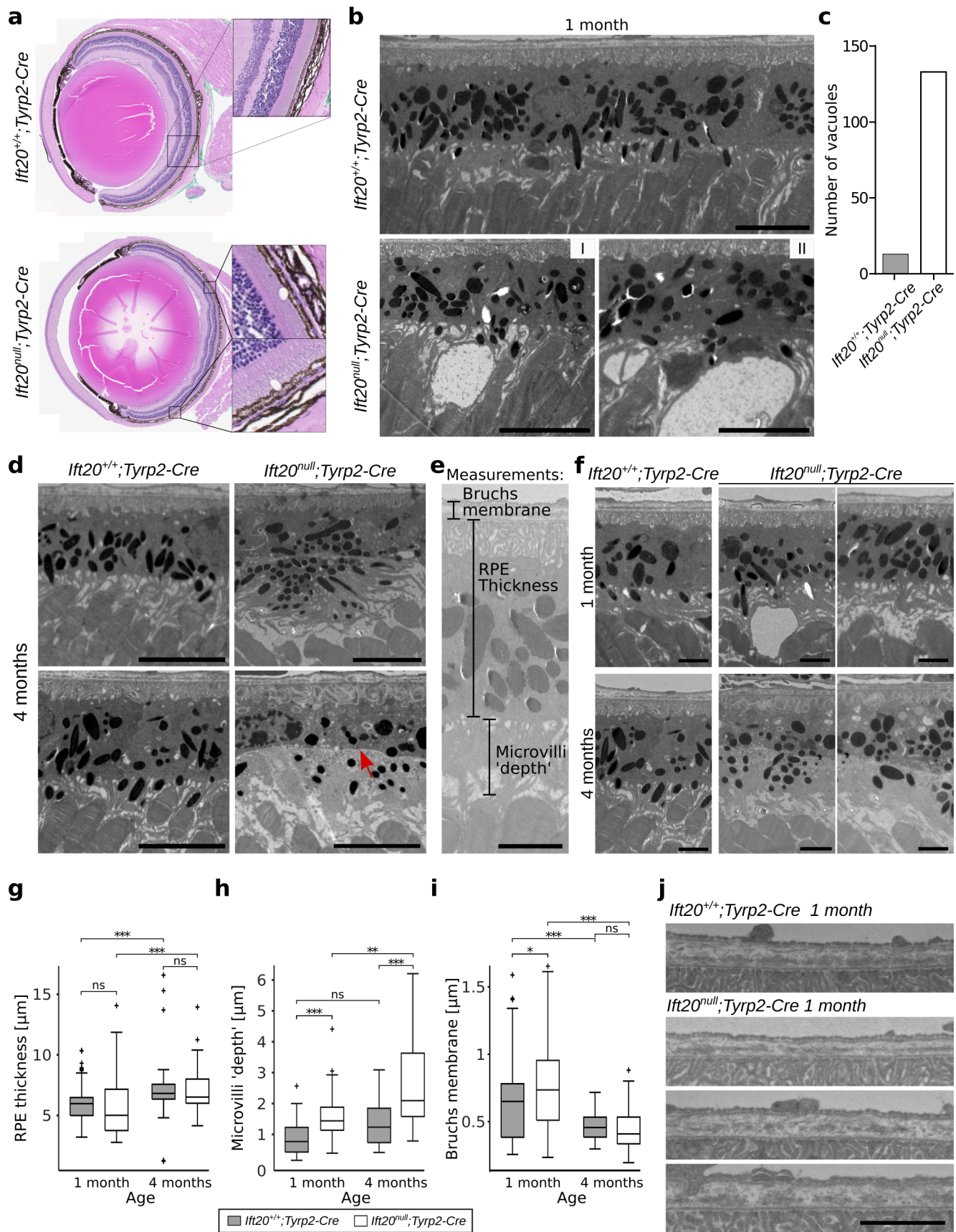


Figure 5

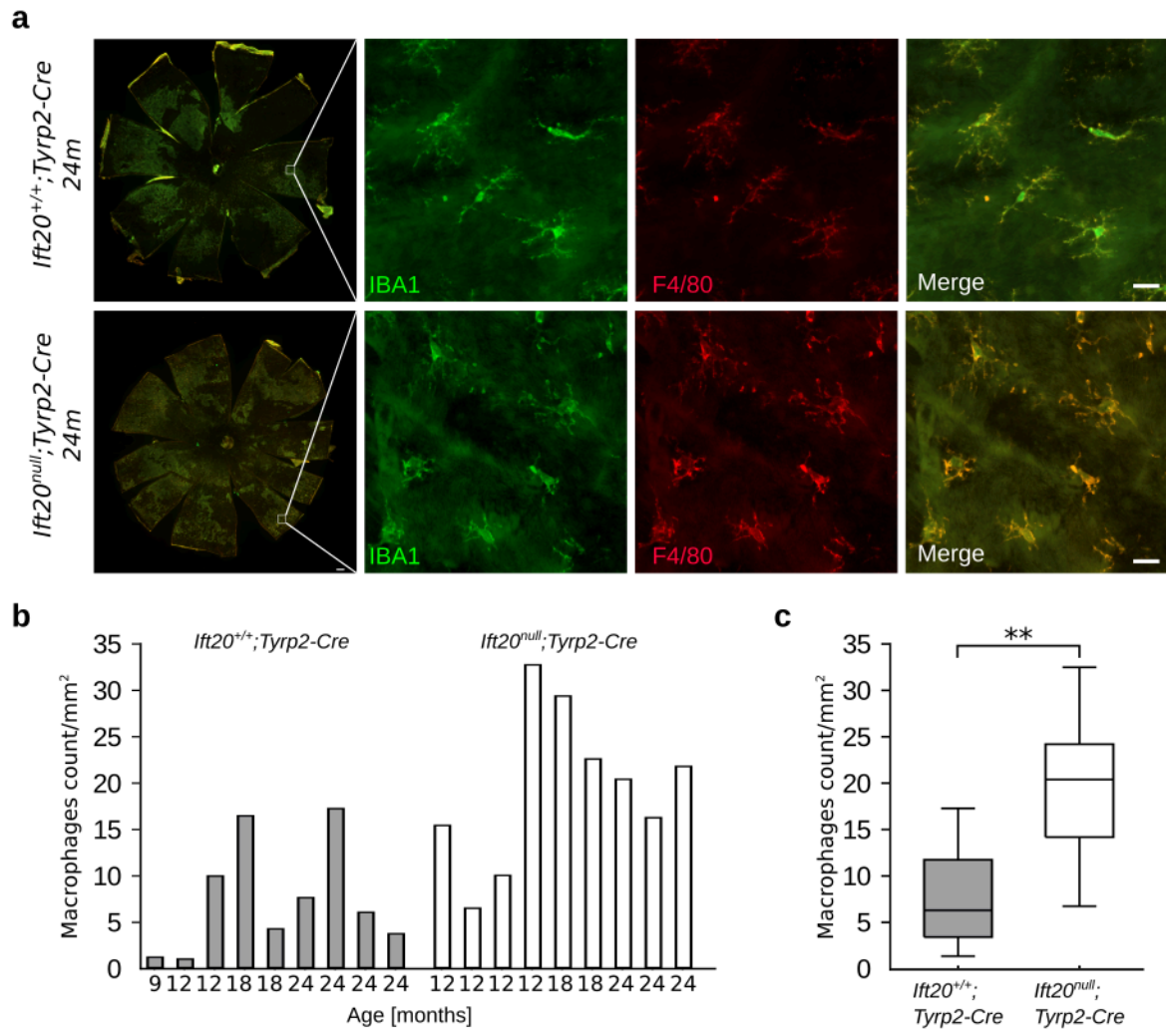


Figure 6

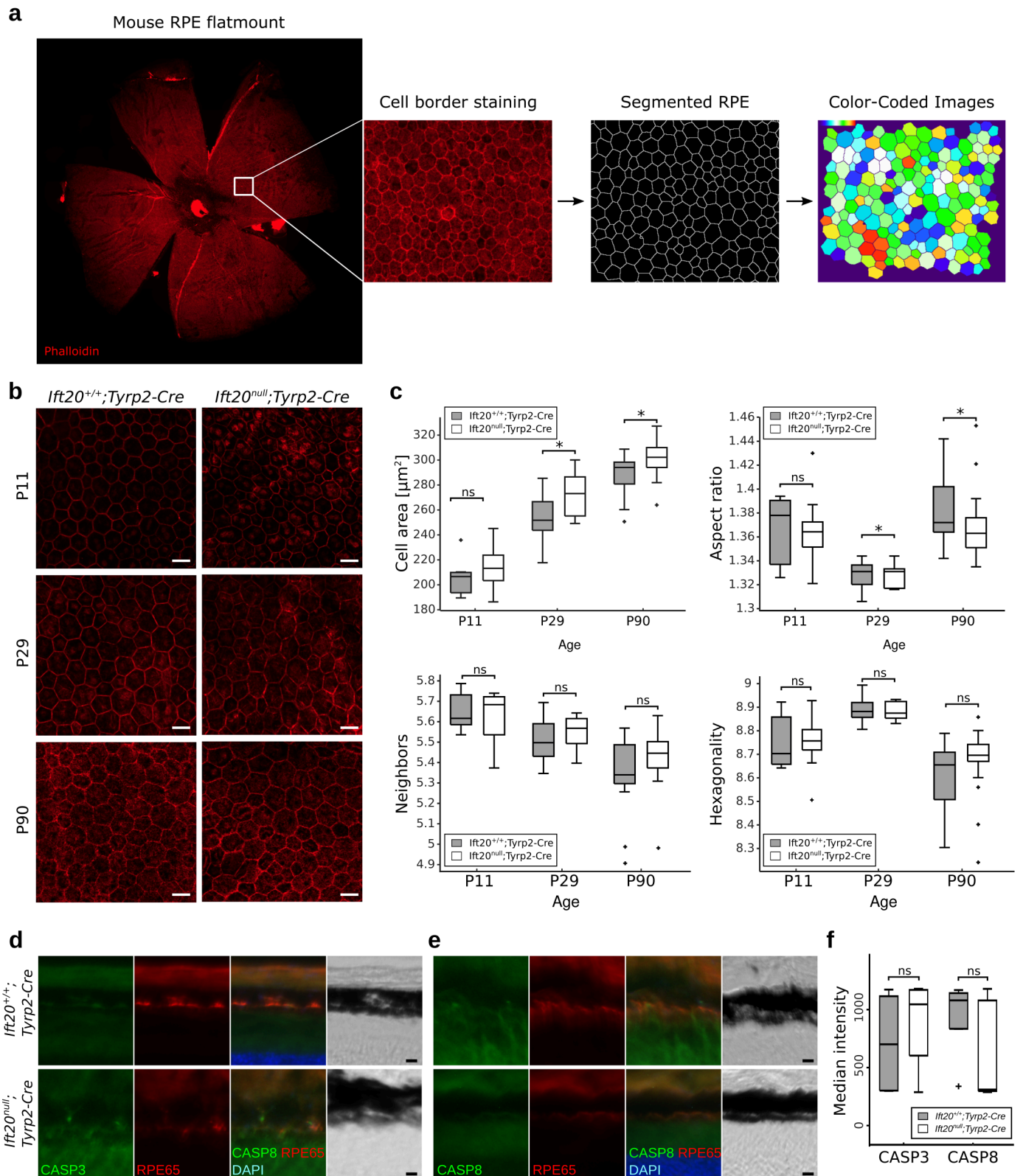


Figure 7

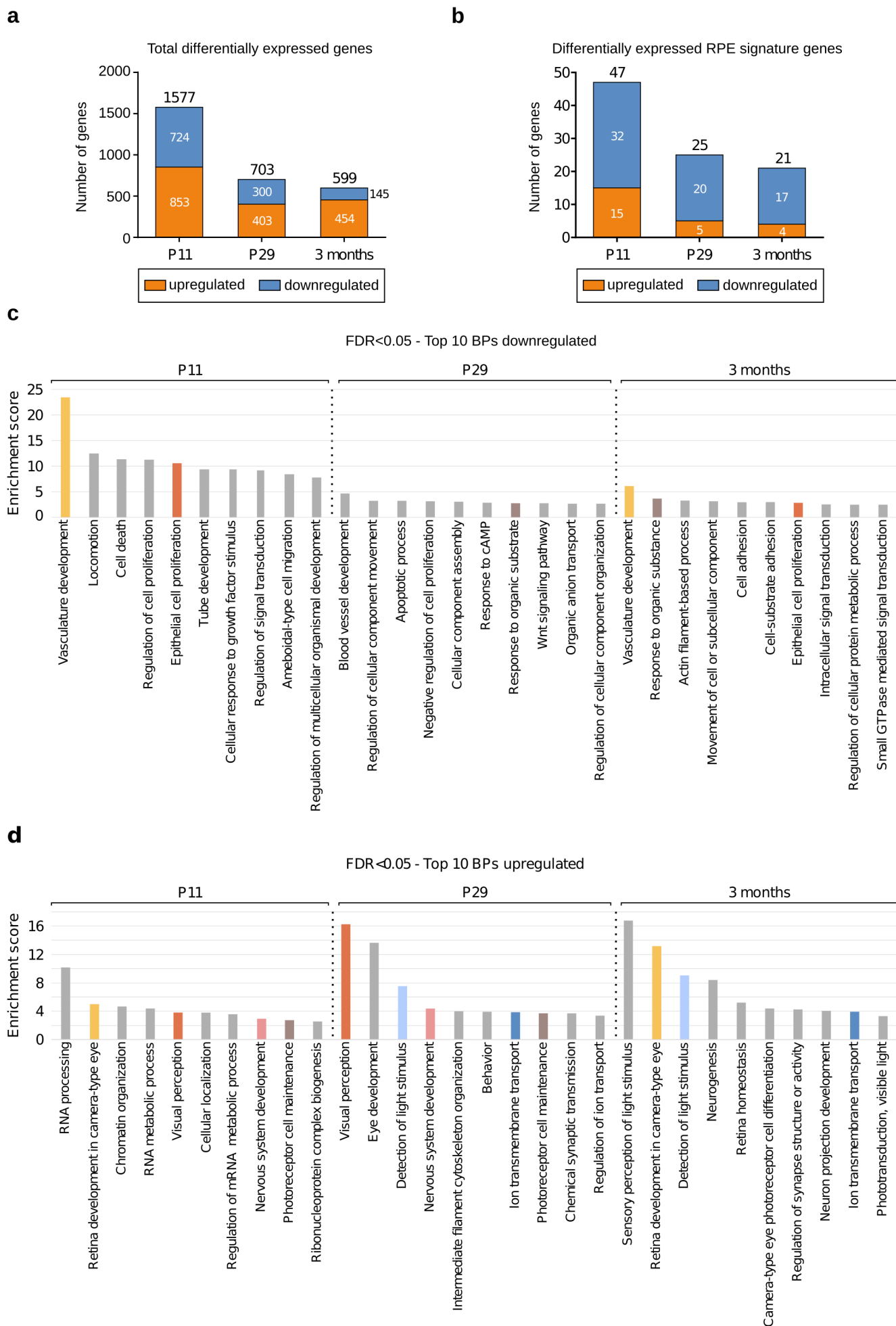
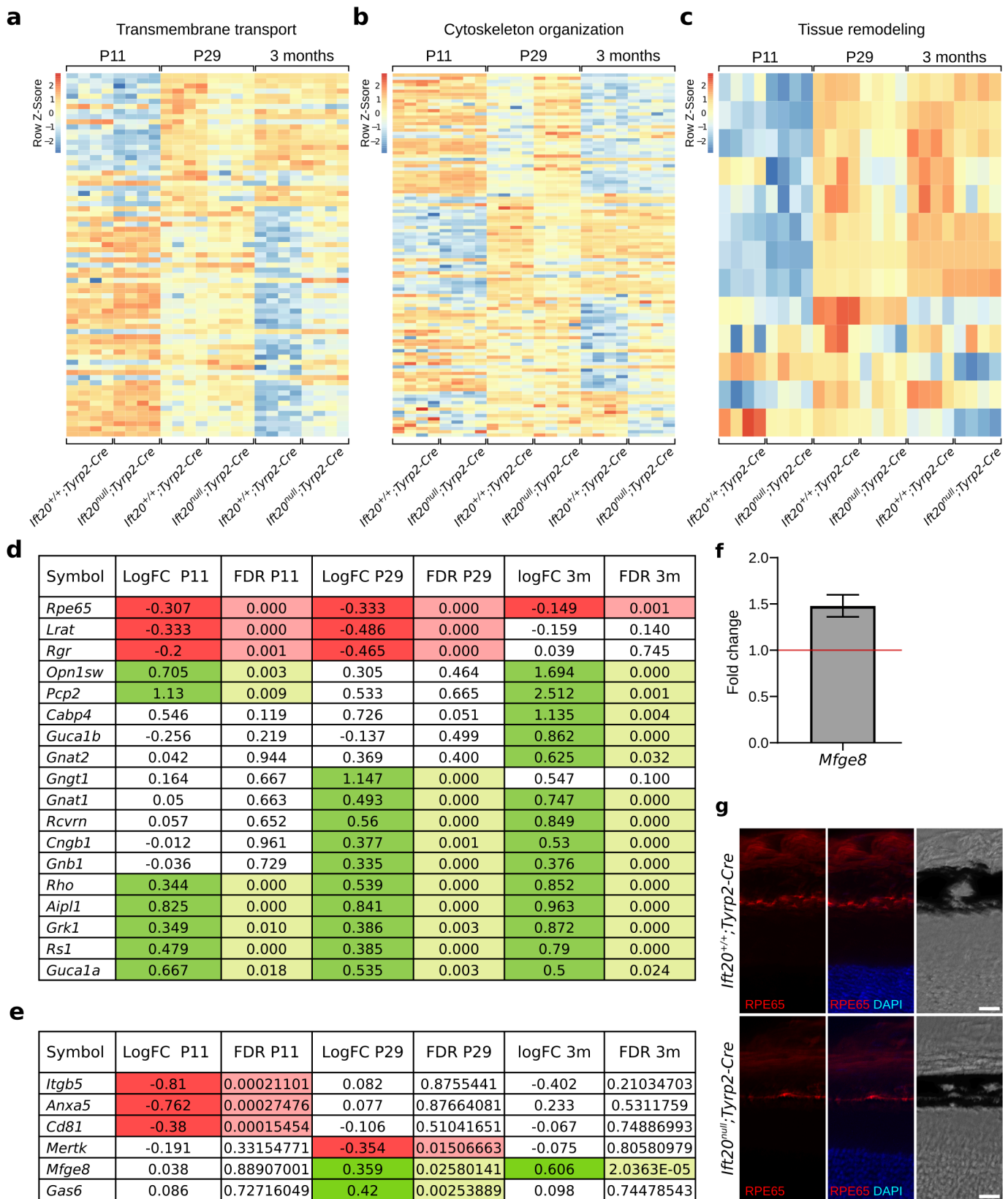


Figure 8



4 Summary and discussion of the results

The overarching aim of this thesis is to further understand the role of primary cilia dysfunction in the RPE and how it may affect retinal dystrophy. In the context of the present thesis, we were able to show that primary cilia dysfunction affects RPE maturation resulting in an abnormal patterning of the RPE (**Publication I**). We further show for the first time that primary cilia dysfunction affects signaling pathways, developmental processes, as well as RPE homeostasis and function resulting in a pathological phenotype of the RPE (**Publication II**). Furthermore, we demonstrate for the first time that ablation of primary cilia exclusively in the RPE results in a progressive ocular pathogenicity leading to visual impairment (**Manuscript I**).

4.1 Effects of primary cilia dysfunction caused by *Bbs8* knockout on the mouse RPE

It is known that the *Bbs8* knockout mice recapitulate the human ciliopathy phenotype. In 2018, May-Simera *et al.* showed that *Bbs8*^{-/-} mice show maturation defects that most probably caused underdeveloped tight junctions, defects in apical microvilli as well as less expression of genes associated with RPE maturation (May-Simera *et al.*, 2018). We showed that in the mouse RPE primary cilia are only temporary present during development and retracts as the tissue matures with the primary cilia being most prominent at E16.5 (**Publication I** Fig. 1, **Publication I** Fig. 2). In E16.5 mouse RPE, after knockout of *Bbs8*, only about 50% of RPE cells showed primary cilia, and if they did, in a less prominent way compared to wildtype RPE (approx. 90%) (**Publication I** Fig. 3). In addition to that, we observed that the *Bbs8*^{-/-} RPE cells showed changes in tight junctions and less uniformly shaped RPE cells compared to controls as both could be seen via staining of zona occludens 1 (ZO-1). (**Publication I** Fig. 3e). These observations are most likely due to defects in signaling during development and maturation of the RPE. Thus, these findings deepened our understanding into the contribution of primary cilia to tissue development and maturation. However, it raised the question on what effects can be further seen in the RPE. Upon ciliary disruption via knockout of *Bbs8*, we could show that the RPE fails to fully mature and exhibits phenotypic defects affecting RPE function even before the adjacent photoreceptors have differentiated (**Publication II**).

Using an unbiased QuantSeq 3' mRNA sequencing analysis of P11 and P29 RPE specimens isolated from *Bbs8*^{-/-} and *Bbs8*^{+/+} mouse eyes, we could show that upon deletion of *Bbs8* RPE maturation is delayed (**Publication II** Fig. 1, **Publication II** Supp. Tables 1-5). Further

investigation of the QuantSeq data revealed that this failure of RPE maturation is accompanied by an alteration of RPE homeostasis and function, including cellular organization, apoptotic processes, visual perception, RPE polarization, and phagocytosis (**Publication II** Fig. 2, **Publication II** Fig. 3, **Publication II** Fig. 4, **Publication II** Supp. Table 6-8). In agreement with the transcriptomic analysis, mass spectrometry-based quantitative proteomics revealed a significant mis-regulation of the proteome (**Publication II** Fig. 5, **Publication II** Supp. Table 9). The combinatorial “omics” approach (QuantSeq 3’ mRNA sequencing and Mass spectrometry) revealed that several dysregulated molecules are involved in adhesion. As RPE function is severely dependent on the tight connection of the RPE cell, we examined the RPE cellular morphology using immunofluorescence staining of tight junctions. It turned out that upon depletion of *Bbs8*, the RPE cells progressively lose their hexagonal structure resulting in significantly impaired RPE cell morphology up to complete disruption of cytoplasmic membranes from P11 onwards (**Publication II** Fig. 6a). Computer-based high-content image analysis revealed that RPE cells are enlarged, and the variance of cell area is significantly enlarged in older mice (**Publication II** Fig. 6b).

Since RPE function is critically dependent on the maintenance of its epithelial phenotype, it was not surprising to find loss of RPE functionality upon loss of ciliary function (Strauss, 2005; Bharti, Miller and Arnheiter, 2011; Adijanto *et al.*, 2012; Chen *et al.*, 2019). In the RPE, apical microvilli engulf the adjacent POS and are indispensable for retinal homeostasis. Upon loss of *Bbs8*, we observed as early abnormal accumulation of apical microvilli staining as P11, which worsened up to predominant absence indicating a worsening of apical microvilli formation in *Bbs8*-deficient RPE (**Publication II** Fig. 7a), indicating an inability to form proper functioning apical microvilli or loss of polarization in the course of time. In agreement with this, we also observed that *Bbs8*^{-/-} RPE displayed increased retinal adhesion *in vivo*, and knockdown of *Bbs8* resulted in decreased phagocytosis of POS *in vitro*.

Based on the analyses already made, there was evidence suggesting an epithelial-to-mesenchymal transition (EMT)-like phenotype in *Bbs8*-deficient RPE. EMT include changes in signaling, reorganization of the cytoskeleton, as well as loss of cell junctions and apical-basal polarity, all of which we detected in the RPE of *Bbs8*-deficient mice (Lamouille, Xu and Derynck, 2014; Ohlmann *et al.*, 2016). This, coupled with the recent findings that dysregulation of primary cilia signaling has already been shown to induce EMT in other tissues and organs (Lamouille, Xu and Derynck, 2014; Ohlmann *et al.*, 2016; Guen *et al.*, 2017; Blom and Feng, 2018; Han *et al.*, 2018), makes us believe that depletion of *Bbs8* might induce an EMT-like phenotype. Furthermore, the recurrence of primary cilia in P81 *Bbs8*^{-/-} but not control RPE also suggest development of an EMT-like phenotype.

Taken together, we were able to demonstrate that upon depletion of *Bbs8*, the RPE shows changes in gene and protein expression causing maturation defects most probably due to

changes in several signaling pathways. Furthermore, the RPE cells start to lose their cellular morphology up to the partial complete disruption of cytoplasmic membranes. This EMT-like phenotype is accompanied by defects in RPE function. However, since primary cilia were ablated globally it must be taken into account that interaction with defective photoreceptors might be also a leading driver to the seen pathogenetic phenotype.

Since the *Bbs8* knockout mouse model results in a global knockout of *Bbs8*, there are few things to consider when interpreting the results. In this mouse model, *Bbs8* is knocked out in all cells, including RPE and photoreceptor cells. Therefore, it is not possible to distinguish between primary defects in the RPE versus secondary effects coming from ciliary defects in the retina. This fact also leads to a more rapid deterioration of the two tissues.

However, in the RPE primary cilia are not completely absent, which leads to remaining primary cilia that may still function but cannot stop any progression. This leads to the fact that for the examination of the effects of primary cilia loss exclusively in the RPE another mouse model is necessary.

4.2 Effects of primary cilia loss exclusively in the RPE on the mouse RPE and visual function

With **Publication II**, we showed that loss of *Bbs8* result in defects of RPE homeostasis and function. However, the *Bbs8* knockout was global, which might lead one to question the impact of primary cilia in the RPE. Therefore, by using the Cre/LoxP-System we aimed at highlighting the events occurring after primary cilia were ablated exclusively in the RPE.

Due to lack of specificity or poor recombination of the currently available inducible RPE-specific Cre recombinases, we first wanted to use a tamoxifen-inducible RPE-specific Cre transgenic-mouse line, which we have generated and characterized (**Publication III**). Despite a high level of uniformly distributed recombination, we observed side effects of the tamoxifen treatment of pregnant dams. Administration of higher doses of tamoxifen is known to induce abortion in pregnant mice early in pregnancy (Ved *et al.*, 2019). However, as we started to administer tamoxifen at E9.5, we observed delivery failure. The embryos failed to be born and continued to develop until the condition of the pregnant mothers deteriorated dramatically, resulting in the death of both the pregnant dams and the embryos. Since, we could not find a way to circumnavigate these side effects we chose to use the non-inducible *Tyrosinase-related protein-2 (Tyrp2)-Cre* transgenic mouse line. In this mouse line, Cre activity in the eye was observed from mouse embryonic day E9.5. Consistent with the gradual *Tyrp2* expression in the developing RPE at E11.5, Cre activity was mainly observed in the dorsal RPE with a patchy activity in the ventral RPE. At E13.5, most of the RPE cells showed Cre activity (Jonassen *et al.*, 2008; Davis *et al.*, 2009). By choosing the *Ift20*

floxed mouse line, we were confident to eliminate all aspects of ciliation in the RPE and thus circumvent any compensatory effect of primary cilia remaining in some RPE cells (**Manuscript I** Fig.1). We were able to show for the first time that loss of primary cilia only in the RPE leads to defects in RPE homeostasis and function ultimately leading to retinal degeneration alongside with visual impairment in mice. Importantly, the adjacent retina was not affected as observed as its morphology was not altered and ERG function was inconspicuous until 2-months of age. In fact, the assessed ERG responses show that despite loss of primary cilia in the RPE, the retina still develops normally showing a stable morphology and function. However, after 2-months of age a progressive retinal degeneration alongside a decline in ERG responses are seen (**Manuscript I** Fig 3).

As the RPE is considered as a functional unit closely associated with the POS of the retina, the tight connection between these two tissues is essential for health, maintenance, and function of both tissues. Loss of primary cilia only in the RPE leads to severe morphologic changes on the apical side where the apical microvilli are located resulting in a disruption of the tight connection between the RPE cells and POS (**Manuscript I** Fig. 2d-g, **Manuscript I** Fig. 4b-f). This is accompanied by decreased phagocytosis and changes in retinal adhesion. In addition to that, an increase in macrophage/microglia was observed in the subretinal space in older mice (**Manuscript I** Fig. 5). This reveals elevated inflammatory and degenerative processes, which might result from continued pathogenesis. When examining the RPE function via dcERG, we observed a significant decrease in the stimulus-related response of the RPE (**Manuscript I** Fig. 2a-c). The observed results mirror the disruption of epithelial homeostasis as one of the RPEs most important functions, namely ion buffering and thus homeostasis of the subretinal space. This finding goes together with the severe defects of apical microvilli. As those morphological defects are seen to start at 1-month of age and worsen until the age of 3 months, it can be concluded that the changes in the dcERG-response at 1-month of age precede the disruption of apical microvilli.

In order to further investigate the effect of primary cilia ablation exclusively in the RPE, RNA-seq was performed to screen for transcriptomic changes and significant changes were observed (**Manuscript I** Fig.7-8, **Manuscript I** Supp. Tables 1-5). Comparison of the observed phenotypic defects of the RPE with all differentially expressed transcripts revealed mis-regulation in underlying gene expression. Interestingly mis-regulation of genes involved in the following signaling pathways were identified: mTOR, PI3K-AKT, Hippo, TGF- β , BMP, NF-kappaB, FGF, cGMP-PKG and of course Wnt. This circumstance shows that ciliary ablation in the RPE significantly impairs signal transduction, which has a major effect on the tissue itself. Our data from the mis-regulated genes in *Bbs8* knockout mice revealed the TGF- β signaling pathway as an overlap, making it a potential candidate for further examination.

Collectively, it has been shown that ablation of primary cilia only in the RPE causes a progressive ocular pathogenicity that ultimately leads to visual impairment. Despite the RPE shows defects in RPE homeostasis and function early on, the retina remains able to develop and function normally until the age of 2 months. This leads to the assumption that any loss of retinal function is a secondary consequence of the RPE defects upon loss of ciliation. These results have a high clinical relevance for inherited ciliopathies, as we have shown that both retinal dysfunction and degeneration occur as a result of RPE defects in the presence of loss of primary cilia. Therefore, it is now of great importance to find the exact mechanisms to prevent these RPE defects and consequently prevent retinal dysfunction in patients.

5 Outlook

This thesis shows that primary cilia dysfunction in the RPE cause retinal defects, which occur even before the retina is fully matured, and ultimately lead to visual impairments of the mice. The most obvious therapy would be to eliminate the cause, i.e., by gene therapy. Since many ocular diseases are hereditary, gene therapy is the emerging technology, especially because cilia-related genes are often lost in recessive eye diseases, so restoring gene expression can restore ciliary function (Zhou and Zhou, 2020). The recent phase I and II gene therapy clinical trials conducted to restore *RPGR* mutations in patients suffering X-linked RP prove that this approach is promising (Zhou and Zhou, 2020). However, the standardized procedure using the non-pathogenic Adeno-associated viruses (AAVs) as vehicles also have its limitations, as DNA fragments should not be bigger than 4.3 kb (Zhou and Zhou, 2020). CRISPR/Cas9 gene editing, which recently revolutionized science in the field of gene editing, now enables the modification of several thousand base pairs of the nucleotide sequence. However, this approach is not yet ready to be applied to humans, although it shows potential. Thus, IVS26 mutations of *CEP290* were successfully repaired in a cellular model mimicking patient with congenital hepatic amaurosis due to *CEP290* mutations (LCA10) (Ruan *et al.*, 2017). It has been shown that primary cilia play an important role in the development of embryonic neural progenitor cells into neural stem cells via the Hedgehog pathway. Therefore, the normal assembly and disassembly of primary cilia play a key role in regulating stem cell proliferation and cellular differentiation, providing a theoretical basis for the regulation of stem cell differentiation by cilia. This has led to ocular stem cell therapy attracting considerable attention recently (Zhou and Zhou, 2020). In 2022, the first patient in a clinical trial received replacement tissue made from patient-derived induced pluripotent stem cells (iPSC). Dr. Kapil Bharti and his team developed an iPSC-derived therapy, which is currently conducted in a phase I/IIa clinical trial to determine the safety of an autologous transplantation of iPSC-derived RPE for geographic atrophy, the advanced dry form of AMD. Preliminary data received from experiments in rat and pig models have been promising (National Eye Institute (NEI), 2019a, 2019b, 2022; Magone De Quadros Costa, 2020).

As these approaches are currently still open to discussion and a restore of gene function is not yet feasible, it is of utmost importance to find the exact mechanisms and signaling pathways to prevent these RPE defects occurring upon loss of primary cilia. This would mean that a larger screen would have to be performed for all signaling pathways possible in the RPE. In the very best case, this would happen at a single-cell level. With an improved RPE cell isolation method, it might be possible to isolate all cells from one eye in such a way that a separation of the cells into cells without primary cilia and cells with residues can be done.

These two populations can then be further analyzed in terms of differences and similarities in their molecular mechanisms in order to find possible therapeutic approaches.

Since primary cilia are essential for signal transduction (“signaling hub of the cell”), the main focus should be on elucidating altered signaling pathways. It has been shown that cytoplasmic function of YAP1 in the RPE is indispensable to maintain adult RPE differentiation. Knockout of *Yap1* in adult mice caused cell depolarization, tight junction breakdown, inhibition of RP65 expression, reduced RPE pigmentation, retraction of microvilli and basal infoldings (Lu *et al.*, 2020). All of these symptoms were also observed in the mouse models we used (*Bbs8* and *Ift20* knockout mouse models), leading to the assumption that the Hippo signaling pathway is worth considering for treatment approaches. Lu *et al.* (2020) also showed that YAP1 plays an important role in actively inhibiting Wnt/ β -catenin signaling, thus downregulating β -catenin nuclear activity and preventing adult RPE dedifferentiation, what would lead to EMT. Primary cilia, however, are responsible for more signaling pathways (i.e., Hedgehog, Notch, GPCR, TGF- β), so it would certainly be worth to acquire an overview of all of them in order to better understand the interrelationships in disease and identify all potential therapeutical targets.

In **Publication I** we showed that primary ciliary dysfunction upon loss of *Bbs8* lead to an EMT-like phenotype of the RPE. It is well known that EMT is a hallmark of age-related macular degeneration (AMD), which is closely related to RPE cell dysfunction (Zhou and Zhou, 2020). Since the *Bbs8* mouse model results in a global knockout of *Bbs8* it is not surprising that we were able to detect this EMT-like phenotype at an early age. However, in the conditional *Ift20* knockout mice we were able to observe minor changes in the RPE cell phenotype. However, because the RPE and retina are considered a functional unit and the retina is not yet damaged, it may be beneficial to look for changes at an older age. This becomes more evident when looking at the comparison of the life phases and maturational rates of mice and humans. As mentioned in the introduction, visual impairments have a reportedly higher prevalence in the ageing society, people from 50 years (Bourne *et al.*, 2021). This would mean that the mice should be approximately 16-months-old (Hagan, 2017). Especially in the *Ift20* knockout mice, the conducted experiments must be performed as well in mice of at least “middle age”, which would be in at least 10-months-old mice (Hagan, 2017). The results obtained may indicate possible changes over time, which could reveal new possible therapeutic approaches. Because of their relative ease of manipulation and the abundance of available instrumentation, mouse models often serve as the model of choice for human disease studies. However, there are significant differences between rodent and human eyes, i.e., in terms of the eye anatomy and morphology. In particular, because rodents are nocturnal, these animals have significant differences in the retina compared to the hu-

man eye. Therefore, experimental designs are needed that are more comparable to humans, such as nonhuman primate models. Although they are an important model in translational approaches, the use of primates as research models presents a difficult ethical debate, especially in basic research (Moshiri, 2021; Hou, Du and Wu, 2022). Pigs are anatomically and physically more similar to humans than rodents, making them an interesting animal model for human diseases. Their relatively short gestational age of 114 days and large number of offspring per litter make them more accessible than nonhuman primate models, for example (Moshiri, 2021; Hou, Du and Wu, 2022). Prof. Dr. Uwe Wolfrum and his team just introduced their pig model for Usher Syndrome 1C (USH1C) showing the combination of vision loss, deafness, and vestibular dysfunction as seen in human patients. This pig model is the first animal model mimicking the ocular symptoms of USH1C as seen in humans. This will promote future research on the molecular mechanisms of the Usher Syndrome and pave the way towards drug therapy development and clinical translation (Grotz *et al.*, 2022). As mentioned recently, also Dr. Kapil Bharti and his team used pig models to validate their finding before starting their clinical trials I/IIa (National Eye Institute (NEI), 2019a, 2019b, 2022; Magone De Quadros Costa, 2020). This shows, that based on results obtained from studies with rodent animal models and human samples, i.e., iPSC-derived RPE, pig models are essential for paving the way towards clinical studies and determining the best possible treatment to prevent and cure retinal degeneration.

Due to the performed studies, we were able to get first insights into the events leading to retinal degeneration upon cilia dysfunction *in vivo*. Dysfunctional primary cilia in the eye lead to severe defects of the RPE up to the loss of its epithelial integrity. These defects could undoubtedly be associated with primary ciliary defects in the RPE, as we have shown that retinal development remained unchanged, and degeneration began much later. Ciliopathy patients exhibit a “double hit”, the first due to the defective primary cilia in the RPE and the second due to the defective cilia in the photoreceptor. However, to date, primary cilia in the RPE have been largely overlooked. Therefore, the absolute next step that needs to be taken for a better understanding of ciliopathies is a more detailed knowledge of the molecular mechanisms that lead to RPE defects upon loss of primary cilia. Only when the overall mechanisms leading to the disease are better understood, promising new therapeutic approaches can be developed.

6 Summary

Inherited visual impairments, which are associated with retinal degeneration, are a serious burden affecting the aging population. The primary cilium is a microtubule-based sensory organelle found on almost every eukaryotic cell type and is essential for many developmental and physiological processes. More than 100 ciliary genes are associated with retinal dystrophies, making the primary cilium an important organelle to study with respect to retinal degeneration. To date, research on retinal degeneration associated with ciliary dysfunction has focused on the neural retina. Consequently, the aim of the present work is to decipher the processes occurring in the retinal pigment epithelium (RPE) after primary ciliary dysfunction. In order to do so, two knockout mouse models have been used, a global knockout of *Bbs8* and a conditional knockout of *Ift20*. The latter, aiming to ablate primary cilia exclusively in the RPE.

In **Publication I**, we show that in mouse RPE primary cilia are temporarily present only during development. Focusing on the molecular control of underlying processes, we were able to identify a BBS protein-mediated regulation of ciliary disassembly. Moreover, we observed that primary cilia dysfunction in *Bbs8* knockout mice resulted in abnormal patterning of the RPE, most likely caused by defective RPE maturation processes.

In **Publication II**, we focused more on the effects of *Bbs8* loss on the RPE. This work provided more insights into the importance of ciliary proteins in the RPE and their contribution to visual disorders. Here, we show that absence of *Bbs8* causes changes in gene and protein expression of components involved in signaling pathways, developmental processes and RPE homeostasis and function. As a consequence, cellular polarization as well as morphology was affected leading to a possible epithelial-to-mesenchymal-transition (EMT)-like phenotype of the RPE cells.

In **Manuscript I**, we aimed at focusing on the examination of the effect of cilia ablation exclusively in the RPE on RPE homeostasis and function, retinal degeneration, and vision. To be able to better investigate the role of RPE-specific primary cilia, an inducible RPE-specific Cre transgenic-mouse line was developed and characterized (**Publication III**). However, due to tamoxifen-induced miscarriages in pregnant mice, we decided to use a non-inducible Cre mouse line to delete *Ift20* starting at E9.5. In this way, we show that the absence of primary cilia exclusively in the RPE leads to progressive pathogenicity of the eye, resulting in visual impairment. For the first time, primary ciliary defects in the RPE have been shown to precede retinal defects and contribute to retinal degeneration.

These findings have high clinical relevance for inherited ciliopathies, as we have shown that both retinal dysfunction and retinal degeneration occur as a consequence of RPE defects

when primary cilia are absent. Deciphering the exact molecular mechanisms to prevent these RPE defects and consequently retinal dysfunction will pave the way for new therapeutic approaches for ciliopathy patients.

7 Zusammenfassung

Mit Netzhautdegenerationen einhergehende vererbare Sehstörungen, sind eine ernste Belastung der alternden Bevölkerung. Das Primärzilium ist ein auf Mikrotubuli basierendes sensorisches Organell, das auf fast allen eukaryontischen Zelltypen zu finden ist und für viele entwicklungsbedingte und physiologische Prozesse wichtig ist. Mehr als 100 Ziliargene werden mit Netzhautdystrophien in Verbindung gebracht, was das Primärzilium zu einem wichtigen Organell macht, welches im Hinblick auf Netzhautdegenerationen untersucht werden muss. Bisher konzentrierte sich die Forschung zur Netzhautdegeneration im Zusammenhang mit ziliärer Dysfunktion auf die Netzhaut. Ziel der vorliegenden Arbeit ist es daher, die Prozesse zu entschlüsseln, die im retinalen Pigmentepithel (RPE) nach einer primären Ziliardysfunktion ablaufen. Zu diesem Zweck wurden zwei Knockout-Mausmodelle verwendet, ein globaler Knockout von *Bbs8* und ein konditionaler Knockout von *Ift20*. Letzterer zielt darauf ab, die primären Zilien ausschließlich im RPE beseitigen.

In **Publikation I** zeigen wir, dass die Primärzilien im RPE der Maus nur während der Entwicklung vorhanden sind. Wir konzentrierten uns auf die molekulare Kontrolle der zugrundeliegenden Prozesse und identifizierten eine durch das BBS-Protein vermittelte Regulation des Zilienabbaus. Darüber hinaus fanden wir heraus, dass eine Fehlfunktion der Primärzilien in *Bbs8*-Knockout-Mäusen zu einer abnormalen Morphologie des RPE führt, die höchstwahrscheinlich durch fehlerhafte RPE-Maturation verursacht wird.

In **Publikation II** konzentrierten wir uns mehr auf die Auswirkungen des *Bbs8*-Verlustes auf das RPE. Diese Arbeit lieferte weitere Erkenntnisse über die Bedeutung der ziliären Proteine im RPE und ihren Beitrag zu Sehbeeinträchtigungen. Hier zeigen wir, dass das Fehlen von *Bbs8* zu Veränderungen in der Gen- und Proteinexpression von Komponenten führt, die an Signalwegen, Entwicklungsprozessen sowie der Homöostase und Funktion des RPE beteiligt sind. Infolgedessen waren sowohl die zelluläre Polarisierung als auch die Morphologie beeinträchtigt, was zu einer epithelial-mesenchymalen Transition (EMT)-ähnlichen Phänotyp der RPE-Zellen führte.

In **Manuskript I** haben wir uns auf die Untersuchung der Auswirkungen der Zilienablation ausschließlich im RPE auf RPE-Homöostase und -Funktion, die Netzhautdegeneration und das Sehvermögen konzentriert. Um die RPE-spezifische Rolle der Primärzilien besser untersuchen zu können, wurde eine induzierbare RPE-spezifische Cre-transgene Mauslinie entwickelt und charakterisiert (**Publikation III**). Aufgrund von Tamoxifen-induzierten Fehlgeburten bei trächtigen Mäusen haben wir uns jedoch entschieden, eine nicht-induzierbare Cre-Mauslinie zu verwenden, um *Ift20* ab E9.5 auszuschalten. Auf diese Weise zeigen wir,

dass das Fehlen der Primärzilien ausschließlich im RPE zu einer fortschreitenden Pathogenität des Auges führt, die sich in einer Sehbeeinträchtigung manifestiert. Zum ersten Mal konnte gezeigt werden, dass Defekte der Primärzilien im RPE retinalen Defekten vorausgehen und zur Degeneration der Netzhaut beitragen.

Diese Ergebnisse sind von großer klinischer Bedeutung für vererbte Ziliopathien, da wir gezeigt haben, dass sowohl Netzhautdysfunktion als auch Netzhautdegeneration als Folge von RPE-Defekten auftreten, wenn Primärzilien fehlen. Die Entschlüsselung der genauen molekularen Mechanismen, die diesen RPE-Defekten und folglich der Netzhautdysfunktion vorausgehen, wird den Weg für neue therapeutische Ansätze für Ziliopathie-Patienten ebnen.

8 Appendix

8.1 References

- Adijanto, J. *et al.* (2012) 'Microphthalmia-associated transcription factor (MITF) promotes differentiation of human retinal pigment epithelium (RPE) by regulating microRNAs-204/211 expression', *Journal of Biological Chemistry*, 287(24), pp. 20491–20503. doi: 10.1074/jbc.M112.354761.
- Beales, P. L. *et al.* (1999) 'New criteria for improved diagnosis of Bardet-Biedl syndrome: Results of a population survey', *Journal of Medical Genetics*, 36(6), pp. 437–446. doi: 10.1136/jmg.36.6.437.
- Bharti, K., Miller, S. S. and Arnheiter, H. (2011) 'The new paradigm: retinal pigment epithelium cells generated from embryonic or induced pluripotent stem cells', *Pigment Cell & Melanoma Research*, 24(1), pp. 21–34. doi: 10.1111/j.1755-148X.2010.00772.x.
- Blom, J. N. and Feng, Q. (2018) 'Cardiac repair by epicardial EMT: Current targets and a potential role for the primary cilium', *Pharmacology and Therapeutics*. Elsevier Inc., 186, pp. 114–129. doi: 10.1016/j.pharmthera.2018.01.002.
- Bourne, R. R. A. *et al.* (2021) 'Trends in prevalence of blindness and distance and near vision impairment over 30 years: An analysis for the Global Burden of Disease Study', *The Lancet Global Health*, 9(2), pp. e130–e143. doi: 10.1016/S2214-109X(20)30425-3.
- Chen, Y. *et al.* (2019) 'Photoreceptor degeneration in microphthalmia (Mitf) mice: Partial rescue by pigment epithelium-derived factor', *DMM Disease Models and Mechanisms*, 12(1). doi: 10.1242/dmm.035642.
- Chuang, J. Z., Zhao, Y. and Sung, C. H. (2007) 'SARA-Regulated Vesicular Targeting Underlies Formation of the Light-Sensing Organelle in Mammalian Rods', *Cell*, 130(3), pp. 535–547. doi: 10.1016/j.cell.2007.06.030.
- Davis, N. *et al.* (2009) 'Pax6 dosage requirements in iris and ciliary body differentiation', *Developmental Biology*. Elsevier Inc., 333(1), pp. 132–142. doi: 10.1016/j.ydbio.2009.06.023.
- Estrada-Cuzcano, A. *et al.* (2012) 'Non-syndromic retinal ciliopathies: Translating gene discovery into therapy', *Human Molecular Genetics*, 21(R1). doi: 10.1093/hmg/ddc298.
- Fliegauf, M., Benzing, T. and Omran, H. (2007) 'When cilia go bad: cilia defects and ciliopathies.', *Nature reviews. Molecular cell biology*, 8(11), pp. 880–93. doi: 10.1038/nrm2278.
- Forsythe, E. and Beales, P. L. (2013) 'Bardet–Biedl syndrome', *European Journal of Human Genetics*, 21(1), pp. 8–13. doi: 10.1038/ejhg.2012.115.
- Goetz, S. C. and Anderson, K. V (2010) 'The primary cilium: a signalling centre during vertebrate development.', *Nature reviews. Genetics*. Nature Publishing Group, 11(5), pp. 331–44. doi: 10.1038/nrg2774.
- Grotz, S. *et al.* (2022) 'Early disruption of photoreceptor cell architecture and loss of vision in a humanized pig model of usher syndromes', *EMBO Molecular Medicine*, 14(4), pp. 1–24. doi: 10.15252/emmm.202114817.
- Guen, V. J. *et al.* (2017) 'EMT programs promote basal mammary stem cell and tumor-initiating cell stemness by inducing primary ciliogenesis and Hedgehog signaling', *Proceedings of the*

National Academy of Sciences of the United States of America, 114(49), pp. E10532–E10539. doi: 10.1073/pnas.1711534114.

Hagan, C. (2017) *When are mice considered old?*, The Jackson Laboratory. Available at: <https://www.jax.org/news-and-insights/jax-blog/2017/november/when-are-mice-considered-old>.

Han, S. J. *et al.* (2018) 'Deficiency of primary cilia in kidney epithelial cells induces epithelial to mesenchymal transition', *Biochemical and Biophysical Research Communications*. Elsevier Ltd, 496(2), pp. 450–454. doi: 10.1016/j.bbrc.2018.01.079.

Hao, L. and Scholey, J. M. (2009) 'Intraflagellar transport at a glance', *Journal of Cell Science*, 122(7), pp. 889–892. doi: 10.1242/jcs.023861.

Hou, N., Du, X. and Wu, S. (2022) 'Advances in pig models of human diseases', *Animal Models and Experimental Medicine*, 5(2), pp. 141–152. doi: 10.1002/ame2.12223.

Ishikawa, H. and Marshall, W. F. (2011) 'Ciliogenesis: building the cell's antenna', *Nature Reviews Molecular Cell Biology*. Nature Publishing Group, 12(4), pp. 222–234. doi: 10.1038/nrm3085.

Jonassen, J. A. *et al.* (2008) 'Deletion of IFT20 in the mouse kidney causes misorientation of the mitotic spindle and cystic kidney disease', *Journal of Cell Biology*, 183(3), pp. 377–384. doi: 10.1083/jcb.200808137.

Kobayashi, T. and Dynlacht, B. D. (2011) 'Regulating the transition from centriole to basal body', *Journal of Cell Biology*, 193(3), pp. 435–444. doi: 10.1083/jcb.201101005.

Lamouille, S., Xu, J. and Derynck, R. (2014) 'Molecular mechanisms of epithelial-mesenchymal transition', *Nature Reviews Molecular Cell Biology*. Nature Publishing Group, 15(3), pp. 178–196. doi: 10.1038/nrm3758.

Lu, Q. *et al.* (2020) 'Yap1 is required for maintenance of adult RPE differentiation', *FASEB Journal*, 34(5), pp. 6757–6768. doi: 10.1096/fj.201903234R.

Magone De Quadros Costa, T. (2020) *Autologous transplantation of induced pluripotent stem cell-derived retinal pigment epithelium for geographic atrophy associated with age-related macular degeneration*, NCT04339764. Available at: <https://clinicaltrials.gov/ct2/show/NCT04339764>.

May-Simera, H. L. *et al.* (2018) 'Primary Cilium Mediated Retinal Pigment Epithelium Maturation is Retarded in Ciliopathy Patient Cells', *CellReports*. Elsevier Company., 22(1). doi: 10.1016/j.celrep.2017.12.038.

May-Simera, H., Nagel-Wolfrum, K. and Wolfrum, U. (2017) 'Cilia - The sensory antennae in the eye', *Progress in Retinal and Eye Research*. Elsevier Ltd, 60, pp. 144–180. doi: 10.1016/j.preteyeres.2017.05.001.

Moshiri, A. (2021) 'Animals Models of Inherited Retinal Disease', *International Ophthalmology Clinics*, 61(3), pp. 113–130. doi: 10.1097/IIO.0000000000000368.

National Eye Institute (NEI) (2019a) *NIH launches first U.S. clinical trial of patient-derived stem cell therapy to replace and repair dying cells in retina*. Available at: <https://www.nei.nih.gov/about/news-and-events/news/nih-launches-first-us-clinical-trial-patient-derived-stem-cell-therapy-replace-and-repair-dying>.

National Eye Institute (NEI) (2019b) *NIH researchers rescue photoreceptors, prevent blindness*

in animal models of retinal degeneration. Available at: <https://www.nei.nih.gov/about/news-and-events/news/nih-researchers-rescue-photoreceptors-prevent-blindness-animal-models-retinal-degeneration>.

National Eye Institute (NEI) (2022) *First U.S. patient receives autologous stem cell therapy to treat dry AMD*. Available at: <https://www.nih.gov/news-events/news-releases/first-us-patient-receives-autologous-stem-cell-therapy-treat-dry-amd>.

Ohlmann, A. *et al.* (2016) 'Epithelial–mesenchymal transition of the retinal pigment epithelium causes choriocapillaris atrophy', *Histochemistry and Cell Biology*. Springer Berlin Heidelberg, 146(6), pp. 769–780. doi: 10.1007/s00418-016-1461-4.

Ruan, G. X. *et al.* (2017) 'CRISPR/Cas9-Mediated Genome Editing as a Therapeutic Approach for Leber Congenital Amaurosis 10', *Molecular Therapy*. Elsevier Ltd., 25(2), pp. 331–341. doi: 10.1016/j.ymthe.2016.12.006.

Sánchez-Bellver, L., Toulis, V. and Marfany, G. (2021) 'On the Wrong Track: Alterations of Ciliary Transport in Inherited Retinal Dystrophies', *Frontiers in Cell and Developmental Biology*, 9(March), pp. 1–25. doi: 10.3389/fcell.2021.623734.

Sheppard, D. (2002) 'Endothelial integrins and angiogenesis: not so simple anymore', *Journal of Clinical Investigation*, 110(7), pp. 913–914. doi: 10.1172/jci16713.

Strauss, O. (2005) 'The retinal pigment epithelium in visual function', *Physiological Reviews*, 85(3), pp. 845–881. doi: 10.1152/physrev.00021.2004.

Suspitsin, E. N. and Imyanitov, E. N. (2016) 'Bardet-Biedl Syndrome', *Molecular Syndromology*, 7(2), pp. 62–71. doi: 10.1159/000445491.

Tobin, J. L. and Beales, P. L. (2009) 'The nonmotile ciliopathies', *Genetics in Medicine*. Elsevier Masson SAS, 11(6), pp. 386–402. doi: 10.1097/GIM.0b013e3181a02882.

Valverde, D., Castro-Sánchez, S. and Álvarez-Satta, M. (2015) 'Bardet-Biedl syndrome: A rare genetic disease', *Journal of Pediatric Genetics*, 02(02), pp. 077–083. doi: 10.3233/PGE-13051.

Ved, N. *et al.* (2019) 'Tamoxifen administration in pregnant mice can be deleterious to both mother and embryo', *Laboratory Animals*, 53(6), pp. 630–633. doi: 10.1177/0023677219856918.

Waters, A. M. and Beales, P. L. (2011) 'Ciliopathies: An expanding disease spectrum', *Pediatric Nephrology*, 26(7), pp. 1039–1056. doi: 10.1007/s00467-010-1731-7.

Willoughby, C. E. *et al.* (2010) 'Anatomy and physiology of the human eye: Effects of mucopolysaccharidoses disease on structure and function - a review', *Clinical and Experimental Ophthalmology*, 38(SUPPL. 1), pp. 2–11. doi: 10.1111/j.1442-9071.2010.02363.x.

Wright, A. F. *et al.* (2010) 'Photoreceptor degeneration: Genetic and mechanistic dissection of a complex trait', *Nature Reviews Genetics*. Nature Publishing Group, 11(4), pp. 273–284. doi: 10.1038/nrg2717.

Zhou, P. and Zhou, J. (2020) 'The Primary Cilium as a Therapeutic Target in Ocular Diseases', *Frontiers in Pharmacology*, 11(June), pp. 1–7. doi: 10.3389/fphar.2020.00977.

8.2 Allocation of the contributions made to the individual publications

This cumulative dissertation consists of a total of three publications and one manuscript. Other scientists have also contributed to all scientific papers. The following are my contributions to each paper.

In **Publication I** (Patnaik et al., 2019), I demonstrated reduced numbers of ciliated cells by immunofluorescence microscopy of E16.5 RPE flatmounts from both *Bbs6*- and *Bbs8*-knock-out mice (Fig. 3 a, e). After quantification and statistical analysis, I was able to verify a significant reduction of ciliated cells in *Bbs6*- and *Bbs8*-knockout RPE.

In **Publication II** (Schneider et al., 2021) I was the first author responsible for the manuscript drafts and the design of the associated figures, which were subsequently revised together with Prof. Dr. Helen May-Simera. For this paper, I performed all immunofluorescence microscopy experiments, which included dissection of the eyes, eye preparation, immunofluorescence staining, preparation of RPE flatmounts, microscopy, image processing and analysis. Furthermore, I quantified the ciliated cells in P29 mouse RPE. For QuantSeq 3' mRNA sequencing, I dissected the eyes and prepared the eyecups, from which the RNA was then isolated. For further preparation of the QuantSeq 3' mRNA sequencing library and QuantSeq 3' mRNA sequencing performed by Dr. Rossella De Cegli and Daniela Intartaglia, the isolated RNA was sent to the Telethon Institute of Genetics and Medicine in Italy. Dr. Rossella De Cegli, Daniele Intartaglia, Prof. Dr. Ivan Conte, Prof. Dr. Helen May-Simera, and I performed the analysis of the data in close collaboration. For mass spectrometry-based quantitative proteomics, I dissected the eyes and isolated the RPE cells from the eyecups. For further lysis and liquid chromatography with tandem mass spectrometry (LC-MS/MS) analysis performed by Dr. Karsten Boldt and Prof. Dr. Marius Ueffing, the frozen RPE cell pellets were sent to Institute for Ophthalmic Research at Eberhard-Karls University in Tübingen. Quantification of RPE cell morphology via high-content image analysis was performed by Jayapriya Nagarajan and Dr. Nathan Hotaling at the National Institutes of Health (NIH) (US), using images immunofluorescence images that I shared with them. Interpretation of the obtained results was done in close cooperation of Jayapriya Nagarajan, Dr. Nathan Hotaling, Prof. Dr. Helen May-Simera and me. Retinal adhesion assay was performed by Dr. Viola Kretschmer and *in vitro* phagocytosis assay was performed by Peter Andreas Matthiessen. I performed eye dissection, tissue preparation, RNA isolation, cDNA transcription and quantitative Real-Time PCR (qPCR) of EMT-associated genes.

In **Publication III** (Schneider et al., 2018) I was the first author responsible for the manuscript drafts and the design of the associated figures, which were subsequently revised together with Prof. Dr. Helen May-Simera. Generation of the transgenic *RPE-Tyrosinase-CreEr^{T2}* was performed by the group of Dr. Kapil Bharti at NIH. For this paper, I performed

all dissections, eye preparations, immunofluorescence stainings, and preparations of RPE and retina flatmounts. Microscopy of the stained RPE flat slides was performed either by myself or, for better resolution of the tile images showing the whole RPE flatmount (i.e., Fig 4), by Dr. Maria Campos at the NIH. For quantification of recombinant expression of tdTomato via high-content image analysis performed by Dr. Nathan Hotaling, I processed the images by removing the background, regardless of whether they were taken by myself or at NIH. Elisabeth Sehn embedded the eyecups and cut the sections after I dissected them and processed the eyes for transmission electron microscopy (TEM) by fixation and dehydration. TEM was performed by Elisabeth Sehn and me together. Furthermore, Elisabeth Sehn prepared the longitudinal cryosections of the eye, before I performed immunofluorescence staining and microscopy analysis (i.e., Fig. 2). Additionally, I quantified the recombinant expression of tdTomato expression in the ciliary body. Longitudinal embryo sections and the corresponding microscopy was performed in the lab of Dr. Kapil Bharti at the NIH. I performed eye dissection, tissue preparation, RNA isolation, cDNA transcription and quantitative Real-Time PCR (qPCR) of EMT-associated genes.

In **Manuscript I** (Kretschmer & Schneider et *al.*, 2023) together with Dr. Viola Kretschmer I am the co-first author responsible for the manuscript drafts and the design of the associated figures, which were subsequently revised together with Prof. Dr. Helen May-Simera. Using immunofluorescence staining of E16.5 mouse RPE flatmounts, I could demonstrate that the used mouse model was sufficient in deleting *Ift20*, thus ablation primary cilia (Fig. 1 a-d). Additionally, I showed that this ablation of primary cilia in the RPE did not affect the retinal development as shown via light microscopy and TEM (Fig. 1 e-f). All specimens used for TEM in this manuscript were dissected and processed by me. After dehydration, Elisabeth Sehn embedded the fixed and dehydrated eyecups and cut the sections. All visual assessment approaches of the mice (dcERG, OCT, ERG, OMR) was performed by Dr. Viola Kretschmer. Assessing RPE function by retinal adhesion and phagocytosis assay was performed by Dr. Viola Kretschmer and Dr. Emeline Nandrot, respectively. I dissected the mouse eyes, that were sent to the Institut de la Vision in Paris, where Dr. Emelina Nandrot isolated the RPE cells and continued with the experimental approach. Quantification of the ultrastructural changes, that were observed in the TEM images, taken by Elisabeth Sehn and myself, was done by Prof. Dr. Helen May-Simera (Fig. 4 g-i). Macrophage/Microglia detection as well as analysis of the apoptosis markers Caspase-3 and -8 via immunohistochemistry and quantification was performed by Peter A. Matthiessen (Fig. 5, Fig. 6 d-f, Supp. Fig. 3). Microscopic analysis of single cells of RPE flatmounts was performed by Dominik Reichert and Dr. Nathan Hotaling at the NIH (Fig. 6 a-c). For QuantSeq 3' mRNA sequencing, I dissected the eyes and prepared the eyecups, from which the RNA was then isolated. For further preparation of the QuantSeq 3' mRNA sequencing library and QuantSeq 3' mRNA

sequencing performed by Dr. Rossella De Cegli, the isolated RNA was sent to the Telethon Institute of Genetics and Medicine in Italy. Dr. Rossella De Cegli and Prof. Dr. Ivan Conte performed the analysis of the data. qRT-PCR was performed by Peter A. Matthiessen (Fig. 8 f). For scanning electron microscopy (SEM), I dissected the eyes and processed the eyecups using standard EM procedures (fixation, dehydration, drying and mounting). SEM was performed by Gunnar Glaßer, Prof. Dr. Helen May-Simera and me at the Max-Planck Institute for Polymer Research.

8.3 CV


8.4 Acknowledgment

8.5 Publication IV – Tissue-dependent differences in Bardet-Biedl syndrome gene expression (Published)

Patnaik SR, Farag A, Brücker L, Volz AK, **Schneider S**, Kretschmer V, May-Simera HL: *Tissue-dependent differences in Bardet-Biedl syndrome gene expression*. Biol Cell. 2020 Feb;112(2):39-52. PMID: 31845361.

As growing evidence suggests that cilia proteins also have ciliary-independent functions contributing to disease etiology, we show with this publication that some Bbs proteins not only function in a complex but might also have alternative organ-specific ciliary-independent functions. However, loss of Bbs6 or Bbs8 affects expression of other Bbs transcripts in a tissue-dependent way. These results shed a light on understanding disease pathogenesis and development of possible treatment strategies.

Tissue-dependent differences in Bardet–Biedl syndrome gene expression

Sarita Rani Patnaik, Aalaa Farag, Lena Brücker, Ann-Kathrin Volz, Sandra Schneider, Viola Kretschmer and Helen Louise May-Simera¹ 

Cilia Cell Biology, Institute of Molecular Physiology, Johannes-Gutenberg University, Mainz 55128, Germany

Background Information. Primary cilia are highly conserved multifunctional cell organelles that extend from the cell membrane. A range of genetic disorders, collectively termed ciliopathies, is attributed to primary cilia dysfunction. The archetypical ciliopathy is the Bardet–Biedl syndrome (BBS), patients of which display virtually all symptoms associated with dysfunctional cilia. The primary cilium acts as a sensory organelle transmitting intra- and extracellular signals thereby transducing various signalling pathways facilitated by the BBS proteins. Growing evidence suggests that cilia proteins also have alternative functions in ciliary independent mechanisms, which might be contributing to disease etiology.

Results. In an attempt to gain more insight into possible differences in organ specific roles, we examined whether relative gene expression for individual *Bbs* genes was constant across different tissues in mouse, in order to distinguish possible differences in organ specific roles. All tested tissues show differentially expressed *Bbs* transcripts with some tissues showing a more similar stoichiometric composition of transcripts than others do. However, loss of *Bbs6* or *Bbs8* affects expression of other *Bbs* transcripts in a tissue-dependent way.

Conclusions and Significance. Our data support the hypothesis that in some organs, BBS proteins not only function in a complex but might also have alternative functions in a ciliary independent context. This significantly alters our understanding of disease pathogenesis and development of possible treatment strategies.



Additional supporting information may be found online in the Supporting Information section at the end of the article.

Introduction

Primary cilia are highly conserved multifunctional cell organelles that extend from the cell membrane. These microtubule-based appendages are vital for development and homeostasis of different organs and tissues and play a role in transduction of intra- and extracellular signals. In contrast to motile cilia,

which are found on specialised tissues, primary cilia are a component of virtually all vertebrate cells, and functional defects cause a wide spectrum of clinical phenotypes. A range of genetic disorders, collectively termed ciliopathies, is attributed to primary cilia dysfunction. The archetypical ciliopathy is the Bardet–Biedl syndrome (BBS), patients of which display retinopathy, kidney dysfunction, obesity, polydactyly, behavioural dysfunction and hypogonadism [Forsythe and Beales, 2013].

The primary cilium acts as a sensory organelle transmitting intra- and extracellular signals [Ishikawa and Marshall, 2011] thereby transducing

¹To whom Correspondence should be addressed (email hmaysime@uni-mainz.de)

Key words: bardet-biedl syndrome, cilia, ciliopathy, gene regulation, mRNA.

Abbreviations: Arl6, ADP-ribosylation factor-like protein 6; ARVO, Association for Research in Vision and Ophthalmology; BBS, Bardet–Biedl syndrome; CCT/TRiC, chaperonin-containing TCP1 complex; cDNA, complementary deoxyribonucleic acid; DNA, deoxyribonucleic acid; DEPC, diethyl pyrocarbonate; GPCR, G protein-coupled receptor; Gapdh, glyceraldehyde 3-phosphate dehydrogenase; IFT, intraflagellar transport; Mkks, McKusick-Kaufman syndrome; mRNAs, messenger ribonucleic acids; OD, optical density; PCR, polymerase chain reaction; qRT-PCR, quantitative real-time polymerase chain reaction; RNA, ribonucleic acids; RNF2, RING finger protein 2; TOR, target of rapamycin; UK, United Kingdom; Usf1, upstream stimulatory factor 1.

This is an open access article under the terms of the Creative Commons Attribution-NonCommercial-NoDerivs License, which permits use and distribution in any medium, provided the original work is properly cited, the use is non-commercial and no modifications or adaptations are made.

various signalling pathways including Wnt [May-Simera and Kelley, 2012], Hedgehog [Goetz and Anderson, 2010], Notch [Ezratty et al., 2011], PDGF [Schneider et al., 2005], TOR [Yuan et al., 2013] and Hippo [Habbig et al., 2011]. Correct signal transduction is essential for tissue development and homeostasis and the Bardet–Biedl syndrome proteins have been shown to play a crucial role in this. To date, 23 BBS genes (BBS1 - 23) have been reported. Most recently two BBS disease causing loci have been found in other cilia associated genes, namely IFT74/BBS22 and SCAPER/BBS23 [Lindstrand et al., 2016; Schaefer et al., 2019; Wormser et al., 2019]. A subset of these genes encodes proteins that form an octameric complex termed the BBSome, which is crucial for ciliary trafficking [Jin et al., 2010]. The assembly of this complex is facilitated by chaperonin-like BBS proteins [BBS6/MKKS, BBS10 and BBS12; Seo et al., 2010; Zhang et al., 2012]. Although a defect in any BBS gene gives rise to a BBS diagnosis, there is a huge degree of phenotypic variation with no clear genotype to phenotype correlation even within families.

Growing evidence suggests that cilia proteins also have alternative functions in ciliary independent mechanisms. Such extraciliary functions include cell cycle regulation, non-ciliary trafficking, regulation of the DNA damage response, and transcriptional control [Vertii et al., 2015; Hua and Ferland, 2018]. In light of this, it is plausible that the BBSome and BBS chaperonin-like proteins also have alternative functions, possibly in an individual protein dependent manner. In an attempt to gain more insight into this, we examined whether relative gene expression for individual *Bbs* genes was constant across different tissues, in order to distinguish possible differences in organ specific roles. Furthermore, we wanted to examine the effect of *Bbs* protein loss on other BBSome or chaperonin-like components.

Results

Differential expression of BBSome transcripts across mouse tissues

To determine tissue specific expression levels of BBSome and chaperonin-like *Bbs* transcripts, we assessed their relative expression in a variety of adult mouse tissues. Quantitative real-time PCR (qRT-PCR) was used to examine the abundance of mRNA transcripts in brain, kidney, lung, spleen, heart, oviduct and

retina. Because alternative splicing can produce transcripts with different stabilities, we designed primers to recognise as many of the different *Bbs* transcripts as possible (Table 1). An important consideration is that expression levels of housekeeping genes can vary across tissues, therefore caution must be used when comparing gene expression levels across multiple tissues and normalizing to expression of a single housekeeping gene. We chose *Gapdh* as a housekeeping control gene since the expression of *Gapdh* was more stable across the tissues examined than *Uyf1* or other cytoskeletal markers (Supporting Information Figure 1). Furthermore we saw no differences in levels of *Gapdh* expression between either of our mutants and their littermate controls.

Our results show that *Bbs* transcripts are differentially expressed in different tissues when normalised against the housekeeping control *Gapdh* (Figure 1a–h). The expression levels of most BBSome transcripts were highest in the retina with the exception of *Bbs18* (Figure 1h). This correlates with the functional role of the BBSome in trafficking across the connecting cilium in photoreceptors [Datta et al., 2015]. Although the BBSome has a trafficking role in all cilia, the volume of traffic required to build and maintain the photoreceptor outer segment is particularly high and requires continuous turnover of ciliary trafficking proteins. Expression of *Bbs18* was most abundant in the spleen and oviduct.

Expression of BBSome transcripts within a tissue is not stoichiometric

Comparison of BBSome expression levels within a specific tissue revealed variable BBSome composition across different tissues. Expression of BBSome mRNAs were not stoichiometric, rather they were differentially expressed in specific tissues (Figure 2a–g). Interestingly, the expression profiles in brain and kidney were strikingly similar (Figures 2a and 2b). *Bbs1* was the most abundantly expressed transcript in brain and kidney, yet one of the least abundant transcripts in heart and oviduct (Figure 2a, 2b, 2e, and 2f). *Bbs18* was most abundant in the spleen, heart and oviduct, yet contributed the least in the retina (Figure 2g). Interestingly, *Bbs9* was highly abundant in the retina and spleen (Figures 2d and 2g). However, mutations in the *BBS9* gene have been implicated in nonsyndromic craniosynostosis [Barba et al., 2018]. These results

Table 1 | Gene symbol, primer sequences, primer efficiency for each evaluated Primer

Gene symbol	Primer sequences Forward n Reverse	Primer efficiency	Transcript identified
<i>Bbs1</i>	CCCTACTTCAAGTTCAGCCTG TCTGCCTTTTCCCTGATGTC	114.35%	ENSMUST0000053506.7
<i>Bbs2</i>	ACATTGCCCCACCTCTTG TCTTCCCATCACCGTCAAAG	115%	ENSMUST0000034206.5
<i>Bbs3</i>	GATACCTTCTGAATCACCCAG CCACGGCTTGTCTTAATGC	107.23%	ENSMUST0000023405.9 ENSMUST0000099646.3 ENSMUST00000118438.1 ENSMUST00000149797.1 ENSMUST0000026265.7
<i>Bbs4</i>	GCTCCAGACTTCCCTATTGTG GCATATTCACATAGCCCCTGAG	109.34%	
<i>Bbs5</i>	ACAAAGTCTATTCTGCCAGTCC AAATACGCCACAAAAGCATCC	98.31%	ENSMUST0000074963.8 ENSMUST00000112286.8 ENSMUST00000134659.7
<i>Bbs6</i>	GTGTGCTCTGCAAGATTTGG AAGACGTGCATTGCTGTTTG	97.74%	ENSMUST00000110089.8 ENSMUST0000028730.12
<i>Bbs7</i>	ATGGATCTGACGTTAAGCCG CCTTTTGTGTAGCCCTTGTCTTGAGGT	112.60%	ENSMUST00000108156.8 ENSMUST0000040148.10 ENSMUST00000108155.7 ENSMUST00000129671.1
<i>Bbs8</i>	GAGGCAGCTGATGTCTGGTACA CATTGGTGGGCCAAGTTTGT	98.25%	ENSMUST0000085109.9 ENSMUST0000079146.12
<i>Bbs9</i>	ACAAATCTCCTGTCAGTCTGC TCGTTGGGATGTTCTGGAAG	96.84%	ENSMUST00000147712.7 ENSMUST00000150395.7 ENSMUST0000039798.15 ENSMUST00000147405.7 ENSMUST00000127296.7 ENSMUST0000040454.4
<i>Bbs10</i>	TCCAGCCTCAGTTTTTCATCG ACTGAGATGCCTGAAACTGTG	111.39%	ENSMUST00000219990.1
<i>Bbs12</i>	CGCCGAGCATTGGATGTAG CATGCACACCCACACGT	104.30%	ENSMUST0000057975.7 ENSMUST00000108121.3
<i>Bbs18</i>	CCCTAAAATCTCTGACGCTGG TGCTTTTCTGCCATTTCTTG	102.75%	ENSMUST00000135402.3 ENSMUST00000236885.1 ENSMUST00000235348.1 ENSMUST00000236370.1 ENSMUST00000236098.1 ENSMUST00000235688.1 ENSMUST00000237049.1
<i>Gapdh</i>	CGACTTCAACAGCAACTCCCACTTCC TGGGTGGTCCAGGGTTTCTTACTCCT	99.58%	ENSMUST00000118875.7 ENSMUST00000117757.8 ENSMUST0000073605.14 ENSMUST00000183272.1

suggested either tissue-dependent differences in BBSome composition and/or protein half-life, or that some of these transcripts are required for alternative non-BBSome-related functions in different tissues.

Less variable expression of BBS chaperonin-like transcripts across mouse tissues

Next, we determined the gene expression patterns of the three chaperonin-like *Bbs* transcripts (*Bbs6/Mkks*, *Bbs10* and *Bbs12*; Figure 3). Overall, we saw less variation of these transcripts across different tissues.

With exception of lung and heart, which both had slightly higher levels of expression; the level of *Bbs6* was relatively constant (Figure 3a). The expression pattern of *Bbs10* was largely consistent across different tissues (Figure 3b). *Bbs12* expression varied the most, with lower expression in brain and kidney and higher expression in the spleen, oviduct and retina (Figure 3c).

When looking at these expression levels within specific tissues, we observe a similar stoichiometry of expression in brain and kidney (Figure 3d,e), akin

Figure 1 | Expression of BBSome transcripts

Bar charts showing gene expression of *Bbs1,2,4,5,7,8,9,18* in different tissues relative to *Gapdh*. Relative expression levels of each sample averaged. Error bars show standard error of the mean. $n = 4$ for all genes, *Bbs8* $n = 3$. Statistics were done using the Dunnett's multiple comparison test * $p \leq 0.05$; ** $p \leq 0.01$; *** $p \leq 0.001$; ns, not significant.

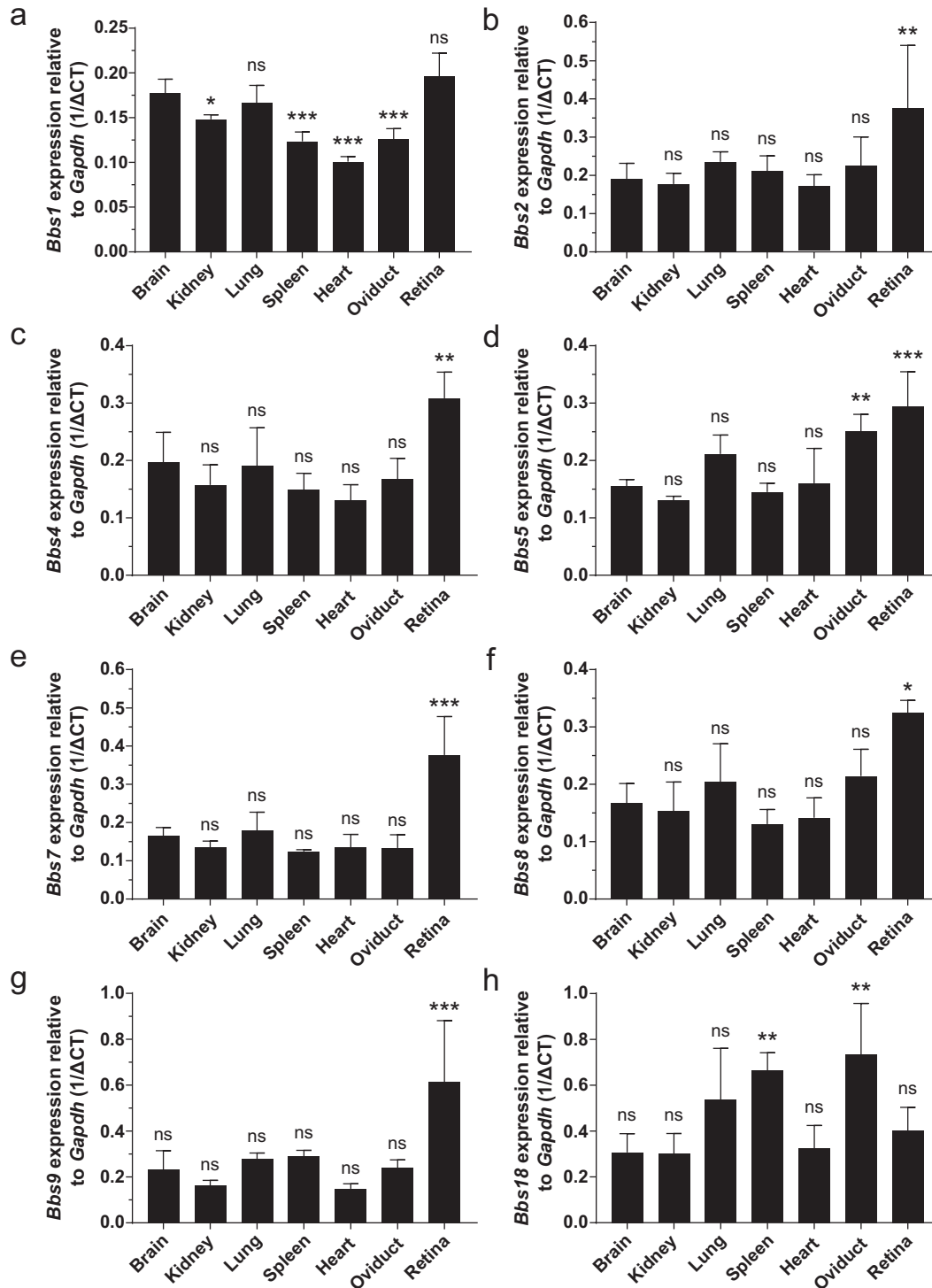
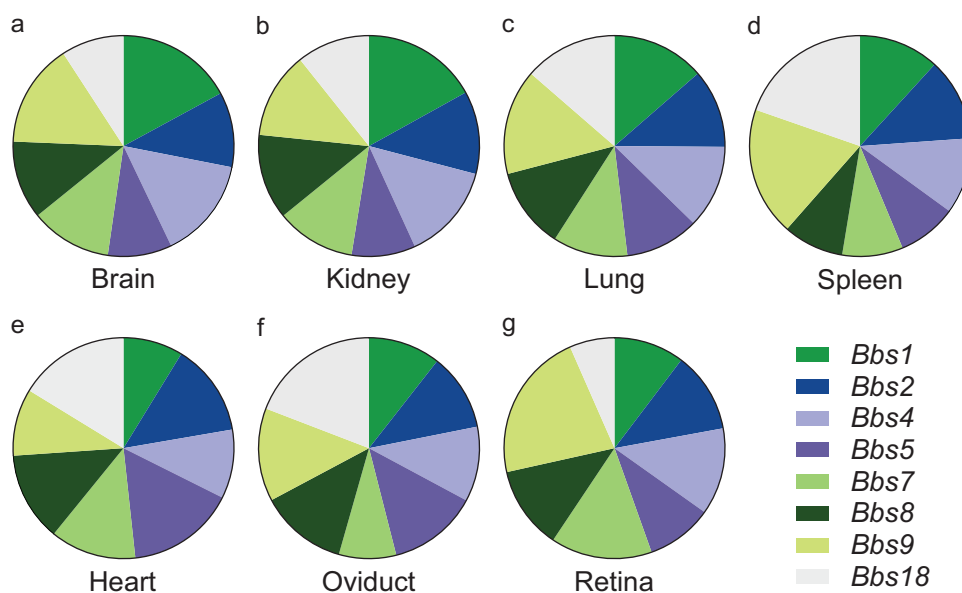


Figure 2 | Relative expression of BBSome transcripts

Pie charts showing relative gene expression of *Bbs1,2,4,5,7,8,9,18* in each tissue. Total expression of all BBSome transcripts is set at 100%. $n = 4$ for all genes, *Bbs8* $n = 3$.



to the trend seen for the BBSome transcripts. The one transcript that stands out is *Bbs12*, which is comparatively more abundant in spleen, oviduct and retina (Figure 3f–j). Overall, relative chaperonin-like *Bbs* expression levels within a specific tissue was less variable across tissues as compared to BBSome transcripts (Figures 3d–j and 2a–g).

Loss of *Bbs8* leads to altered expression of other *Bbs* transcripts

Previous studies from our lab have shown aberrant gene expression of ciliary proteins upon loss of BBS function [Patnaik et al., 2019]; however, very little is known about the transcriptional control of BBSome genes upon loss of one subunit. To assess the expression of BBSome subunits in the absence of *Bbs8/Ttc8*, we utilised a knock out mouse model. We measured mRNA expression levels of the other seven BBSome components as well as the three chaperonin-like genes in tissues harvested from adult *Bbs8^{+/+}* and *Bbs8^{-/-}* littermate mice.

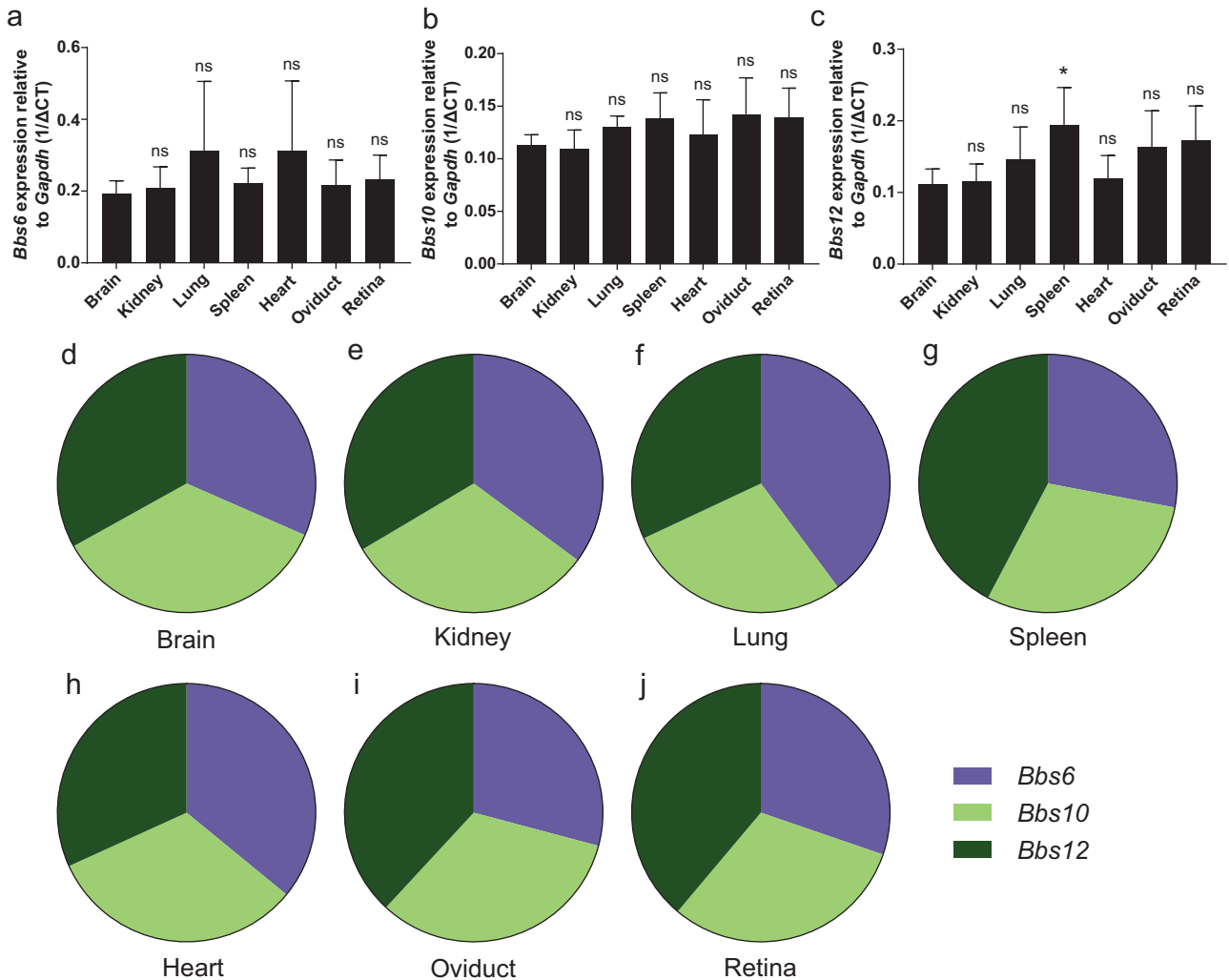
We observed significant changes in BBSome mRNA levels in the absence of *Bbs8* suggesting a possible transcriptional control mechanism (Figure 4a–n). mRNA levels were either lower or unchanged in *Bbs8^{-/-}* mice compared to *Bbs8^{+/+}* in all tissues

analysed (Figure 4a–n). We did not see a significant increase in mRNA expression of other BBSome subunits in an attempt to compensate for the loss. Intriguingly, the expression of *Bbs7* was significantly lower in all knock out tissues tested, while *Bbs9* did not show any significant changes in expression (Figures 4e and 4f). *Bbs18* was only downregulated in heart. Similar to what was observed above, expression patterns in brain and kidney were remarkably similar. In these two tissues, only *Bbs7* was significantly downregulated (Figures 4h and 4i). This could possibly suggest a similar mechanism of transcriptional control in these two organs. Other organs (lung, spleen, heart, oviduct, and retina) have numerous BBSome subunits that are significantly less expressed in *Bbs8^{-/-}* mice compared to control (Figure 4j–n). Since *Bbs3 (Arl6)* has extremely close functional links to the BBSome [Fan et al., 2004; Klink et al., 2017], we also analyzed the expression levels of this gene in *Bbs8^{-/-}* tissues. We found that *Bbs3* had a unique pattern of expression change that did not resemble any of the changes in expression for individual BBSome components (Supporting Information Figure 2a).

We next assessed the mRNA expression levels of chaperonin-like components in *Bbs8^{+/+}* and *Bbs8^{-/-}* tissues (Figure 5a–j). Again, we observe tissue- and

Figure 3 | Expression of BBS chaperonin-like transcripts

a–c) Bar chart showing gene expression of *Bbs6*, *Bbs10* and *Bbs12* in different tissues relative to *Gapdh*. Relative expression levels of each sample averaged. Error bars show standard error of the mean. Statistics were done using the Dunnett's multiple comparison test $*p \leq 0.05$; ns not significant. **d–j)** Pie charts showing relative gene expression of *Bbs6/Mkks*, *Bbs10* and *Bbs12* in each tissue. Total expression of all *Bbs*-chaperonin transcripts is set at 100%. $n = 5$ for *Bbs10* and 12, *Bbs6* $n = 3$.



gene-dependent differences. Loss of *Bbs8* affected the expression levels of all three transcripts, *Bbs6/Mkks*, *Bbs10* and *Bbs12*, variably (Figure 5a–c). In mutant mice *Bbs6* expression was reduced compared to control in brain, oviduct and retina, while *Bbs10* showed lower expression in lung and heart (Figures 5a and 5b). The expression of *Bbs12* was comparable between mutant and control with the exception of oviduct, in which *Bbs12* was increased (Figure 5c). This was the only case in which loss of *Bbs8* lead to

an increase in expression of an alternative *Bbs* gene. When focusing on individual tissues, brain and retina had a similar change in expression pattern, as well as lung and heart (Figures 5d, 5j, 5f and 5h). Decreased expression of *Bbs6* is only compensated by increased expression of *Bbs12* in oviduct (and not in brain or retina). This highlights a possible importance of *Bbs6* in the reproductive system. The expression of chaperonin-like genes were unaffected in kidney and spleen (Figures 5e and 5g).

Figure 4 | Expression of BBSome transcripts in *Bbs8*^{-/-} tissues

a–g) Bar chart showing gene expression of *Bbs1,2,4,5,7,8,9,18* in different tissues from *Bbs8*^{-/-} tissues relative to control *Bbs8*^{+/+} (red line). Coloured bars indicate significantly downregulated genes. Relative expression levels of each sample averaged. Error bars show standard error of the mean. ****p* ≤ 0.001, ***p* ≤ 0.01, **p* ≤ 0.05. **h–n)** Graphical representation of different tissue with respective genes downregulated (coloured boxes) in *Bbs8*^{-/-} tissues relative to control. Experiments were performed in triplicates from three individual animals.

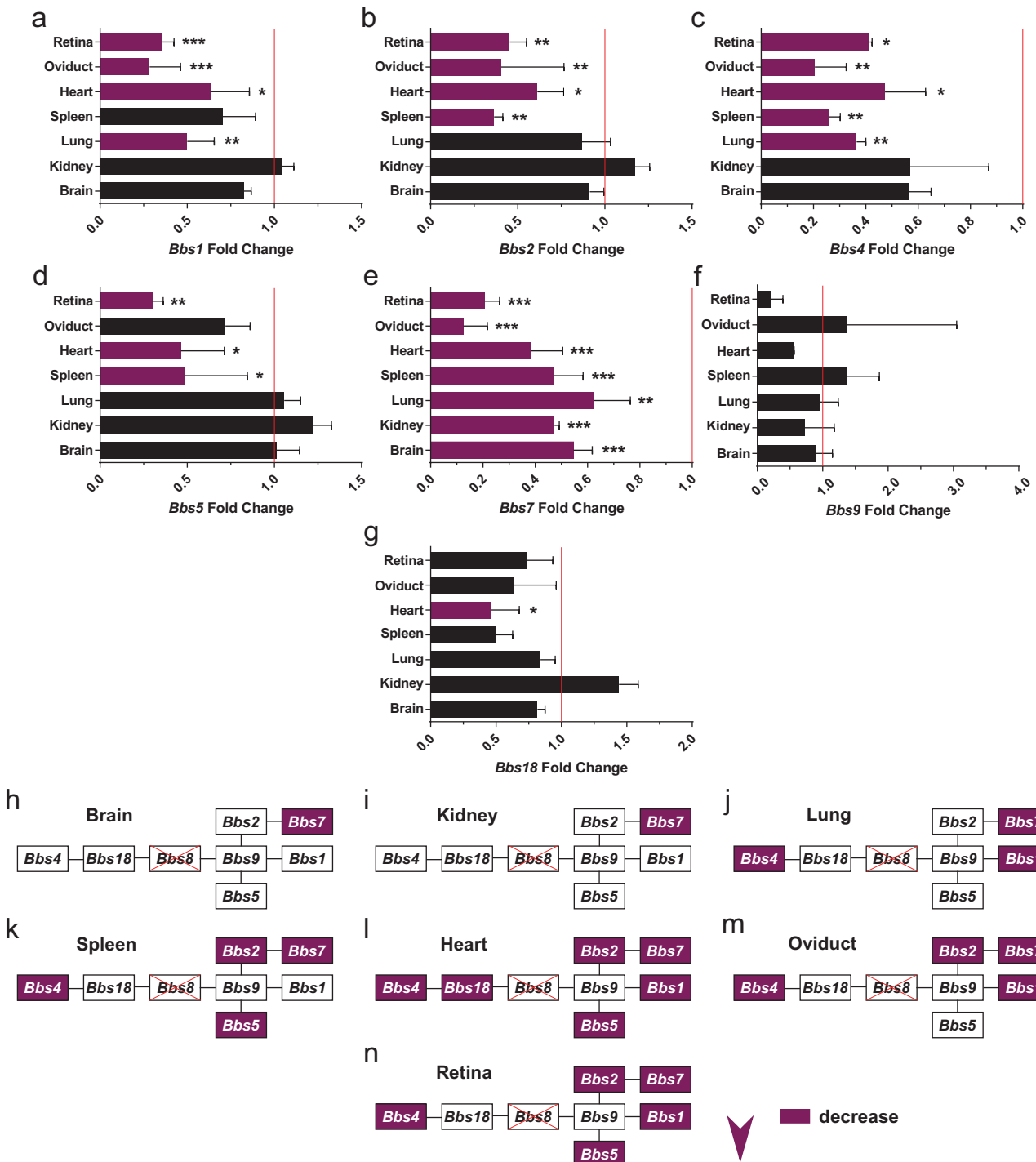
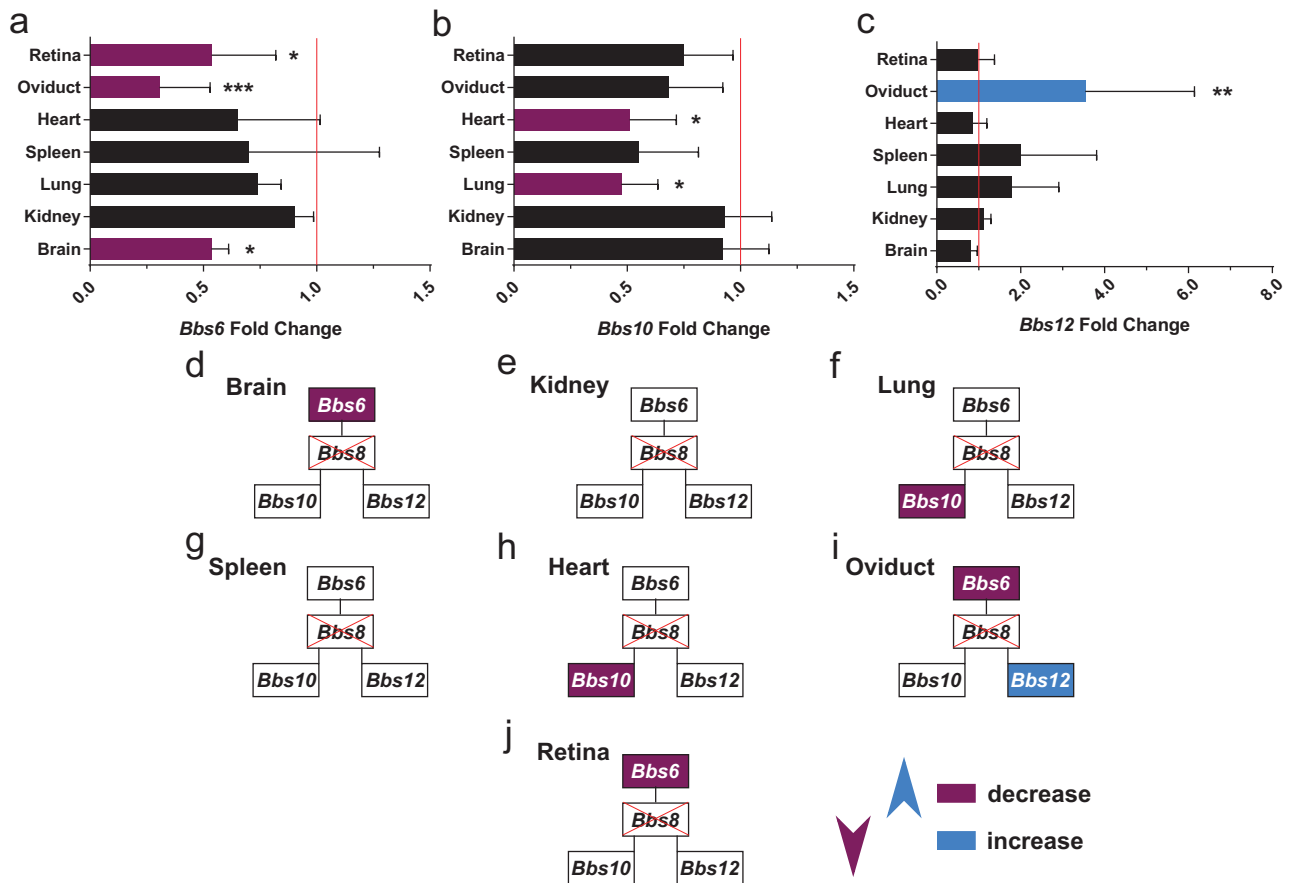


Figure 5 | Expression of BBS chaperonin-like transcripts in *Bbs8*^{-/-} tissues

a–c) Bar chart showing gene expression of *Bbs6*, *10* and *12* in different tissues from *Bbs8*^{-/-} tissues relative to control *Bbs8*^{+/+} (red line). Purple coloured bars indicate significantly downregulated genes, blue coloured bar indicates significantly upregulated gene. Relative expression levels of each sample averaged. Error bars show standard error of the mean. ****p* ≤ 0.001, ***p* ≤ 0.01, **p* ≤ 0.05. **d–j)** Graphical representation of different tissues with respective genes downregulated or upregulated (coloured boxes) in *Bbs8*^{-/-} tissues relative to control. Purple indicates significantly downregulated genes, blue significantly upregulated genes. Experiments were performed in triplicates from three individual animals.



Effect of *Bbs6* loss on other *Bbs* transcripts

Lastly, we examined the loss of a BBS chaperonin-like component on *Bbs* transcript expression. We started by analysing the expression variability of BBSome components in different tissues in *Bbs6*^{-/-} adult mice compared to *Bbs6*^{+/+} littermate controls. Perhaps unsurprisingly, in contrast to *Bbs8*^{-/-} mutant mice, the expression of BBSome mRNA remained stable in most tissues compared to the control, with the exception of spleen and lung (Figure 6a–o). All BBSome components except for *Bbs2* showed significantly higher expression in spleen (Figure 6l). In *Bbs6*^{-/-} lung *Bbs2*, *Bbs4* and *Bbs18* ex-

pression was increased (Figure 6k). This increased expression (albeit only in spleen and lung) is in contrast to the decreased expression of BBSome transcripts in *Bbs8*^{-/-} mice. As for the *Bbs8*^{-/-} tissue, we also analyzed the expression levels of *Bbs3* in *Bbs6*^{-/-} tissues. Similarly, we found that *Bbs3* also had a unique pattern of expression change upon loss of *Bbs6* (Supporting Information Figure 2b).

Similar to the BBSome transcripts, expression levels of chaperonin-like components were also less variable in *Bbs6*^{-/-} adult mice compared to controls (Figure 7a–i). The only differences were observed in spleen, in which *Bbs10* was significantly increased

Tissue-dependent differences in Bardet-Biedl syndrome gene expression Research article

Figure 6 | Expression of BBSome transcripts in *Bbs6*^{-/-} tissues

a-h) Bar chart showing gene expression of *Bbs1,2,4,5,7,8,9,18* in different tissues from *Bbs6*^{-/-} tissues relative to control (red line). Coloured bars indicate significantly upregulated genes. Relative expression levels of each sample averaged. Error bars show standard error of the mean. ****p* ≤ 0.001, ***p* ≤ 0.01, **p* ≤ 0.05. **i-o**) Graphical representation of different tissues with respective genes upregulated (coloured boxes) in *Bbs6*^{-/-} tissues relative to control. Experiments were performed in triplicates from three individual animals.

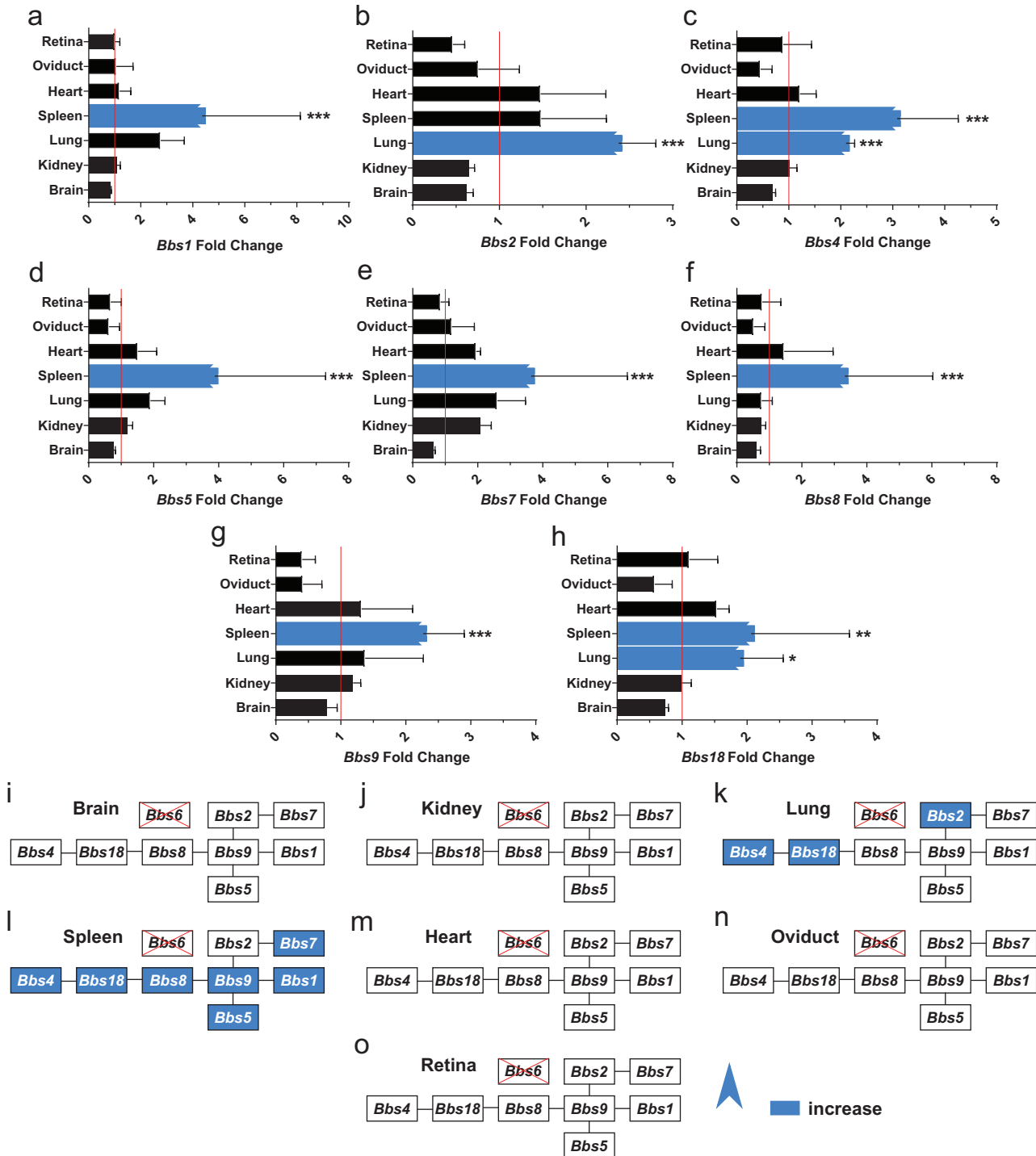
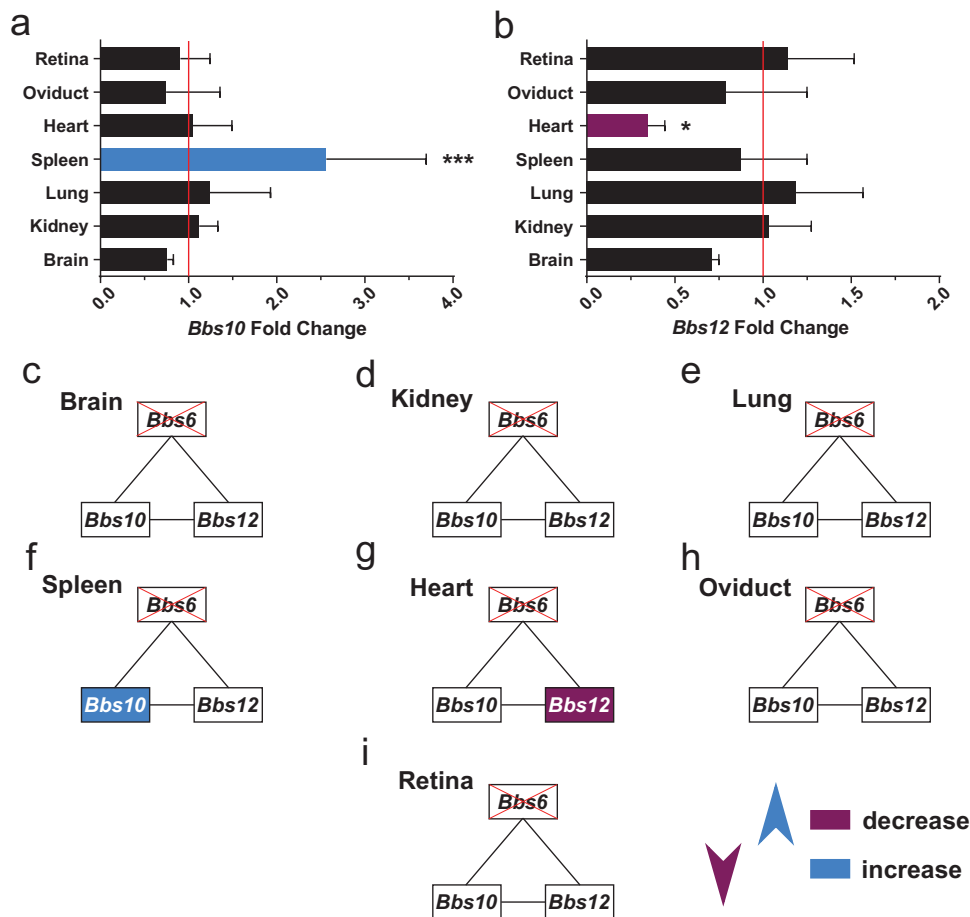


Figure 7 | Expression of BBS chaperonin-like transcripts in *Bbs6*^{-/-} tissues

a and **b**) Bar chart showing gene expression of *Bbs6*, *10* and *12* in different tissues from *Bbs6*^{-/-} tissues relative to control (red line). Blue coloured bar indicates significantly upregulated gene, purple coloured bars indicates significantly downregulated gene. Relative expression levels of each sample averaged. Error bars show standard error of the mean. ****p* ≤ 0.001, ***p* ≤ 0.01, **p* ≤ 0.05. **c–i**) Graphical representation of different tissues with respective genes upregulated or downregulated (coloured boxes) in *Bbs6*^{-/-} tissues relative to control. Blue indicates significantly upregulated genes, purple significantly downregulated genes. Experiments were performed in triplicates from three individual animals.



(Figure 7a and 7f), and in heart in which *Bbs12* was significantly decreased (Figures 7b and 7g). Overall, loss of the chaperonin-like component *Bbs6* did not have a profound effect on transcripts encoding BB-Some or chaperonin-like mRNA expression.

Discussion

Mutations in *BBS* genes cause a multitude of phenotypes affecting various organs and tissues. The predominant understanding is that BBS proteins facilitate ciliary membrane trafficking. In this context,

the BBSome proteins (BBS1, 2, 4, 5, 7, 8, 9 and 18) form an octomeric protein complex that bind GPCRs and other receptors as a cargo adaptor during IFT [Nachury et al., 2007; Klink et al., 2017; Liu and Lehtreck, 2018]. In particular, BBSome-mediated trafficking is crucial for retrieval of GPCRs back into the cell [Wei et al., 2012; Nager et al., 2017; Ye et al., 2018]. The *BBS* chaperonin-like genes encode proteins (BBS6, 10, 12) that form a complex with the CCT/TRiC family chaperonins which is essential for BBSome assembly. However, the idea that BBS proteins are only functional in a ciliary context

might be an oversimplification. In recent years, there has been increasing interest in highlighting functions of ciliary proteins at extra-ciliary sites and in non-ciliary contexts. Such functions include intracellular trafficking, regulation of the cytoskeleton, mitosis, cell cycle regulation, regulation of the DNA damage response and transcriptional control [Vertii et al., 2015; Hua and Ferland, 2018]. Several studies also suggest that some of the BBS proteins might take on extra-ciliary roles, possibly in a non BBSome/chaperonin dependent manner that could be relevant to the aetiology of the disorder [Novas et al., 2015]. Alternative functions might be dependent on both time point and tissue type.

To gain more insight into BBS functionality, we set out to examine whether relative gene expression for individual BBS genes was constant across different tissues. We wanted to test the stoichiometric composition of *Bbs* at the level of mRNA across tissues. We postulated that if the BBSome and Bbs chaperonin-like genes only encode proteins that function in a defined complex, then their relative expression levels should be stoichiometrically conserved between different tissues.

We found that *Bbs* transcripts are differentially expressed in different tissues. Overall, there was a higher degree of variation among BBSome transcripts as opposed to BBS chaperonin-like transcripts. These results suggested possible tissue-dependent differences in BBSome composition and/or protein half-life, or that some of these transcripts might also be required for alternative non-BBSome-related functions in different tissues. A more stoichiometric expression of BBS chaperonin-like transcripts suggests that their individual functions might be more closely coupled. Interestingly, several tissues had similar distribution of expression, which might allude to similar functionality on a molecular level. For example in brain and in kidney, the stoichiometry of both BBSome and BBS chaperonin-like transcripts were more similar compared to other tissues.

When we analysed mRNA expression of other BBSome components upon loss of BBSome component *Bbs8*, we observed that numerous transcripts were decreased, which might suggest a transcriptional control mechanism. Alternatively loss of *Bbs8* might have a stronger impact on tissue health or function and therefore a greater impact on overall gene transcription. Surprisingly, we did not see a significant

increase in mRNA expression of other BBSome subunits that would suggest compensation for the loss of *Bbs8*. Interestingly there was little consistency in which transcripts were affected with the exception of *Bbs7*, which was significantly decreased in all tissues examined, and *Bbs9*, which was stable across tissues. Loss of *Bbs8* also affected the expression of individual chaperonin-like genes differently. *Bbs6* and *Bbs10* were decreased in several tissues. In contrast, *Bbs12* was found to be upregulated in oviduct. As in the control tissues, several tissues "responded" in a similar manner, such as brain and kidney in terms of BBSome transcripts and brain and retina in terms of chaperonin-like transcripts, alluding to similar functionalities of these molecules in these tissues.

Loss of BBS chaperonin-like component *Bbs6* had little effect on the expression of BBSome transcripts in most tissues, yet surprisingly virtually all BBSome mRNAs in spleen and half in lung were upregulated. This might suggest that *Bbs6* has some alternative role in spleen and lung tissue that is not present in any of the other tissues. Loss of *Bbs6* also increased the expression of the other chaperonin-like component, *Bbs10*, but only in spleen. Again, this suggests a possible alternative molecular function of *Bbs6*, which is possibly more prevalent in spleen. Although spleen defects are not readily reported in BBS patients.

Since alternative splicing can produce transcripts with different stabilities, we designed primers to recognise as many of the different BBS transcripts as possible. Nonetheless, alternative transcripts could result in different mRNA levels, which might contribute to the differences in expression levels described above. Absolute expression values must always be measured in relation to a housekeeping control the selection of which is crucial. We chose *Gapdh*, since it was the best option available to us, but are aware that variation in expression of housekeeping controls across tissues, which can always distort comparisons.

While our approach reveals differences in transcription that presumably affect protein abundance and consequent function, we were unable to show this directly due to technical limitations related to BBS proteins. Antibodies against these proteins are notoriously inconsistent and difficult to use. Numerous Western blots were performed using various tissues but give that certain antibodies failed or either detected bands at incorrect sizes or in knock

out tissues, the data were unreliable. To overcome issues related to antibody specificity, protein abundance was also quantified via mass spectroscopy but proved imprecise due to the relatively low abundance of Bbs proteins in each sample.

As mentioned above previous studies have already shown that BBS protein functions are not restricted to the primary cilium. Such functions include intracellular trafficking. BBSome components have been found to assist retrograde dynein mediated melanosome transport in zebrafish [Yen et al., 2006] as well as trafficking of various receptor molecules (Notch and Vangl2) to the cell membrane [Leitch et al., 2014; May-Simera et al., 2015]. An active role in regulation of the cytoskeleton has also been shown for BBS4, 6 and 8 via manipulation of actin polymerisation [Hernandez-Hernandez et al., 2013]. Associations with the centrosome, centriolar satellites and the mid body might also underlie BBS4 and 6 facilitation of cell cycle regulation and mitosis [Kim et al., 2004, 2005; Zhang et al., 2014]. More recently, there have been reports showing that several BBS proteins enter the nucleus where they can influence gene expression through interactions with the polycomb group member protein RNF2 [Gascue et al., 2012; Scott et al., 2017].

Although our results suggest BBS proteins might have alternative functions independent of each other in different tissues, it is important to mention the evidence that argues against this hypothesis. Overall there is little evidence of a genotype–phenotype relationship among individuals affected with BBS, with a lack of tissue-specific defects in BBS patients carrying mutations in different BBS genes. The one exception here is the renal phenotype. A recent meta-analysis study in the Czech Republic found that the core BBSome subunits BBS2, 7 and 9 manifest as more critical in the kidney [Niederlova et al., 2019]. Similarly, the risk factor for severe renal disease were found to vary between patients harbouring BBS1, 2, 9, 10 or 12 mutations in a detailed study with 350 BBS patients in the UK [Forsythe et al., 2017]. An additional argument is that most functionally tagged BBSome proteins tend to show the same expression pattern (exclusively ciliary localisation) in cultured cells [Barbelanne et al., 2015; Ye et al., 2018]. Lastly, biochemical analyses have shown that the BBSome proteins consistently build one stable functional complex [Nachury et al., 2007; Klink et al., 2017].

In conclusion, we have seen that *Bbs* transcripts are not stoichiometrically expressed in different tissues and that loss of Bbs function affects expression of other transcripts differently. These data support the hypothesis that in some tissues at least, BBS proteins do not only function in a complex but might also have alternative functions in a ciliary independent context independent of one another.

Materials and methods

Animals

All mouse work was performed as per ethical approval from appropriate governing bodies. Experiments were performed in accordance with guidelines provided by Association for Research in Vision and Ophthalmology (ARVO). Animals were maintained on a cycle of 12 hours of light (200 lux) and 12 hours of darkness. The generation and characterisation of *Bbs6/Mkks* and *Bbs8/Ttc8* knock out (KO) mice have been previously described. For analysis of wild-type tissues, organs were harvested from C57BL/6 mice aged between 6 and 8 months. For comparison between control and *Bbs* knock out tissues, littermate controls of the same age were used in all experiments.

Biological materials

Mice were euthanised by cervical dislocation. Brain, kidney, lung, spleen, heart, oviduct and retina tissue samples were dissected from adult female mice. Tissues were placed immediately in TRIzol Reagent (Thermo Fisher Scientific) (for RNA) or snap frozen (for Western blotting) and stored at -80°C until further use.

RNA isolation

Total RNA was isolated from tissue samples using TRIzol Reagent (Thermo Fisher Scientific). Tissues were homogenised using a FastPrep[®]-24 classic (MP Biomedicals) bead-basher at a setting of six (6 m/s) for 20–60 s, periodically placing the samples on ice in between pulses. RNA extraction was performed according to manufacturer's instructions and stored at -80°C . RNA quality and quantity were measured using a Nanodrop ND-1000 spectrophotometer (Thermo Fisher Scientific) following manufacturer's instructions. Only samples with an $\text{OD}_{260/280}$ reading between 1.8 and 2.1 were used for gene qRT-PCR experiments.

Reverse transcription and qRT-PCR

For analysis of target gene mRNA expression, 4 μg of RNA was reverse transcribed into cDNA in a 20 μL reaction volume using the SuperScript[™] III first-strand synthesis system (Thermo Fisher Scientific) according to manufacturer's instructions.

Reverse transcription products were diluted in DEPC H_2O . The cDNA was diluted 1:50 or 1:20 while using *Gapdh* or *Bbs* primers respectively. One microliter of the diluted cDNA was used in each qPCR reaction, with a total volume of 10 μL . qRT-PCR amplification was performed using the SYBR[®]-Green reagent (Life Technologies) on a Step One Plus[™] Real-Time PCR machine (Applied Biosystems; Thermo Fisher Scientific,

Inc.). The thermocycler conditions were as follows: Initial denaturation at 95°C for 10 min, followed by 40 cycles of 95°C for 10 s, 60°C for 30 s; and a final extension at 72°C for 1 min. mRNA expression of the *Bbs* genes were calculated using the $2^{-\Delta\Delta Ct}$ method. All primer sequences used for qRT-PCR analysis are listed below (Table 1).

Melt curve analysis was performed to assess the amplification of single specific product (Supporting Information Figure 3). Primer amplification efficiency was determined prior to carrying out qPCR analysis (Table 1). Since alternative splicing can produce transcripts with different stabilities, we designed primers to recognise as many of the different BBS transcripts as possible (Table 1).

' ΔCt ' is the difference in expression of a gene of interest (*Bbs* genes) and the reference gene, namely *Gapdh*. '1/ ΔCt ' termed as 'expression factor' was used to show the relative gene expression across tissues. The expression factor (mean of 1/ ΔCt values) was used to make the pie charts. The expression factors of BB-Some mRNAs (*Bbs1*, *Bbs2*, *Bbs4*, *Bbs5*, *Bbs7*, *Bbs8*, *Bbs9* and *Bbs18*) in different organs were normalised to either brain or heart. The sum of normalised values of all BB-Some components in each organ was set as 100%. The percentage expression of individual *Bbs* gene was calculated and represented as a pie chart. Similarly, all three chaperonin-like gene expression percentages (*Bbs6*, *Bbs10* and *Bbs12*) are plotted as pie charts.

Statistical Analysis

Statistical differences between multiple groups were assessed using ANOVA followed by Dunnett's multiple comparison test (GraphPad Prism 6.0, GraphPad Software, San Diego, CA). Error bars represent the mean \pm standard deviation. Results are considered statistically significant if $p < 0.05$.

Author Contribution

S.R.P. and H.L.M.-S. were responsible for conception and experimental design. S.R.P., A.F., A.-K.V., L.B., S.S. and V.K. carried out experimental work. S.R.P. generated figures. S.R.P. and H.L.M.-S. co-wrote the manuscript.

Funding

This work was supported by the Alexander Von Humboldt Foundation, Johannes Gutenberg University, Mainz and the Deutsche Forschung Gemeinschaft (SPP2127).

Acknowledgements

The authors would like to thank Petra Gottlöber, Jana Kurpinski and Rike Hähnel for their technical assistance. They would also like to acknowledge the unwavering commitment of the animal care teams at the JGU, Mainz that made this research possible.

Conflict of interest statement

The authors have declared no conflict of interest.

References

- Barba, M., Di Pietro, L., Massimi, L., Geloso, M.C., Frassanito, P., Caldarelli, M., Michetti, F., Della Longa, S., Romitti, P.A., Di Rocco, C., Arcovito, A., Parolini, O., Tamburrini, G., Bernardini, C., Boyadjiev, S.A. and Lattanzi, W. (2018) BBS9 gene in nonsyndromic craniosynostosis: Role of the primary cilium in the aberrant ossification of the suture osteogenic niche. *Bone* **112**, 58–70
- Barbelanne, M., Hossain, D., Chan, D.P., Peränen, J. and Tsang, W.Y. (2015) Nephrocystin proteins NPHP5 and Cep290 regulate BBSome integrity, ciliary trafficking and cargo delivery. *Hum. Mol. Genet.* **24**, 2185–200
- Datta, P., Allamargot, C., Hudson, J.S., Andersen, E.K., Bhattarai, S., Drack, A. V., Sheffield, V.C. and Seo, S. (2015) Accumulation of non-outer segment proteins in the outer segment underlies photoreceptor degeneration in Bardet-Biedl syndrome. *Proc. Natl. Acad. Sci. U. S. A.* **112**, E4400–9
- Ezratty, E.J., Stokes, N., Chai, S., Shah, A.S., Williams, S.E. and Fuchs, E. (2011) A role for the primary cilium in notch signaling and epidermal differentiation during skin development. *Cell* **145**, 1129–1141
- Fan, Y., Esmail, M. A., Ansley, S.J., Blacque, O.E., Boroevich, K., Ross, A.J., Moore, S.J., Badano, J.L., May-Simera, H., Compton, D.S., Green, J.S., Lewis, R.A., van Haelst, M.M., Parfrey, P.S., Baillie, D.L., Beales, P.L., Katsanis, N., Davidson, W.S. and Leroux, M.R. (2004) Mutations in a member of the Ras superfamily of small GTP-binding proteins causes Bardet-Biedl syndrome. *Nat. Genet.* **36**, 989–993
- Forsythe, E. and Beales, P.L. (2013) Bardet–Biedl syndrome. *Eur. J. Hum. Genet.* **21**, 8–13
- Forsythe, E., Sparks, K., Best, S., Borrows, S., Hoskins, B., Sabir, A., Barrett, T., Williams, D., Mohammed, S., Goldsmith, D., Milford, D. V., Bockenbauer, D., Foggensteiner, L. and Beales, P.L. (2017) Risk factors for severe renal disease in Bardet–Biedl syndrome. *J. Am. Soc. Nephrol.* **28**, 963–970
- Gascue, C., Tan, P.L., Cardenas-Rodriguez, M., Libisch, G., Fernandez-Calero, T., Liu, Y.P., Astrada, S., Robello, C., Naya, H., Katsanis, N. and Badano, J.L. (2012) Direct role of Bardet-Biedl syndrome proteins in transcriptional regulation. *J. Cell Sci.* **125**, 362–375
- Goetz, S.C. and Anderson, K.V. (2010) The primary cilium: a signalling centre during vertebrate development. *Nat. Rev. Genet.* **11**, 331–344
- Habbig, S., Bartram, M.P., Muller, R.U., Schwarz, R., Andriopoulos, N., Chen, S., Sagmuller, J.G., Hoehne, M., Burst, V., Liebau, M.C., Reinhardt, H.C., Benzing, T. and Schermer, B. (2011) NPHP4, a cilia-associated protein, negatively regulates the Hippo pathway. *J. Cell Biol.* **193**, 633–642
- Hernandez-Hernandez, V., Pravincumar, P., Diaz-Font, A., May-Simera, H., Jenkins, D., Knight, M. and Beales, P.L. (2013) Bardet-Biedl syndrome proteins control the cilia length through regulation of actin polymerization. *Hum. Mol. Genet.* **22**, 3858–3868
- Hua, K. and Ferland, R.J. (2018) Primary cilia proteins: ciliary and extraciliary sites and functions. *Cell. Mol. Life Sci.* **75**, 1521–1540
- Ishikawa, H. and Marshall, W.F. (2011) Ciliogenesis: building the cell's antenna. *Nat. Rev. Mol. Cell Biol.* **12**, 222–234
- Jin, H., White, S.R., Shida, T., Schulz, S., Aguiar, M., Gygi, S.P., Bazan, J.F. and Nachury, M. V. (2010) The conserved Bardet-Biedl syndrome proteins assemble a coat that traffics membrane proteins to cilia. *Cell* **141**, 1208–1219

- Kim, J.C., Badano, J.L., Sibold, S., Esmail, M.A., Hill, J., Hoskins, B.E., Leitch, C.C., Venner, K., Ansley, S.J., Ross, A.J., Leroux, M.R., Katsanis, N. and Beales, P.L. (2004) The Bardet-Biedl protein BBS4 targets cargo to the pericentriolar region and is required for microtubule anchoring and cell cycle progression. *Nat. Genet.* **36**, 462–470
- Kim, J.C., Ou, Y.Y., Badano, J.L., Esmail, M.A., Leitch, C.C., Fiedrich, E., Beales, P., Archibald, J.M., Katsanis, N., Rattner, J.B. and Leroux, M.R. (2005) MKKS/BBS6, a divergent chaperonin-like protein linked to the obesity disorder Bardet-Biedl syndrome, is a novel centrosomal component required for cytokinesis. *J. Cell Sci.* **118**, 1007–1020
- Klink, B.U., Zent, E., Juneja, P., Kuhlee, A., Raunser, S. and Wittinghofer, A. (2017) A recombinant BBSome core complex and how it interacts with ciliary cargo. *Elife* **6**, e27434
- Leitch, C.C., Lodh, S., Prieto-Echagüe, V., Badano, J.L. and Zaghoul, N.A. (2014) Basal body proteins regulate Notch signaling through endosomal trafficking. *J. Cell Sci.* **127**, 2407–2419
- May-Simera, H.L., Petralia, R.S., Montcouquiol, M., Wang, Y.-X., Liu, Y., Szarama, K.B., Deans, M.R., Lin, W., Deans, M.R., Pazour, G.J. and Kelley, M.W. (2015) Ciliary proteins Bbs8 and Ift20 promote planar cell polarity in the cochlea. *Development* **142**, 555–566
- Lindstrand, A., Frangakis, S., Carvalho, C.M.B., Richardson, E.B., McFadden, K.A., Willer, J.R., Pehlivan, D., Liu, P., Pediaditakis, I.L., Sabo, A., Lewis, R.A., Banin, E., Lupski, J.R., Davis, E.E. and Katsanis, N. (2016) Copy-number variation contributes to the mutational load of Bardet-Biedl syndrome. *Am. J. Hum. Genet.* **99**, 318–336
- Liu, P. and Lehtreck, K.F. (2018) The Bardet-Biedl syndrome protein complex is an adapter expanding the cargo range of intraflagellar transport trains for ciliary export. *Proc. Natl. Acad. Sci. U. S. A.* **115**, E934–E943
- May-Simera, H.L. and Kelley, M.W. (2012) Cilia, Wnt signaling, and the cytoskeleton. *Cilia* **1**, 7
- Nachury, M. V., Loktev, A. V., Zhang, Q., Westlake, C.J., Peranen, J., Merdes, A., Slusarski, D.C., Scheller, R.H., Bazan, J.F., Sheffield, V.C. and Jackson, P.K. (2007) A core complex of BBS proteins cooperates with the GTPase Rab8 to promote ciliary membrane biogenesis. *Cell* **129**, 1201–1213
- Nager, A.R., Goldstein, J.S., Herranz-Pérez, V., Portran, D., Ye, F., Garcia-Verdugo, J.M. and Nachury, M.V. (2017) An actin network dispatches ciliary gpcrs into extracellular vesicles to modulate signaling. *Cell* **168**, 252–263.e14
- Niederlova, V., Modrak, M., Tsyklauri, O., Huranova, M. and Stepanek, O. (2019) Meta-analysis of genotype-phenotype associations in Bardet-Biedl syndrome uncovers differences among causative genes. *Hum. Mutat.* **40**, 2068–2087
- Novas, R., Cardenas-Rodriguez, M., Irigoín, F. and Badano, J.L. (2015) Bardet-Biedl syndrome: is it only cilia dysfunction? *FEBS Lett.* **589**, 3479–3491
- Patnaik, S.R., Kretschmer, V., Brücker, L., Schneider, S., Volz, A.-K., Oancea-Castillo, L.D.R. and May-Simera, H.L. (2019) Bardet-Biedl syndrome proteins regulate cilia disassembly during tissue maturation. *Cell. Mol. Life Sci.* **76**, 757–775
- Schaefer, E., Delvallée, C., Mary, L., Stoetzel, C., Geoffroy, V., Marks-Delesalle, C., Holder-Espinasse, M., Ghomid, J., Dollfus, H. and Muller, J. (2019) Identification and characterization of known biallelic mutations in the IFT27 (BBS19) gene in a novel family with Bardet-Biedl syndrome. *Front. Genet.* **10**, 21
- Schneider, L., Clement, C.A., Teilmann, S.C., Pazour, G.J., Hoffmann, E.K., Satir, P. and Christensen, S.T. (2005) PDGFR α signaling is regulated through the primary cilium in fibroblasts. *Curr. Biol.* **15**, 1861–1866
- Scott, C.A., Marsden, A.N., Rebagliati, M.R., Zhang, Q., Chamling, X., Searby, C.C., Baye, L.M., Sheffield, V.C. and Slusarski, D.C. (2017) Nuclear/cytoplasmic transport defects in BBS6 underlie congenital heart disease through perturbation of a chromatin remodeling protein. *PLoS Genet.* **13**, e1006936
- Seo, S., Baye, L.M., Schulz, N.P., Beck, J.S., Zhang, Q., Slusarski, D.C. and Sheffield, V.C. (2010) BBS6, BBS10, and BBS12 form a complex with CCT/TRiC family chaperonins and mediate BBSome assembly. *Proc. Natl. Acad. Sci. U. S. A.* **107**, 1488–1493
- Vertii, A., Bright, A., Delaval, B., Hehny, H. and Doxsey, S. (2015) New frontiers: discovering cilia-independent functions of cilia proteins. *EMBO Rep.* **16**, 1275–1287
- Wei, Q., Zhang, Y., Li, Y., Zhang, Q., Ling, K. and Hu, J. (2012) The BBSome controls IFT assembly and turnaround in cilia. *Nat. Cell Biol.* **14**, 950–957
- Wormser, O., Gradstein, L., Yogev, Y., Perez, Y., Kadir, R., Goliand, I., Sadka, Y., El Riati, S., Flusser, H., Nachmias, D., Birk, R., Iraqi, M., Kadar, E., Gat, R., Drabkin, M., Halperin, D., Horev, A., Sivan, S., Abdu, U., Elia, N. and Birk, O.S. (2019) SCAPER localizes to primary cilia and its mutation affects cilia length, causing Bardet-Biedl syndrome. *Eur. J. Hum. Genet.* **27**, 928–940
- Ye, F., Nager, A.R. and Nachury, M.V. (2018) BBSome trains remove activated GPCRs from cilia by enabling passage through the transition zone. *J. Cell Biol.* **217**, 1847–1868
- Yen, H.J., Tayeh, M.K., Mullins, R.F., Stone, E.M., Sheffield, V.C. and Slusarski, D.C. (2006) Bardet-Biedl syndrome genes are important in retrograde intracellular trafficking and Kupffer's vesicle cilia function. *Hum. Mol. Genet.* **15**, 667–677
- Yuan, S., Zhao, L. and Sun, Z. (2013) Dissecting the functional interplay between the TOR pathway and the cilium in zebrafish. *Methods Enzymol.* **525**, 159–189
- Zhang, Q., Yu, D., Seo, S., Stone, E.M. and Sheffield, V.C. (2012) Intrinsic protein-protein interaction-mediated and chaperonin-assisted sequential assembly of stable Bardet-Biedl syndrome protein complex, the BBSome. *J. Biol. Chem.* **287**, 20625–35
- Zhang, Y., Seo, S., Bhattarai, S., Bugge, K., Searby, C.C., Zhang, Q., Drack, A. V., Stone, E.M. and Sheffield, V.C. (2014) BBS mutations modify phenotypic expression of CEP290-related ciliopathies. *Hum. Mol. Genet.* **23**, 40–51

Received: 17 September 2019; Revised: 20 November 2019; Accepted: 28 November 2019; Accepted article online: 17 December 2019

9 Affidavit

I hereby declare in lieu of oath that I have prepared this dissertation independently and only with the help of the indicated aids.

I have not made any previous attempts at a doctorate.

Mainz,

Sandra Schneider